THÈSE

En vue de l'obtention du

DOCTORAT DE L'UNIVERSITÉ DE TOULOUSE

Délivré par : *l'Université Toulouse 3 Paul Sabatier (UT3 Paul Sabatier)*

Présentée et soutenue le *30/09/2022* **par :**

Naïs FARGETTE

Le rôle de la reconnexion magnétique dans la formation de cordes de flux et "switchbacks" dans l'héliosphère

-

The role of magnetic reconnection in the formation of flux ropes and switchbacks in the heliosphere

---

JURY

Karine ISSAUTIER	Rapporteuse	Directrice de recherche
Fouad SAHRAOUI	Rapporteur	Directeur de recherche
Aurélie MARCHAUDON	Examinatrice	Directrice de recherche
Tai PHAN	Examinateur	Senior Fellow
Marco VELLI	Examinateur	Professeur
Benoit LAVRAUD	Directeur de thèse	Directeur de recherche
Alexis P. ROUILLARD	Co-directeur de thèse	Chargé de recherche

---

École doctorale et spécialité :
SDU2E : Astrophysique, Sciences de l'Espace, Planétologie

Unité de Recherche :
Institut de Recherche en Astrophysique et Planétologie (UMR 5277)

Directeur(s) de Thèse :
Benoit LAVRAUD et *Alexis P. ROUILLARD*

Rapporteurs :
Karine ISSAUTIER et *Fouad SAHRAOUI*

And so, does the destination matter ? Or is it the path we take ? I declare that no accomplishment has substance nearly as great as the road used to achieve it. We are not creatures of destinations. It is the journey that shapes us.

BRANDON SANDERSON - The Way of Kings

A mes grands-parents, Olga et Yves, qui seraient si fiers.

Remerciements

La réalisation d'une thèse n'est pas un travail individuel. Ces trois dernières années n'auraient pas abouti à l'écriture de ce manuscrit sans la contribution et le soutien de mes collègues et de mes proches. On ne rend pas souvent ses lauriers à la chance après une étape de vie, et je souhaite ici reconnaitre la chance que j'ai eue d'être si bien entourée, encouragée et soutenue. Cela passe par l'expression de mon attachement et de ma reconnaissance envers celles et ceux qui ont contribué, directement et indirectement, à l'aboutissement de ma thèse mais, aussi, à la construction de la personne que je suis aujourd'hui.

En premier lieu je souhaite remercier mes directeurs de thèse, Benoit et Alexis. J'ai eu la chance d'être encadrée par des personnes exceptionnelles, humaines et passionnées, et je leur dois énormément dans ce travail. Cette thèse ne serait pas ce qu'elle est sans leurs idées, leur implication et leur encadrement basé sur la confiance mutuelle. Merci en particulier à Benoit pour sa grande disponibilité, son calme et sa bonne humeur.

Mes deux compagnons de bureau, Quentin et Victor, ont quant à eux toujours été là pour partager les hauts et les bas du quotidien de la thèse avec légèreté et humour. C'est une compagnie qui donne envie chaque matin de se rendre au laboratoire. Merci donc, car je n'aurais pas pu avoir de meilleurs co-bureaux. J'aimerais également remercier Om, Sid, Léa et Nicolas pour leur gentillesse à toute épreuve.

De manière plus large, je souhaite remercier tout le personnel de l'IRAP avec qui j'ai pu travailler, échanger, déjeuner... tous contribuent à instaurer dans le laboratoire une ambiance de travail bienveillante et chaleureuse que j'ai rarement trouvée ailleurs. En tout particulier merci à Philippe Louarn and Geneviève Soucail pour l'attention qu'ils portent au bien-être des doctorants dans leur rôle de direction, et à Dorine Roma qui - miraculeusement - rend toutes les démarches administratives simples et agréables.

A côté de la vie professionnelle, mon cercle familial est un de mes piliers les plus importants.

Je veux remercier mes parents pour tout le soutien qu'ils m'ont apporté, et pour le réconfort qu'ils ont toujours représenté. Toute réussite de ma part, je la leur dois en très grande partie. Je rends hommage à leur tolérance, leur intelligence, leur sensibilité, dont j'essaie de m'inspirer au quotidien. J'ai une pensée également pour mes grands-parents, qui n'ont pas pu assister à la partie la plus heureuse de ma vie, et à qui je dédie cette thèse. Eux m'ont appris que le courage ne se négociait pas, qu'il fallait de la volonté pour porter ses

convictions.

Merci à ma sœur, Amélie, qui me connait si bien, d'avoir toujours été là depuis mes un an pour recueillir mes états d'âmes. Sans elle le bateau Naïs aurait pris l'eau de toute part ! Une sœur qui rayonne partout où elle passe, et sur laquelle je sais que je peux compter. Je n'oublie pas Vivien et Angèle, un frère et une sœur dont j'admire les parcours. Avec l'un je partage le goût des sciences et des débats, et avec l'autre le goût des voyages et de l'aventure. Et puis je n'oublie pas Baghy, membre à part entière de cette famille, qui distribue les câlins ronronnants tous les matins.

J'aimerai également remercier Isabelle et Vincent, qui m'ont accueillie à mon arrivée à Toulouse et qui en continu durant cette thèse, m'ont proposé d'assister à des parenthèses artistiques bienvenues.

Merci enfin à ma famille étendue, Arlette, Claude, Cathy et Guillaume, de m'accueillir chaque été avec autant de gentillesse, c'est toujours une pause estivale ressourçante entre deux années de recherche acharnée.

Et puis,

Aux Pix'arts de Nantes, je dois deux années d'insouciance. Et même si nos liens se sont un peu distendus avec le temps, c'est toujours un plaisir de partager un moment avec eux, au détour d'une soirée ou d'un restaurant. Une pensée particulière pour Nathan, Joris et De Pat qui furent mes colocataires à différents moments. Un grand merci à Ulysse, Marie, Nathan et Nathan qui m'ont soutenue dans ma bataille contre le poulpe géant des calanques, qui a bien failli mettre fin à cette thèse.

Aux amis de Stockholm, Adrien, Ben, Sek, Félix, Fanny, Lucas, Marto, Iratxe, Charlotte, Théo, Florian et Florian je dois une grande partie de ma confiance en moi. Des années Erasmus qui forgent une personne, où me reviennent en flash des randonnées dans l'archipel de Stockholm, un voyage en Laponie, des cours de suédois... mais surtout des soirées ! Des années de fêtes pour profiter de la vie, que je suis ravie de prolonger aujourd'hui.

Et puis il y a ceux qui comptent énormément pour moi depuis maintenant presque douze ans : à Alice, qui a la capacité à mettre tout le monde à l'aise et à toujours organiser des tas de trucs, à Damien, la personne la plus extravertie que je connaisse, à Florian avec qui j'ai partagé mon plus beau voyage, à Hugo pour son ouverture d'esprit et sa capacité à me faire changer (un peu !) d'avis dans les débats, à Joyce pour son entrain et son enthousiasme, et qui s'est enfin convertie à la rando, à Kévin le gars sérieux parti aux US, qui n'arrivait pas à nous gérer à la cantine, à Lucas qui nous apprend quelles baies on peut manger dans la forêt, à Mariam la débrouillarde qui part en vadrouille solo cette année, à Philou sur qui on peut toujours compter quand ça ne va pas, à Robin qui me conseille les meilleurs livres, à Thomas, avec qui je peux parler foot, et à Yann pour ses conversations et ses histoires qu'on aime toujours écouter. En bref, un groupe du LOL parfait <3.

Enfin merci à Pierre, complice de chaque instant,
source de sérénité dans ce que j'entreprends,
avec qui je partage mes projets et mes rêves.

Abstract

Plasmas are ubiquitous in the universe where most matter is in such a state, constituting stars, the interplanetary, interstellar and intergalactic medium, nebulae, and so forth. In the solar system for instance, a plasma sphere (the Sun) continuously ejects into the interplanetary medium a plasma (the solar wind) that interacts with the plasmas (magnetospheres) surrounding the Earth or other planets. This makes the near-Earth environment a perfect astrophysical laboratory to study space plasmas. In plasma physics, magnetic reconnection is a fundamental process omnipresent in astrophysical systems. This unique mechanism converts magnetic energy into kinetic and thermal energy at kinetic scales, accelerating and heating the plasma while allowing a global reconfiguration of the magnetic topology. Spectacularly, changes induced on microscopic scales lead for instance to the drastic large-scale remodeling of a planet's or a star's magnetic field. In the past decades, various space missions have been launched to investigate the in-situ properties of astrophysical plasmas in the Sun-Earth environment, as well as to study the process of magnetic reconnection. They were equipped to unveil new features of their surrounding media, and in that they succeeded, particularly in bringing to light structures that were not observed before, either due to a lack of instrumental resolution or to the absence of previous data.

In this manuscript, we focus on structures observed both at the Earth's magnetopause and in the solar wind, and of significant importance to the dynamics of their environment. In our approach, we aim to shed light on the physical processes at stake for the formation of these structures, using modeling and statistical analysis to infer their properties and potential formation models.

In the first part of the manuscript, we present the investigation of a type of coherent magnetic structure often observed traveling along the Earth's magnetopause and carrying a significant amount of energy, called Flux Transfer Events (FTE). Particularly, a new type of FTE was observed with magnetic reconnection resolved in its core. Such a signature questions the usual model put forward to explain the internal structure of FTEs. Through a statistical analysis of FTE, we were able to better understand their magnetic topology and determine the factors playing a role in their occurrence, gaining insights into how they may be produced through magnetic reconnection at the dayside magnetopause. We also report on observations of similar structures in the solar wind, underlining that the process at work at the magnetopause is probably occurring in the solar wind as well.

In the second part of the manuscript, we move from the near-Earth environment to the inner heliosphere, focusing on magnetic switchbacks that are a key feature of the near-Sun solar wind. Magnetic switchbacks are deflections of the magnetic field, sometimes reversing the

radial component of the field, and made of accelerated plasma relative to the background solar wind. Through a systematic study of their characteristic scales and orientation, we highlight that switchbacks are probably linked to solar surface features like granulation and supergranulation, and we show that their properties are consistent with a formation through the process of interchange reconnection in the low solar atmosphere.

Magnetic reconnection is a common thread of this work, being ubiquitous at the Earth's magnetopause and in the solar wind, and most probably involved in the formation of switchbacks in the low corona as well. In the last part of the manuscript, we describe a new promising approach, based on visual identification, that permits to automatically detect magnetic reconnection exhausts in-situ in the solar wind. An automated detection algorithm may lead to large statistical analysis of reconnection jets in the solar wind, a significant step forward in understanding the process of magnetic reconnection.

Résumé

En physique des plasmas, la reconnexion magnétique est un processus fondamental, omniprésent dans les systèmes astrophysiques. Ce mécanisme remarquable convertit l'énergie magnétique en énergie cinétique et thermique sur des échelles cinétiques, de ce fait accélérant et chauffant le plasma tout en permettant une reconfiguration globale de la topologie du champ magnétique. De façon spectaculaire, les changements induits à l'échelle microscopique conduisent, par exemple, à un remodelage complet et à grande échelle du champ magnétique d'une planète ou d'une étoile. De par son accessibilité, l'environnement proche de la Terre est un parfait laboratoire astrophysique pour étudier les plasmas spatiaux. Ces dernières années, de nombreuses missions spatiales ont été lancées pour étudier les propriétés in situ des plasmas dans l'environnement Soleil-Terre, ainsi que le processus de reconnexion magnétique. Equipées pour dévoiler de nouvelles caractéristiques sur ces milieux, elles ont notamment mis en lumière des structures qui n'avaient pas été observées auparavant de part une résolution instrumentale insuffisante ou une absence de données antérieures.

Ce manuscrit se concentre sur des structures observées à la magnétopause terrestre d'une part et dans le vent solaire d'autre part, et qui ont un impact significatif sur leur environnement. Notre approche a pour but d'expliquer les processus de formation en jeu pour ces structures à travers des études statistiques.

Dans une première partie, nous étudions des structures magnétiques qui se propagent le long de la magnétopause terrestre, transportant des quantités importantes d'énergie et appelées Evènements de Transfert de Flux (FTE). Plus particulièrement, des FTE d'un nouveau genre ont été observés ces dernières années, présentant une signature de reconnexion magnétique en leur centre. Une telle observation remet en cause les modèles classiquement mis en avant pour expliquer leur structure interne. A travers une étude statistique des FTEs, nous avons pu mieux comprendre leur topologie magnétique et déterminer les facteurs environnementaux jouant un rôle dans leur apparition. Ces analyses nous renseignent sur les mécanismes de formation des FTE qui implique le processus de reconnexion magnétique sur le côté jour de la magnétopause. Nous présentons également des observations de structures similaires dans le vent solaire, soulignant que le processus en jeu à la magnétopause terrestre est probablement également à l'œuvre dans le vent solaire.

Dans une seconde partie, nous passons de l'environnement terrestre à l'héliosphère interne, où les switchbacks magnétiques sont omniprésents dans le vent solaire proche du Soleil. Les switchbacks sont des déflections du champs magnétique qui vont jusqu'à renverser sa composante radiale, et qui sont de plus accélérées par rapport au vent solaire ambiant. A travers une étude systématique de leurs échelles caractéristiques ainsi que de leur orientation, nous

montrons que les switchbacks sont probablement liés à des structures de surface telles que la granulation ou la supergranulation. Nous concluons que leurs propriétés sont cohérentes avec une formation dans la basse atmosphère à travers le processus de reconnexion d'interchange.

La reconnexion magnétique est un fil conducteur dans ce travail, omniprésente à la magnétopause terrestre et dans le vent solaire, et menant à la formation de structures impactant significativement leur environnement. Dans la dernière partie du manuscrit, nous présentons une nouvelle méthode prometteuse de détection automatique des signatures de jets de reconnexion, inspirée du processus d'identification visuelle de ces jets. Un tel algorithme de détection automatique permet d'envisager des études statistiques de jets de reconnexion observés dans le vent solaire, ce qui serait une avancée importante dans la compréhension du phénomène de la reconnexion magnétique.

Contents

Introduction (FR)

Ce chapitre est un résumé de l'introduction proposée au chapitre 1, introduisant les principaux éléments nécessaires à la compréhension du sujet. Cette section se base largement sur le livre Meyer-Vernet (2007).

Les plasmas

Dans notre environnement, les trois états classiques de la matière - solide, liquide, gazeux - nous sont familiers. De par une interaction quotidienne, leur définition nous vient naturellement, intuitivement, et c'est ensuite à travers de potentielles études qu'on apprend qu'au niveau microscopique, les liaisons entre les atomes diffèrent pour chaque état et confèrent ainsi à la matière des propriétés et des comportements différents. Un plasma est un état distinct de ces trois derniers, souvent appelé le quatrième état de la matière. Nous comprenons que lorsqu'un chauffage (par exemple) est appliqué à la matière, les liaisons atomiques s'affaiblissent, et un solide peut ainsi fondre en un liquide qui, lui-même, s'évaporera ensuite sous une forme gazeuse. L'état de plasma représente l'étape suivante, atteint lorsque suffisamment d'énergie est injectée dans le gaz pour que la cohésion des atomes eux-mêmes soit fragilisée. Cela mène à la séparation des ions et des électrons, qui forment alors un mélange de particules chargées. Plus globalement, un plasma est un gaz formé de particules chargées et/ou neutres, qui vérifie la quasi-neutralité en termes de charges électriques, qui a un comportement dit collectif et est influencé par les forces électromagnétiques.

Contrairement aux autres états de la matière, les plasmas sont rares sur Terre. On les trouve dans des phénomènes spectaculaires et hypnotiques comme les aurores boréales, les éclairs ou le feu, mais également - de manière moins poétique - dans certains écrans de télévision, des lampes fluorescent ou des expériences de laboratoires. Les plasmas sont en revanche omniprésents dans le reste de l'univers où la majorité de la matière visible est à l'état de plasma. Ils constituent les étoiles, les milieux interplanétaires, interstellaires, intergalactiques, les nébuleuses, etc. Dans le système solaire par exemple, une boule de plasma (le Soleil) émet continuellement dans le milieu interplanétaire un flot de plasma (le vent solaire), qui lui-même interagira avec les plasmas (les magnétosphères) qui entourent la Terre et d'autres planètes. Le système solaire, de par son accessibilité comparé au reste de l'univers, est un parfait laboratoire pour l'étude des plasmas astrophysiques, et de nombreuses missions spatiales ont été lancées dans ce but.

Dans un plasma, il existe une rétroaction constante entre le déplacement des particules chargées et la variation du champ électromagnétique. Caractériser le mouvement des particules

dans un plasma est un processus complexe, de par le nombre de particules en jeu et la nature de leurs interactions. Différentes approches existent, présentant chacune un certain niveau de complexité et de précision. Dans une approche particulaire, chacune des particules est caractérisée par sa position $\mathbf{r}$ et son vecteur vitesse $\mathbf{v}$. L'évolution du système dans le temps est ensuite calculée à travers les équations du mouvement. Une telle approche nécessite d'importantes capacités de calcul, et se trouve donc cantonnée à un nombre restreint de particules. Pour changer d'échelle, il est usuel d'utiliser la description cinétique des plasmas, c'est à dire d'étudier la fonction de distribution des particules dans l'espace des phases $f(\mathbf{r}, \mathbf{v}, t)$. Cette dernière quantité représente la probabilité d'observer des particules à un temps t et comprises dans un volume élémentaire six-dimensionnel dans l'espace des phases, centré en ($\mathbf{r}$, $\mathbf{v}$) avec des dimensions ($\mathbf{dr}$, $\mathbf{dv}$). L'évolution de la fonction de distribution dans un plasma non collisionnel est donnée par l'équation de Vlassov :

$$\frac{\partial f}{\partial t} + \mathbf{v} \cdot \frac{\partial f}{\partial \mathbf{r}} + \frac{d\mathbf{v}}{dt} \cdot \frac{\partial f}{\partial \mathbf{v}} = 0 \tag{1}$$

En fonction des échelles caractéristiques des phénomènes que l'on veut étudier, différentes approches peuvent être envisagées avec différents niveaux de complexité. En passant d'une description particulaire à une description cinétique puis à une description bi-fluide ou fluide, les exigences en termes de capacités de calcul changent, et par conséquent choisir une de ces approches est un équilibre à définir entre la description de la physique en jeu et la complexité du système que nous sommes prêts à envisager.

La reconnexion magnétique

La reconnexion magnétique est un processus fondamental de la physique des plasmas magnétisés, omniprésent dans les systèmes astrophysiques. Ce mécanisme remarquable convertit l'énergie magnétique en énergie cinétique et thermique sur des échelles cinétiques, de ce fait accélérant et chauffant le plasma tout en permettant une reconfiguration globale de la topologie du champ magnétique. Sur des temps suffisament longs dans les plasmas astrophysiques, les particules de plasmas sont dites gelées dans le champs magnétique (ou inversement). Cela signifie que des particules qui suivent une certaine ligne de champ n'ont pas la possibilité de se lier à une autre ligne de champs, on dit que la connectivité du plasma est conservée. Toutefois, de manière localisée dans le plasma, la condition de champ gelé peut ne plus être vérifiée, ce qui entraine une reconfiguration de la topologie du champ magnétique ainsi qu'un transfert d'énergie, c'est le processus de reconnexion magnétique.

Une configuration typique de la reconnexion magnétique en deux dimensions est reproduite en Figure 1. Dans ce schéma, deux écoulements de plasma convergent l'un vers l'autre et forment une région de courant électrique intense - appelée feuille de courant - à leur interface. L'endroit où les particules se désolidarisent du champ magnétique et où les lignes de champs perdent leur connectivité d'origine se nomme la région de diffusion. Ici, les différentes espèces de particules (ions, électrons) ne se comportent pas de la même manière. Les ions se découplent du champ magnétique dans la région de diffusion ionique (IDR) au sein de laquelle les électrons restent liés au champ. La démagnétisation des électrons s'effectue dans la plus petite région de diffusion électronique (EDR) comprise dans l'IDR. Dans ces zones, les lignes de champs magnétique voisines et de polarité opposée se "brisent" puis se

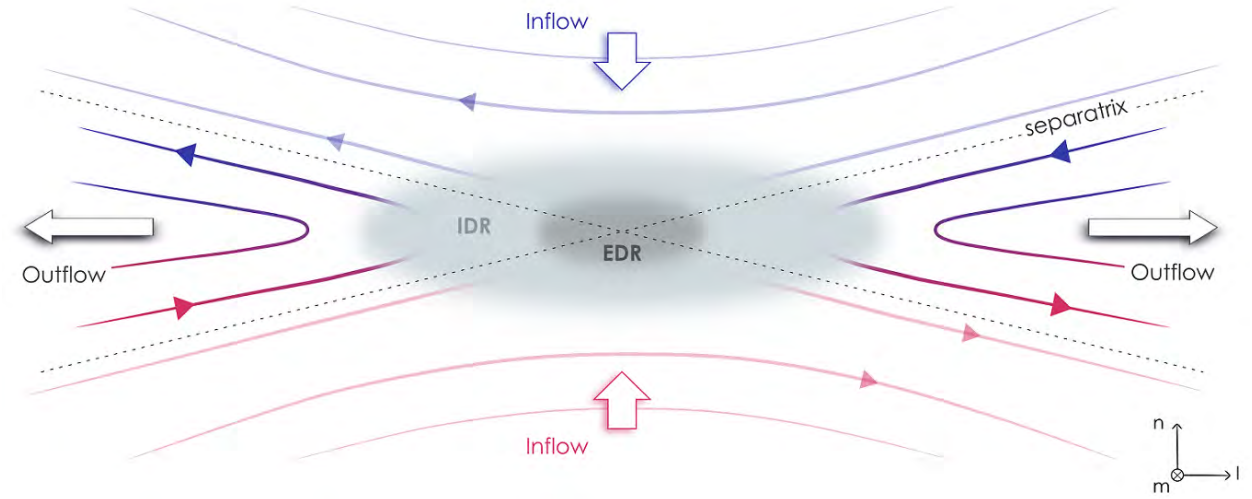

FIGURE 1 : Topologie 2D d'un site de reconnexion magnétique. Les flèches blanches représentent la vitesse du plasma et les lignes de champ magnétique sont colorées par le signe de leur composante l. Les lignes de champs reconnectées sont en gras, et les séparatrices sont en lignes pointillées.

reconnectent avec leur vis-à-vis, mixant donc deux plasmas auparavant imperméables l'un à l'autre. De nouvelles lignes de champs coudées sont ainsi créées et éjectées dans un écoulement de plasma chauffé et accéléré, tangentiel à la feuille de courant. Par ce processus, l'énergie magnétique est convertie en énergie cinétique et thermique, produisant ce qu'on appelle des jets de reconnexion.

C'est donc par le processus de reconnexion magnétique que, de façon spectaculaire, des changements induits à l'échelle microscopique conduisent par exemple à un remodelage complet et à grande échelle du champ magnétique d'une planète ou d'une étoile. Les paragraphes suivants illustrent d'ailleurs le rôle fondamental que joue la reconnexion dans la dynamique du système Soleil-Terre.

L'environnement Soleil-Terre

Le Soleil

L'étoile de notre système solaire est une boule de plasma incandescente située à 150 millions de kilomètres (une unité astronomique) de notre Terre. S'il est de sens commun que le Soleil est nécessaire à la vie sur Terre, il peut également affecter notre quotidien à travers un phénomène moins connu, son activité magnétique. Dans cette section nous décrivons certains phénomènes de surface du Soleil et les aspects topologiques clef du champ magnétique solaire.

Phénomènes de surface

Le soleil est constitué d'un noyau, d'une enveloppe interne radiative et d'une enveloppe externe convective. Si la zone radiative tourne de manière rigide à l'intérieur de l'étoile, l'enveloppe convective elle présente une rotation différentielle en latitude, avec des pôles

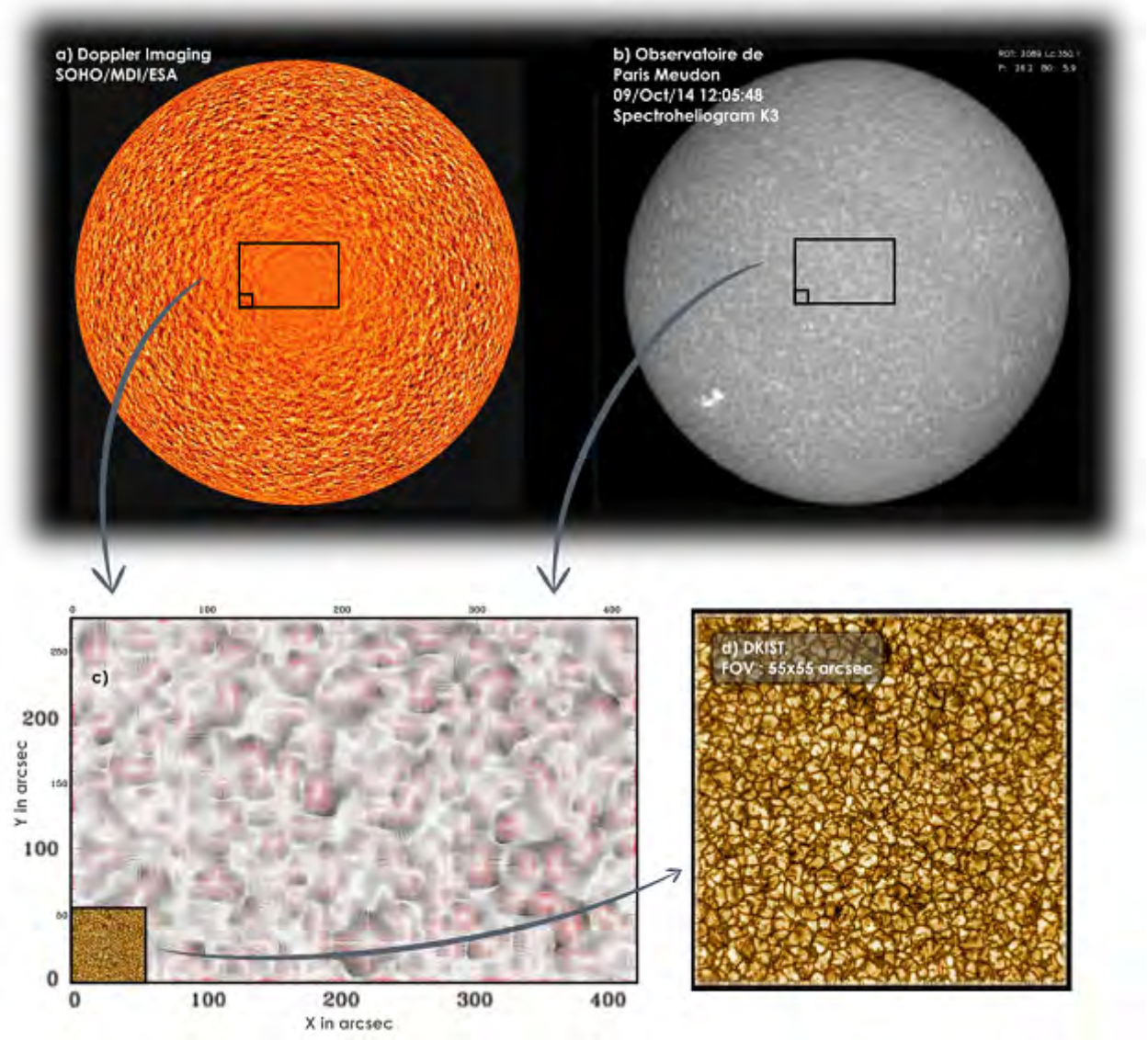

FIGURE 2 : La supergranulation et la granulation. Le panneau *a* est un dopplergramme du soleil, le panneau *b* une image du réseau photosphérique dans la raie du Ca+ K3 à 393.37 nm. Le panneau *c* montre l'échelle de la supergranulation avec le champ de vitesse tracé et les contours de sa divergence superposés (Rieutord et al., 2008). Le panneau *d* montre les échelles de la granulation à travers un image obtenue avec le DKIST télescope sur un champ de vue de 55x55 arcsec (Rimmele et al., 2020). Figure adaptée de Rieutord et al. (2008)

tournant plus lentement (période de 34 jours) que l'équateur (27 jours) (Spiegel & Zahn, 1992). Ce phénomène est visible sur la surface du soleil, aussi appelée photosphère. En plus de la rotation différentielle, la photosphère présente des motifs cellulaires visibles à deux échelles spatiales distinctes illustrés en Figure 2, on parle de supergranulation et de granulation. La supergranulation est un motif cellulaire détecté dans les champs de vitesse à la surface du Soleil au moyen de dopplergrammes (panneau 2*a*). Ses échelles caractéristiques sont de l'ordre de 30 Mm avec un temps dynamique de 24 à 48 h (Rincon & Rieutord, 2018). L'origine de ce phénomène semble complexe et demeure un sujet de recherche aujourd'hui. Par ailleurs, la

supergranulation et le champ magnétique de surface (panneau 2*b*) sont corrélés , et les lignes de champs magnétiques sont ancrées à la frontière des supergranules (Roudier et al., 2009; Wedemeyer-Böhm et al., 2009). La granulation solaire quant à elle (panneau 2*d*), intervient sur de plus petites échelles de l'ordre de 1 Mm et 10 minutes. Elle est associée à des cellules de convection qui résultent du transfert thermique à l'intérieur du soleil.

Le champ magnétique solaire

La configuration du champ magnétique solaire varie en fonction du temps et suit un cycle de 11 ans appelé le cycle solaire. Ce cycle est particulièrement visible lors de l'observation des tâches solaires, des régions assombries de la photosphère associées à des chutes locales de température de surface et à un fort champ magnétique. Le nombre de tâches solaires varie avec une période de 11 ans, ce qui est visible en Figure 3, et on appelle maximum solaire et minimum solaire les périodes associées aux extrema de cette courbe. Ces deux périodes sont associées à des niveaux d'activité du Soleil très différents, avec un Soleil calme durant le minimum solaire et un Soleil présentant de nombreux phénomènes éruptifs pendant le maximum solaire. La configuration du champ magnétique solaire change également drastiquement en fonction de ces périodes. La Figure 3 montre les observations de la mission Ulysses durant un cycle solaire complet (Figure de McComas et al. (2003)) ainsi que deux schémas représentant la structure du champ magnétique solaire pour chaque période d'activité (schémas de Suess et al. (1998)). Les images du Soleil (en UV) et de la couronne qui l'entoure (en lumière blanche) sont caractéristiques des périodes de minimum et maximum solaire. Les structures lumineuses de la couronne soulignent la structure du champ magnétique et correpondent aux schémas du haut de l'image. Durant le minimum solaire, le champ magnétique solaire adopte une structure dipolaire., tandis que durant le maximum solaire, la configuration est multipolaire. Lorsque le Soleil passe d'une période calme à une période active, le nombre d'évènements éruptifs se multiplie jusqu'à atteindre un pic au maximum solaire.

Le vent solaire

Le Soleil émet continuellement dans le milieu interplanétaire un écoulement de particules chargées appelé vent solaire. Ce plasma est constitué principalement de protons (H^+), d'ions alpha (H_e^{2+}) et d'électrons. Le vent solaire est souvent décomposé en deux catégories, le vent lent et le vent rapide. En plus de présenter des vitesses distinctes, ces deux types de vent diffèrent par leur densité, leur composition et leur variabilité. Le vent solaire lent ($\sim$ 400 km/s) est dense ($\sim$ 7 cm^{-3}) et structuré, tandis que le vent solaire rapide ($\sim$ 750 km/s) est ténu ($\sim$ 2.5 cm^{-3}) et plus uniforme. Ils ne semblent pas non plus provenir des mêmes sources à la surface du Soleil. Cela est illustré par les vitesses de vent mesurées par Ulysses et présenté en Figure 3. Durant le minimum solaire, il est clair que le vent rapide provient des pôles, tandis que le vent lent est concentré près de l'écliptique. Au maximum solaire, les vitesses comme le champ magnétique sont moins organisées, avec les deux types de vents observés à toutes les latitudes.

Le champ magnétique du vent solaire, aussi appelé champ magnétique interplanétaire (IMF pour l'acronyme anglais), est gelé dans le plasma du vent solaire et advecté dans le milieu interplanétaire. En raison de la rotation du Soleil, les lignes de champ de l'IMF prennent une forme de spirale appelée la spirale de Parker (Parker, 1958). L'angle de cette spirale dans

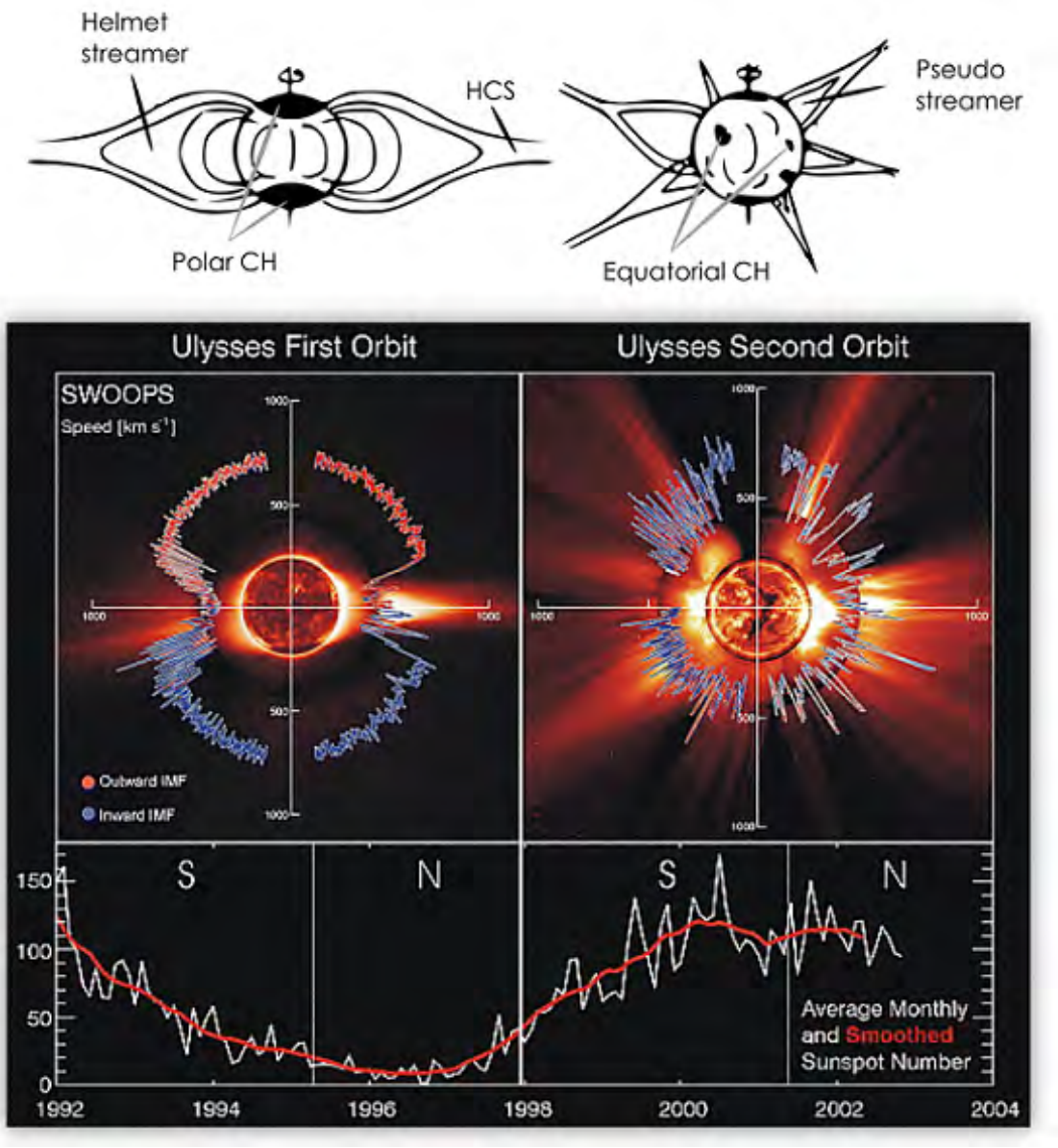

FIGURE 3 : Champ magnétique solaire et cycle solaire. Les schémas de Suess et al. (1998) en haut de l'image représentent la structure du champ magnétique solaire en période de minimum (gauche) et maximum (droite) solaire. La Figure associée de McComas et al. (2003) montre les observations de la mission Ulysse de la vitesse du vent solaire en fonction de la latitude. Les images du Soleil sont obtenues grâce à l'observatoire spatial SOHO et au coronographe de Mauna Loa (voir McComas et al. (2003)). Le panneau du bas montre le nombre de tache solaire en fonction du temps sur la période d'observation de la mission Ulysses.

l'écliptique α_p peut être calculée à travers l'équation :

$$\alpha_p = \arctan\left(\frac{-\Omega_\odot\,(r - r_0)}{V_r}\right) \tag{2}$$

avec $\Omega_\odot = 2.9 \times 10^{-6}$ s^{-1} le moment angulaire du Soleil (ici pris à l'équateur), r la distance

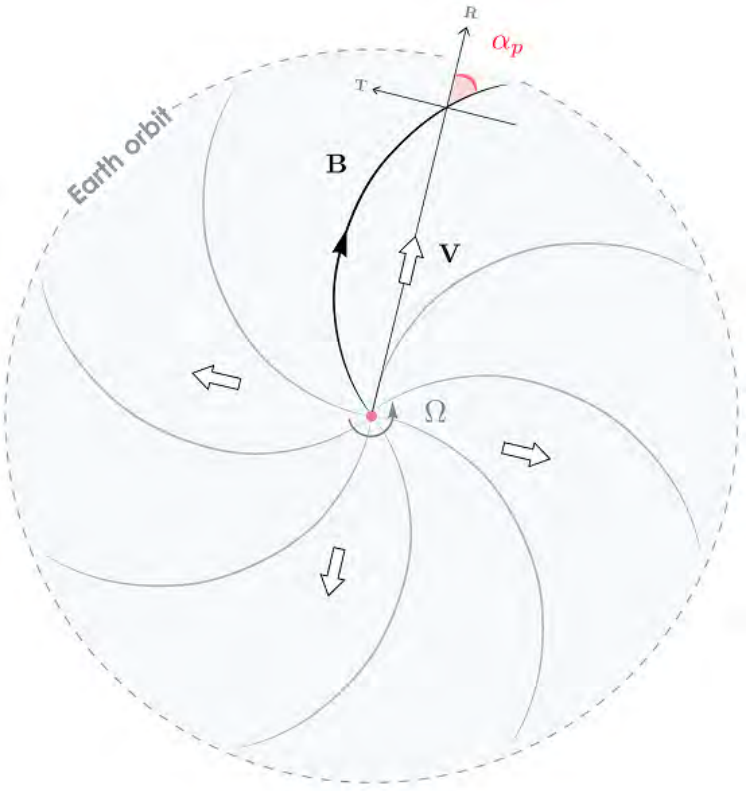

FIGURE 4 : Illustration de la spirale de Parker. Les lignes de champ magnétique sont représentées par des lignes grises, et la vitesse du vent solaire par des flèches blanches. Sur une ligne de champ particulière, l'angle de spirale de Parker α_p est mis en évidence près de l'orbite terrestre dans le plan RTN, tel que défini dans l'éq. (2). Figure adaptée de Parker (1958).

au Soleil, r_0 la distance source de la spirale de Parker et V_r la vitesse radiale du vent. Près du Soleil, l'angle de la spirale est proche de zéro et le champ magnétique est radial. A l'orbite de la Terre, l'IMF possède un angle d'environ 45° avec la direction radiale. Cette configuration est illustrée dans la Figure 4.

Si le vent solaire avait le dernier mot, toute planète se trouvant sur son passage se retrouverait stérile et inhabitable. Les particules chargées du vent enlèveraient continuellement la matière atmosphérique de la planète et bombarderaient sa surface. Certaines planètes, cependant, développent de puissants boucliers magnétiques contre le vent solaire et les éruptions solaires, on les appelle des magnétosphères.

La magnétosphère terrestre

La magnétosphère d'une planète est la région entourant la planète dans laquelle son champ magnétique propre est prédominant (Chapman et al., 1930). Le champ magnétique interne des planètes est généré par un effet dynamo dû à la rotation de leur cœur métallique (Russell, 1993). Plusieurs planètes du système solaire possèdent une magnétosphère intrinsèque, à savoir Mercure, la Terre, Jupiter, Saturne, Uranus et Neptune, tandis que Mars et Vénus en sont dépourvues. La magnétosphère terrestre est remplie d'un plasma ténu, froid et à fort

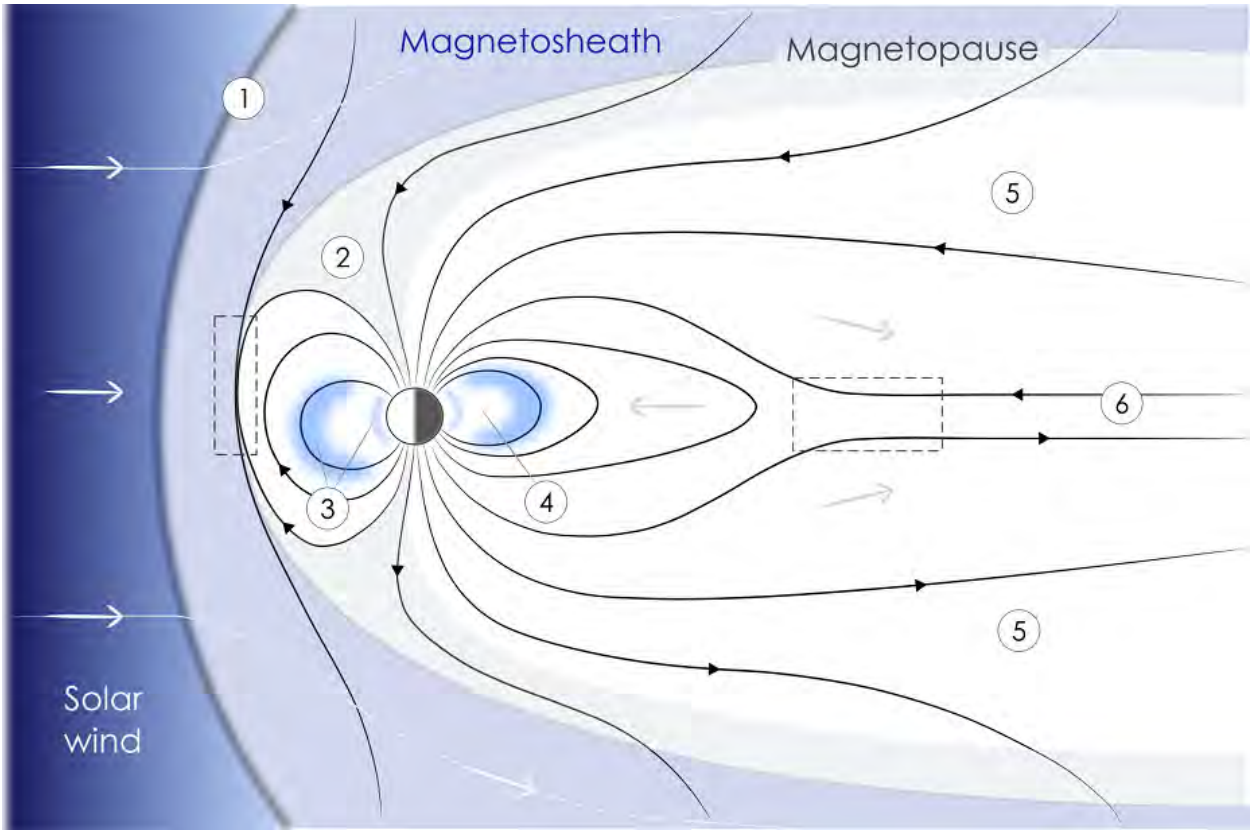

FIGURE 5 : Illustration de l'environnement terrestre proche et des régions qui résultent de l'interaction entre le vent solaire et la magnétosphère terrestre. Cette dernière est délimitée par la magnétopause. Les lignes de champ magnétique sont représentées par des lignes noires pleines tandis que l'écoulement global du plasma est représenté par des flèches ponctuelles fines. Diverses frontières et régions d'intérêt sont indiquées : 1) l'arc de choc, 2) les cornets polaires, 3) les ceintures de radiation de Van Allen, 4) la plasmasphère, 5) les lobes de la queue magnétosphérique et 6) la feuille de plasma. Les rectangles en pointillés indiquent les endroits où la reconnexion magnétique est favorisée pour un IMF orienté vers le sud. Figure adaptée de Lang (2013).

champ magnétique, dont la frontière externe est appelée la magnétopause. L'environnement spatial proche de la Terre est illustré en Figure 5. On y retrouve plusieurs régions d'importance. La présence d'un obstacle (la planète) dans un écoulement supersonique crée un choc appelé arc de choc, frontière au-delà de laquelle le vent solaire devient subsonique. Il rentre alors dans la magnétogaine, une région turbulente située entre l'arc de choc et la magnétopause, où le vent solaire s'écoule autour de la magnétosphère. La magnétosphère elle-même prend une forme particulière. Son dipôle originel est compressé côté jour par le vent solaire et étiré côté nuit en une longue queue magnétique. A la magnétopause, on trouve les cornets polaires, indentations situées aux pôles où le plasma de la magnétogaine peut interagir directement avec l'ionosphère (couche supérieure de l'atmosphère terrestre). A l'intérieur de la magnétosphère, les ceintures de radiation de Van Allen sont des régions en forme de tore contenant des particules de haute énergie provenant du vent solaire et piégées dans le champ magnétique terrestre. La plasmasphère quant à elle possède un plasma de basse énergie provenant de l'ionosphère. Enfin la feuille de plasma est la région de lignes de champ fermées

qui s'étend dans la queue de magnétosphère équatoriale et qui contient un plasma plus dense et plus chaud d'origine solaire et ionosphérique.

L'interaction dynamique entre la magnétosphère et l'IMF se fait à travers le processus de reconnexion magnétique[1] (Dungey, 1962). Des régions de cisaillement magnétique élevé - qui favorisent les conditions d'apparition de la reconnexion magnétique - apparaissent à différents endroits de la magnétopause en fonction de l'orientation de l'IMF. Côté jour, le champ magnétique terrestre est orienté vers le nord, par conséquent lorsque l'IMF est orienté vers le sud, la reconnexion est favorisée au point subsolaire. Les lignes de champ reconnectées sont alors advectées au-dessus des pôles, transférant l'énergie du vent solaire à la queue magnétique. En revanche, lorsque l'IMF est orienté vers le nord, la reconnexion côté jour se produit à des latitudes plus élevées, au-dessus des cornets polaires. La reconnexion magnétique se produit également dans la queue de la magnétosphère au niveau de la feuille de plasma, où le cisaillement magnétique est proche de 180°. À cet endroit, les jets de reconnexion s'écoulent à la fois vers la Terre et dans la direction opposée, propageant une partie du plasma du vent solaire dans la magnétosphère interne. Les particules accélérées par ce processus de reconnexion circulent le long des lignes de champ vers la Terre et sont à l'origine des aurores boréales visibles dans les régions polaires.

Missions spatiales

L'environnement Soleil-Terre est à portée d'une exploration scientifique directe, et les agences spatiales sont en mesure d'envoyer des missions spatiales afin de mesurer directement in-situ les propriétés du plasma. Les travaux réalisés au cours de cette thèse ne sont rendus possibles que par l'existence de ces missions spatiales qui sondent le milieu interplanétaire. Nous décrivons ici succinctement les trois missions actuellement en cours qui fournissent les données que nous utilisons tout au long de ce manuscrit.

La mission "Magnetospheric Multiscale" (MMS) de la NASA (Burch et al., 2016) a été lancée en 2015, avec pour but d'étudier la reconnexion magnétique jusqu'aux échelles cinétiques dans l'environnement proche de la Terre. La mission possède quatre satellites identiques en formation tétraédrique, ce qui permet de reconstruire une vision 3D du processus de reconnexion. La première phase de la mission se concentre sur l'étude de la magnétopause terrestre côté jour, et a lieu de 2015 à 2017. Lors d'une seconde phase, l'orbite de MMS a été modifiée pour étudier la queue de la magnétosphère côté nuit. MMS dispose d'instruments qui permettent la mesure les champs électromagnétiques, la composition et les propriétés du plasma ainsi que les propriétés des particules énergétiques. Plus particulièrement, l'instrument FPI (en partie développé et produit à l'IRAP) est en capacité de mesurer les fonctions de distribution des ions et des électrons à des résolutions temporelles inédites et aujourd'hui inégalées.

La mission Parker Solar Probe (PSP , Fox et al. (2016)) de la NASA a été lancée en 2018 pour élucider les mystères de la couronne solaire. Les objectifs scientifiques de la mission sont d'identifier les processus en jeu dans le chauffage de la couronne solaire, la formation et l'accélération du vent solaire, et l'accélération des particules énergétiques. Pour atteindre

[1] voir par exemple https://solarsystem.nasa.gov/resources/2286/modeling-earths-magnetism/ pour une visualisation dynamique de la reconnexion magnétique à la magnétopause terrestre.

ces objectifs, l'orbite de PSP s'approche au plus près du Soleil, avec un périhélie sous 10 $R_\odot$ (rayons solaires) prévu à Noël 2024. La distance au Soleil des différents périhélies de PSP sont résumés dans le tableau 1. Le satellite possède quatre suites d'instruments qui lui permettent de mesurer les champs électromagnétiques, les propriétés du plasma ainsi que les propriétés des particules énergétiques. Il possède par ailleurs un instrument d'imagerie en lumière blanche qui filme le vent solaire sur son côté.

Perihelion ($R_\odot$, (AU))	Encounters	Date
35.6 (0.166)	E_1 to E_3	11-2018
27.8 (0.130)	E_4 to E_5	01-2020
20.3 (0.095)	E_6 to E_7	09-2020
16.0 (0.074)	E_8 to E_9	04-2021
13.2 (0.061)	E_{10} to E_{16}	11-2022
11.3 (0.053)	E_{17} to E_{21}	09-2023
9.9 (0.046)	E_{22} to E_{26}	12-2024

TABLE 1 : Distance des périhélies de PSP au Soleil, où E_x signifie orbite numéro x.

La mission Solar Orbiter (Müller et al., 2013) est une mission de l'ESA réalisée en collaboration avec la NASA et lancée en 2020. Avec des objectifs scientifiques similaires à ceux de PSP, Solar Orbiter se concentre sur le chauffage de la couronne, la formation et l'accélération du vent solaire et, plus particulièrement, l'origine du cycle solaire de 11 ans. La mission Solar Orbiter diffère toutefois de la mission PSP en termes d'instrumentation et d'orbite, ce qui rend les deux missions complémentaires. L'orbite de Solar Orbiter s'approche à 0,3 AU du Soleil (environ 65 $R_\odot$) sur une orbite elliptique. Une spécificité clé de la mission est d'atteindre progressivement une orbite hors écliptique ($> 33°$ d'inclinaison en 2029) en utilisant plusieurs assistances gravitationnelles de Vénus, ce qui permettra d'obtenir pour la toute première fois des images détaillées des pôles solaires grâce à une orbite allant à des latitudes supérieures à 30°. La mission Solar Orbiter peut mesurer les champs électromagnétiques, les propriétés du plasma ainsi que les propriétés des particules énergétiques. L'instrument PAS de Solar Orbiter permettant de caractériser la fonction de distribution des ions a été développé, produit et testé à l'IRAP. Le satellite possède d'autre part de nombreux instruments de télédétection dans plusieurs longueurs d'onde.

Plan de la thèse

Les différentes missions lancées par la NASA et l'ESA ont apporté de nouvelles réponses dans le domaine de la physique des plasmas. Grâce à leur instrumentation ambitieuse, ces satellites ont mis en évidence des structures qui n'avaient pas été observées auparavant, soit en raison d'un manque de résolution instrumentale, soit en raison de l'absence de données antérieures. Ce manuscrit se concentre sur des structures observées à la magnétopause terrestre d'une part et dans le vent solaire d'autre part, et qui ont un impact significatif sur leur environnement. Notre approche a pour but d'expliquer les processus de formation en jeu pour ces structures en réalisant des études statistiques des évènements observés et en comparant les résultats aux modèles de formation existants.

Dans une première partie (I), nous étudions des structures magnétiques qui se propagent le long de la magnétopause terrestre (chapitre 2), transportant des quantités importantes d'énergie et appelées Evènements de Transfert de Flux (FTE pour l'acronyme anglais). Plus particulièrement, des FTE d'un nouveau genre ont été observées ces dernières années (Øieroset et al., 2016; Kacem et al., 2018), présentant une signature de reconnexion magnétique en leur centre. Une telle observation remet en cause les modèles classiquement mis en avant pour expliquer la structure interne des FTEs. Une étude statistique de ces structures nous permet de mieux comprendre leur topologie magnétique ainsi que de déterminer les facteurs environnementaux jouant un rôle dans leur apparition. Ces analyses nous renseignent sur le processus de formation des FTEs qui implique le processus de reconnexion magnétique sur le côté jour de la magnétopause. Dans le chapitre 3, nous rapportons des observations de structures similaires dans le vent solaire par la mission PSP soulignant que le processus en jeu à la magnétopause se produit probablement aussi dans le vent solaire.

Dans une seconde partie (II) , nous passons de l'environnement terrestre à l'héliosphère interne, où les switchbacks magnétiques sont omniprésents dans le vent solaire proche du Soleil. Les switchbacks magnétiques sont des déflections du champs magnétique qui vont jusqu'à renverser sa composante radiale, et qui sont de plus accélérées par rapport au vent solaire de fond. Nous présentons d'abord une syntèse de la littérature scientifique des switchbacks magnétiques à ce jour (chapitre 4), puis nous présentons une étude de leurs échelles caractéristiques par une analyse en ondelettes (chapitre 5) mettant en évidence leur lien probable avec des caractéristiques de surface comme la granulation et la supergranulation. Nous constatons enfin que les switchbacks présentent une orientation préférentielle dans leur déflection (chapitre 6), cohérente avec une formation proche de la surface solaire par le processus de reconnexion d'échange.

La reconnexion magnétique est un fil conducteur dans ce travail, omniprésente à la magnétopause terrestre et dans le vent solaire, et menant à la formation de structures impactant significativement leur environnement. L'observation des signatures de la reconnexion magnétique dans les données est un indice primordial pour la compréhension des processus physiques en jeu. Dans la dernière partie du manuscrit (III, chapitre 7), nous présentons une nouvelle méthode de détection automatique des signatures de jets de reconnexion, méthode inspirée du processus d'identification visuelle de ces jets. Une première application aux données de Solar Orbiter donne des résultats prometteurs, avec une centaine de jets de reconnection détectés sur un mois de données.

Nous concluons (chapitre 8) ce manuscript en résumant les implications de ce travail et les perspective ouvertes pour de futurs projets de recherche.

Chapter 1

Introduction

Contents

1.1 Elements of plasma physics

A plasma is a medium where matter is partially or completely ionised. Its behaviour is not usually familiar to us due to its rarity on Earth and the intervention of the magnetic field, by contrast with fluid dynamics. This section is meant as a theoretical background for this manuscript, reviewing the equations to understand how a plasma behaves and can be described in various conditions. This section is largely inspired by Meyer-Vernet (2007).

1.1.1 A plasma

In our direct surroundings, we interact daily with three states of matter that are the solid, liquid and gaseous states. Definitions for these come naturally, intuitively, and academic studies may teach us that at the microscopic level, bounds between atoms differ for each state and grant the matter different properties and behaviours. A plasma is matter in yet another state, often referred to as the fourth fundamental state of matter[1]. We understand that when heated, a solid can melt into a liquid, and a liquid evaporates into gas, as the bounds between atoms weaken and break. The plasma state is the next state, reached when sufficient energy is injected into the gas for the atoms themselves to be dismantled, separating ions and electrons in a mixture of freely moving charged particles. More rigorously, a plasma is a quasi-neutral gas containing charged and possibly neutral particles, which behaviour is collective and influenced by electromagnetic forces.

[1] Many other states exist, see for instance https://en.wikipedia.org/wiki/List_of_states_of_matter

Plasmas remain anecdotal on Earth compared to other states of matter, and may be found in hypnotic elements such as a fire, lightnings or auroras, and less poetically in TV screens, fluorescent lamps, or laboratory experiments. They are, however, ubiquitous in the universe where most visible matter is in a plasma state, constituting stars, the interplanetary, interstellar and intergalactic medium, nebulae, and so forth. In the solar system for instance, a plasma sphere (the Sun (1.3.1)) continuously ejects a plasma (the solar wind (1.3.2)) into the interplanetary medium that will interact with the plasma (magnetospheres (1.3.3)) surrounding the Earth or other planets. This makes the near-Earth environment a perfect astrophysical laboratory to study space plasmas, and several missions have been launched for this very purpose.

1.1.2 Charged particle motion

Before considering the equations governing the behavior of a plasma, let us first study the dynamics of a single charged particle immersed in a magnetic field $\mathbf{B}$ and an electric field $\mathbf{E}$. This particle of charge q and mass m is then subjected to the Lorentz force $\mathbf{F_L}$, and the equation of motion writes[2]:

$$m\frac{d\mathbf{v}}{dt} = \mathbf{F_L} = q\left(\mathbf{E} + \mathbf{v} \wedge \mathbf{B}\right) \tag{1.1}$$

where $\mathbf{v}$ is the velocity of the particle.

Helical motion

In the case where $\mathbf{E} = \mathbf{0}$ and $\mathbf{B}$ is constant, equation (1.1) implies that the particle will have a uniform motion in the direction parallel to $\mathbf{B}$ and a circular motion in the perpendicular plane (with a gyrofrequency $w_g = |q|B/m$), hence undergoing a helical trajectory around $\mathbf{B}$. Associated with this helical motion, an adiabatic invariant can be defined and is called the magnetic moment μ. It is a quantity that remains constant when changes are made slowly in the system, and can be written here as the ratio of perpendicular kinetic energy to magnetic field strength:

$$\mu = \frac{mv_\perp^2}{2B} \tag{1.2}$$

As such, both quantities are correlated and if B increases (decreases) on a timescale way larger than a gyration period, the particle perpendicular kinetic energy will increase (decrease) as well. On panel *a* of Figure 1.1, we display the helical motion of a particle around a constant magnetic field, with the velocity vector of the particle decomposed between its parallel and perpendicular components.

Drift velocity

Now, if an additional force $\mathbf{F}$ independent of $\mathbf{v}$ comes into play (for instance $q\mathbf{E}$), then its parallel component will affect the particle velocity along $\mathbf{B}$, while its perpendicular component will generate a constant drift velocity given by

$$\mathbf{v_D} = \frac{\mathbf{F} \wedge \mathbf{B}}{qB^2} \tag{1.3}$$

[2] considering non relativistic particles

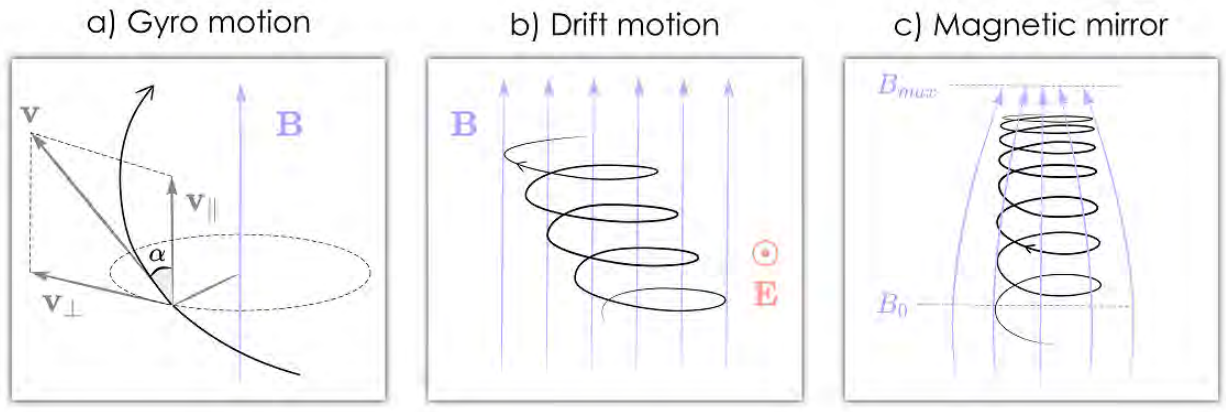

Figure 1.1: Particle motion in an electromagnetic field. In panel a, a particle in a constant magnetic field follows a helical motion, in panel b the particle drifts perpendicularly to the magnetic field when submitted to an additional electric field, and in panel c the magnetic mirror configuration is illustrated, with a particle approaching its turning point as the magnetic field magnitude increases along a magnetic field line.

From equation eq. (1.3), we can see that ions and electrons will drift in opposite directions. This drift velocity can be generated by any force with a component perpendicular to $\mathbf{B}$, such as the electric field as mentioned above (in that case, $\mathbf{v_D} = \mathbf{E} \wedge \mathbf{B}/B^2$), but also gravity, pressure gradient or magnetic field gradient if the field is not uniform. In panel b of Figure 1.1, we illustrate the motion of a particle in the presence of constant magnetic and electric fields.

Magnetic mirror

Let us consider the effect of a gradient of B in the parallel direction on the particle's motion, on scales larger and slower than the gyroradius and gyroperiod. The adiabatic invariant from eq. (1.2) can be re-written

$$\mu = \frac{mv^2 \sin^2 \alpha}{2B} \tag{1.4}$$

where α is the angle formed between $\mathbf{v}$ and the magnetic field, displayed in Figure 1.1 (left panel) and called the pitch angle of the particle ($\tan \alpha = v_\perp / v_\parallel$). By assuming the conservation of the particle's kinetic energy, this yields that $\sin^2(\alpha)/B$ is constant, directly meaning that as B increases, the particle's pitch angle increases as well while the parallel velocity decreases. This gradient in $B_\parallel$ leads to a configuration called a magnetic bottle or magnetic mirror, named as such because some particles will be reflected while others may escape. Indeed, consider a configuration where the magnetic field strength increases from B_0 to B_{max}, and let α_0 be a particle pitch angle at $B = B_0$. This type of configuration is displayed in the right panel of Figure 1.1. By conservation of the first adiabatic invariant μ, the pitch angle of the particle as it propagates along the magnetic field writes $\sin^2 \alpha = (B/B_0) \sin^2 \alpha_0$. The particle will turn when α reaches $\pm\pi/2$, or equivalently when $B = B_0 / \sin^2 \alpha_0$. As such, if $B_{max} > B_0 / \sin^2 \alpha_0$, the particle is reflected before it reaches the neck of the magnetic bottle, while if $B_{max} < B_0 / \sin^2 \alpha_0$, the particle is able to escape along the magnetic field beyond the bottle neck.

To summarise, a particle gyrates around the magnetic field due to the $\mathbf{v} \wedge \mathbf{B}$ term of the Lorentz force. Additional forces parallel to $\mathbf{B}$ accelerate the particle along the field lines, while perpendicular forces induce a perpendicular drift. All of these motions are illustrated in Figure 1.1.

1.1.3 Kinetic and fluid descriptions

Now that we have an intuition on the behaviour of one particle in an electromagnetic field, we may consider an ensemble of N particles that form a plasma, and take into account the retro-action between electric and magnetic fields and particles' movement.

In a full particle description, each particle is characterised by its position $\mathbf{r}$ and velocity vector $\mathbf{v}$, and the system's evolution can be computed over time through the equation of motion of each particle. Such an approach requires huge calculation capacities and is usually restrained to a small number of particles. To move up in scale, it is usual in a kinetic description to reason with the probability distribution function of each particle species $f(\mathbf{r}, \mathbf{v}, t)$. It represents the probability of finding particles at a given time within a small six-dimensional elementary volume, centered on $(\mathbf{r}, \mathbf{v})$ and with dimensions $(\mathbf{dr}, \mathbf{dv})$. The number of particles inside this volume is then given by $dN = f(\mathbf{r}, \mathbf{v}, t)\mathbf{drdv}$. Computing the evolution of the system now amounts to computing the evolution of f over time , which is given in a collisionless plasma by the Vlasov equation:

$$\frac{\partial f}{\partial t} + \mathbf{v} \cdot \frac{\partial f}{\partial \mathbf{r}} + \frac{d\mathbf{v}}{dt} \cdot \frac{\partial f}{\partial \mathbf{v}} = 0 \tag{1.5}$$

Here the effect of the eletromagnetic field is hidden in the $d\mathbf{v}/dt$ term which is given by eq. (1.1) if the Lorentz force is the only external force.

This change of perspective is illustrated in two dimensions in Figure 1.2. In an "all particles" approach, the system is characterized by the positions and velocity vectors of all particles (left panel), while in a kinetic approach, it is characterised by the distribution function $f(\mathbf{r}, \mathbf{v})$ (right panel).

In a fluid approach, the system is further simplified as the distribution function is reduced to its moments. The i^{th}-order moments of a distribution function can be computed through (from now on, the dependency of f on $(\mathbf{r}, t)$ is implied to simplify the notation):

$$\mathcal{M}_i = \int \mathbf{v}^i \; f(\mathbf{v}) \; \mathbf{dv} \tag{1.6}$$

Moments of order 0, 1, 2 and 3 can respectively be linked to the density n, the average velocity vector $\mathbf{V}$ also referred to as the bulk velocity vector, the pressure tensor $\mathcal{P}$ and the heat flux vector $\mathbf{Q}$. They are given by the following set of equations:

$$n = \int f(\mathbf{v}) \; \mathbf{dv} \tag{1.7a}$$

$$n\mathbf{V} = \int \mathbf{v} \; f(\mathbf{v}) \; \mathbf{dv} \tag{1.7b}$$

$$\mathcal{P} = m \int (\mathbf{v} - \mathbf{V}) \otimes (\mathbf{v} - \mathbf{V}) \; f(\mathbf{v}) \; \mathbf{dv} \tag{1.7c}$$

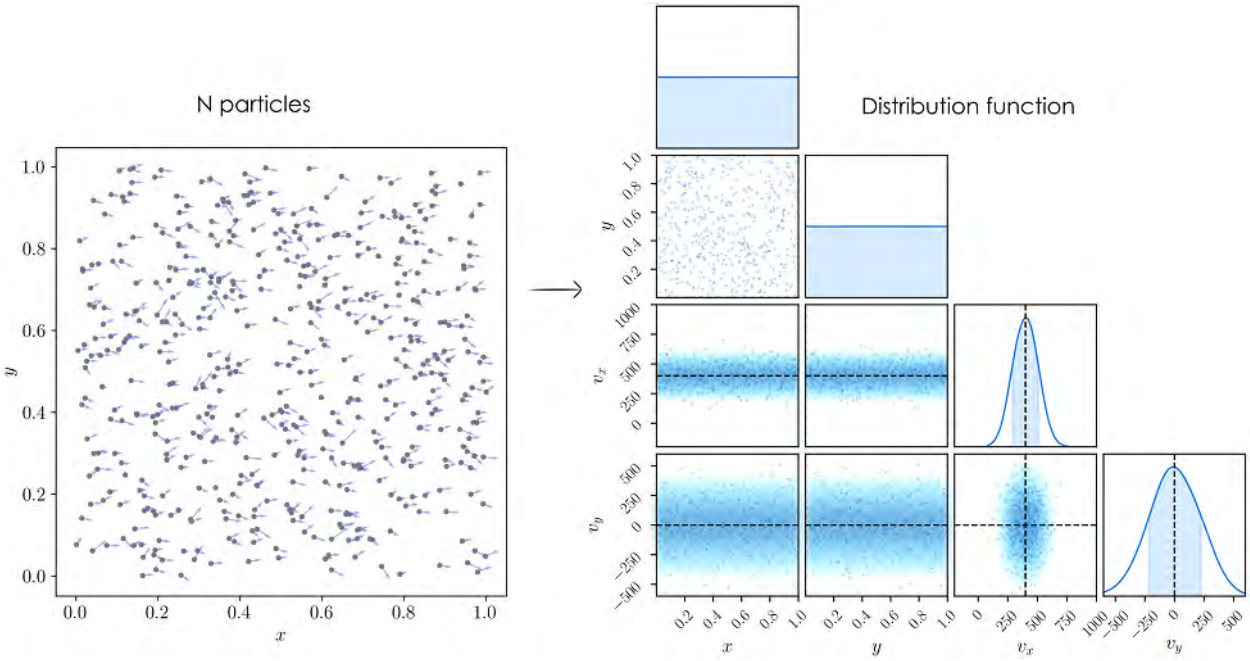

Figure 1.2: Illustration of the particle and kinetic description of a plasma, considering 500 particles uniformly distributed in a 2D space, and normally distributed in velocity. The left panel displays a scatter plot of the position (grey dots) as well as a representation of their velocity vectors (blue). The right panel shows cuts of the distribution function $f(\mathbf{r}, \mathbf{v})$ in a corner plot.

$$\mathbf{Q} = \frac{m}{2} \int |\mathbf{v} - \mathbf{V}|^2 \, (\mathbf{v} - \mathbf{V}) \, f(\mathbf{v}) \, \mathbf{dv} \tag{1.7d}$$

Depending on the characteristic scales of the phenomena one wants to study, different approaches can be considered with various levels of complexity. By going from a particle description to a kinetic one to a bi-fluid or fluid one, the requirements in terms of computation capacities will change, and to choose which approach to use is hence a trade-off between the physics at stake and the complexity of the system one is ready to consider. Let us now review some collective behaviours displayed by a plasma and define useful quantities in the context of this work.

1.1.4 Electromagnetism and Magnetohydrodynamics

Electromagnetism

In a plasma, a constant retro-action exists between the particles motion and the electromagnetic field evolution. We saw that an electromagnetic field induces a displacement of charged particles (eq. (1.1), (1.5)), and this particle motion in turn generates an electrical current. The latter then influences the electromagnetic field behaviour, and so the process is repeated. This second part is well conveyed by Maxwell's equations that are decomposed into the Maxwell-Gauss, Maxwell-Thompson, Maxwell-Faraday and Maxwell-Ampère equations, respectively:

$$\nabla \cdot \mathbf{E} = \frac{\rho_c}{\epsilon_0} \tag{1.8a}$$

$$\nabla \cdot \mathbf{B} = 0 \tag{1.8b}$$

$$\nabla \wedge \mathbf{E} = -\frac{\partial \mathbf{B}}{\partial t} \tag{1.8c}$$

$$\nabla \wedge \mathbf{B} = \mu_0 \left(\mathbf{j} + \epsilon_0 \frac{\partial \mathbf{E}}{\partial t} \right) \tag{1.8d}$$

where $\mathbf{E}$ is the electric field in the plasma frame, ρ_c the charge density, $\mathbf{j}$ the electric current and ϵ_0 and μ_0 are respectively the vacuum permittivity and permeability (with $\mu_0 \epsilon_0 = c^{-2}$, c being the speed of light).

Magnetohydrodyamics

Let us now introduce the magnetohydrodyamics (MHD) description of a plasma. MHD is a specific fluid approach of plasma dynamics studying the evolution over time of the moments of f. It assumes a single species fluid (electrons and ions are indiscernible) that verifies quasi-neutrality ($\rho_c \mathbf{E} = 0$). The term $\frac{1}{c^2}\frac{\partial \mathbf{E}}{\partial t}$ can be neglected in the Maxwell-Ampère equation (1.8d) as we consider non-relativistic plasmas where changes occur slowly (Galtier, 2016), and the electric field $\mathbf{E}$ can be further expressed through the Ohm's law :

$$\mathbf{E} + \mathbf{V} \wedge \mathbf{B} = \eta \, \mathbf{j} \tag{1.9}$$

with η the electric resistivity of the plasma. Different types of MHD exist, stemming from different levels of approximation. Ideal MHD equates the right-hand side (RHS) of eq (1.9) to zero, and the frozen-in condition is thereby conserved in the plasma. In this paragraph, we use the frame of resistive MHD set by eq. (1.9) that describes effects down to the resistive timescale. The generalised Ohm's law (discussed in section 1.2, eq. (1.17)) includes additional terms and allows a description of the plasma at kinetic scales.

One behaviour that ensues from Maxwell's equations and Ohm's law (eq. (1.9)) is the so-called *frozen-in* condition. By combining equations (1.8c), (1.8d) and (1.9), we can deduce:

$$\frac{\partial \mathbf{B}}{\partial t} = \frac{\eta \nabla^2 \mathbf{B}}{\mu_0} + \nabla \wedge (\mathbf{V} \wedge \mathbf{B}) \tag{1.10}$$

This equation underlines the coupling between the velocity and magnetic field in a plasma. The first term of the equation's RHS (a) corresponds to the diffusion of the magnetic field, and the second term (b) to its convection by the bulk velocity of the plasma. To determine which term is predominant, one may compute the order of magnitude of the ratio (b/a) between both terms, which will give the magnetic Reynolds number:

$$R_m = \frac{\mu_0 V L}{\eta} \tag{1.11}$$

where L is a characteristic length. If $R_m << 1$, then equation (1.10) becomes a diffusion equation, while if $R_m >> 1$, we are then in the context of ideal MHD and we obtain:

$$\frac{\partial \mathbf{B}}{\partial t} = \nabla \wedge (\mathbf{V} \wedge \mathbf{B}) \tag{1.12}$$

A direct consequence of this last equation is that the magnetic field is then frozen-in the plasma, and the evolution of $\mathbf{V}$ and $\mathbf{B}$ is coupled. This can be formally demonstrated by considering the change of magnetic flux ϕ_B through a surface S moving with the plasma. The frozen-in condition (1.12) yields [3]

$$\frac{d\phi_B}{dt} = \frac{d}{dt}\left(\int_S \mathbf{B}\cdot\mathbf{dS}\right) = 0 \tag{1.13}$$

A flux tube may then be defined starting from the surface S and following the magnetic field lines. From eq. (1.13) we can deduce that the flux tube will keep its identity and the plasma inside will stay confined in it. Another way of formulating this is to say that the connectivity of the flux tube is conserved. Taking the limit of this theorem with an infinitely thin flux tube yields the frozen-in field lines.

Finally, one question remains when the frozen-in condition is verified: between the plasma and the magnetic field, which is dominant over the other in the plasma dynamics? In essence, this will depend on which energy density dominates, namely the thermal pressure $P_T = nk_BT$ and the magnetic pressure $P_B = B^2/(2\mu_0)$. Indeed, in the MHD framework, the equation of motion writes:

$$\rho\frac{d\mathbf{V}}{dt}\left(= \frac{\partial\rho\mathbf{V}}{\partial t} + \nabla\left(\rho V^2\right)\right) = -\nabla P + \frac{(\nabla\wedge\mathbf{B})}{\mu_0}\wedge\mathbf{B} \tag{1.14}$$

with ρ the plasma mass density. The equation can be transformed into:

$$\rho\frac{d\mathbf{V}}{dt} = -\nabla(P_t + P_B) + \frac{1}{\mu_0}(\mathbf{B}\cdot\nabla)\mathbf{B} \tag{1.15}$$

The second term of the RHS represent the magnetic tension, which is the restoring force opposing the curvature of magnetic field line, and is equal to zero if the field lines are straight. The first term of the RHS is relevant to the current problem (who's frozen in who) and allows us to introduce the ratio of thermal to magnetic pressures:

$$\beta = \frac{nk_BT}{\left(\frac{B^2}{2\mu_0}\right)} \tag{1.16}$$

It is now intuitive to state that if $\beta >> 1$, the plasma motion will dominate the magnetic field and subsequently due to equation (1.12), will advect the magnetic field lines that are frozen-in the plasma. By contrast if $\beta << 1$, the magnetic field will drive the plasma motion, the plasma will follow the magnetic field lines and particles will be frozen-in the magnetic field.

In the course of this manuscript we will encounter plasmas in various β regimes, such as the solar corona and the Earth's magnetosphere ($\beta << 1$), the magnetosheath and magnetopause $\beta >> 1$), or media with more complex behaviour like the solar wind or coronal loops in the photosphere ($\beta \sim 1$) (a more detailed description of these plasmas is given in section 1.3). All of these plasmas, however, usually present a high magnetic Reynolds number and are

[3] proof: $\frac{d\phi_B}{dt} = \int_S \frac{\partial\mathbf{B}}{\partial t}\cdot\mathbf{dS} - \oint \mathbf{v}\wedge\mathbf{B}\cdot\mathbf{dl} = \int_S \frac{\partial\mathbf{B}}{\partial t}\cdot\mathbf{dS} - \int \nabla\wedge(\mathbf{v}\wedge\mathbf{B})\cdot\mathbf{dS} = 0$

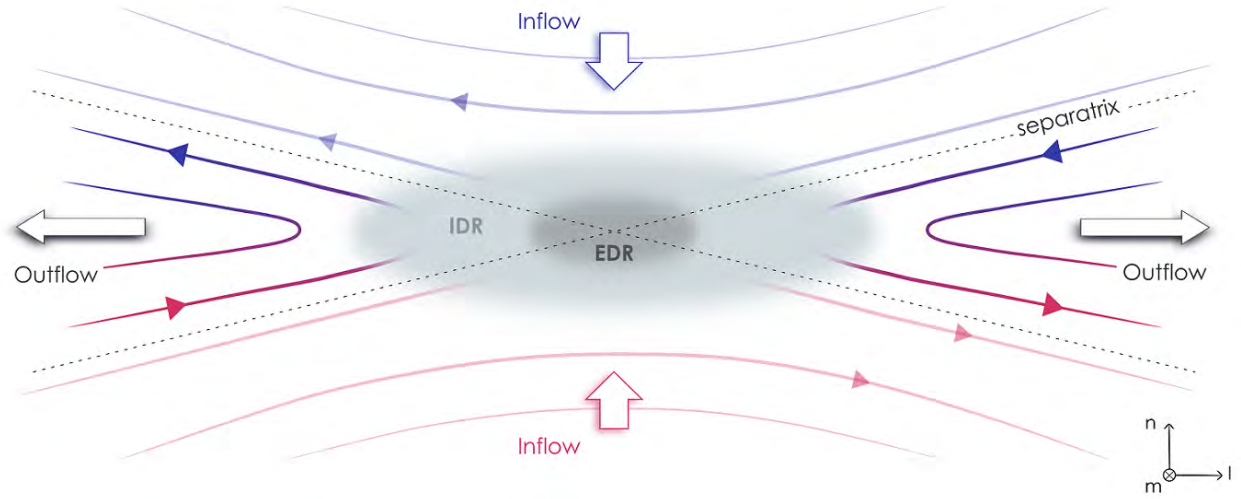

Figure 1.3: Topology of a magnetic reconnection site. The white arrows show the plasma velocity and the magnetic field lines are colored in blue (red) depending on their L component value. The reconnected field lines are in bold, and the separatrices are shown as dotted lines.

therefore frozen-in. This can be directly interpreted in terms of field line connectivity: a particle on a given field line cannot jump to another field line. However, very locally in the plasma, the frozen-in condition may break down and lead to a reconfiguration of the magnetic field topology along with energy transfer. This is the process of *magnetic reconnection*.

1.2 Magnetic reconnection

Magnetic reconnection is a fundamental process in plasma physics, ubiquitous in astrophysical systems. This unique process accelerates and heats the plasma at kinetic scales by converting magnetic energy into kinetic and thermal energy, while allowing a global reconfiguration of the magnetic field topology. In this section, we propose an overview of the magnetic reconnection process, and present its expected signature in situ.

1.2.1 Configuration

As introduced in section 1.1, magnetic reconnection occurs whenever the frozen-in condition (eq (1.12)) of the plasma is locally broken, permitting magnetic field lines to change their connectivity. Such conditions are usually achieved locally in the plasma in regions where a strong current develops (as a strong current will contribute to the diffusive term of eq. (1.10) in resistive MHD). Magnetic reconnection subsequently occurs at local current sheets, i.e. planes with enhanced electric current, which are associated with a localised rotation of the magnetic field (eq (1.8d)).

A typical 2D configuration resulting from magnetic reconnection is displayed in Figure 1.3. Two plasma inflows of opposite magnetic field converge toward each other forming a current sheet at their boundary, and the region where the frozen-in condition is locally broken is called the diffusion region. Here, distinct particle species may behave differently. The ions are the first to decouple from the magnetic field in the ion diffusion region (IDR) while

the electrons remain frozen-in. The latter are in turn de-magnetized in the smaller electron diffusion region (EDR) contained within the IDR. In these regions, neighboring magnetic field lines of opposite directions break and then reconnect with their counterpart, thereby connecting the two initially unmixed plasmas. This creates new bent field lines that are ejected in heated plasma jets tangential to the initial current sheet. Magnetic energy is by this process converted into kinetic and thermal energies, and the region of plasma outflow is often called the exhaust region. The magnetic boundaries separating the different plasma flows are called the separatrices, while the central point of the figure where the separatrices cross is the X-point. As magnetic reconnection is a 3D process, the 2D view of Figure 1.3 can be extended in the out-of-plane direction, whereupon the separatrices become planes and the X-point becomes an X-line.

It is important to keep in mind that Figure 1.3 displays a simplified version of a reconnection site while more complex configurations usually arise in observations and simulations. Figure 1.3 shows for instance a symmetric reconnection site where both plasma inflows present similar characteristics in terms of plasma β. Magnetic reconnection, however, can be asymmetric with drastically different inflows, inducing an asymmetry in the site's topology. Such an asymmetry is encountered during reconnection between the solar wind and the Earth's magnetosphere for example as discussed in section 1.3.3. In addition, the reconnecting magnetic fields may possess an out-of-plane component, also called *guide field*, hence reducing the magnetic shear, which is the angle between the inflowing magnetic fields.

1.2.2 Theoretical description

To understand where the IDR and EDR come from, we have to stray from the single species fluid approach and take into account effects induced by the ion and electron dynamics. In section 1.1, we considered the Ohm's law in a (non-ideal) MHD framework through eq. (1.9), where the LHS of the equation contributed to the diffusive term of equation (1.10), allowing the frozen-in condition to be locally broken. In reality, ions and electrons follow different behaviours near the reconnection site and their specificity needs to be distinguished in a multi-species approach. By writing the equation of motion for each species and using the electric current expression $\mathbf{j} = ne(\mathbf{v_i} - \mathbf{v_e})$ to combine them, one may obtain the generalized Ohm's law, a complexified version of equation (1.9) (see for instance Sisti (2021) for a demonstration):

$$\mathbf{E} + \mathbf{v_i} \wedge \mathbf{B} = \eta\, \mathbf{j} + \frac{\mathbf{j} \wedge \mathbf{B}}{ne} - \frac{\nabla \cdot \mathcal{P}_e}{ne} + \frac{m_e}{ne^2}\left[\frac{\partial \mathbf{j}}{\partial t} + \nabla \cdot \left(\mathbf{j} \otimes \mathbf{v_i} + \mathbf{v_i} \otimes \mathbf{j} + \frac{\mathbf{j} \otimes \mathbf{j}}{ne}\right)\right] \tag{1.17}$$

where the subscripts i and e stand for ions and electrons (due to charge neutrality, $n = n_i = n_e$) and e is the elementary electric charge. All terms on the RHS can break the frozen-in condition at different scales. As previously seen, the first term $\eta\ \mathbf{j}$ may trigger what is called resistive reconnection, that will come into play at resistive scales. This is the basis of the Sweet-Parker model (Parker, 1957), also known as slow reconnection. In space plasmas, however, the resistivity usually remains small and the other terms of the equation come into play. The second term $\frac{1}{ne}\mathbf{j} \wedge \mathbf{B}$ conveys the decoupling of ions and electrons, creating the IDR where ions are demagnetized while the frozen-in condition still holds for the electrons (indeed, if we keep only this term in the RHS of eq. (1.17), we get

$\mathbf{E} + \mathbf{v_i} \wedge \mathbf{B} - (\mathbf{j} \wedge \mathbf{B})/ne = \mathbf{E} + \mathbf{v_e} \wedge \mathbf{B} = 0$, which translates into frozen-in electrons). The remaining part of the equation becomes significant at electronic scales, characterising the EDR of the reconnection site where electrons demagnetize.

To quantify the size of the IDR and EDR, we need to introduce a fundamental parameter in plasma physics, the plasma frequency ω_p. In a plasma, an imbalance of positive and negative charges creates an electric field that in turn tends to restore the neutrality of the media. This induces an oscillation for each particle species at the frequency:

$$\omega_p = \sqrt{\frac{ne^2}{\epsilon_0 m}} \tag{1.18}$$

The ion and electron inertial lengths - also called skin depths - can be defined from there as $d_i = c/\omega_{pi}$, $d_e = c/\omega_{pe}$. They represent the scale at which the particles decouple from the magnetic field, and so are the typical scales of respectively the IDR and EDR. These regions are very small[4] (particularly the EDR) and subsequently are rarely observed in spacecraft data, as one needs to get extremely lucky to cross them. Fortunately, other broader features of the magnetic reconnection site can be more easily identified and will be the topic of the next section.

1.2.3 Identification in-situ

All of the signatures and analysis described in this section are extensively illustrated throughout the manuscript (see for instance sections 2.4.2, 3.2, 7), and so are only briefly described here.

Magnetic reconnection signatures

Magnetic reconnection is known to produce a magnetic field configuration as shown in Figure 1.4, with a plasma jet bounded by two discontinuities that are akin to rotational discontinuities (Gosling et al., 2005). A spacecraft crossing a reconnection exhaust would exhibit several characteristics in its measured in-situ data. Such a trajectory is illustrated in Figure 1.4 as a dashed line. First, as the spacecraft moves across the exhaust between the two inflows, an ion jet as well as an electron jet would be observed, coincidental with a sharp rotation in the magnetic field and an electric current (the so-called current sheet). These are the most visually striking signatures that one may search for in in-situ data, though additional signatures may also arise such as a decrease in the magnetic field strength owing to energy conversion, an increase in electron temperature, as well as an increase in density (e.g, Gosling et al. (2005); Paschmann et al. (2013)). In order to best identify the reconnection signatures in the magnetic field and velocity, the lmn coordinate system associated with the current sheet is usually used, with the l direction being the one of maximum variance of the magnetic field, the n direction the normal to the current sheet, and the m direction completing the frame (illustrated in Figure 1.3). In this coordinate system, the reconnection jet should appear solely on the l direction of the lmn frame, making it easier to confirm and characterize. Another frame that is classically used when studying magnetic reconnection

[4]For instance in the solar wind (see section 1.3.2), the typical length of the IDR is around 140 km and that of the EDR is around 3 km (Verscharen et al., 2019).

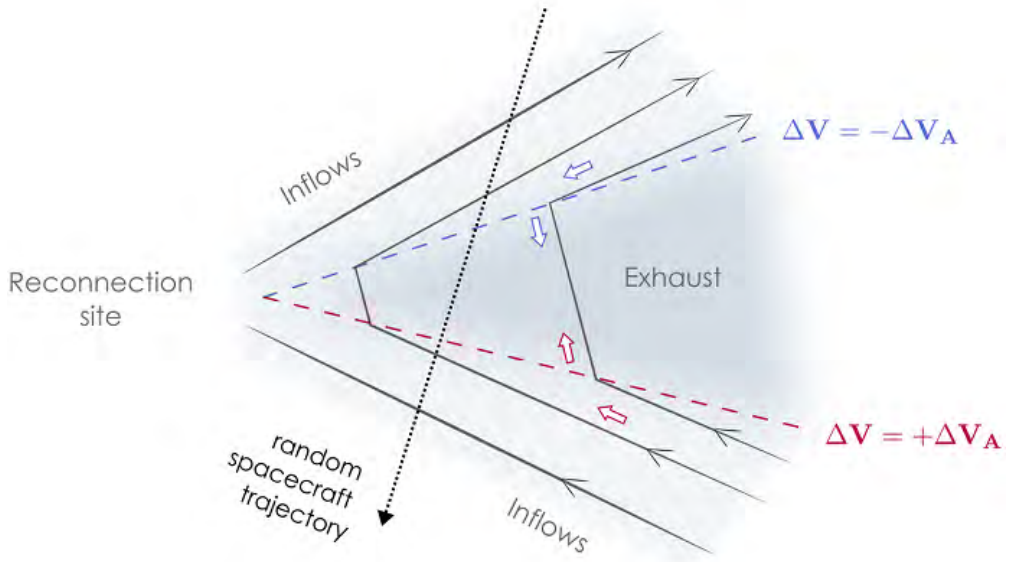

Figure 1.4: Illustration of the Walén relation across a reconnection site, in a representation similar to Figure 1.3. Magnetic field lines are drawn in black while white arrows represent the plasma flow in the De Hoffman Teller frame. Dashed lines delimit the exhaust, with their color indicating which sign of the Walén relation applies at this boundary. A random spacecraft trajectory is plotted as a dotted arrow. Figure adapted from Gosling et al. (2005)

exhaust is the de Hoffman-Teller frame (de Hoffmann & Teller, 1950), in which $\mathbf{V} \wedge \mathbf{B} = 0$. This corresponds in our case to the exhaust frame.

The Walén relation

To test whether a plasma jet is indeed consistent with a rotational discontinuity, and thus possibly also the result of reconnection, a test called the Walén relation is often performed. The Walén relation basically consists in testing the alfvénicity of a discontinuity, and derives from jump properties for an alfvénic rotational discontinuity (Hudson, 1970). It states that the change in velocity across a rotational discontinuity should follow:

$$\Delta \mathbf{V} = \pm \, \Delta \mathbf{V_A} \tag{1.19}$$

with:

$$\mathbf{V_A} = \frac{\mathbf{B}}{\sqrt{\mu_0 \rho}} \sqrt{1 - (P_{\parallel} - P_{\perp}) \, \frac{\mu_0}{B^2}} \tag{1.20}$$

where $\mathbf{V_A}$ is the local Alfvén velocity, $(P_{\parallel} - P_{\perp}) \, \frac{\mu_0}{B^2}$ the pressure anisotropy correction with $P_{\parallel}, P_{\perp}$ are respectively the pressures parallel and perpendicular to the magnetic field. As the spacecraft crosses the exhaust, it encounters two rotational discontinuities with opposite correlations. Hence, $\Delta \mathbf{V}$ and $\pm \, \Delta \mathbf{V_A}$ should correlate across the considered jet, with a change in the correlation sign at the heart of the exhaust. This is illustrated in Figure 1.4 where, at each boundary, the sign of the Walén relation changes as indicated by the direction of the flow in the De Hoffman-Teller frame . A spacecraft flying through the exhaust would

first see an anticorrelation between $\mathbf{V}$ and $\mathbf{V_A}$ upon entry into the exhaust, followed by a correlation when exiting the exhaust.

In observations, reconnection jets are usually sub-Alfvénic due to complex phenomena occurring at the boundaries (Phan et al., 2020). This overestimation of the jet speed by the Walén relation is not totally understood. In some cases it may be explained by the proximity to the X-line because in the ion diffusion region next to the reconnection site, the ion jet may not be fully developed. Phan et al. (2020) discuss several other possible explanations, such as non-ideal rotational discontinuities at the boundaries of the jet (e.g., Liu et al. (2011)) or ion temperature anisotropy in the exhaust (Haggerty et al., 2018). The Walén relation should however remain valid in order of magnitude at least. An example of the Walén test on spacecraft data is given in section 2.4.2, Figure 2.8.

To conclude this section, it is puzzling to realise that a change occurring on such microscopic scales (IDR and EDR are of the order of each particle inertial length) will sometimes lead to the global re-configuration of a planet's or a star's magnetic field. In the following section, the fundamental role of magnetic reconnection in the dynamics of the Sun-Earth environment is highlighted.

1.3 The Sun-Earth environment

We attempt in this section a description of the general features of the Solar atmosphere, the solar wind and the Earth's magnetosphere. This is no small task and we hope to be thorough without straying into too many details.

1.3.1 The Sun

The Sun, the star of our planetary system, is a plasma sphere located at 150 million km (1 AU) from the Earth. It is a star on the main sequence, hence burning hydrogen, formed around 4.6 billion years ago, with a mass $M_\odot = 1.99 \times 10^{30}$ kg, and a radius $R_\odot = 696340$ km. The Sun's internal structure is composed of a radioactive core that burns helium, an inner radiative zone and an outer convective zone. It is common knowledge that the Sun is essential to life on Earth, conveniently providing tremendous amounts of power (through nuclear reactions in its core) to heat our atmosphere to suitable temperatures. But the Sun can also affect our daily lives through another of its key dynamical process: its magnetic activity. In this section, we focus on some solar surface processes, the structure of the solar atmosphere and review the key features of the solar magnetic field, as well as describe some of the eruptive events that result from its activity.

Solar surface processes

The photosphere, or solar surface, is the region where the plasma goes from optically thick (solar interior) to increasingly optically thin (solar atmosphere). It features a differential rotation visible for instance through the observation of solar sunspots, with a plasma rotating faster at the equator (25 day period) than at the poles (34 day period). Helioseismology revealed that this feature was not a shallow one and actually involves the whole convective zone, while the radiative zone rotates rather rigidly (Spiegel & Zahn, 1992). This differential

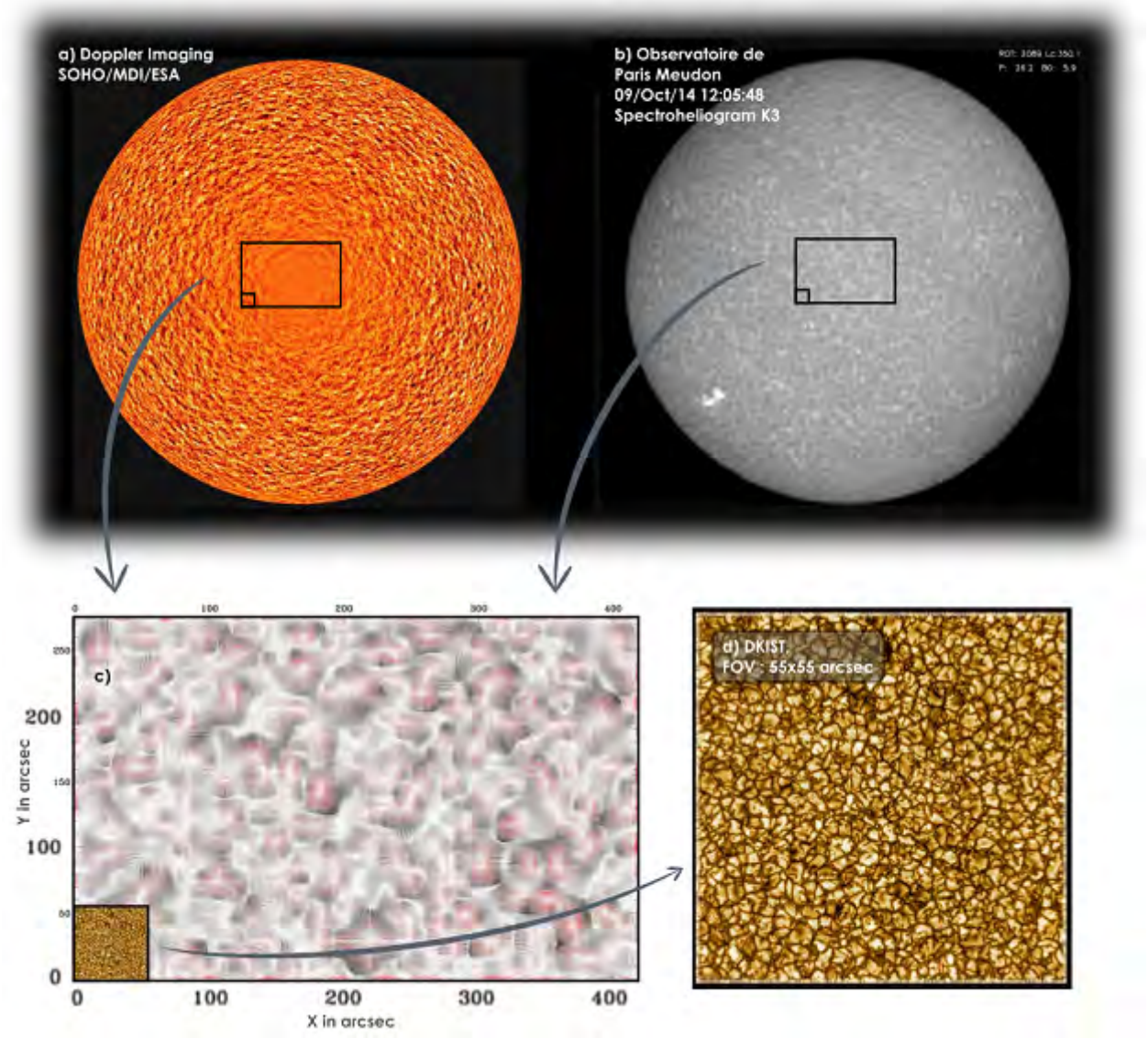

Figure 1.5: Supergranulation and granulation. In panel *a* we show a dopplergram of the Sun, and in panel *b* an imaging of the chromospheric network in the Ca+ K3 line at 393.37 nm. The inset of panel *c* shows the supergranulation scale, with the velocity field plotted with the divergence contours superimposed (Rieutord et al., 2008). Panel *d* is a zoom on granulation obtained with the DKIST telescope on a 55x55 arcsec field of view (Rimmele et al., 2020). Figure adapted from Rieutord et al. (2008).

rotation is thought to be due to turbulent motions of the convective envelop of the star (Brun & Toomre, 2002). The photosphere exhibits a cellular pattern at two distinct spatial scales, illustrated in Figure 1.5. Supergranulation is a cellular flow pattern detected in dopplergrams of the Sun such as illustrated in panel 1.5*a*. It features a typical horizontal scale of approximately 30 Mm and a dynamical evolution time of 24 to 48 h (Rincon & Rieutord, 2018). The physical origin of supergranulation and its characteristics remains unclear. In parallel, the surface magnetic field network also exhibits a cellular structure that is correlated with the pattern of solar supergranulation (Roudier et al., 2009). This is visible

in panel 1.5*b*, which a view of the magnetic network exhibiting a spatial scale similar to the one seen in panel 1.5*a*. In practice, the open magnetic flux aggregates at the boundaries of supergranules, indicating that open field lines are rooted there (e.g. Wedemeyer-Böhm et al. (2009)). At a much smaller scale, solar granulation (panel 1.5*d*) is observed. Solar granules are convection cells associated with heat transfer with typical scales of 1 Mm and 10 minutes.

From the photosphere to the corona

The solar atmosphere is structured into regions that present drastically different plasma properties (Gary, 2001; Aschwanden, 2005; Meyer-Vernet, 2007). Right above the photosphere is the chromosphere, the basis of the solar atmosphere that is a few thousands of kilometers thick. There, density decreases with altitude until the so-called transition region is reached. In this latter region, the temperature jumps to around millions of Kelvins while the density suddenly decreases. The physical process at the origin of such a sharp variation in plasma properties is today still unclear, and this remains one of the modern mystery of our star. Above the transition region lies the solar corona, a region at first dominated by its extremely strong magnetic field that becomes gradually dominated by the plasma of the solar wind, with ultimately β becoming superior to 1 after the main acceleration region. The characteristics in term of density, temperature and plasma β of these various regions are laid out in Figure 1.6, which is adapted from both Gary (2001) and Aschwanden (2005). We can see from this figure that the solar magnetic field dominates the dynamics in the upper chromosphere / lower corona, while at the photosphere and in the solar wind, it is dominated by the plasma fluid motions. At the photosphere, it means that the footpoints of magnetic field lines are embedded in the rotating plasma of the solar surface, while in the solar wind, the dynamic pressure of the solar wind drags the field lines into the interplanetary medium. Let us now study the structure of the solar magnetic field in-between, where the plasma β is low.

The solar magnetic field

The Sun is a magnetized body, generating its own magnetic field through a dynamo effect (e.g. Moffatt (1978); Parker (1979)). The configuration of the solar magnetic field varies over time, following an 11-year cycle called the solar cycle. During each cycle, the Sun's polarity[5] is reversed, making it in reality a 22-year cycle. The origin of the 11-year periodicity of the solar cycle and its associated polarity reversals remains unclear. The solar cycle is quite apparent through the observation of solar sunspots over time. Sunspots are darkened regions of the photosphere associated with a local drop in gas temperature induced by the presence of strong magnetic fields. Sunspots generally emerge in pairs of opposite magnetic polarities (though not always, as turbulent motions in the convection zone can induce fragmentation of magnetic flux tubes that can emerge as complex sunspot groups). The sunspot number varies with a near 11-year period, and the times corresponding to extrema of the sunspot number are referred to as the solar minimum and solar maximum. These two main periods are associated with different levels of magnetic activity (i.e. number of eruptive events) on the

[5]The polarity of a magnetic field line is linked to the sign of its radial component, a field line has a negative (positive) polarity if it is pointing towards (or away) from the Sun

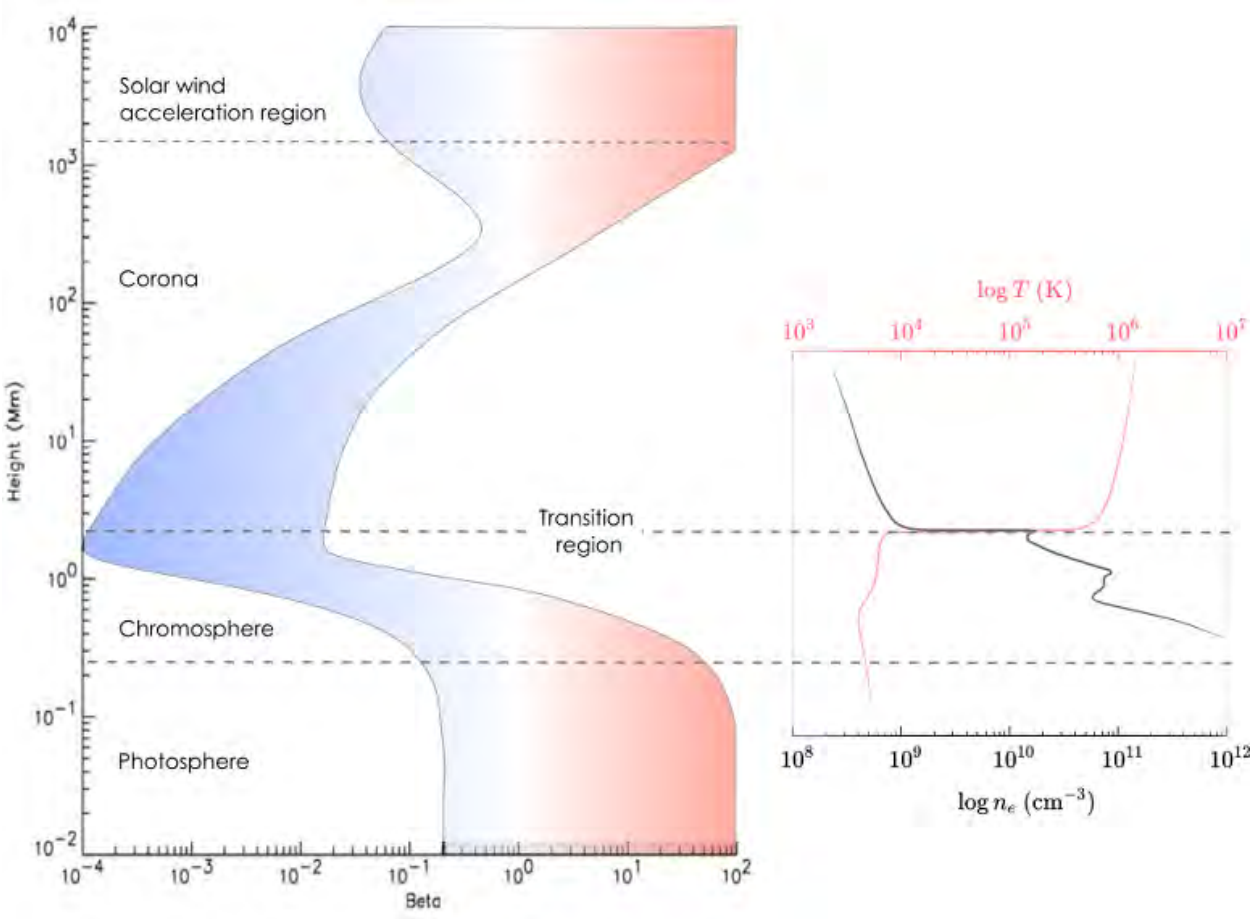

Figure 1.6: Structure of the solar atmosphere displaying the variations of β (left), n_e and T (right) as a function of altitude. β is colored in blue when< 1 and in red when > 1. The figure is adapted from Gary (2001) (β) and Aschwanden (2005) (n_e, T)

Sun, with a quiet Sun during solar minimum and an active Sun during solar maximum. The configuration of the magnetic field is quite different depending on the period of observation.

Figure 1.7 illustrates the evolution of the solar magnetic field structure during the solar cycle, with schematics representing the solar magnetic field structure for both solar minimum and maximum (top). The inserted figure shows images of the Sun (in EUV) and the solar corona (white light) characteristic of solar minimum and maximum, together with solar wind observations made by the Ulysses mission during a complete solar cycle (further described in the next section (1.3.2)). The bright density structures, visible in the white-light images of the corona, outline the structure of the underlying magnetic field. They reveal significant changes in the topology of the solar corona during each period of the solar cycle, also illustrated in the sketches of Figure 1.7. During solar minimum, the solar magnetic field adopts a dipole-like configuration (Fig. 1.7, left). The areas of open magnetic field lines, here primarily located at the Sun's poles, are called coronal holes (CH), they appear darker on the solar disc in extreme ultraviolet images of the corona. The loops of closed field lines in-between regions of opposite polarity located around the equator are the helmet streamers. The heliospheric current sheet (HCS) is the plane extending into the interplanetary medium where field lines of opposite direction are adjacent. The tip of the helmet streamers

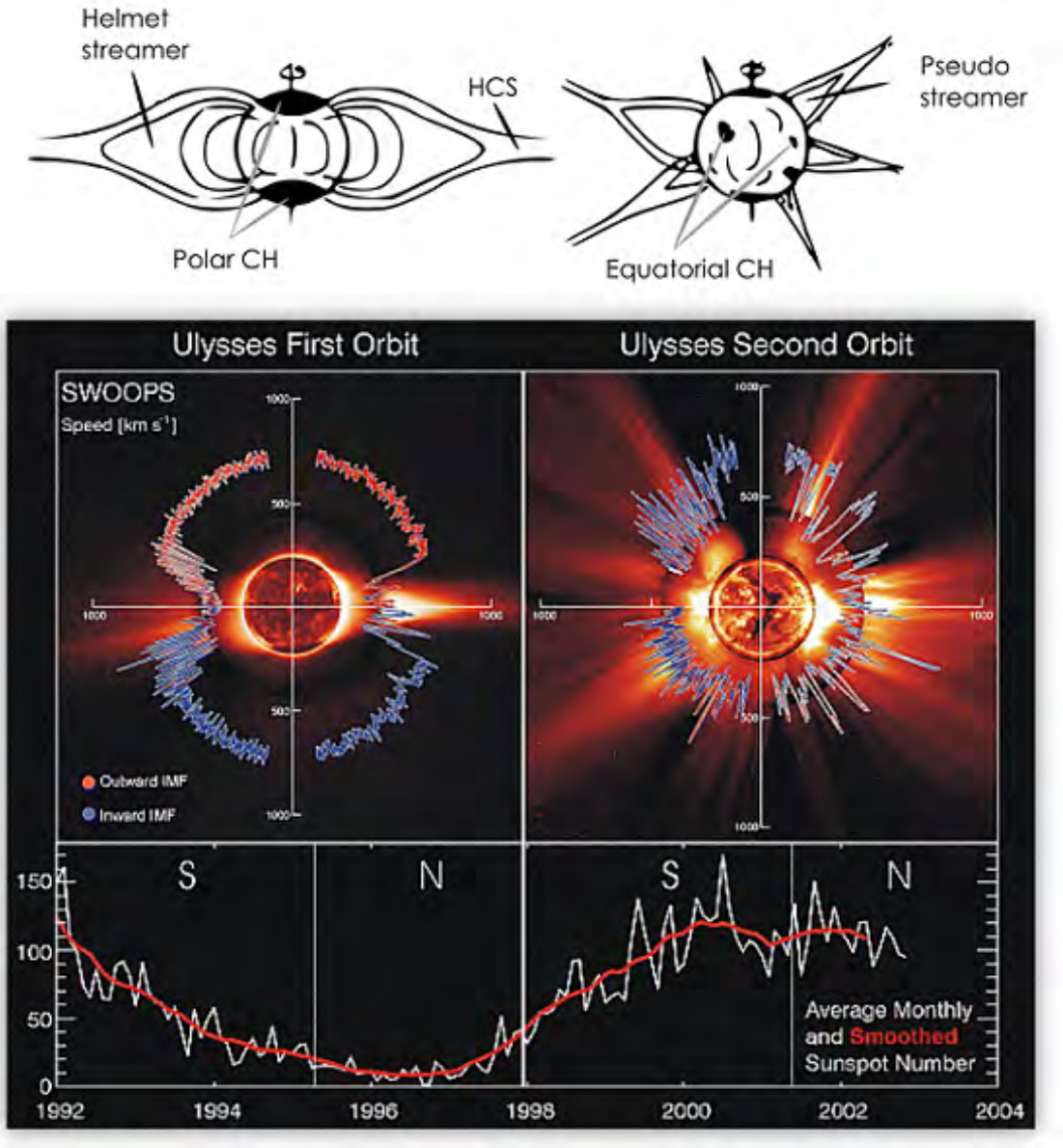

Figure 1.7: Schematics from Suess et al. (1998) representing the solar magnetic field structure for solar minimum and maximum, together with observations made by the Ulysses mission (figure from McComas et al. (2003)). The inserted figure shows "solar images characteristic of solar minimum (8/17/96) and maximum (12/07/00); from the center out, these images are from the Solar and Heliospheric Observatory (SOHO) Extreme ultraviolet Imaging Telescope (Fe XII at 195 Å), the Mauna Loa K-coronameter (700–950 nm), and the SOHO C2 Large Angle Spectrometric Coronagraph (white light)" (McComas et al., 2003). Measurements of the solar wind are overplotted in a dial plot, with the color indicating the polarity of the magnetic field (blue for inward, red for outward). The bottom panel displays the sunspot number over the period of observation of Ulysses.

and the HCS are particularly suitable regions for magnetic reconnection to occur. By contrast, at solar maximum, the Sun displays a multi-polar configuration (Fig. 1.7, right). The configuration is less neatly defined with equatorial coronal holes, active regions and pseudo

streamers (loops of closed field lines in-between regions of similar polarity) appearing at any latitude.

Eruptive events

As mentioned, as the Sun goes from a quiet state to an active one, the level of magnetic activity and the number of eruptive events increase until the peak of solar maximum. On the solar surface, it is usual for active regions to emerge. Active regions are often associated with sunspots, and are characterized by intense and complex closed magnetic field lines. Due to footpoint motion of field lines (either caused by differential rotation or surface convection), some magnetic structures of active regions get stretched, twisted, until the magnetic field reconnects and erupt in an explosive display of power also called a solar flare. Solar flares accelerate particles both downward, producing a local brightening on the solar surface, and outward in a heated plasma jet. A solar flare is sometimes followed by a coronal mass ejection (CME), which corresponds to the spectacular expulsion of solar plasma and magnetic field.

Let us pause a moment here to introduce the notion of magnetic flux rope that is apropos in this section and will be useful in the course of the manuscript. We introduced the magnetic flux tube in section 1.1 when discussing the connectivity of field lines in a vision where they were essentially straight. For a magnetic flux rope, the notion of connectivity is conserved but they are rather constituted of twisted field lines that wind around a common axis, forming a helical structure (see e.g. Russell et al. (1990)). The field lines closest to the magnetic axis are straighter while the ones farther are more twisted. Flux ropes are ubiquitous in space plasma, and are the core structure of various eruptive phenomena in the solar atmosphere (Liu, 2020). Particularly to come back to the topic at hand, a CME core structure is a large scale flux rope, also called a magnetic cloud, that propagates in the interplanetary medium, often at a high speed, and impacts the planetary environment it encounters. In Figure 1.8 we show the observation of a CME together with a schematic of the structure of a CME with its helical field lines. On Earth, CME collisions / interactions with the Earth's magnetic field (1.3.3) is correlated with brighter auroras and can affect electrical systems, putting some human activities at risk. A more complete description of magnetic flux ropes is given in section 2.3.

CMEs may occur several times a week during solar minimum and several times a day during solar maximum. But beside eruptive events, the Sun is also continuously ejecting a plasma in the interplanetary medium on a more stationary basis: the solar wind.

1.3.2 The solar wind

The existence of the solar wind was first theorised by Parker (1958) by considering an isothermal interplanetary medium. By writing the conservation of energy under relatively simple assumptions, the author found that the solar wind particles' velocity should increase with radial distance r following $V(r) \underset{\infty}{\sim} 2V_s(\ln r)^{1/2}$ (with V_s the sound speed). That the Sun should be able to emit a supersonic wind was a revolutionary concept at the time and, when first proposed, this theory was hotly debated and refuted by contemporary scientists (Meyer-Vernet, 2007). The debate was settled by observations: in 1962, the solar wind's existence was officially confirmed by the Mariner 2 mission who measured its velocity around 500 km/s (Neugebauer & Snyder, 1966).

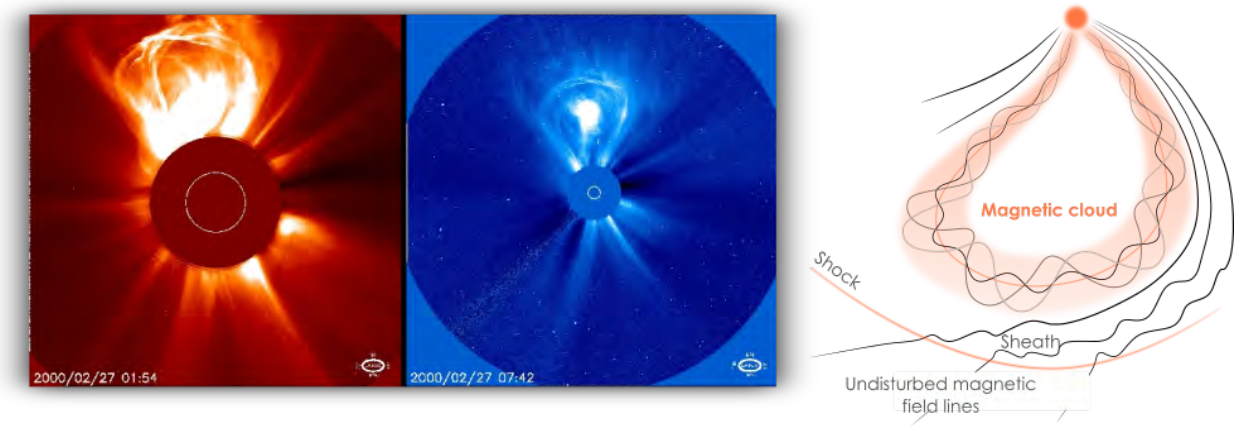

Figure 1.8: White light observation of a CME taken by LASCO C2 and C3 on the 27^{th} of February 2000, together with a schematic of the structure of a CME, adapted from Zurbuchen & Richardson (2006); Wang et al. (2018).

Two types of wind

Since these early observations, the properties of the solar wind have been measured extensively. It is a plasma mainly constituted of protons (H^+), alphas (H_e^{2+}) and electrons propagating into the interplanetary medium (with only traces of heavier, higher charge-state ions). The solar wind is often decomposed into two types of wind, a slow one and a fast one. Beside having obviously different velocity ranges, the two types of wind also differ in density, composition and variability. The slow wind ($\sim$ 400 km/s) is dense ($\sim$ 7 cm^{-3}) and structured, while the fast wind ($\sim$ 750 km/s) is tenuous ($\sim$ 2.5 cm^{-3}) and more uniform (values from Meyer-Vernet (2007)). Additionally they do not seem to originate from the same solar sources. This is nicely illustrated by the Ulysses' measurements of solar wind speed displayed in Figure 1.7. During solar minimum, it is clear that the fast wind is measured above the polar coronal holes, while the slow wind is measured near the ecliptic when the spacecraft is flying near the HCS. During solar maximum, the picture is less organized and both winds are observed at all latitudes. The fast solar wind can be traced back to coronal holes with open magnetic field lines in the low corona (e.g., Cranmer (2009)), while the origin of the slow solar wind is less clear, as different source regions are identified and advocated for in the literature. They include 1) the boundary of coronal holes as well as low latitude coronal holes where flux tube expansion may accelerate the plasma (e.g., Wang (1994), Bale et al. (2019)), and 2) the release of transients through magnetic reconnection at the tip of the coronal streamer (e.g., Lapenta & Knoll (2005), Antiochos et al. (2011), Sanchez-Diaz et al. (2017)). This classical picture of two different winds, however, is today challenged and the solar wind has been found to categorize into more than two types of wind. Xu & Borovsky (2015) for instance classify the solar wind observed at 1 AU in four types of plasmas: originating from coronal-holes, from the streamer-belt, from sector-reversal regions, and ejecta, which are associated with solar transients.

Regardless of the type of plasma that constitutes the solar wind, the latter displays a peculiar global magnetic structure in the heliosphere called the Parker spiral.

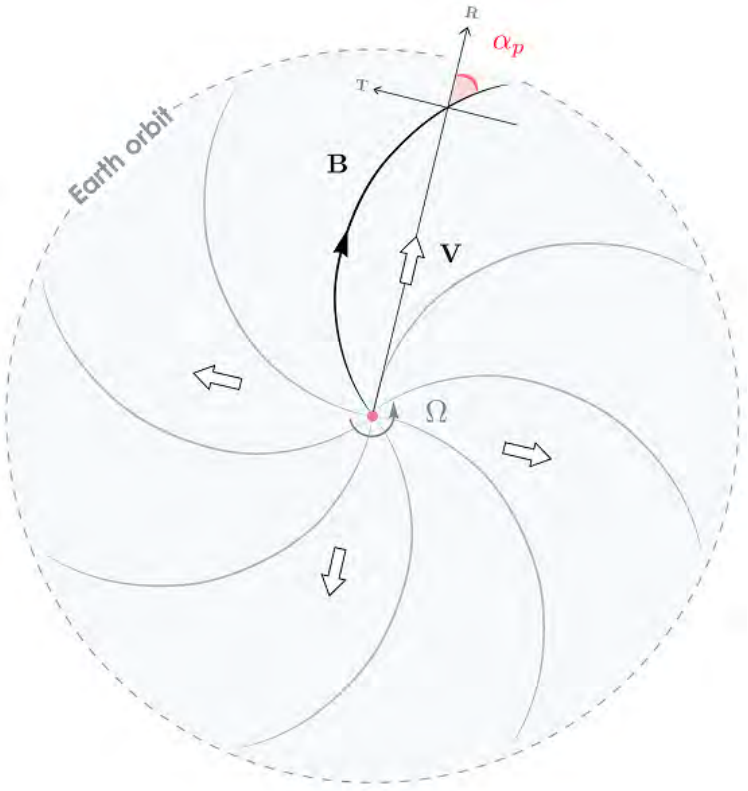

Figure 1.9: Illustration of the Parker spiral. The magnetic field lines are represented as grey lines, and the solar wind velocity as white arrows. On one particular field line, we highlight the Parker spiral angle α_p near the Earth orbit in the RTN plane, as defined in eq. (1.21). Figure adapted from Parker (1958).

The Parker spiral

The solar wind magnetic field, called the interplanetary magnetic field (IMF), is frozen in the solar wind plasma and advected into the interplanetary medium. Therefore, due to the rotation of the Sun, the field lines of the IMF take the shape of a spiral named the Parker spiral (Parker, 1958). The Parker spiral angle α_p in the ecliptic can be calculated through:

$$\alpha_p = \arctan\left(\frac{-\Omega_\odot\,(r - r_0)}{V_r}\right) \tag{1.21}$$

where $\Omega_\odot = 2.9 \times 10^{-6}$ s^{-1} is the Sun's rotational frequency (here taken at the equator) and r_0 is the source distance of the Parker spiral (see also section 4.3.2). Near the Sun, the Parker spiral angle is around zero as the magnetic field is radial, while at the Earth it is around 45°. The configuration of the Parker spiral until the Earth orbit is displayed in Figure 1.9.

If the solar wind had its way unhindered, it would make any planet that stand in its path barren and uninhabitable, as its particles would continuously be removing the planet's atmospheric material and shelling its surface. Some planets, however, develop strong magnetic shields against the raging solar wind and solar eruptions. They are called magnetospheres.

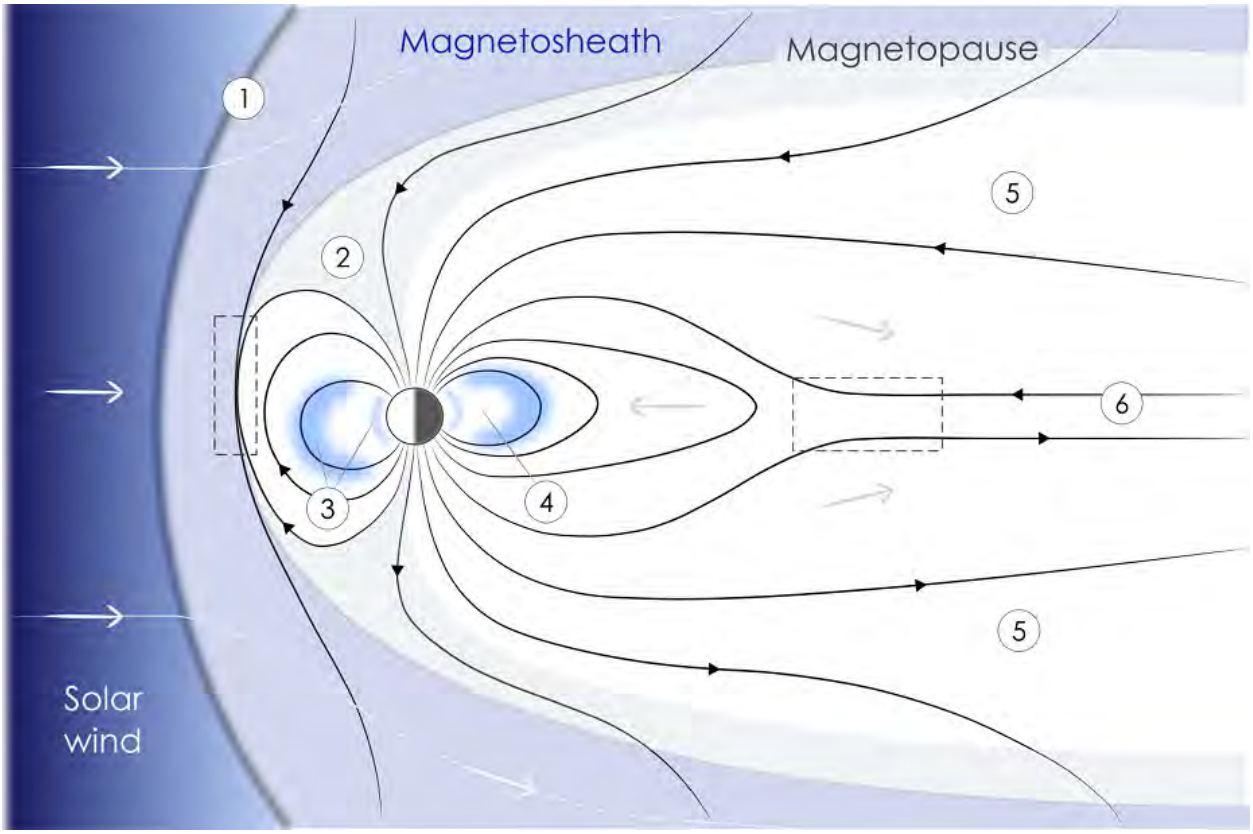

Figure 1.10: Near Earth environment displaying the regions resulting from the interaction of the solar wind with the Earth's magnetosphere. The latter is bounded by the magnetopause. Magnetic field lines are shown as solid black lines while the overall plasma flow is depicted with slim arrows. Various boundaries and regions of interest are indicated: 1) the bow shock, 2) the polar cusps, 3) the Van Allen radiation belts, 4) the plasmasphere, 5) the tail lobes and 6) the plasma sheet. The dashed rectangles indicate preferred locations for magnetic reconnection to occur for a southward IMF. Figure adapted from Lang (2013).

1.3.3 The Earth's magnetosphere

Configuration

The magnetosphere of a planet is the region around it where its own magnetic field is predominant (Chapman et al., 1930). This inner magnetic field is thought to be generated through a dynamo effect by the rotation of its metallic inner core (see e.g. Russell (1993)). Several planets of the solar system present such a magnetosphere, namely Mercury, the Earth, Jupiter, Saturn, Uranus and Neptune, while Mars and Venus lack one. In the case of the Earth, the core rotation generates a magnetic dipole with a magnetic dipole moment of 8.10^{22} Am^2, which is the strongest of the rocky planets. The Earth's magnetosphere, whose outer boundary with the solar wind plasma is called the magnetopause, is filled with a globally tenuous, cold and low β plasma.

Due to the interaction with the solar wind, the shape of an ideal dipole only holds close to the planet but is otherwise not maintained. On the dayside, the ram pressure applied by the solar wind causes the magnetosphere to shrink until pressure equilibrium is reached through

$\rho V^2 = B^2/(2\mu_0)$, where ρ and V are respectively the density and velocity of the solar wind, and B is the Earth's magnetic field magnitude (proportional to r^{-3}, with r the distance to the Earth). The stand-off distance of the magnetopause, or the extent of the magnetosphere in the dayside direction, normally varies between 6 and 10 Earth radii (R_E) depending on solar wind speed (300 to 800 km/s) and density (3 to 10 cm^{-3}). By contrast, on the night side, the solar wind stretches the Earth's magnetosphere into a magnetotail that can extend for hundreds of Earth radii.

The Earth's magnetosphere is displayed in Figure 1.10 together with other key features of the Earth's close environment (Borovsky & Valdivia, 2018):

- the *bow shock*, the boundary where the supersonic wind is shocked to subsonic values,
- the *magnetosheath*, the region located between the bow shock and the magnetopause, where the shocked solar wind is deflected around the magnetosphere in a turbulent flow,
- the *polar cusps*, the regions of open magnetic field lines located at the planet's poles where the magnetosheath plasma gains direct access to the ionosphere (Russell, 2000),
- the *Van Allen radiation Belts*, donut-shaped regions made of high energy particles trapped by the Earth's magnetic field,
- the *plasmasphere*, the very low energy (few eV) plasma of ionospheric origin trapped in the inner part of the Earth's magnetosphere,
- the *tail lobes*, mostly devoid of plasma and constituting the high latitude parts of the magnetotail with open magnetic fields pointing respectively toward (northern lobe) and outward (southern lobe) from the Earth,
- the *plasma sheet*, is the region of closed field lines stretching out in the equatorial magnetotail and containing denser and hotter plasma of both solar and ionospheric origins.

Dynamics

The dynamic interaction between the Earth's magnetosphere and the IMF embedded in the solar wind largely involves the process of magnetic reconnection[6] (Dungey, 1962). The location of high magnetic shear regions - that favor the conditions for magnetic reconnection onset - will change depending on the IMF orientation. On the planet dayside, the Earth's magnetic field is oriented northward. Subsequently when the IMF is oriented southward, reconnection is favored at the subsolar point. It creates bended reconnected field lines that are advected above the poles, transferring energy (plasma and momentum) from the solar wind to the magnetotail. By contrast, when the IMF is northward, reconnection occurs at higher latitudes above the polar cusps. Magnetic reconnection also occurs in the magnetotail at the plasma sheet, where the magnetic shear is close to 180°. There reconnection exhausts flow both toward and away the Earth, propagating part of the solar wind plasma into the inner magnetosphere. The particles accelerated by this reconnection process flow along field

[6]see https://solarsystem.nasa.gov/resources/2286/modeling-earths-magnetism/ for a dynamic visualisation

lines towards the Earth and are at the origin of the auroras visible from the Earth's surface in polar regions.

The Sun-Earth environment just described has the strong advantage of being within reach of direct scientific exploration. In addition to remote observation, scientists are able to send spacecraft to measure directly in situ the properties of the plasma. This work is only made possible by the existence of these space missions that probe the interplanetary medium. In the next section, we describe the three currently operating missions that provide the data we use throughout this manuscript.

1.4 Space missions and instrumentation

1.4.1 Magnetospheric Multiscale Mission

The NASA Magnetospheric Multiscale (MMS) mission (Burch et al., 2016) was launched on March 12^{th} 2015, with the purpose to study magnetic field reconnection down to electron scales in the near-Earth environment. The mission is constituted of four identical spacecraft flying in a tetrahedron formation, allowing to construct a 3D view of the reconnection process. The MMS mission includes two operational phases with different orbits, that are laid out in Figure 1.11. The first one focuses on dayside magnetopause reconnection (phase 1a and 1b, 2015-2017), while the second phase - which is out of the scope of this work - focuses on night-side magnetotail reconnection. Two data modes are available on MMS, a burst mode, which provides the high time resolution measurements necessary to resolve magnetic reconnection at electron scales, and a survey mode with lower time resolution. The high time resolution of the burst mode data imply a quick filling of storage space on-board the spacecraft and subsequently, they must be downloaded to Earth regularly. Hence, the Scientists In The Loop (SITLs), who are scientific investigators of the MMS mission, take turns to monitor the low resolution MMS measurements and flag data that they deem of interest following a given list of priority, and only flagged data intervals are then downloaded to Earth in burst mode.

Each MMS spacecraft carries a set of instrument suites, namely:

- the Fast Plasma Investigation (FPI, Pollock et al. (2016)) analysing the properties of the fast evolving low energy plasma by measuring electron and ion properties,
- the Hot Plasma Composition Analyzer (HPCA, Young et al. (2016)) that analyse the composition of the heavier ion populations known to be present in the magnetopshere (e.g., O^+, H_e^+),
- the Energetic Particles Detector suite (EPD, Mauk et al. (2016)), measuring the properties of the fast-moving, energetic particles accelerated through reconnection and other processes,
- the FIELDS Suite (Torbert et al., 2016), measuring the electric and magnetic fields and associated waves.

An illustration of one MMS spacecraft with its full set of instruments is presented on the left panel of Figure 1.11. In this manuscript - and especially Chapter 2 - we mostly analyse

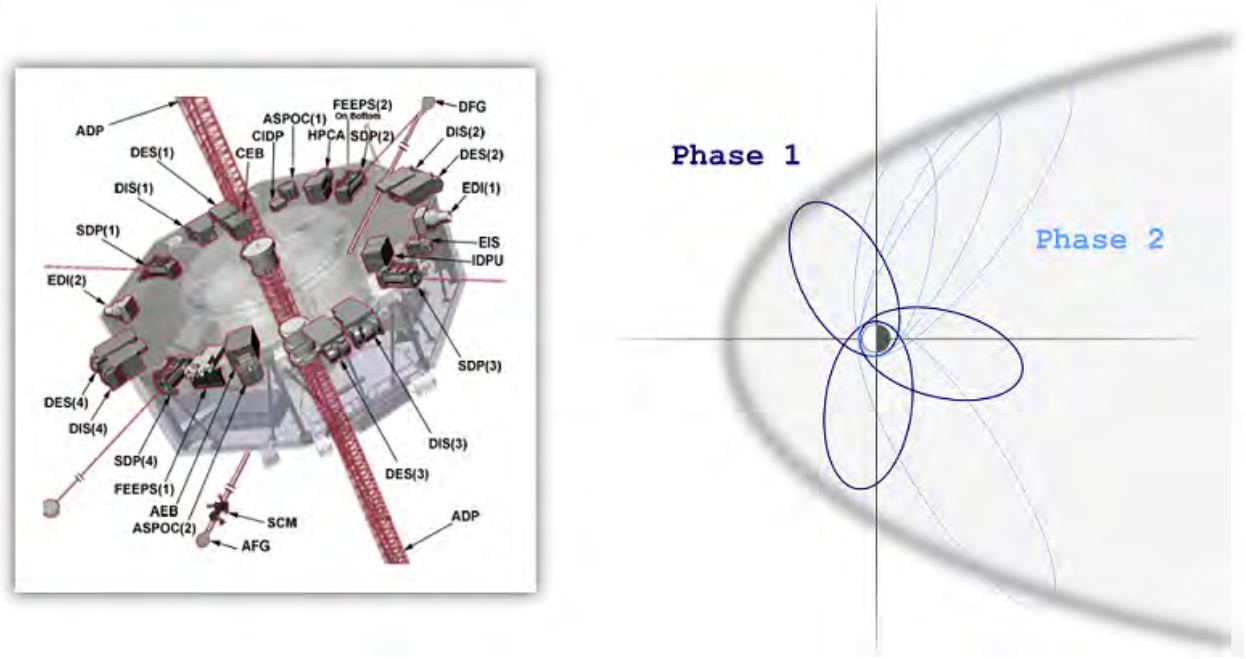

Figure 1.11: Left panel: Instrumentation of one MMS spacecraft (credits NASA), right panel: illustration of MMS operational phases, where phase 1 (dark blue) focuses on dayside magnetopause reconnection, while phase 2 (light blue) focuses on night-side magnetotail reconnection (adapted from Burch et al. (2016))

ion end electron data provided by the FPI instruments, and the fluxgate magnetometers (Russell et al., 2016) from the FIELDS suite. The data is presented in the Geocentric Solar Ecliptic (GSE) coordinate system where $\mathbf{x_{GSE}}$ is the Earth to Sun unit vector, $\mathbf{z_{GSE}}$ points North out of the ecliptic and $\boldsymbol{y_{GSE}}$ completes the oriented frame.

FPI measures the distribution functions of electrons and ions at unprecedented (and to this day unrivalled) time resolutions. Its burst mode achieves a 150 ms time resolution for ions and a 30 ms resolution for electrons. FPI is indeed constituted of two sets of spectrometers, the Dual Electron Sensors (DES) and the Dual Ion Sensors (DIS), both covering an energy range from 10 eV to 30 keV. Four pairs of each are dispatched around each of the four spacecraft, reducing the bias in azimuthal sampling and allowing for a fast coverage of the full three-dimensional field of view, as displayed in Figure 1.11. IRAP contributed to the development of the DIS instrument, being in charge of the provision and testing of all the DIS detectors (micro channel plates).

The Flugate Magnetometers of the FIELDS suite may acquire data at 128 Hz and with a 0.1 nT precision. Three sensors are present on each spacecraft and located on deployable booms: two independently designed fluxgate magnetometers (AFG and DFG, permitting redundancy to avoid one point failure), measure the low frequency (DC) magnetic field at two separate locations, while a search coil magnetometer measures the high frequency (AC) magnetic field.

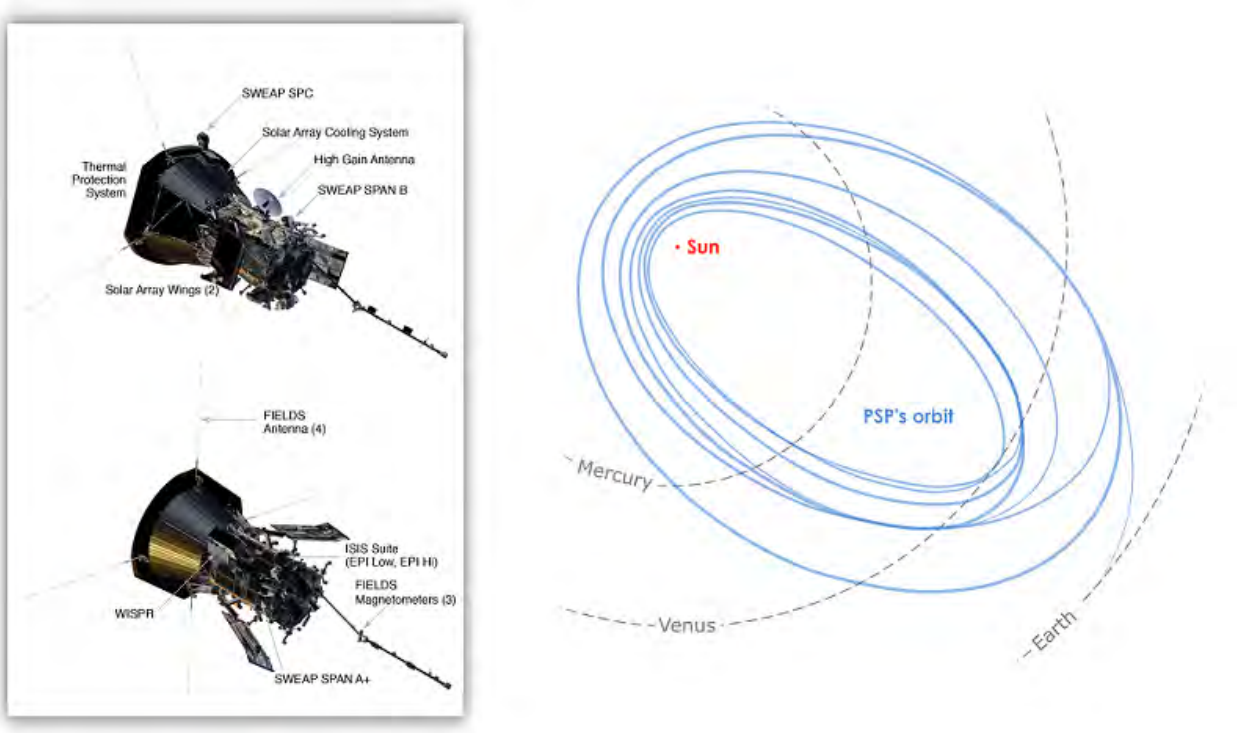

Figure 1.12: PSP instrumentation and orbit. Left panel: Instrumentation of the PSP spacecraft (credits: JHUAPL), right panel: illustration of PSP's orbit (adapted from JHUAPL)

1.4.2 Parker Solar Probe

The Parker Solar Probe (PSP, Fox et al. (2016)) mission was launched by NASA in August 2018 to investigate several remaining mysteries of the solar corona. The scientific objectives of the mission are to identify which processes come into play in the heating of the solar corona, the formation and acceleration of the solar wind, and the acceleration of energetic particles. To do so, the spacecraft's orbit will bring it closer to the Sun than any other previous mission, with a closest approach expected on Christmas 2024 below 10 $R_\odot$ (solar radii). This is, as NASA puts it, a mission to "touch the Sun". The orbit of PSP is displayed in Figure 1.12. The spacecraft gradually scans the solar wind deeper into the solar corona, as Venus gravity assists bring the perihelion of its highly elliptic orbit closer to the Sun. The closest approach per orbit are summarized in table 1.1

Perihelion ($R_\odot$, (AU))	Encounters	Date
35.6 (0.166)	E_1 to E_3	11-2018
27.8 (0.130)	E_4 to E_5	01-2020
20.3 (0.095)	E_6 to E_7	09-2020
16.0 (0.074)	E_8 to E_9	04-2021
13.2 (0.061)	E_{10} to E_{16}	11-2022
11.3 (0.053)	E_{17} to E_{21}	09-2023
9.9 (0.046)	E_{22} to E_{26}	12-2024

Table 1.1: Closest approaches of PSP to the Sun, where E_x stands for encounter (or orbit) number x.

As PSP is diving deeper into the solar corona, it has to withstand the ever higher temperatures induced by the proximity of the Sun. Hence, the spacecraft is compact, all instrumentation being protected behind its heat shield that points toward the Sun. PSP has four instrument suites that are indicated in the insert of Figure 1.1:

- the FIELDS suite (Bale et al., 2016) providing the magnetic and electric field data,
- the Solar Wind Electrons Alphas and Protons suite (SWEAP, Kasper et al. (2016)), measuring the properties of the solar wind particles,
- the Wide-field Imager for Solar Probe camera (WISPR, Vourlidas et al. (2016)), imaging the solar wind in white light with a field of view covering the ram spacecraft side,
- the Integrated Science Investigation of the Sun suite (IS⊙IS, McComas et al. (2016)), investigating energetic particles.

In this manuscript, we mostly analyse magnetic field data provided by the magnetometers of the FIELDS instrument suite and particle data provided by the SWEAP instrument suite. The latter includes plasma moments from the Solar Probe Cup (SPC) (Case et al., 2020) and distribution functions for ions and electrons from the Solar Probe ANalyzers (SPANs) (Whittlesey et al., 2020). The SPC and SPAN instruments are complementary in measuring the solar wind due to a particular setup. SPC is actually the only plasma detector from PSP that heads out from the spacecraft's heat shield, pointing directly at the Sun to measure the inflow of solar wind particles. The SPAN instruments on the other hand possesses two units that are located on the sides of the spacecraft. They are hence able to measure the particles of the solar wind only if the spacecraft has a high tangential velocity, for instance at the orbit perihelion. The specificity of this configuration along with PSP's highly elliptic orbit implies that far from the Sun the SPC instrument will be more accurate, whereas close to the Sun the SPAN measurements will take over (Kasper et al., 2016). The data we use is shown in the RTN frame of reference, with $\mathbf{R}$ (radial) being the Sun to spacecraft unit vector, $\mathbf{T}$ (tangential) being the cross product between the Sun's spin axis and $\mathbf{R}$, and $\mathbf{N}$ (normal) completes the direct orthogonal frame.

1.4.3 Solar Orbiter

The Solar Orbiter (Müller et al., 2013) is an ESA mission in collaboration with NASA, and was launched in February 2020. It has similar science objectives to the PSP mission, focusing on the heating of the corona, formation and acceleration of the solar wind and, in addition, the origin of the 11-year solar cycle. The Solar Orbiter mission, however, differs largely from PSP in instrumentation and orbit, making both mission complementary. The orbit of Solar Orbiter will bring it as close to the Sun as 0.3 AU (around 65 $R_\odot$) in an elliptic orbit. A key specificity of the mission is to gradually reach an out-of-ecliptic orbit ($> 33°$ inclination in 2029) by using several Venus gravity assists, as displayed in Figure 1.13. This will hopefully allow us to get for the very first time a detailed image of the Sun's pole taken from high latitudes.

By staying farther from the Sun, Solar Orbiter is less constrained thermally than PSP and is thus able to transport more instrumentation and, importantly, remote-sensing instruments directly imaging the Sun (that were absent from the PSP mission). The different instrument

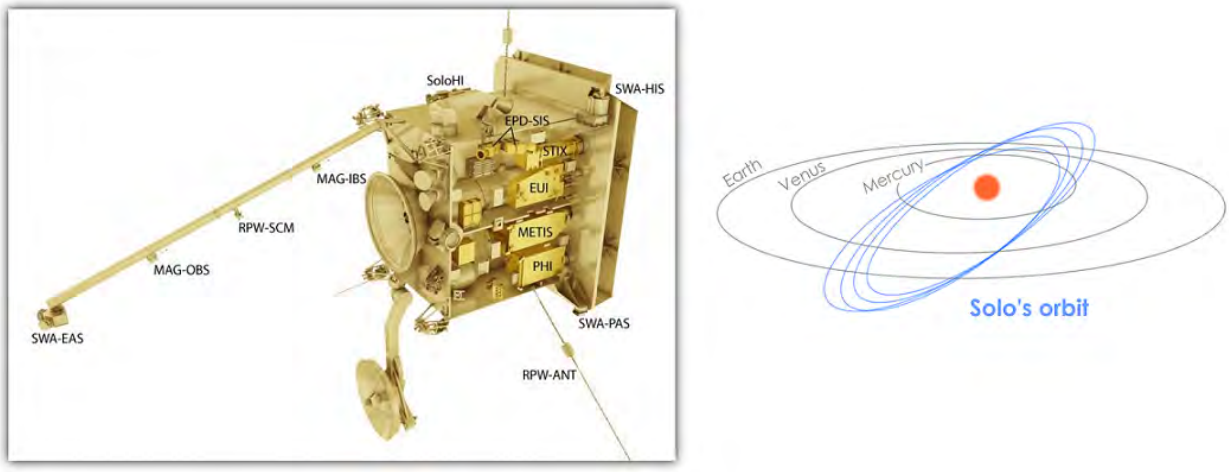

Figure 1.13: Solar Orbiter instrumentation and orbit. Left panel: Instrumentation of the Solar Orbiter spacecraft (credits: ESA), right panel: illustration of Solar Orbiter's orbit (adapted from ESA).

suites present on the spacecraft can be distinguished into two categories: in-situ and remote-sensing instruments, all displayed in Figure 1.13. The remote sensing instruments include:

- Extreme Ultraviolet Imager (EUI), imaging the Sun in extreme ultraviolet (EUV) wavelength,
- Multi Element Telescope for Imaging and Spectroscopy (METIS), a coronograph imaging the corona in both visible and EUV wavelength
- Polarimetric and Helioseismic Imager (PHI) producing magnetograms of the Sun's surface with both full disc and close-up fields of view,
- Solar Orbiter Heliospheric Imager (SolOHI) imaging the solar wind in visible wavelength,
- Spectral Imaging of the Coronal Environment (SPICE), a EUV spectrometer mapping the Sun's plasma,
- X-ray Spectrometer/Telescope (STIX), surveying X-rays during solar flares.

The in-situ instruments include:

- Solar Wind Analyzer (SWA) suite, measuring the properties of the thermal solar wind particles,
- Magnetometer (MAG), measuring the magnetic field,
- Radio and Plasma Waves (RPW), measuring the changes in the variation of electromagnetic fields,
- Energetic Particle Detector (EPD) measuring the properties of energetic particles.

As for the MMS and PSP missions presented above, we will mainly use data from the magnetometers of the MAG instrument (Horbury et al., 2020a) and the particle data from the SWA suite (Owen et al., 2020). The latter includes three instruments dedicated to

different types of particles, an Electron Analyser System (SWA-EAS), a Proton and Alpha particle Sensor (SWA-PAS), and a Heavy Ion Sensor (SWA-HIS). Particularly, the PAS instrument was designed, manufactured and tested at IRAP. IRAP also contributed to parts of the HIS instrument (optics and high voltages).

1.5 Thesis outline

The various missions launched by NASA and ESA (section 1.4) evidently brought new answers to the field of plasma physics. They were equipped to unveil new features of their surrounding media, and in that they succeeded, particularly in bringing to light structures that were not observed before, either due to a lack of instrumental resolution or to the absence of previous data. In this manuscript, we focus on structures observed both at the Earth's magnetopause and in the solar wind, and of significant importance to the dynamics of their environment. In our approach, we aim to shed light on the physical processes at stake for the formation of these structures, using modeling and statistical analysis to infer their properties and potential formation models.

In the first part (I), we focus on a type of magnetic structure resembling magnetospheric flux transfer events (FTEs), that is observed both at the magnetopause (chapter 2) and in the solar wind (chapter 3). In chapter 2, we study FTEs at the magnetopause, and particularly focus on a new FTE type that was observed for the first time by MMS (Øieroset et al., 2016; Kacem et al., 2018) with magnetic reconnection resolved in its core. Such a signature questions the usual model put forward to explain the internal structure of FTEs. Through a statistical analysis of FTE, we were able to better understand their magnetic topology and determine the factors playing a role in their occurrence, gaining insights on how they may be produced through magnetic reconnection at the dayside magnetopause. In chapter 3, we report on observations of similar structures in the solar wind, underlining that the process at work at the magnetopause is probably occurring in the solar wind as well.

In the second part (II) of the manuscript, we move from the near-Earth environment to the inner heliosphere, focusing on magnetic switchbacks that are a key feature of the near-Sun solar wind. Magnetic switchbacks are deflections of the magnetic field, sometimes reversing the radial component of the field, and made of accelerated plasma relative to the background solar wind. We first give an overview of magnetic switchbacks (chapter 4), then present a study of their characteristic scales through a wavelet analysis (chapter 5) highlighting their probable link to solar surface features like granulation and supergranulation. We finally find that they present a preferential orientation (chapter 6), inconsistent with turbulent generation and consistent with a formation through the interchange reconnection process in the low solar atmosphere.

Magnetic reconnection is a common thread of this work, being ubiquitous both at the Earth's magnetopause and in the solar wind, and most probably involved in the formation of switchbacks lower in the corona as well. Particularly, the work presented in the previous chapters underlined how observing or not observing reconnection exhausts can greatly improve our understanding of the global processes at stakes. In the last part of the manuscript (III, chapter 7), we describe a new promising approach, inspired from visual identification, that permits to automatically detect magnetic reconnection exhausts in solar wind from in-situ

data. We apply the devised detection algorithm to Solar Orbiter data with promising results.

We conclude (chapter 8) by summarising the implications of this work and the perspective we see for future projects.

Part I

Flux ropes, interlaced flux tubes and magnetic reconnection

Chapter 2

Flux Transfer Events at the magnetopause

Contents

In this chapter, we study magnetic structures called *Flux Transfer Events*, observed along the Earth's magnetopause. We first give an overview of the magnetopause properties and shape. We then detail the definition of an FTE and present a method to fit a flux rope model to FTE observations. We focus on a particular type of FTE that includes a magnetic reconnection signature in its core and perform a statistical analysis on 229 events including 43 with a reconnecting current sheet. We find that FTEs with reconnecting current sheets are consistent with a structure of interlaced flux tubes and are only formed under peculiar IMF conditions. This result was published in Fargette et al. (2020) and, starting from section 2.4, large parts of the text are transposed from the paper.

2.1 The Earth's Magnetopause

The magnetopause, as first mentioned in the introduction (section 1.3) is the boundary separating the magnetospheric plasma (magnetosphere) from the shocked solar wind (magnetosheath), delimiting the closed field lines of the Earth on the day side and the extended magnetotail on the night side. It is a dynamic boundary, continuously undergoing magnetic reconnection often in the subsolar region (southward IMF) or at higher latitude (northward IMF). This magnetic reconnection process allows the mixing of solar wind and magnetospheric plasma. The magnetopause shape is to first order characterised by the stand-off

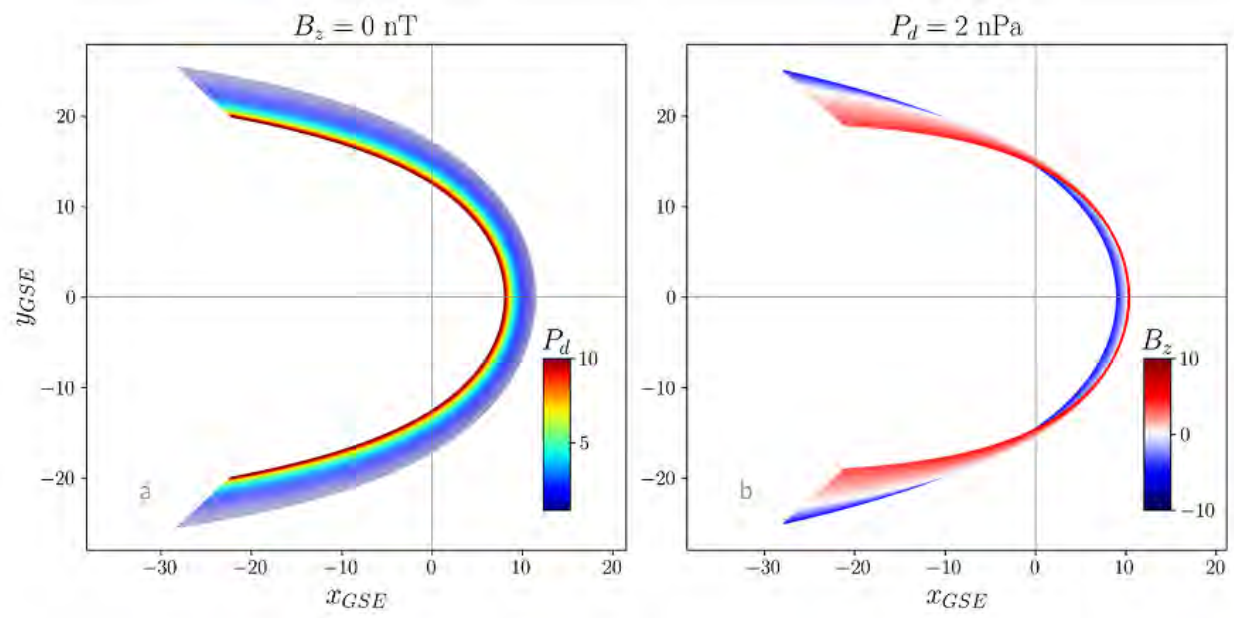

Figure 2.1: Magnetopause model from Shue et al. (1997) for different values of the solar wind relevant parameters B_z and $P_d = \rho V^2$.

distance (defined in section 1.3.3) and the level of tail flaring, which quantifies the angular opening and width of the night-side magnetopause.

Several models aiming to reproduce the magnetopause shape exist. Among them, the Shue et al. (1997) model is one of the most simple and most used to approximate the magnetopause location. It assumes a symmetry of revolution around the $\mathbf{x_{GSE}}$ axis and yields a good first order approximation of the magnetopause shape through the equation

$$r(\theta) = r_0(B_z, P_d)\left(\frac{2}{1+\cos\theta}\right)^{\alpha(B_z,P_d)} \tag{2.1}$$

where θ is the elevation and $r(\theta)$ is the distance of the magnetopause. In this equation, the stand-off distance of the magnetosphere r_0 and the level of tail flaring α are both functions that depend on solar wind parameters. They depend on the dynamic pressure of the solar wind $P_d = \rho V^2$ and on the southward component of the magnetic field B_z (Shue et al., 1997). The first one plays a role on the magnetopause stand-off distance through direct pressure balance, while B_z might impact the magnetopause location and shape through magnetic reconnection (erosion of the dayside magnetopause) or through the enhancement of Birkeland currents that impact the pressure balance (Sibeck et al., 1991) Shue et al. (1997) fitted the parameters r_0 and α to observations of magnetopause crossing locations and derived the following relations:

$$r_0 = (11.4 + 0.013\ B_z)\left(\frac{1}{P_d}\right)^{\frac{1}{6.6}} \qquad \text{for } B_z \geq 0 \tag{2.2a}$$

$$r_0 = (11.4 + 0.14\ B_z)\left(\frac{1}{P_d}\right)^{\frac{1}{6.6}} \qquad \text{for } B_z < 0 \tag{2.2b}$$

$$\alpha = (0.58 - 0.010\ B_z)\ (1 + 0.010\ P_d) \tag{2.2c}$$

Figure 2.1 illustrates how the two solar wind parameters influence the magnetopause shape. In the first panel, B_z is fixed at 0 nT and P_d varies from 1 to 10 nPa; while on the second panel P_d is fixed at 2 nPa and B_z changes from -10 to 10 nT (all are values typically observed at 1 AU). We see in these visualisations the main effect of each parameter. When P_d increases, the magnetosphere is compressed and the magnetopause shrinks, reducing its stand-off distance (2.1a). A change of B_z, however, mainly impacts the shape of the magnetopause at high latitudes and along the flanks, with negative values increasing the flaring (2.1b).

The Shue et al. (1997) model is still largely used today as it is a simple and relatively accurate model. However, it remains a first order approximation, and for instance its assumption of a symmetrical magnetopause is not verified (see e.g. Nguyen et al. (2022a) and references therein). Several models have since then incorporated additional effects. Shue et al. (1998) improved the magnetopause model slightly, making it more accurate for extreme solar wind conditions. More drastic changes were made by Lin et al. (2010) and Liu et al. (2015), who adapted the model to include the magnetopause asymmetries, indentations at the polar cusps, and additional dependencies such as on the dipole tilt angle or on the IMF orientation. If these two latter models do reproduce finer traits of the Earth's magnetopause, they end up being more complex (fitted to respectively 22 and 27 constants) than the Shue et al. (1997, 1998) models (fitted to 7 and 8 constants). More recently Nguyen et al. (2022a) demonstrated through a massive statistical analysis that the Shue et al. (1998) model actually better reproduced the locations of the stand-off distance compared to Lin et al. (2010); Liu et al. (2015), and was valid up to lunar distances. Subsequently, Nguyen et al. (2022b) proposed a simpler adaptation of the Shue et al. (1998) model (fitted to 9 constants) to take into account the magnetopause asymmetry and dependencies, but not reproducing the polar cusp indentations.

In the context of our work, we study structures observed by MMS along the magnetopause mostly near the subsolar region and in the ecliptic plane. Subsequently, and since we do not encounter drastic solar wind conditions in our study (see section 2.4.4), we use the Shue et al. (1997) model hereafter.

2.2 Flux Transfer Events

2.2.1 Observations

Flux Transfer Events (FTEs) are transient phenomena that frequently occur at the Earth's magnetopause, resulting from the dynamic interaction of the solar wind with the magnetosphere. They were first observed by Russell & Elphic (1978) in ISEE data as structures of increased magnetic field strength propagating on the magnetopause, and presenting a bipolar signature in the magnetic field component normal to the magnetopause (Russell & Elphic, 1978). This internal structure of FTEs (increased B amplitude and bipolar signature in the normal magnetic field) suggest that they are magnetic flux ropes. As previously mentioned

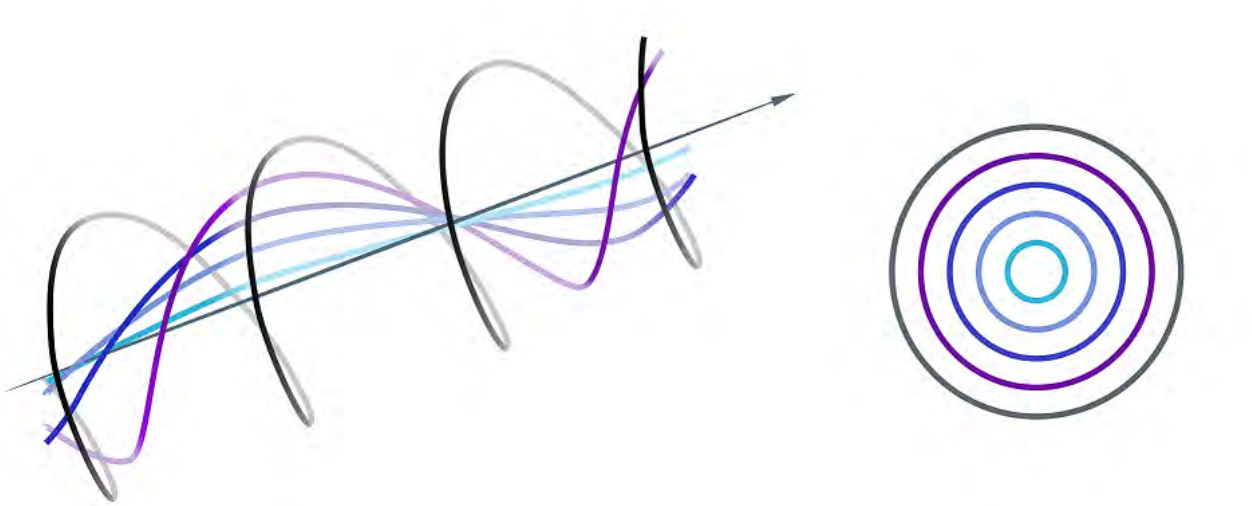

Figure 2.2: Illustration of a flux rope structure showing the helical field lines that wind around the magnetic axis. We also display on the right a view of the flux rope with a line of sight along the magnetic axis.

when presenting CME propagation in the solar wind (section 1.3.1), a magnetic flux rope presents a helical magnetic field, with rather straight field lines in the core of the structure and gradually more wound field lines with an increasing azimuthal component towards its boundary (Saunders et al., 1984). An illustration of a magnetic flux rope is given in Figure 2.2. Spacecraft measurements reveal that FTEs are constituted of a mixture of magnetosheath and magnetospheric plasma (Paschmann et al., 1982), this indicates that they are created through magnetic reconnection between both media at the Earth's magnetopause. Subsequently, solar wind conditions should impact FTE occurrence and properties. Indeed, FTEs are found to occur preferentially under southward IMF conditions (Berchem & Russell, 1984; Russell et al., 1996), this underlines that they form near the subsolar region. The IMF orientation seems to be the key factor in controlling the spatial distribution of FTEs, while other parameters such as solar wind β, P_d or Mach number show little influence (Kuo et al., 1995; Wang et al., 2006; Fear et al., 2012). Several models were proposed to explain FTE formation.

2.2.2 Formation models

In the early model of Russell & Elphic (1978), FTEs result from bursty and patchy magnetic reconnection, and consist in elbow-shaped flux tubes moving away from the subsolar region. Two main models were later proposed. The first one proposed by Southwood et al. (1988) and Scholer (1988), is based on a single spatially stable X-line at the subsolar magnetopause, but whose reconnection rate varies over time. This time variation leads to the formation of magnetic field bulges that are identified as FTEs. The other main model is the multiple X-line scenario proposed by Lee & Fu (1985), relying on two X-lines appearing sequentially on the magnetopause. As the first X-line forms and then drifts towards the poles, a second X-line reforms near the equator (and remains connected to the first one). The FTE is then trapped in between these two reconnection lines. In all of these views, FTEs resemble flux

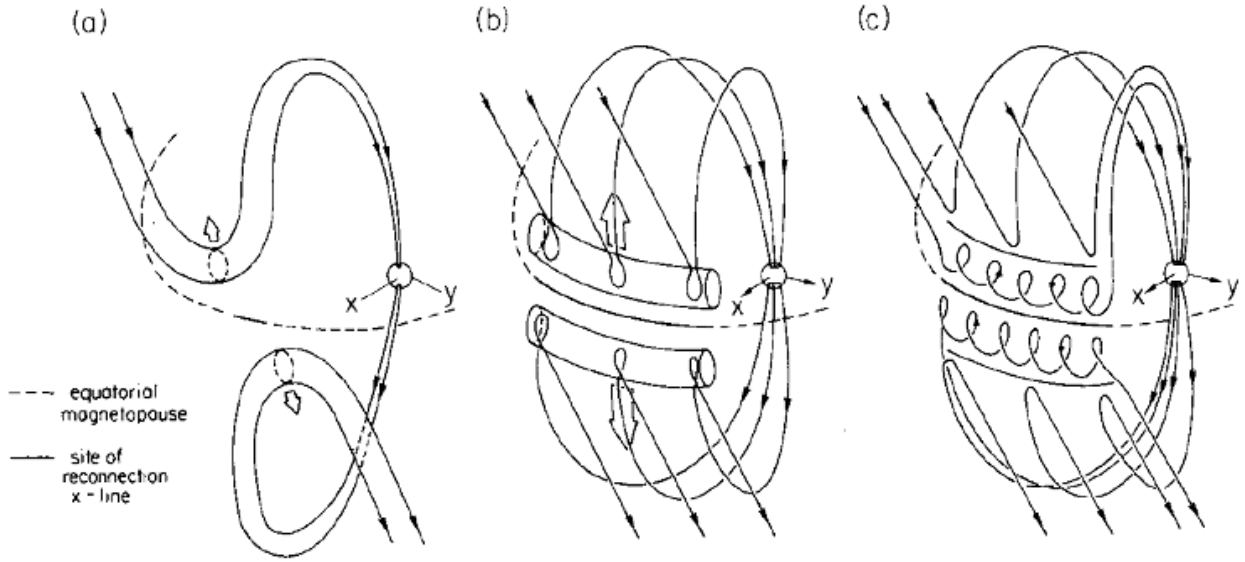

Figure 2.3: Illustration of the models proposed to explain FTE formation. Panel *a* displays the elbow shaped flux tubes proposed by Russell & Elphic (1978), panel *b* the single x-line reconnection with varying reconnection rate proposed by Southwood et al. (1988) and Scholer (1988), panel *c* the multiple x-line reconnection model of Lee & Fu (1985). Figure from Lockwood et al. (1990).

ropes and are thought of as three-dimensional helical structures as presented in Figure 2.2. The three models just described are illustrated in Figure 2.3, taken from Lockwood et al. (1990).

2.3 Flux rope modeling

In this section, we present a classic flux rope model that can be fitted to FTE data. It is used to both confirm that the model is accurate and infer the geometry of the event. This model was develop by Burlaga (1988) and Lepping et al. (1990) to study magnetic interplanetary clouds, the internal part of a CME.

2.3.1 Model of force-free flux ropes

In a force-free configuration, the magnetic field satisfies $(\nabla \wedge \mathbf{B}) \wedge \mathbf{B} = 0$. Lundquist (1951) devised that in a cylindrical symmetry around an axis $\mathcal{A}$ with a direction $\mathbf{u_A}$, a stable solution to this configuration is given by a magnetic field composed of the Bessel functions J_0 and J_1 such that:

$$B_A = B_0 J_0(aR) \tag{2.3a}$$

$$B_T = B_0 H J_1(aR) \tag{2.3b}$$

$$B_R = 0 \tag{2.3c}$$

where B_A is the axial component of the magnetic field, B_T its tangential component and B_R its radial component; R is the distance to the axis, H is the handedness of the cloud (± 1), B_0 is the field amplitude and a is a constant.

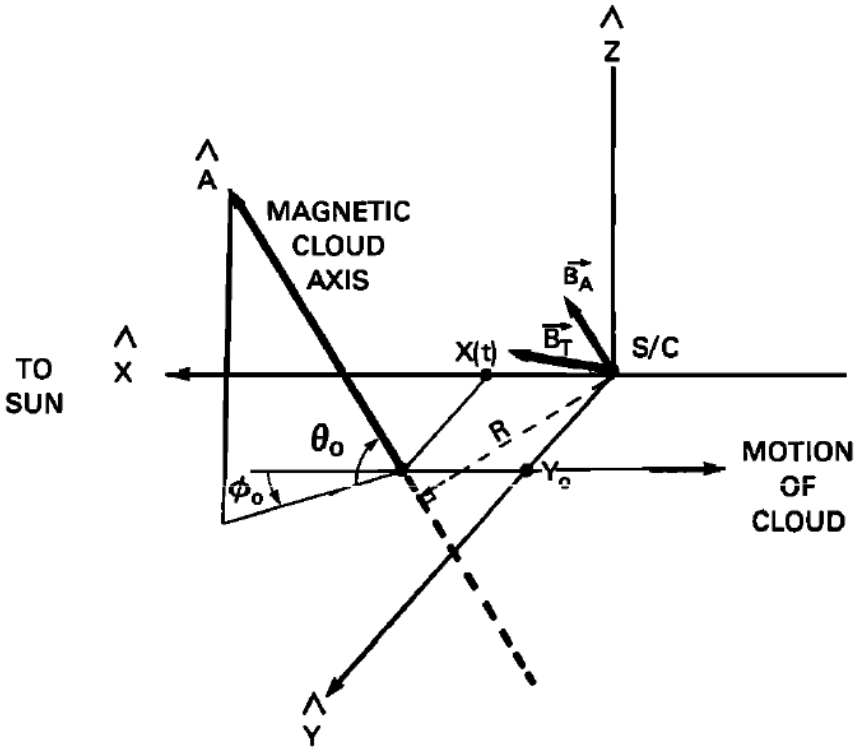

Figure 2.4: Configuration assumed of a magnetic cloud moving past a spacecraft, and used to model a magnetic field profile to fit observations. Figure from Burlaga (1988)

Burlaga (1988) uses this model to fit magnetic clouds near Earth, with a configuration displayed in Figure 2.4 using the GSE coordinate system. The magnetic cloud is assumed to move radially away from the Sun at a constant speed V. The model uses 3 parameters to characterize the magnetic axis:

- $\phi_0 \in [-180, 180]^\circ$ is the axis azimuthal angle, i.e. the angle between the $\mathcal{A}$ axis projection on the ecliptic plane and the $\mathbf{x}$ axis
- $\theta_0 \in [-90, 90]^\circ$ is the $\mathcal{A}$ axis elevation to the ecliptic plane
- Y_0 is the distance between the x axis and the line drawn by $\mathcal{A}(t) \cap (\mathbf{u_x}, \mathbf{u_y})$, where $\mathcal{A}(t)$ is the plane formed by the propagating magnetic axis, and $\mathbf{u_x}, \mathbf{u_y}$ are the unit vectors associated with the x and y axis.

Additionally, $H = \pm 1$ determines the handedness of the cloud. In his work, Burlaga (1988) fits these four parameters to the observations by trial and errors, and the article states that it would be *"desirable to devise a scheme for fitting the data to the model"*.

Several problems arise with the Burlaga (1988) model. First, Y_0 is not a totally relevant parameter to consider, for one thing it is not defined for $\theta_0 = 0$, and it has no real physical interpretation. Particularly, when we consider flux ropes near the Sun, we rather expect a magnetic axis orientation around $\theta_0 = 0$ and $\phi_0 = \pm 90$, so it is important to find a better set up. Moreover, edge effects and window width are not addressed, so the method is very

sensitive to the event delimitation. Most of these setbacks were addressed by Lepping et al. (1990), where a more regular impact parameter is defined. We now describe how we adapted the Burlaga (1988) model to magnetospheric FTEs, using an impact parameter instead of Y_0 and addressing boundary sensitivity.

2.3.2 An alternative parametrisation

For now, let us use the same frame (GSE) as Burlaga (1988), with the cloud propagating solely along $-\mathbf{u_x}$. The coordinates of $\mathbf{u_A}$ are given by:

$$\mathbf{u_A} = \begin{bmatrix} \cos\theta_0 \cos\phi_0 \\ \cos\theta_0 \sin\phi_0 \\ \sin\theta_0 \end{bmatrix} \tag{2.4}$$

with θ_0 and ϕ_0 the angles as represented in Figure 2.4.

We know that $\mathbf{u_A}$ propagates along $\mathbf{u_x}$. As $\mathbf{u_x} \wedge \mathbf{u_a} \neq 0$ (otherwise the problem is ill-defined), these two vectors form a plane $\mathcal{P}$ whose normal vector is given by:

$$\mathbf{n} = \mathbf{u_x} \wedge \mathbf{u_a} \tag{2.5}$$

The plane equation is by definition $n_x x + n_y y + n_z z + b_0 = 0$ where b_0 is a constant (note that $n_x = 0$). Actually, b_0 is precisely the distance of the plane to the origin, where the spacecraft is placed, and will be our new parameter to replace the Y_0 from Burlaga (1988). It is defined for $\theta_0 = 0$.

Let us consider $P_0 \in \mathcal{P}$ the orthogonal projection of the origin on $\mathcal{P}$, written $\mathbf{P_0} = -b_0\mathbf{n}$. It is the point of closest approach of the cloud to the spacecraft, and it is associated with the center of our event observed in-situ at a time t_0. We call $P(t)$ the line parallel to $\mathbf{u_x}$ and passing by P_0, with $P(t_0) = P_0$. Hence, over time, each magnetic axis $\mathcal{A}(t)$ is defined by the point $P(t)$ and the axis direction $\mathbf{u_A}$. These new parameters are illustrated in Figure 2.5.

Formally, we have (from equation 2.5 and by assuming the $-\mathbf{u_x}$ propagation)

$$\mathbf{P}(t) = \begin{bmatrix} -V(t - t_0) \\ \dfrac{b \sin\theta_0}{\sqrt{\sin^2\theta_0 + \cos^2\theta_0 \sin^2\phi_0}} \\ \dfrac{-b \cos\theta_0 \sin\phi_0}{\sqrt{\sin^2\theta_0 + \cos^2\theta_0 \sin^2\phi_0}} \end{bmatrix} \tag{2.6}$$

with V the propagation speed of the magnetic cloud, and t the time vector. Then, we may write the equation of the magnetic axis over time, stating that for any given point A on a magnetic axis $\mathcal{A}(t)$, it may be written as $\mathbf{A}(t, x_A) = \mathbf{P}(t) + x_a\mathbf{u_A}$ with $x_a \in \mathbb{R}$.

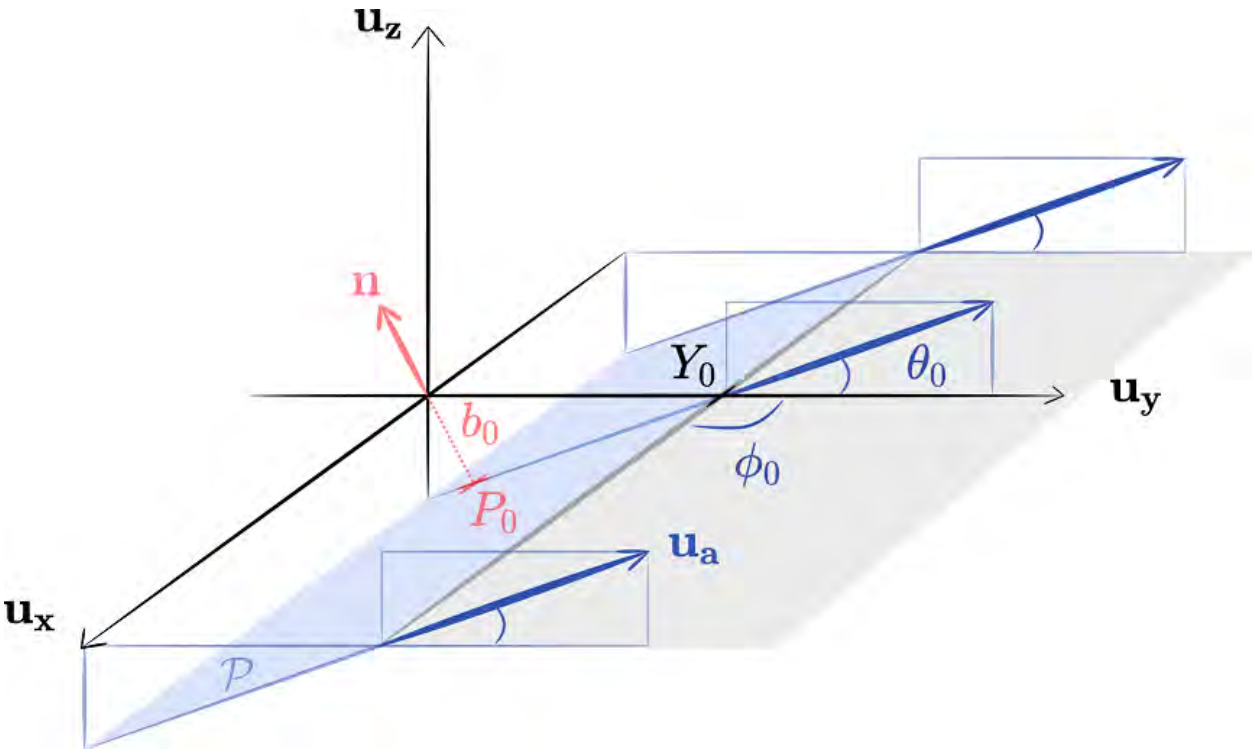

Figure 2.5: Illustration of the alternative parametrisation for a magnetic cloud moving past a spacecraft along $-\mathbf{u_x}$, displaying the new parameter b_0 together with P_0 the point of closest approach. The plane $\mathcal{P}$ is in light blue and its normal vector $\mathbf{n}$ in light red. On this figure, ϕ_0 is taken at $\pi/2$ for a simpler representation, but note that P_0 and Y_0 are not on the same axis in a more general case.

Mathematically, it writes $\forall A \in \mathcal{A}(t)\ \exists!\ x_{_A} \in \mathbb{R}$ such that

$$\mathbf{A}(t, x_{_A}) = \begin{bmatrix} -V(t-t_0) + x_{_A} \cos\theta_0 \cos\phi_0 \\ \dfrac{b \sin\theta_0}{\sqrt{\sin^2\theta_0 + \cos^2\theta_0 \sin^2\phi_0}} + x_{_A} \cos\theta_0 \sin\phi_0 \\ \dfrac{-b \cos\theta_0 \sin\phi_0}{\sqrt{\sin^2\theta_0 + \cos^2\theta_0 \sin^2\phi_0}} + x_{_A} \sin\theta_0 \end{bmatrix} \tag{2.7}$$

where x_A represents the coordinate of the point A on the $\mathcal{A}(t)$ axis with origin $P(t)$.

We now need to project the origin on each $\mathcal{A}(t)$. The $x_{_{Amin}}$ that minimizes the norm of $\mathbf{A}(t, x_{_A})$ is given by:

$$x_{_{Amin}}(t) = V(t-t_0)\cos\theta_0 \cos\phi_0 \tag{2.8}$$

It is independent of b_0, which makes sense, since the locus of points followed over time by this projection of the origin does not depend on the distance of the plane to the origin.

We can now compute the distance R and the direction of this projection $\mathbf{u_R}(t)$:

$$R(t) = ||\mathbf{A}\left(t, x_{_{Amin}}(t)\right)|| = \sqrt{V^2(t-t_0)^2(1 - \cos{\theta_0}^2 \cos{\phi_0}^2) + b_0^2} \tag{2.9}$$

$$\mathbf{u_R}(t) = \frac{\mathbf{A}\left(t, x_{Amin}(t)\right)}{R(t)} \tag{2.10}$$

We may then derive $\mathbf{u_T} = \mathbf{u_R} \wedge \mathbf{u_A}$.

One final subtlety is that the $R(t)$ we compute is homogeneous to a length, and physically represents the distance of the magnetic axis to the spacecraft. The Bessel functions, however, are quasi-periodic and defined on $\mathbb{R}$. One way to solve this issue is to normalise R to the characteristic scale of the magnetic cloud taken as $R_{max} = \max(R(t))$, and assume that we are fitting between the first roots of the J_0 Bessel function, numerically equal to ± 2.4. This prevents the core field of the flux rope to reverse. We may then introduce an additional parameter a (reminiscent of the a constant of the Burlaga (1988) model) which represents the erosion of the cloud. Erosion of a magnetic cloud corresponds to the decrease and dissipation of magnetic flux at the flux rope boundaries (for instance through magnetic reconnection), resulting in a trimming of the structure's edges. Here, $a = 1$ means no erosion, while $a < 1$ means that the cloud is eroded. In practice, we allow a to be greater than one to be more flexible with the events boundary definition. With this last assumption, we can finally write the modeled magnetic field (intentionally we explicit all the dependencies of the various terms):

$$\begin{aligned}\frac{\mathbf{B_{model}}}{B_0}(t, \theta_0, \phi_0, b_0, t_0, a, H) = J_0\left(2.4\ a\ \frac{R(t, \theta_0, \phi_0, b_0, t_0)}{R_{max}}\right)\mathbf{u_A}(\theta_0, \phi_0) \\ + H J_1\left(2.4\ a\ \frac{R(t, \theta_0, \phi_0, b_0, t_0)}{R_{max}}\right)\mathbf{u_T}(t, \theta_0, \phi_0, b_0, t_0)\end{aligned} \tag{2.11}$$

The model thus obtained depends on 7 parameters, $[\theta_0, \phi_0, b_0, t_0, a, H, B_0]^{\mathrm{T}}$.

2.3.3 Fitting algorithm

Now let us present how to fit this model to observational data. We consider two events observed by the MMS1 spacecraft, occurring respectively on 2015/11/12, 07h20:20-07h20:36 (also described in more details in section 2.4.1) and 2017/01/29, 01h57:07-01h57:23 (presented in Kieokaew et al. (2021)). Their magnetic field is shown in the top panels of Figure 2.6 in the GSE coordinate system.

Frame definition

One key assumption of the Burlaga (1988) model is that the structure propagates along $-\mathbf{u_x}$. All calculations rely on this hypothesis, and so in order to use the model we should always place ourselves in a frame such that $\mathbf{u_x} = -\mathbf{V}/V$. When analysing structures in undisturbed the solar wind, this straightforwardly yields the spacecraft-to-Sun vector. At the magnetopause, however, we compute $\mathbf{u_x}$ based on the velocity measured by the spacecraft. We then choose to define $\mathbf{u_z} = \mathbf{n}$, with $\mathbf{n}$ the vector normal to the magnetopause (in Burlaga (1988), $\mathbf{u_z}$ was the normal to the ecliptic plane), and $\mathbf{u_y}$ completes the direct orthogonal frame. The second row of Figure 2.6 presents the magnetic field in this new frame, and we clearly see for both events that the bipolar signature is on the z component as expected. We also display the ion velocity vector in this new frame (third row) frame to check that the velocity is indeed along $-\mathbf{u_x}$.

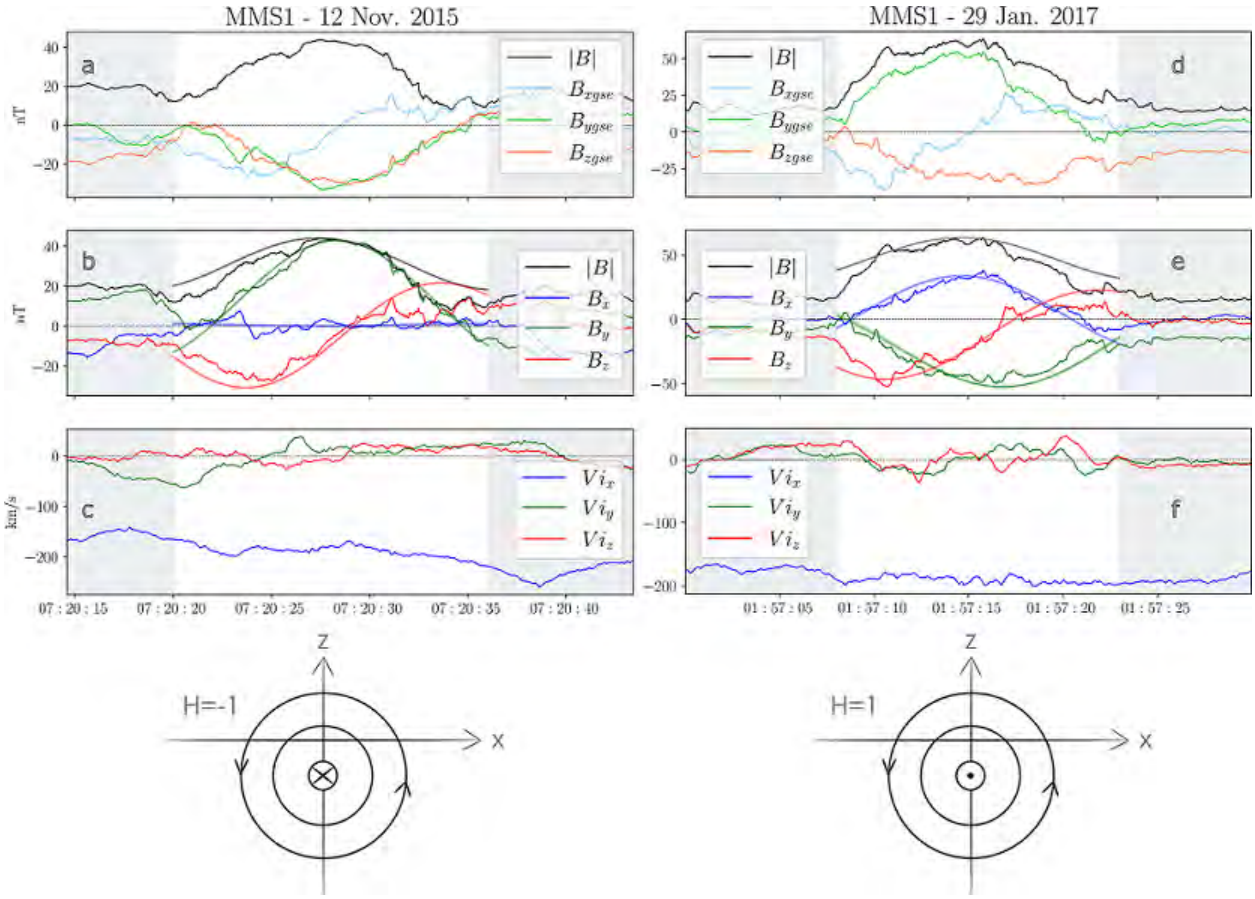

Figure 2.6: Fitting two flux ropes with the described model, occurring respectively on 2015/11/12, 07h20:20-07h20:36 and 2017/01/29, 01h57:07-01h57:23. Grey shaded areas surround the events. Panels a and d show the magnetic field in the GSE coordinate system, while panels b and e display B in the xyz frame. Panels c and f show the velocity vector in the xyz frame. Sketches on the bottom illustrate the helicity of each event.

Helicity sign determination

In the approach presented in Kieokaew et al. (2021), the H parameter is fitted to determine the helicity sign (or handedness). This means fitting the data twice, once with each value $H = 1$ or $H = -1$, and compare which of these achieves a better fit. But actually, H can be directly retrieved from the data by comparing the magnetic field vector at the leading (or trailing) edge and at the centre of the event. Indeed, the vector at the center of the event roughly indicates the direction of the magnetic axis $\mathbf{u_a}$. By looking at the schematics on the fourth row of Figure 2.6, we can be convinced that H is given by

$$H = \text{sign}(\mathbf{B}(t = t_0) \wedge \mathbf{B}(t = 0)) \tag{2.12}$$

Both methods (a successive fit or using equation (2.12)) should yield similar results, but to reduce the number of parameters to fit we choose the direct determination of H.

Maximum posterior probability

We are then down to 6 parameters to fit, $[\theta_0, \phi_0, b_0, t_0, a, B_0]^{\mathrm{T}}$. In practice, we avoid considering B_0 (the magnetic field strength at the center of the flux rope) by normalising both the quantity $\mathbf{B_{model}}/B_0$ and the observed vector $\mathbf{B}$ by their maximum amplitude. To reduce further the number of parameters, we could also determine t_0 directly from the data by taking it where B is maximum. However, we refrain from this hypothesis as noise can make the determination uncertain. Finally, we get 5 parameters to fit, that we gather in a parameter vector $\mathbf{\Theta} = [\theta_0, \phi_0, b_0, t_0, a]^{\mathrm{T}}$. Here, we may refer the reader to appendix A, where we give the basic frame of Bayesian statistics that we use in this section.

We assume that the dispersion of our data ($\mathbf{B}$) around its expected value ($\mathbf{B_{model}}$) is well approximated by a white noise model with a 10% dispersion σ. From here for a given set of parameter $\mathbf{\Theta}$, the likelihood of the data follows a normal distribution and may be written for each data point measured at t_i

$$\mathrm{p}(\mathbf{B}(t_i) \mid t_i, H, \mathbf{\Theta}) = \mathcal{G}\left(\mathbf{B}(t_i),\ \mathbf{B_{model}}(t_i, H, \mathbf{\Theta}),\ \sigma^2 \mathbb{1}\right) \tag{2.13}$$

where $\mathrm{p}(\mathbf{B}(t_i) \mid t, H, \mathbf{\Theta})$ designates the probability of observing $\mathbf{B}(t_i)$ at this given time t_i knowing $(H, \mathbf{\Theta})$, $\mathcal{G}$ is a 3D Gaussian distribution and $\mathbb{1}$ is the identity matrix.[1]

More explicitly by assuming independent measurements[2], and taking the logarithm of this expression, the log-likelihood of the data is expressed by:

$$\begin{aligned} \ln\left(\mathrm{p}(\mathbf{B} \mid t, H, \mathbf{\Theta})\right) &= \sum_i \ln\left(\mathrm{p}(\mathbf{B}(t_i) \mid t_i, H, \mathbf{\Theta})\right) \\ &= -\frac{1}{2\sigma^2} \sum_{i=1}^{n_p} |\mathbf{B}(t_i) - \mathbf{B_{model}}(t_i, H, \mathbf{\Theta})|^2 - \frac{3n_p}{2} \ln\left(2\pi\sigma^2\right) \end{aligned} \tag{2.15}$$

where n_p is the number of points in our data set. The second term of the RHS of the equation is a constant, so in essence we are seeking to maximise the first term.

In Bayesian statistics, the prior probability is the *a priori* probability of the parameters themselves (see appendix A). Here, we use uniform priors on the different parameters included in $\mathbf{\Theta}$, with the constraints $\theta_0 \in [-\pi/2, \pi/2]$, $\phi_0 \in [-\pi, \pi]$, $b_0 \in [-1, 1]$ R_E, $t_0/t_{n_p} \in [0.4, 0.6]$, $a \in [0.5, 1.5]$. We can now find the most probable parameters to fit our distribution, and hence seek to maximise the log-posterior probability of the model through the Bayes equation:

$$\ln \mathrm{p}(\mathbf{\Theta} \mid t, H, \mathbf{B}) = \ln \mathrm{p}(\mathbf{\Theta}) + \ln\left(\mathrm{p}(\mathbf{B} \mid t, H, \mathbf{\Theta})\right) + \mathrm{C} \tag{2.16}$$

where C is a constant. We sample the parameter space using the *emcee* python library (Foreman-Mackey et al., 2019) which is based on a Monte-Carlo Markov chain algorithm, using 32 walkers and 2000 iterations (see appendix A).

[1] With an arbitrary number of dimensions N, the Gaussian distribution writes:

$$\mathcal{G}(x, \mu, \Sigma) = \frac{1}{(2\pi)^{N/2}|\Sigma|^{1/2}} e^{-\frac{1}{2}(x-\mu)^{\mathrm{T}}\Sigma^{-1}(x-\mu)} \tag{2.14}$$

with μ the mean vector, Σ the covariance matrix and $|\Sigma|$ its determinant.

[2] Independent measurements yield $\mathrm{p}(\mathbf{B} \mid t, H, \mathbf{\Theta}) = \prod_i \mathrm{p}(\mathbf{B}(t_i) \mid t_i, H, \mathbf{\Theta})$

Fitting results

The fitting results for both considered flux ropes are shown in table 2.1 and overplotted in the second row of Figure 2.6.

FR	θ_0 (°)	ϕ_0 (°)	b_0 (R_E)	t_0/t_{n_p}	a
12/11/2015	$-19.19^{+3.04}_{-2.46}$	$95.17^{+4.87}_{-6.3}$	$-0.010^{+0.012}_{-0.016}$	0.465 ± 0.005	1.33 ± 0.025
29/01/2017	$-13.29^{+3.09}_{-9.0}$	$-26.93^{+7.45}_{-12.6}$	$-0.041^{+0.019}_{-0.014}$	$0.442^{+0.008}_{-0.002}$	1.21 ± 0.029

Table 2.1: Best parameters found by the fitting method for the two considered flux ropes.

This work shows that some FTEs are to the first order very well approximated by the Burlaga (1988) and Lepping et al. (1990) models using Bessel functions. In subsequent studies, part of this algorithm was used to determine the helicity of FTEs observed at the magnetopause by comparing the fits performed with $H = 1$ and $H = -1$, and we detail these results in section 2.5.

2.4 Two types of FTEs

The MMS mission (section 1.4.1) with its high-resolution instrumentation has unveiled new features of FTEs. In particular, structures that look like classical FTEs have been reported to display reconnection signatures in their center, with clear ion jets correlated with a thin current sheet. While thin current sheets inside FTEs had previously been observed with the THEMIS mission (Hasegawa et al., 2010; Øieroset et al., 2011), only the recent MMS measurements enabled to confirm that magnetic reconnection was sometimes occurring there (Øieroset et al., 2016, 2019; Kacem et al., 2018). Detailed studies of such structures led to the conclusion that they did not match the regular magnetic flux rope configuration, but rather consisted of interlaced flux tubes with a central reconnecting current sheet separating two magnetically disconnected regions (Kacem et al., 2018; Øieroset et al., 2019). The interpretation of some FTE-type phenomena as complex 3D structures with interlaced flux tubes was first proposed by Nishida (1989) and Hesse et al. (1990). It was studied through simulations (Lee et al., 1993; Otto, 1995; Cardoso et al., 2013; Farinas Perez et al., 2018) and observed in Cluster data (Louarn et al., 2004) prior to MMS.

In this part, we describe the statistical analysis performed on the FTEs observed by MMS, investigating in more depth the occurrence and implications of reconnection signatures found inside FTEs. We show that 19% of FTEs present these signatures in their core, and are consistent with the magnetically disconnected flux tube structure similar to Kacem et al. (2018). We also find that the IMF orientation plays a significant role in the formation of such structures.

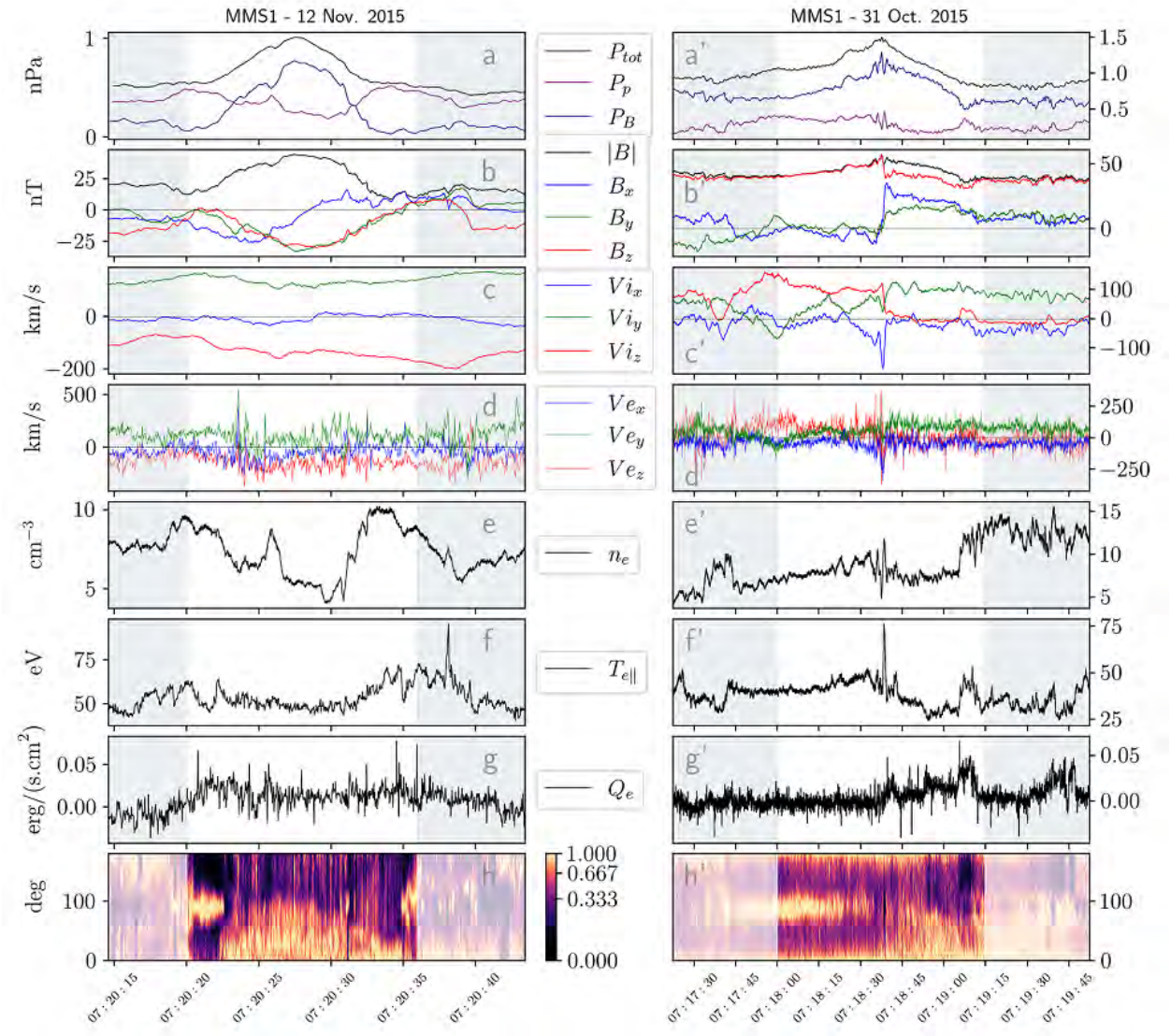

Figure 2.7: Illustration of the two types of FTE-like structures observed by MMS, delimited by grey shaded areas. Left: Standard flux rope event from 2015/11/12, 07h20:20-07h20:36; Right: Event with core reconnection from 2015/10/31, 07h18:00-07h19:15. From top to bottom, the panels present *a*) the total, magnetic and particle thermal pressure P_{tot}, P_B, P_p; *b*) the magnetic field (GSE); *c*) the ion velocity (GSE); *d*) the electron velocity (GSE); *e*) the electron density, *f*) the electron parallel temperature; *g*) the electron parallel heat flux and *h*) the pitch angle distribution of electrons with energy of 250-700 eV.

2.4.1 Event illustration

Let us first describe two time-intervals that are representative of the types of events we hereby distinguish. They are laid out in Figure 2.7 with slightly larger time intervals. The first event (2015/11/12, 07h20:20-07h20:36) is a standard flux rope-type FTE at the magnetopause, and the second one (2015/10/31, 07h18:00-07h19:15) presents a strong reconnection signature at a central current sheet. The latter was studied in more depth by Øieroset et al. (2016), who provided evidence of magnetic reconnection using both observations and simulations.

In the first event (panels 2.7*a*-*h*), the total pressure is dominated by the plasma thermal pressure except in the core of the event where magnetic pressure dominates and total pressure enhances. The magnetic field variation is smooth and presents a bipolar signature in B_x. Density and magnetic field (2.7*e*, 2.7*b*) indicate that the event takes place in the magnetosheath, which typically presents a density around 10 cm^{-3}. There are no striking features to note in ion velocity, electron velocity or electron parallel temperature. In the pitch angle distribution (PAD) of suprathermal electrons (250–700 eV, panel 2.7*h*), large fluxes can be noted at 90° at the beginning and end of the event. They correspond to local minima in the magnetic field strength (2.7*b*), which suggests these are local magnetic bottle configurations leading to local particle trapping. The second event (2.7a'-h') also shows a core enhancement in total pressure (albeit being dominated by magnetic pressure throughout) and a bipolar variation in the B_x component. In contrast with the previous event, the variation is sharp and consistent with a localized thin current sheet at the center of the structure. Concomitant with this current sheet, the ion velocity (2.7c') displays a jet at 07h18:38s with a Vi_x spike around -150 km/s. A coincident electron jet (2.7d') with Ve_x around -280 km/s is also observed, together with an increase in electron parallel temperature (2.7f') from 40 to 75 eV. All these signatures are consistent with magnetic reconnection occurring at this thin current sheet in the core of the event. Finally, PADs (2.7h') are drastically different on each side, with combined populations of bidirectional (0° and 180° PA) and trapped 90° PA) electrons before the current sheet, but a much broader and mostly field-aligned PAD after it. This feature is further discussed in section 2.4.5.

2.4.2 Selection process

In order to investigate statistically the potential differences between the two types of FTEs just described, we established a database of events through the following selection process. Although we try to be as objective as possible, part of it relies on data visual inspection and thus is susceptible to subjectivity. For reproducibility purposes, the timetables of all selected events are available in the supporting information file of Fargette et al. (2020).

FTE selection

To build the FTE database, we examined all the events listed as potential FTEs and flux ropes by the SITL of the MMS mission for phase 1A and 1B. We discarded events that were eventually not FTEs (e.g., magnetopause crossings, bow shock crossings or other associated features). We selected the FTEs based on visual inspection of the data and focusing on the following prime signatures:

- an increase in the total and magnetic pressures
- a bipolar signature in one of the components of the magnetic field

This manual selection process was done using data plots in GSE coordinates, and thus there was no a priori requirement as to which component of the magnetic field was showing a bipolar signature suggestive of a flux rope. After this selection process, 229 events remained. The boundaries of the events were defined based on sharp variations in the profiles of one or more of the following parameters : magnetic field, ion and electron velocity, densities and temperatures.

Reconnection identification

We now need to distinguish the FTEs presenting a magnetic reconnection signature in their core, similarly to the second event of section 2.4.1. The criteria used to identify reconnecting current sheets in the structures are:

- an ion jet signature in the ion velocity (in the l component from hybrid minimum variance analysis (MVA) as detailed next). For very sharp current sheets, the electron velocity was also used (higher time resolution);
- a sharp gradient (monotonous or sometimes bifurcated) in the associated l component of the magnetic field;
- a decrease in the magnetic field strength owing to energy conversion;
- an increase in electron temperature;
- an increase in density.

All signatures were not necessarily required at the exact same time for all events. The importance of the last three signatures in particular varies with parameters such as plasma β and asymmetries across the current sheet. In order to best identify the reconnection signatures in the magnetic field and velocity, we determined the current sheet lmn coordinate system through a hybrid MVA (Gosling & Phan, 2013). The current sheet normal is given by $\mathbf{n} = (\mathbf{B_1} \wedge \mathbf{B_2}) \,/\, (|\mathbf{B_1} \wedge \mathbf{B_2}|)$ where $\mathbf{B_1}$ and $\mathbf{B_2}$ are the asymptotic magnetic fields across the current sheet; $\mathbf{m} = \mathbf{l'} \wedge \mathbf{n}$ where $\mathbf{l'}$ is the direction of maximum variance of the magnetic field obtained from straight application of MVA (Sonnerup & Cahill, 1967); finally $\mathbf{l} = \mathbf{n} \wedge \mathbf{m}$ completes the orthogonal frame. In this frame, the reconnection jet should appear solely on the l direction of the lmn frame, making it easier to confirm through visual inspection.

As an illustration, we display in Figure 2.8 the MVA result on the reconnection jet comprised in the second event of section 2.4.1. We retrieved the median value of the magnetic field 3.5 s before and after the jet, to use as the asymptotic magnetic field $\mathbf{B_1} = [-9.0, -2.2, 48.5]^{\mathrm{T}}_{GSE}$ nT and $\mathbf{B_2} = [25.2, 14.2, 42.6]^{\mathrm{T}}_{GSE}$ nT. The shear across the current sheet is of 44.7°. The transformation matrix we obtain is displayed in table 2.2, and unsurprisingly the $\mathbf{l}$ vector is mainly carried by the $\mathbf{x}$ direction of the GSE coordinate system.

	x	y	z
l	**0.86**	0.41	-0.29
m	-0.25	-0.16	**-0.95**
n	-0.44	**0.9**	-0.04

Table 2.2: lmn vector coordinates in the GSE frame for the reconnection jet occurring within the 2015-10-31 event (see section 2.4.1), resulting from the MVA analysis described in the text. The main component of each vector is highlighted in bold.

In Figure 2.8, the magnetic field and the solar wind speed are plotted in the lmn coordinate system (panels a and b). We can clearly see that the magnetic field rotation as well as the ion jet signature appear only on the l component, while they were before distributed over the x, y and z direction (see Figure 2.7b', c'). The B_n component is close to zero throughout the jet, which is consistent with the $\mathbf{n}$ direction being normal to the current sheet.

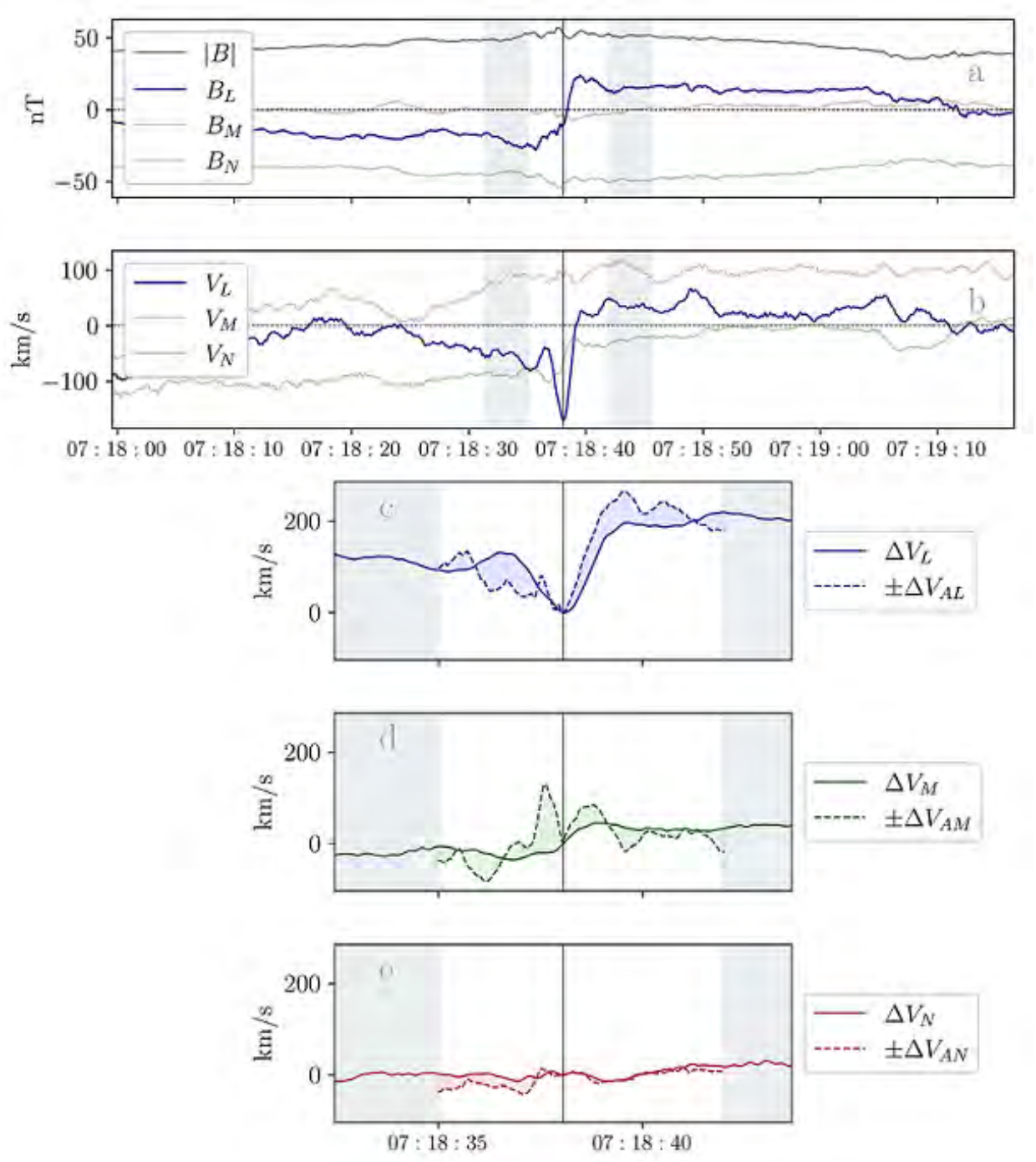

Figure 2.8: Test of the Walén relation for the reconnection jet occurring from 2015/10/31, 07h18:35 to 07h18:42, in the center of the second event described in section 2.4.1. Panels *a* and *b* display the magnetic field and ion velocity vectors transformed in the *lmn* frame. The 3.5 s greyed areas highlight the intervals used to calculate the asymptotic magnetic field vectors. Panels *c* to *e* zoom in on the jet and compare the quantities $\mathbf{\Delta V}$ (full lines) and $\mp\mathbf{\Delta V_A}$ (dashed lines), their difference is highlighted with a colored shaded area.

To further confirm this identification of a reconnection jet, we perform the Walén test on the exhaust, which amounts to testing the validity of the Walén relation introduced in section

1.2.3. According to the latter, we expect

$$\Delta \mathbf{V} = \mp \Delta \mathbf{V_A} \tag{2.17}$$

across the considered jet, with a change in the correlation sign at the heart of the exhaust. In panels 2.8*c-e* we zoom-in on the ion jet and display in full lines the vector $\Delta \mathbf{V} = \mathbf{V}(t) - \mathbf{V}(t_0)$, where t_0 is taken at 07:18:38.5. In addition we plot in dashed lines the vector $\mp \Delta \mathbf{V_A} = \mp (\mathbf{V_A}(t) - \mathbf{V_A}(t_0))$, with a negative correlation before t_0 and a positive one afterwards. In panel 2.8*c* where the jet is most visible, we can see that compared to the data ($\Delta \mathbf{V}$), the Alfvénic jet ($\mp \Delta \mathbf{V_A}$) is less steep on the left-hand side of t_0, and has higher amplitude on the right-hand side, while correctly reproducing the overall shape. The change of correlation before and after t_0 is clearly visible, especially in the l and m components. The mean error averaged over time between the two vectors is of $[40.5, 31.6, 11.7]^{\mathrm{T}}$ km/s in the respective l, m and n directions.

We performed these analysis on all the previously selected FTEs that included a current sheet in their core. After a transformation in the *lmn* frame and an assessment of the validity of the Walén relation, 43 events were identified as FTE-like structures with core magnetic reconnection. They amount to 19% of our 229 FTE database. Here after, the *regular FTEs* (i.e. fitting a flux rope description) will be depicted in blue, while *reconnecting FTEs* (i.e. with a central reconnecting current sheet) will be depicted in red. Let us now investigate statistically the potential differences between the two types of events.

2.4.3 Spatial distribution of FTEs

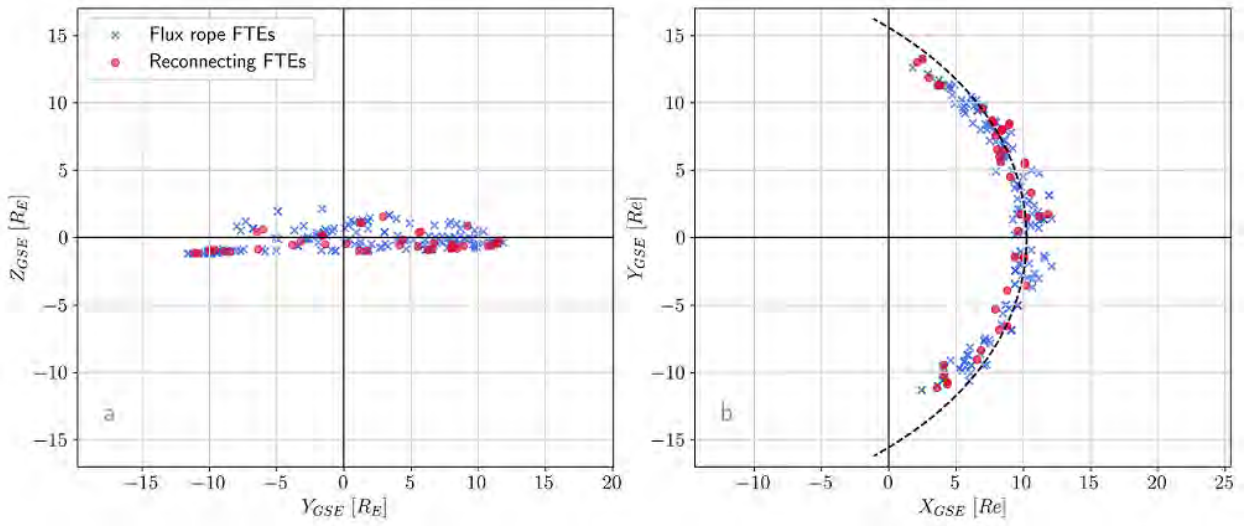

Figure 2.9: Positions of the observed FTEs, with regular flux ropes as blue crosses and reconnecting FTEs as red filled circles. In panel *a* we display the positions scattered in the (Y_{GSE}/Z_{GSE}) plane. In panel *b* we display a generic magnetopause calculated over averaged solar wind conditions (dashed black) as well as the normalised position of the FTEs compared to this magnetopause. More details are available in the text.

A first effect to investigate is whether or not these different FTEs are observed at different locations on the Earth's magnetopause, and to this extent Figure 2.9a displays the locations

of the observed FTEs in the (Y_{GSE}/Z_{GSE}) plane. The positions of regular flux rope FTEs and reconnecting FTEs do not show major trends, both types are distributed uniformly along the equator and across all longitudes. The coordinates of the two particular events presented in section 2.4.1 are respectively $[11.51, 2.82, -0.75]^{\mathrm{T}}$ and $[10.73, 4.13, -0.57]^{\mathrm{T}}$ R_E in the GSE coordinate system.

The FTE locations in panel b are plotted in such a way as to highlights their distance to a modeled magnetopause. For each event, the B_z component of the IMF and the dynamic pressure of the solar wind P_d were computed from OMNI data and averaged over the 15 minutes preceding the FTE. This is used to calculate a magnetopause shape from Shue et al. (1997) (section 2.1, equation 2.1) as well as the distance of the spacecraft to this magnetopause. We can then calculate a generic magnetopause shape associated with the solar wind conditions averaged over the complete set of events, namely $B_z = -1.25$ nT and $P_d = 1.82$ nPa. This generic magnetopause is plotted as a black dashed line in Figure 2.9b, in the (X_{GSE}/Y_{GSE}) plane. Subsequently, the scattered points are not the actual positions of the FTEs in the GSE frame, but rather the positions normalized to this generic magnetopause. This means that the distance between each spacecraft position and the displayed magnetopause in dashed black is representative of the distance between their actual position and the actual magnetopause associated with their specific solar wind conditions. As before, no specific difference arises between regular FTEs and reconnecting FTEs in the (X_{GSE}/Y_{GSE}) plane. Additionally, this visualisation allows us to see that the Shue et al. (1997) model is accurate at the subsolar point, but becomes less reliable on the flanks of the magnetopause, and especially on the dusk flank. This is consistent with the points highlighted in section 2.1, as Shue et al. (1997) assume a symmetry of revolution that is not verified by the magnetopause (Lin et al., 2010; Liu et al., 2015; Nguyen et al., 2022a,b).

2.4.4 Solar wind conditions for FTE formation

We now investigate if solar wind conditions have an impact on the formation of reconnecting FTEs. We compared the distributions of the solar wind parameters during the time preceding FTEs to their standard distribution (computed from observations covering the whole period 2015-2017). The solar wind conditions were obtained from the OMNI database (King & Papitashvili, 2005), which is constructed through the aggregation of datasets originating from several different missions, such as ACE, Wind, IMP8, Geotail or GOES, and provides a permanent monitoring of the solar wind. Data from OMNI were averaged over 15 minutes before each FTE to yield the solar wind parameters most likely associated with its formation. Consistency of the results was checked by averaging over different time intervals from 5 to 25 minutes, and the results remained similar.

Interplanetary Magnetic field orientation

FTEs are formed through magnetic reconnection between the IMF and the Earth's magnetic field at the subsolar point (section 2.2.2). The southward component of the IMF is particularly important as it controls the location of the reconnection sites on the magnetopause (Dungey, 1962), and defines the shape of the magnetopause itself (section 2.1). To investigate the IMF's influence, we studied the distributions of the IMF clock angle $\theta = \arctan(B_Y/B_Z)$ before our FTE observations.

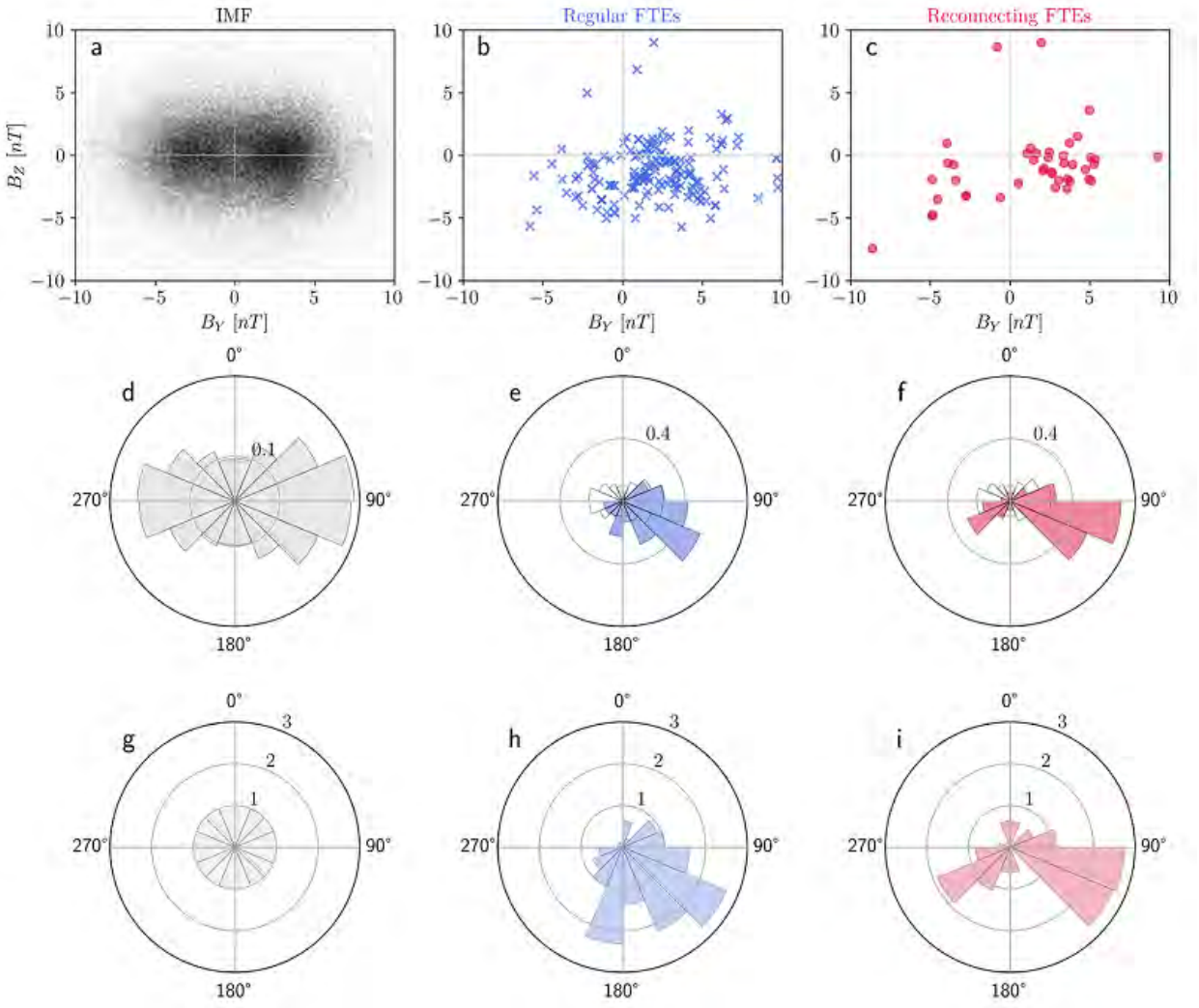

Figure 2.10: IMF orientation prior to FTEs. The top panels (a, b, c) display the scatter plot of the IMF components B_Z versus B_Y for respectively the whole period of observation 2015-2017 (∼140000 data points) (a), 15 minutes prior to 182 regular FTEs (b) and 15 minutes prior to 43 reconnecting FTEs (c). The middle panels (d, e, f) show the normalized polar histograms of these scatter plots, or in other terms the IMF clock angle distributions of each category. Finally, the bottom panels (g, h, i) show the same histograms standardised to the IMF distribution (panel d). We represent the percentage of events observed in one bin, divided by the percentage of solar wind measurements in the same bin, meaning that a distribution independent of the IMF would be isotropic and equal to 1, as in panel g.

In Figure 2.10, the influence of the IMF clock angle is presented. The standard distribution of the IMF (panel d) presents an oval shape and is extended in the Y_{GSE} direction. This is expected as the result of the preferential Parker spiral orientation of the IMF in the ecliptic plane (e.g., Kivelson & Russell (1995)). This standard distribution of the IMF is reminded in panels e and f for comparison. In the latter, the clock angle distribution of the IMF before FTEs present some significant features. A first clear trend is that the IMF is mostly directed southward before the FTE observations, consistently with previous studies focusing on the clock angle's influence on FTE occurrence (e.g., Rijnbeek et al. (1984); Russell et al.

(1985); Fear et al. (2012)) and is consistent with the role of magnetic reconnection in the formation of FTEs (Raeder, 2006). A second trend is that the distribution for regular flux rope FTEs (e) shows a significant duskward component (+90°). This trend is also present in the standard IMF distribution, though less marked. It conveys the fact that throughout this period of observation, the IMF was statistically more prone to be oriented toward the Sun[3] (i.e with a negative polarity). Finally, of particular interest here is the strongly marked tendency for large B_Y in the case of FTEs with reconnecting current sheets (f), with a much smaller occurrence for purely southward IMF. Over the complete set of events, 150 fall into bins with large B_Y values ($[45° - 135°]$; $[225° - 315°]$), and amongst these 150 events with large B_Y, 37 (25%) are reconnecting FTEs. These results leads us to think that the B_Y component of the IMF plays a significant role in creating reconnecting FTEs, and we discuss this result further in section 2.5.

To complete the study on the influence of the IMF orientation, we also investigated the IMF cone angle computed through $\phi = \arctan 2(B_Y / B_X)$. The results are redundant (because not independant) with the clock angle analysis just presented, because at 1 AU, the magnetic field follows the Parker spiral with an angle of around 45° to the radial direction. Hence, a result on B_Y can be transposed to B_X through $\tan 45 = 1 = B_X / B_Y$.

Solar wind plasma parameters

Beside the IMF orientation, we investigated several additional solar wind characteristics that could play a role in FTE formation. For most of these parameters, however, no significant differences were noticed between the solar wind standard distribution and the observed values prior to FTEs. This is highlighted in Figure 2.11 where the distributions of the solar wind density n, speed V, temperature T, plasma beta β, electric field E_Y and mach number M, are displayed. The distributions corresponding to the solar wind state prior to regular and reconnecting FTE observations seem to correspond to the standard distribution. The only notable difference is apparent in the electric field distribution (panel e), which is shifted to positive values for both FTE groups. This is expected and corresponds to the predominance of southward IMF orientations prior to the events (Rijnbeek et al., 1984), as $\mathbf{E} = -\mathbf{V} \wedge \mathbf{B}$ with $\mathbf{V}$ mainly along $\mathbf{X_{GSE}}$.

2.4.5 Event properties

Let us now investigate whether the reconnecting FTEs present different intrinsic properties compared to the regular FTEs.

Duration

In Figure 2.12 we show the normalised distribution of event duration for the two types of FTEs. The median of the distributions for regular FTEs is 19.7 s while it is 34.0 s for reconnecting FTEs. It appears that overall, the reconnecting FTEs tend to be slightly longer than the regular FTEs, which is discussed in section 2.5.

[3] As B_y and B_x are linked through the Parker spiral, a positive B_y means a positive B_x at 1 AU, with the magnetic field pointing towards the Sun

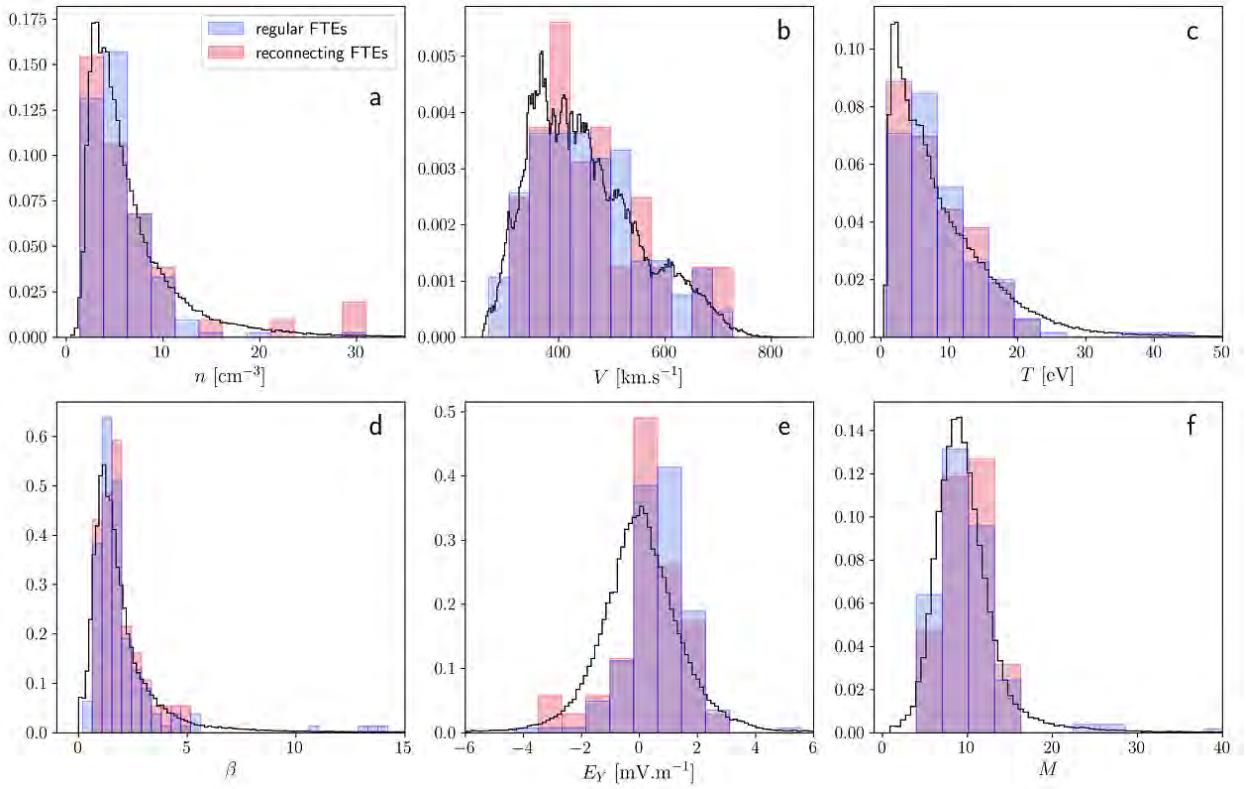

Figure 2.11: Distribution of solar wind characteristics for respectively the whole period of observation 2015-2017 (black curve), 15 minutes prior to 182 regular FTEs (blue) and 15 minutes prior to 43 reconnecting FTEs (red). The parameters displayed are the solar wind density n, speed V, temperature T, plasma beta β, electric field E_Y and mach number M.

A change in connectivity

In section 2.4.1, we identified that a key difference between the two studied events resided in their suprathermal electron PAD signatures. Such features are of particular interest because they are linked to the FTE's magnetic connectivity. Indeed, suprathermal electrons (300-700 eV) move essentially freely along magnetic field lines and are thus good tracers of magnetic topology. Accordingly, their PAD along a given field line should not change much. If density and magnetic field variations may induce changes in the absolute value of the flux, or the width of the field-aligned / anti-field-aligned peaks, the basic structure of the PAD should persist. This is the case in Figure 2.7g, where the PAD throughout the event is essentially always field-aligned with some broadening occurring with magnetic field strength enhancement towards the core of the FTE. For our second event, however, in Figure 2.7g' the PAD across the reconnecting current sheet are vastly different. These distinct regions are therefore not magnetically connected to each other, unlike what would be expected in a helical magnetic structure such as regular flux ropes.

A way to quantify this change in the PAD distribution of suprathermal electrons is to compute the parallel electron heat flux $Q_{e\|}$. This third order moment (see section 1.1, equation (1.7d)) yields information on the suprathermal electrons that constitute the tail of the plasma distribution. If a PAD presents mostly field-aligned electrons, then the term $\mathbf{v} - \mathbf{V}$ in the

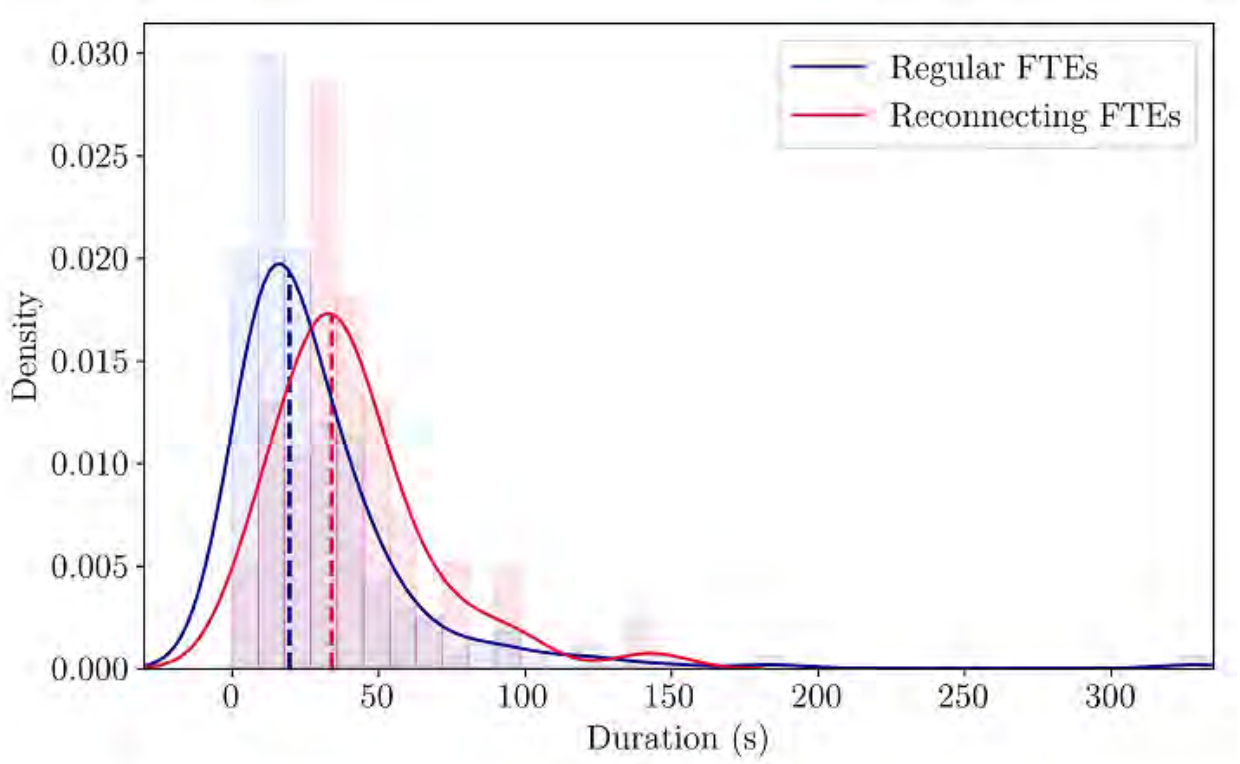

Figure 2.12: Normalised distribution of event duration for the regular FTEs in blue and the reconnecting FTEs in red. The full lines are the kernel density estimation (kde) associated with the histograms. The dashed lines show the distributions' median values.

integral of equation (1.7d) leads $Q_{e\|}$ to be positive. Similarly, a bidirectional population has near null $Q_{e\|}$ while an anti-field-aligned population presents negative $Q_{e\|}$. This is largely visible in Figure 2.13. As just described, the symmetry in fluxes of suprathermal electrons in PADs at the leading edge of the event induces a near-zero $Q_{e\|}$, while the more field aligned population of the trailing edge leads to a clearly positive $Q_{e\|}$.

Although one cannot predict what the pitch angle distribution may be on either side of the reconnecting current sheet (because one does not know where the field lines are connected at their ends, ie. solar wind or ionosphere), one yet expects that regular flux ropes should have the same rough $Q_{e\|}$ throughout the event while reconnecting events should statistically show a much larger difference between the $Q_{e\|}$ before and after their reconnecting current sheet, assuming they have a different connectivity as for the second event in Figure 2.7; To assess the existence of such a difference, we proceeded as follow:

- for reconnecting FTEs, the time average of $Q_{e\|}$ is computed before (leading part) and after (trailing part) the identified reconnection jet and within the FTE's bounds.
- for regular FTEs, the time average of $Q_{e\|}$ is computed before and after the center of the flux rope, where the magnetic field strength is maximum.
- we then compute the heat flux change between the leading and trailing parts of all the events as
  $\Delta < Q_{e\|} > = < Q_{e\|} >_{lead} - < Q_{e\|} >_{trail}$

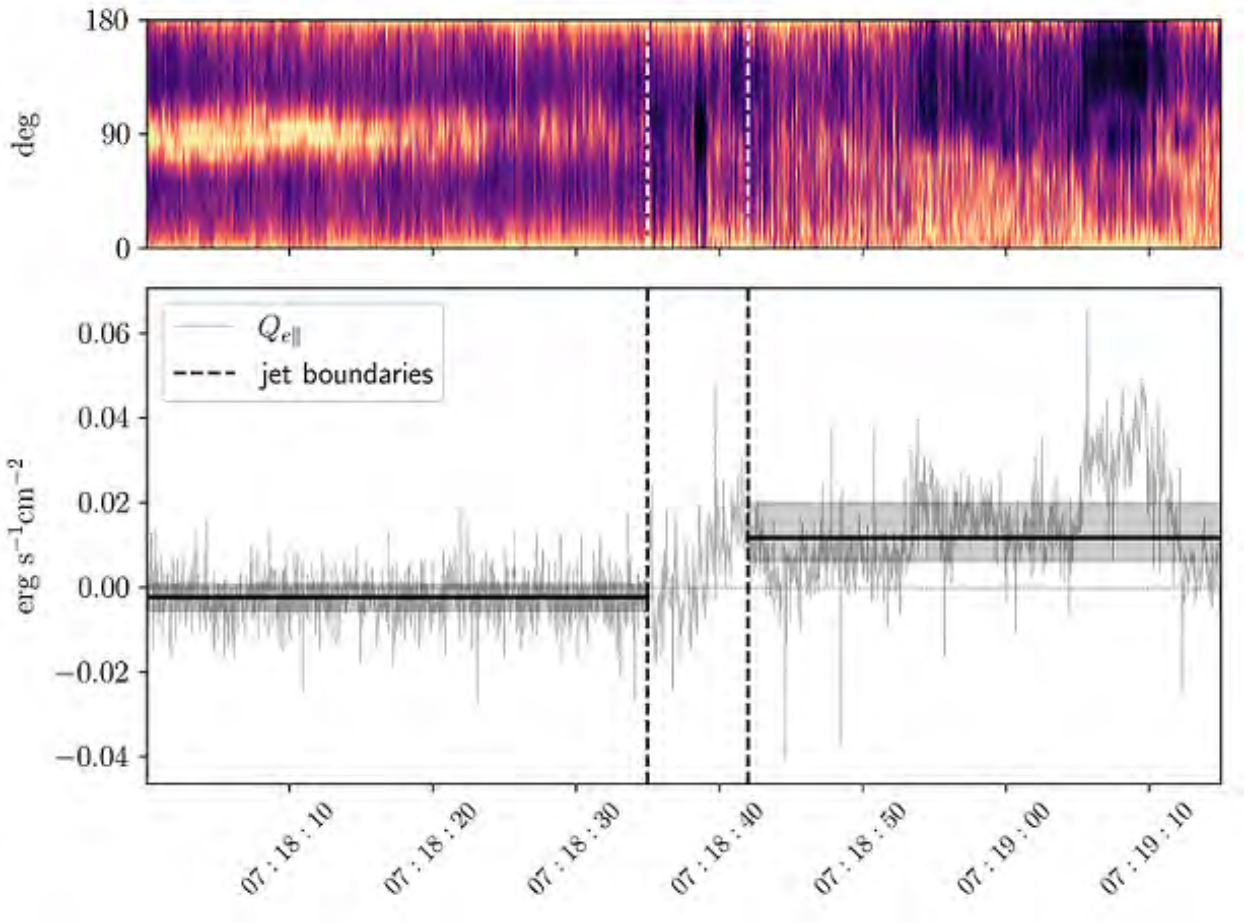

Figure 2.13: Parallel electron heat flux for the 2015/10/31 event (section 2.4.1). In the top panel, the PAD of the event is reminded for clarity. The bottom panel shows the parallel electron heat flux $Q_{e\parallel}$ throughout. The vertical dashed lines indicate the jet boundaries, the horizontal black lines are the heat flux median on each side of the jet, and the shaded grey areas indicating the 25 and 75 percentiles around the median.

Figure 2.14 shows the change in electron heat flux accross the FTEs. From the two top panels, one observes a larger scatter for the reconnecting FTEs (b) compare to the regular FTEs (a). This becomes clear when we analyse the distribution of $\Delta < Q_{e\parallel} >$ (c), this quantity being proportional to the distance between the scattered points and the dashed line of the top panels. In panel 2.14c we see that the regular FTEs distribution (blue) peaks at $\Delta < Q_{e\parallel} >= 0$ and presents a rather small dispersion ($\sigma = 0.025$ erg s^{-1}cm^{-2}), indicating that overall the electron heat flux do no undergo major changes throughout the events. The dispersion of the reconnecting FTE distribution (red), however, is more than twice larger ($\sigma = 0.061$ erg s^{-1}cm^{-2}), showing that the heat flux is more prone to vary within these events. This shows that for most of these events, the electron heat flux typically changes much more than for regular FTEs between the leading and trailing segments of the structure across its reconnecting current sheet, hinting that these two parts are magnetically disconnected.

We observe that some reconnecting FTEs have similar heat fluxes between their leading

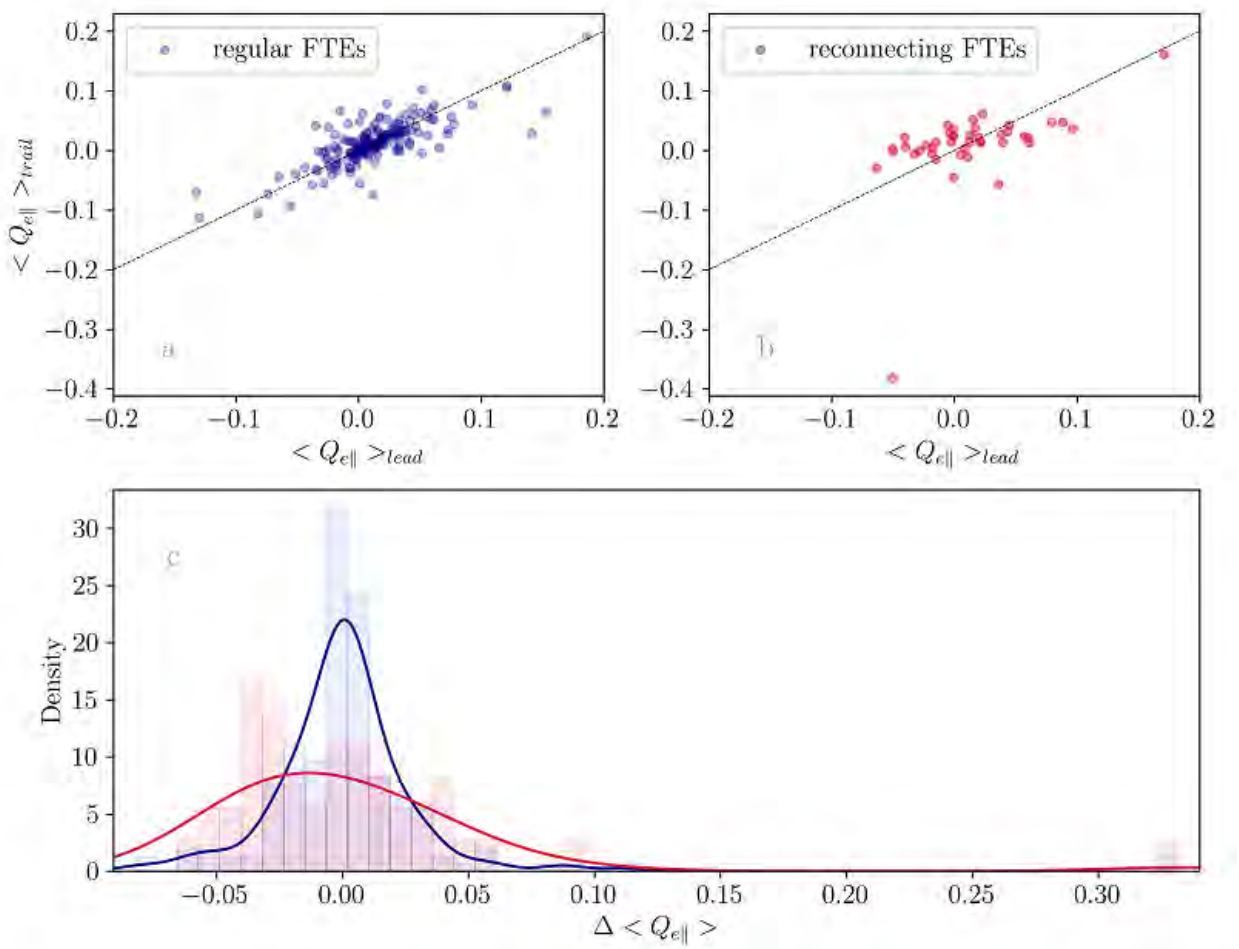

Figure 2.14: Change of electron heat flux accross the FTEs. The top panels display a scatter plot of $< Q_{e\|} >_{lead}$ versus $< Q_{e\|} >_{trail}$ for regular (a) and reconnecting (b) FTEs. The dashed lines represent the case were both quantities are equal. The bottom panel shows for each population the normalised distribution of $\Delta < Q_{e\|} >$.

and trailing parts (bins around $\Delta < Q_{e\|} >= 0$). This is not necessarily inconsistent with a change of connectivity between the two parts of the structure. It may be that, despite having no change in heat flux, the FTE's PAD properties are still different across their current sheet since $< Q_{e\|} >$ is an integral quantity. Furthermore, if their PAD is indeed unchanged, it does not preclude the two parts of the structure to be connected to different regions despite the electron source properties being similar.

2.4.6 The onset of magnetic reconnection

We now study the properties of the reconnection jets we detected and check if their boundary conditions are consistent with the occurrence of magnetic reconnection.

Through theoretical work and simulation, Swisdak et al. (2003) established a necessary condition for magnetic reconnection to occur, relying on the effect of the diamagnetic drift on the stability of a current sheet with respect to the reconnection process. In principle, in an asymmetric configuration where a pressure gradient exists across the current sheet,

the X-line is induced to drift at a velocity $v_\star$. This drift may oppose the development of the expected ion jet along the exhaust direction, and Swisdak et al. (2003) purport that magnetic reconnection should thus be suppressed when $v_\star > v_A$, with v_A the local Alfvén speed. This condition can be rewritten as a function of the jump in plasma β accross the current sheet and magnetic shear Θ (Swisdak et al., 2003, 2010) and therefore predicts that magnetic reconnection should not develop if

$$\Delta\beta > 2\frac{L}{\lambda_i}\tan\frac{\Theta}{2} \tag{2.18}$$

with L the characteristic length of the current sheet and λ_i the ion inertial length. This theoretical prediction was confirmed through statistical analysis of current sheets observed in the solar wind and at the magnetopause, for instance by Phan et al. (2010, 2013).

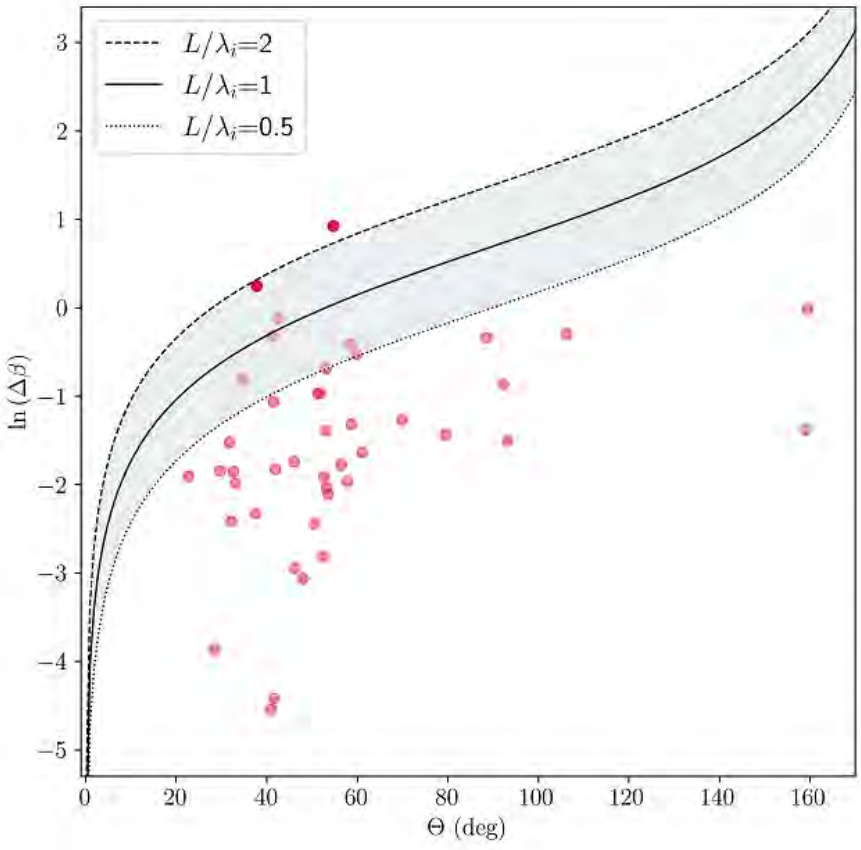

Figure 2.15: Scatter plot of $\ln\Delta\beta$ as a function of the magnetic shear across each of the current sheets (red dots), together with the limit (shaded area) for the onset of magnetic reconnection from equation 2.18, corresponding to $L/\lambda_i \in [0.5, 1, 2]$. Two brighter dots do not fully satisfy the Swisdak et al. (2003) condition.

We now investigate if the reconnection jets we identified in section 2.4.2 comply with this condition. The boundaries of each current sheet were determined manually (available in

the supporting information file of Fargette et al. (2020)) and asymptotic conditions were computed on intervals before and after the current sheet lasting a third of the jet duration. We use such short duration intervals consistently with the analysis of Øieroset et al. (2019), who found that the magnetic pressure pile up in FTEs was essential in regions allowing magnetic reconnection to occur. Hence, we aim to use β and $\mathbf{B}$ asymptotic values inside of this pile up, quite near the current sheet. We tested changing slightly this interval duration and the results remained similar. In Figure 2.15, we compare our events to the Swisdak et al. (2003) condition for magnetic reconnection. The majority of the current sheets fall in the region where magnetic reconnection can develop, close or below the $L = \lambda_i$ curve, consistent with previous studies (Phan et al., 2010, 2013; Øieroset et al., 2019). We also observe that most of the current sheets have a low shear, with a median value around 50°. Two events do not fully satisfy the condition for magnetic reconnection albeit displaying clear ion jet signatures (events 12 and 29 in the supporting information file of Fargette et al. (2020), shown in brighter red in Figure 2.15). This might be explained by a significant distance to the X-line, where the shear and β conditions could have evolved (Phan et al., 2010, 2013).

2.5 Impacts on FTE formation theory

2.5.1 Interlaced flux tubes

The first main and unexpected result of this study is the fact that magnetic reconnection occurs frequently inside FTE-type structures. Out of 229 events, 43 show signatures of magnetic reconnection within their core, amounting to 19%. Such signatures are not expected in regular flux rope FTEs. Indeed, even though Øieroset et al. (2016) noted that field lines originating from two X-lines could form a current sheet and cause reconnection in the center of the FTE, Kacem et al. (2018) found that the suprathermal electron PAD across the central current sheet were drastically different. This observation is inconsistent with the connectivity implied by a three-dimensional helical magnetic field, and rather indicates that the two sides of the structure are not magnetically connected. Kacem et al. (2018) thus suggested that the 3D interaction of magnetic field lines originated from two X-lines forms interlaced flux tubes (akin to the model by Nishida (1989), Hesse et al. (1990) and observations by Louarn et al. (2004)) that resemble an FTE. For the majority of the reconnecting cases studied here, the leading and trailing parts of the structures seem disconnected (Figure 2.14). We find that the events with a reconnecting current sheet have PADs and heat flux properties statistically consistent with the model of interlaced flux tubes. The fact that they are slightly longer than regular flux ropes (Figure 2.12) is also consistent with them being two structures rather than one. We also found that the IMF displays a very strong B_Y component just prior to the observation of reconnecting FTEs (section 2.4.4). Based on all these facts and recent literature, we now discuss several possible interpretations.

First, the influence of the IMF B_Y on the occurrence of interlaced flux tubes was investigated through simulation by Cardoso et al. (2013) and more recently by Farinas Perez et al. (2018). When imposing a strong B_Y component on the IMF together with a southward B_Z, they observed the formation of two interlaced flux tubes (called IFT) out of five FTE-type structures generated in the simulation. They identified two distinct formation processes for each event. For one, the strong B_Y component of the IMF leads to the formation of two

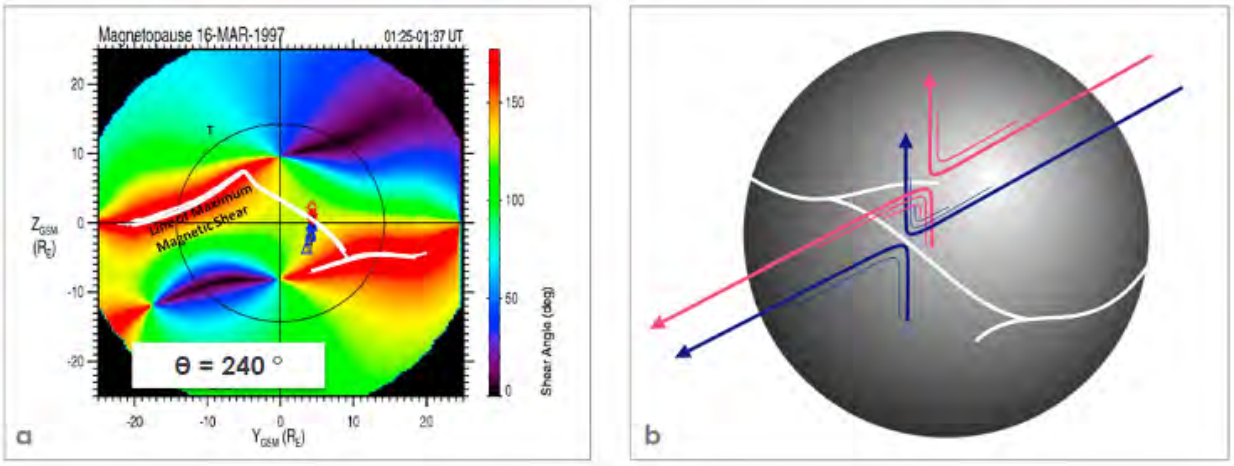

Figure 2.16: Proposition of a configuration for the formation of interlaced flux-tube FTEs, based on a bifurcation of the X-line at the dayside magnetopause for large IMF B_Y. Panel *a*: magnetic shear angle between the IMF (240°) and the magnetosphere in the (Y_{GSM}/Z_{GSM}) plane, from Trattner et al. (2012). Panel *b*: schematic showing in white a bifurcated reconnection line on the Earth's magnetopause for such a clock angle. In blue and red, we show field lines produced by two distinct reconnection sites, and whose geometry is proposed to generate interlaced flux tubes.

reconnection sites, respectively northward and southward of the equator. This is explained as a consequence of resistive tearing instability at the subsolar point. Both reconnection sites then generate distinct sets of flux tubes with different connectivity, that interlace and form what resembles an FTE in a fashion very similar to the scenario described in Kacem et al. (2018). By contrast, their second event is shown to originate as a standard flux rope FTE. It evolves afterwards into an interlaced flux tube structure with different connectivity as well, but through processes that remain to be explained.

Another formation mechanism is now proposed. It is based on the known effect of the IMF B_Y component on dayside X-line geometry and location as studied by, e.g., Trattner et al. (2007, 2012); Petrinec et al. (2014). The maximum magnetic shear model (Trattner et al., 2007) suggests that for a B_Y-dominated IMF, the X-line could be "bifurcated" in some specific locations on the magnetopause, as displayed in the left panel of Figure 2.16 (from Trattner et al. (2012)). This figure shows[4] the magnetic shear angle across the magnetopause projected onto the YZ-plane. The IMF clock angle in this case is of 240°. The white lines represent the X-line location related to the maximum magnetic shear angle location. We note that this model allows for the existence of two coincidental X-lines at the same longitude. As shown with the blue and red field lines in Figure 2.16b, we propose that such a configuration may lead to the formation of complex structures such as interlaced flux tubes. Importantly, we note that unlike the sequential X-line model, which is based on successive X-line formation (temporally), the present model does not require sequential X-line formation. Under large B_Y IMF, various regions at the magnetopause feature large magnetic shears, and therefore are good candidates to initiate reconnection and sustain an X-line. This may allow simultaneous co-existence of multiple X lines and facilitate interlacing

[4]Figure done for a given event unrelated to the present study, here used for illustrative purposes

between flux tubes. This is thus largely different from the regular sequential X-line model for FTE formation, that may lead to the formation of regular flux rope FTEs.

2.5.2 FTE Handedness

Regarding the formation process of regular flux rope FTEs, a follow up on this work was performed by Kieokaew et al. (2021), focusing on the helicity sign of magnetospheric FTEs. In this paper, a force-free flux rope model akin to the one described in section 2.3 was fitted to FTE data to determine their handedness. 84 events with good fits were selected, and the solar wind conditions were investigated prior to these events. We find in this paper that the FTE handedness and the preceding IMF B_Y are correlated, meaning that positive (negative) helicity flux ropes are mainly formed under IMF with a positive (negative) B_Y component. Kieokaew et al. (2021) argue that this finding is consistent with flux ropes being formed through a multiple X-lines reconnection mechanism at the subsolar point, with the twist direction of the flux ropes being controlled by the IMF B_Y component.

2.6 Conclusion

This chapter of the thesis focused on magnetic structures called Flux Transfer Events (FTEs) observed at the Earth's magnetopause. They are formed through magnetic reconnection in the subsolar region and their main in-situ signatures are an increase in magnetic field strength and a bipolar signature in the component normal to the magnetopause. Their structure is that of magnetic flux ropes with a helical internal magnetic field.

In section 2.3, we present a model of magnetic flux ropes that can be fitted to data, adapted from Burlaga (1988) and akin to Lepping et al. (1990). This model allows to retrieve the geometry of the flux rope, including parameters such as:

- its handedness,
- the orientation of its magnetic axis,
- the impact parameter of the spacecraft trajectory,
- the central time of the event,
- the erosion of the flux rope.

We present two fit examples of flux rope events, showing that the model seems very accurate to first order.

In a second part (section 2.4), we performed a statistical analysis on FTE-like structures observed by the MMS mission throughout phase 1, with particular emphasis on the occurrence of magnetic reconnection inside these structures. We find that magnetic reconnection occurs inside 19% of them (43/229 events), with events looking like FTEs but inconsistent with their classical description as they present a marked current sheet in their core. We analyzed the parallel electron heat flux inside FTEs as it is a good tracer of magnetic connectivity. We find that across the current sheet of reconnecting FTEs, the variation of the parallel electron heat flux $Qe_{\parallel}$ is statistically more important than throughout regular flux rope FTEs. This is consistent with reconnecting FTEs being constituted of regions magnetically disconnected

from each other. We also investigated solar wind conditions prior to the observed FTEs. While most other parameters essentially remain unchanged, the IMF clock angle distribution is found to be directed mainly southward and duskward for regular FTEs while it has a much stronger B_Y component in the case of events with a reconnecting current sheet.

Our statistical analysis thus supports the recent work by Kacem et al. (2018) and Øieroset et al. (2019), where FTE-like structures are described as interlaced flux tubes. We further discuss (section 2.5) the link between a prevailing large IMF B_Y component in the solar wind and the formation of such structures. Two mechanisms were proposed by Farinas Perez et al. (2018) on the basis of simulation, and suggest that interlaced flux tubes may form either through resistive tearing instability developing in the subsolar region or through the evolution of a regular FTE into a more complex 3D structure. We propose an additional formation mechanism based on the maximum magnetic shear angle model at the magnetopause (Trattner et al., 2007), which can produce bifurcated X-lines at the dayside magnetopause for large IMF B_Y. It can lead to the interlacing of flux tubes from two spatially distinct X-lines at the same longitude. This mechanism is different from the most studied FTE formation mechanism based on temporally sequential reconnection (Raeder, 2006) that could still form regular non-reconnecting FTEs. In recent work, Kieokaew et al. (2021) found a clear correlation between the handedness of flux rope FTEs and the orientation of the IMF prior to observations, further confirming the multiple X-line formation process for these structures.

A lot remains to be discovered on the structure and formation process of FTEs. The model we propose for the formation of interlaced flux tubes (based on the maximum shear model of Trattner et al. (2007)) needs to be either confirmed or disproved through theoretical work and numerical simulations. By using the list of FTEs provided in this work and the flux rope model developed, further studies could focus on the statistical distribution of properties of FTEs such as their orientation and erosion. Another interesting topic would be the detailed analysis of the reconnection jets found within FTEs in terms of plasma properties and geometry of the reconnection site. These few trails should be investigated in future work, but what drew our attention - and what we chose to pursue further in this PhD work - was the observation of a reconnecting FTE (or interlaced flux tube)... in the solar wind.

Chapter 3

Flux ropes and interlaced flux tubes in the solar wind

Contents

We studied in the previous chapter peculiar magnetic structures that were observed at the Earth's magnetopause. Their main characteristics were an increase in magnetic pressure, a bipolar signature in the normal magnetic field component and - unexpectedly as explained in chapter 2 - a signature of magnetic reconnection in their core with different suprathermal electron properties in the leading and trailing parts of the structure. In this chapter, we now move from the Near-Earth environment to the inner heliosphere, and we focus on similar structures observed by the PSP mission in the solar wind. We chose to call these events "Magnetic Increases with Central Current Sheet" (MICCS). We first begin with an introduction on the HCS, its properties and dynamics together with the observation of flux ropes in its vicinity, which is relevant to the formation of such magnetic structures. We then present an overview of previous observations of MICCS in the solar wind as they have been observed by past missions (though without magnetic reconnection being resolved in their core). We introduce their initially proposed formation mechanisms involving an interaction between the plasma and dust particles. We then investigate two striking events observed by PSP in detail, both showing the presence of a central current sheet with a visible ion jet and general characteristics consistent with the occurrence of magnetic reconnection. We performed a statistical study on 20 of these MICCS and, in particular, do not find a correlation between dust enhancement and MICCS observation. We rather conclude that, similarly to the reconnecting FTEs of chapter 2, they are overall consistent with a double flux tube-configuration that would result from initially distinct flux tubes which interact

during solar wind propagation. This work was published in Fargette et al. (2021a), and from section 3.2 the text is transposed from the article.

3.1 Dynamics of the Heliospheric Current Sheet

In the heliosphere, the HCS plays an important role in structuring the solar wind. The HCS is a current sheet that originates near the tip of the bipolar helmet streamer, the latter being constituted of closed solar magnetic field lines adjacent to open magnetic field lines of opposite polarity. Therefore, a bipolar streamer and its HCS extension separates regions of opposite magnetic polarities or magnetic sectors (e.g., Gosling et al. (1981)). Due to the combined effects of the solar rotation, the solar dipole tilt and deviations from the ideal dipole configuration, the HCS takes on a wavy form. This is shown in Figure 3.1, which displays an MHD simulation of the HCS close to solar minimum. The HCS is usually easily identified in situ, by a reversal of the radial component of the magnetic field, and a roughly 180° flip of the pitch angle of suprathermal electrons (this suprathermal electron population is also called the strahl), which is a marker of magnetic connectivity.

We illustrate the signatures of HCS crossings in situ in Figure 3.2. In this Figure, we consider PSP data while the spacecraft is undergoing its 7^{th} orbit, and scans the heliosphere from 40 to 20 $R_\odot$. It goes through the HCS twice, once on January 17 and once more on January 19. In panels *a* and *d*, the HCS locations are clearly characterised by the reversal of the radial

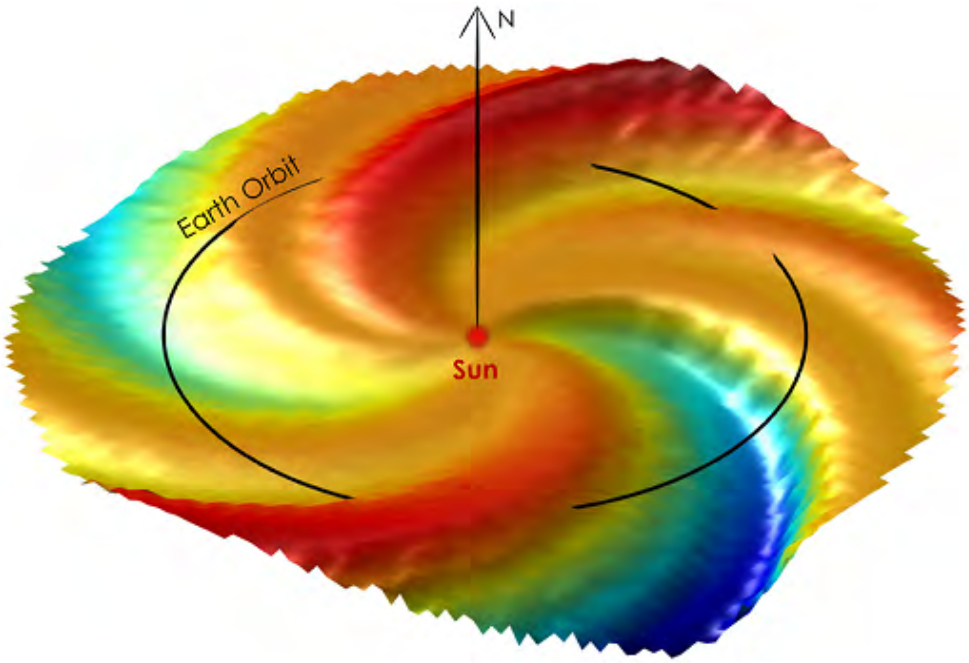

Figure 3.1: The HCS is displayed up to a distance of around 1 AU, with a color scale indicating its elevation from the ecliptic plane (red above, blue under). The Sun is represented in the center together with the vector normal to the ecliptic. The black line is the Earth orbit that crosses the HCS several times. Figure adapted from Owen et al. (2020) and resulting from a coupled corona-heliosphere MHD simulation from Odstrcil et al. (2004).

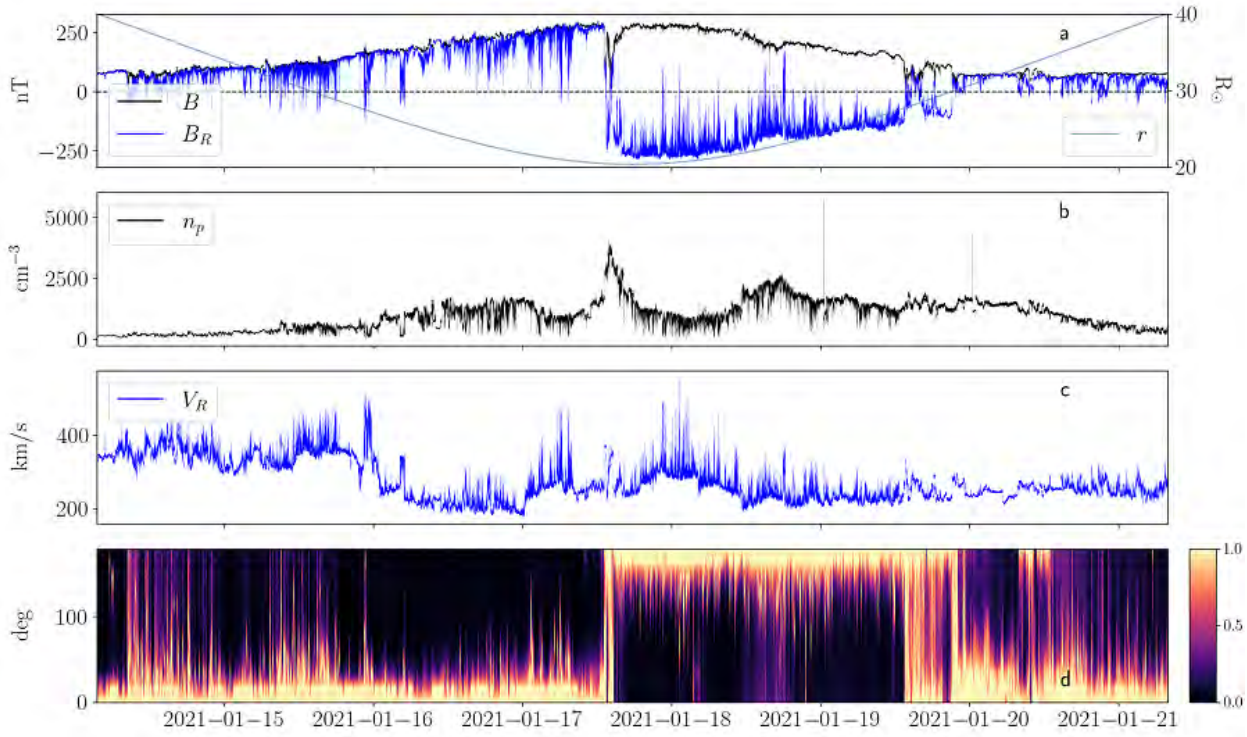

Figure 3.2: HCS crossings in-situ signatures: (a) magnetic field amplitude and radial component as well as radial distance of the spacecraft to the Sun; (b) proton density; (c) radial solar wind speed; (d) PAD of suprathermal electrons (300-2000 eV) normalised to the maximum flux at a given time.

magnetic field coincidental with the reversal of the strahl PAD. The PAD of suprathermal electrons has a maximum flux of 0 ° (180 °) when PSP is located over (under) the current sheet, i.e. in the positive (negative) magnetic polarity sector. Near the HCS, we find a region of the heliosphere that is characterized by a high β plasma with suprathermal electron strahl drop out and complex magnetic configurations. The first HCS crossing presents a significant increase in the proton density, while strahl drop-out regions are intervals where the normalised flux is independent of the pitch angle, which is particularly visible during both crossings. The HCS global structure is in fact dominated by magnetic flux ropes alternating with high-density regions (Sanchez-Diaz et al., 2017, 2019; Lavraud et al., 2020). This is consistent with magnetic reconnection continuously occurring at the tip of the helmet streamers and releasing these transients. This is particularly striking in PSP data, and both Lavraud et al. (2020) and Phan et al. (2021) show that close to the Sun, HCS crossings always correspond to the observations of flux ropes and reconnection jets. This was further backed by simulations shown in Figure 3.3 and performed by Réville et al. (2022), highlighting that these flux ropes form at the base of the heliospheric current sheet. This allows us to draw the parallel between flux ropes observed at the HCS and flux-rope FTEs observed at the Earth's magnetopause, as they present similar in-situ signatures and are formed in a similar way through magnetic reconnection (even though the context and plasma properties of the inflows regions obviously differ). In this chapter, we report on structures in the solar wind resembling the magnetospheric reconnecting FTEs. Hence it seemed natural to investigate a possible link between these structures and a potential proximity to the HCS at the time

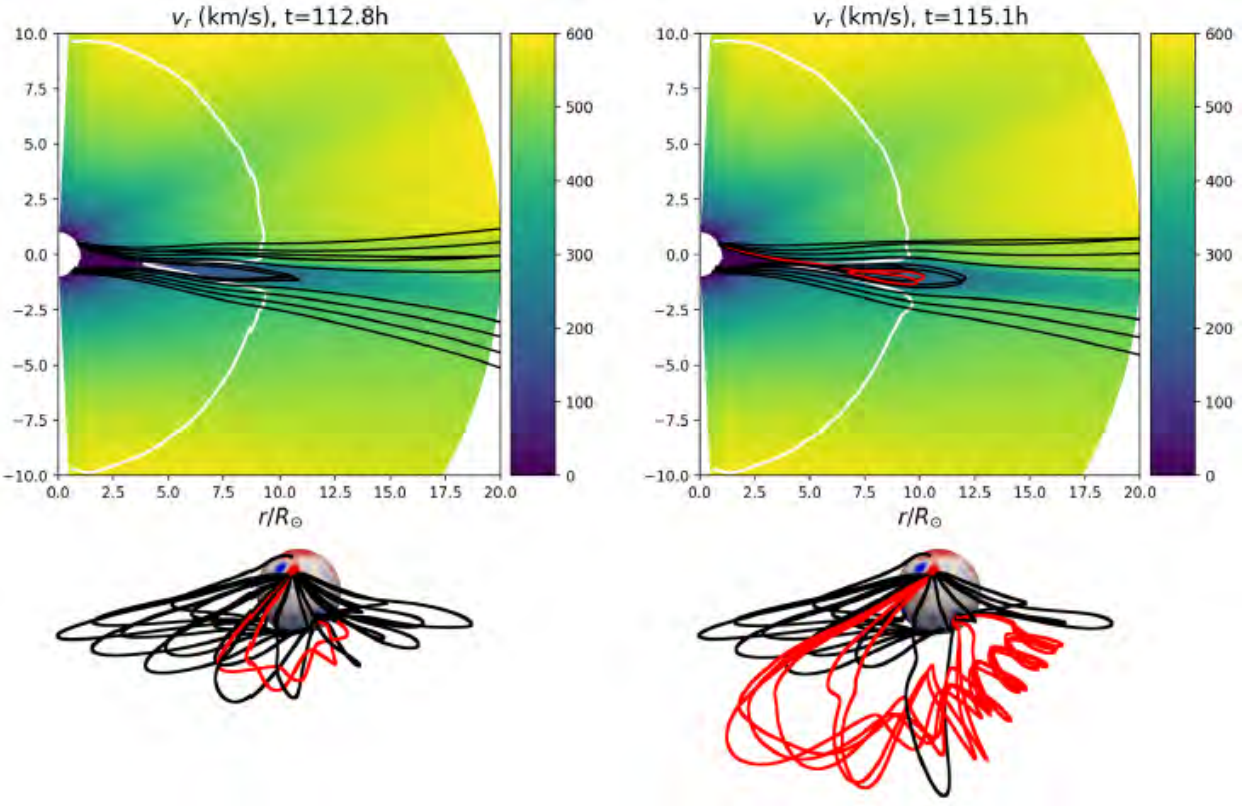

Figure 3.3: Snapshots of an MHD simulation taken at two different times, showing the formation of a flux rope through magnetic reconnection at the tip of the helmet streamers. The top panels show a 2D view of field lines traced from the HCS and connecting to the surface with the background colored by the radial speed of the solar wind. The white rounded curve shows the Alfvén surface ($V = V_A$) and field lines are plotted in red when they possess a helical structure. The bottom panel shows a 3D view of the same epochs before and after the main reconnection event and the creation of the flux rope. Figure and caption from Réville et al. (2022).

of observations. Subsequently in this chapter, we distinguish two types of locations for our observations. We refer to "regular slow and fast solar wind" for plasma exhibiting no complex magnetic configuration with a uniform strahl propagating outward from the Sun. By contrast, we refer to "nearby HCS" for events that are observed in the direct vicinity or inside the HCS, as identified on the basis of plasma, magnetic field, and strahl properties, as explained above. Let us now present the structures we have been dancing around in the last few pages.

3.2 Interlaced flux tubes

In the solar wind, significant fluctuations in the amplitude of the IMF B are typically due to specific magnetic structures associated with both small and large scale disturbances of the ambient plasma. At large scales, typical perturbations are associated with CMEs or compression regions, such as corotating interaction regions (CIRs), typically as the result of

stream interactions, the creation of pressure waves and shocks, etc. At smaller scales, disturbances in the magnetic field amplitude can stem from either velocity shears and turbulence in general (e.g., Bruno & Carbone (2013)), or from small scale magnetic structures. The latter typically consists of the following : flux tubes, as in the view of Borovsky (2008), for example, where they constitute the very texture of the solar wind; flux ropes often observed close to the HCS; and interplanetary field enhancements.

The specific kind of disturbance in the solar wind magnetic field called interplanetary field enhancements (IFEs) were first reported by Russell et al. (1984) from observations with the Pioneer Venus spacecraft. The main signature of these structures is a strong peak in the amplitude of the magnetic field, lasting from minutes to several hours, that is very distinguishable from the background field. The second main feature that they present is a thin current sheet in their core. They propagate at the solar wind speed (Russell et al., 2010b) and were observed from 0.3 to 1 AU with several missions, such as Helios, STEREO, ACE, or Wind (Russell et al., 2010a; Lai et al., 2015). These structures were proposed to have been formed through an interaction between the interplanetary magnetic field and dust trails of asteroids in the solar wind (Russell, 1990; Jones et al., 2003a,b). This explanation is still debated within the scientific community, as the physical process to transform small dust particles to a strong **B** disturbance remains unclear. Mass loading of the solar wind by cometary dust trails was put forward as a possible explanation, but it was found to be insufficient (Mann et al., 2010).

Interestingly, these IFEs present signatures that are quite similar to the reconnecting FTEs observed at the Earth's magnetopause. We have shown that these FTEs presenting a thin current sheet in their center did not fit a flux rope configuration, but were rather interpreted as interlaced flux tubes, with the reconnecting current sheet separating two magnetically disconnected regions (see chapter 2 for more details and relevant literature). The primary goal of this work is to report the observation of solar wind structures similar to IFEs by the PSP mission, between 0.1 and 0.6 AU (20 - 120 $R_\odot$). In this study we choose to use a new descriptive term for the observed events, and from now on refer to them as "Magnetic Increases with Central Current Sheet" (MICCS). This choice was made in order to avoid confusion with other phenomena that lead to interplanetary field enhancement - such as CMEs and other small-scale flux ropes or compression regions - and so as to avoid any bias regarding their still debated origin.

3.3 PSP observations of MICCS

3.3.1 Event of November 2, 2018

During its first encounter with the Sun, PSP observed a striking event, similar to those described in the section 3.2, presenting a clear and smooth magnetic strength increase and an embedded reconnecting current sheet. The structure was observed at 44 $R_\odot$ (0.2 AU) from the Sun on November 2, 2018, when PSP was probably magnetically connected to a small equatorial coronal hole (Bale et al. (2019), Badman et al. (2020), Réville et al. (2020)). In Figure 3.4 we display the event from November 2, 2018. To reduce instrumental artifacts and improve data visualization, we applied a median filter of 1.5 seconds on the SPC moments; nevertheless, some instrumental variations remain. The event lasted 14 minutes from 12:36

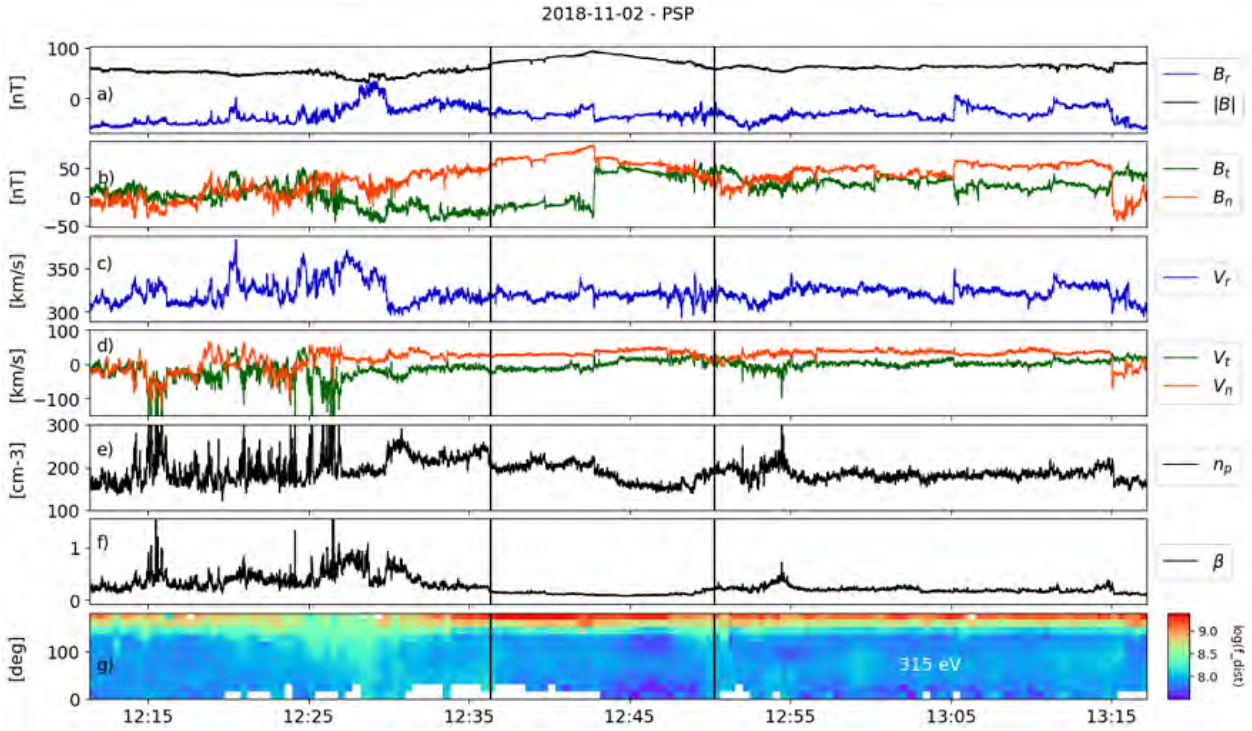

Figure 3.4: Event from November 2, 2018 (12:36 to 12:50, boundaries in black vertical lines). From top to bottom, panels present *a*) the magnetic field's amplitude B and its radial component B_R; *b*) the tangential and normal magnetic field components B_T and B_N; *c*) the radial ion velocity V_R; *d*) the tangential and normal ion velocity V_T and V_N; *e*) the proton density n_p; *f*) the plasma β; and *g*) the pitch angle distribution of electrons at 315 eV, with f_{dist} being the phase space density in s^3/km^6.

to 12:50, and moved at 321 km/s in the radial direction on average. The maximum magnetic field was measured at 94 nT at 12:42:50 while the background field was around 65 nT (45% increase). The proton density fluctuates around the central current sheet with a mean value of 213 $\pm$ 9 cm^{-3} before it and 172 $\pm$ 15 cm^{-3} afterwards. The plasma β parameter remains constant around 0.1 during the event. The suprathermal electrons show a strahl mainly anti-parallel to the magnetic field with a peak at a 180° pitch angle (3.4g), even though pitch angle scattering seems to occur right before the event between 12:20 and 12:30. The occasional lack of data (white pixels) near the 0° pitch angle corresponds to directions that are affected by spacecraft effects and were thus removed.

The central current sheet of the event is coincidental with the magnetic peak and was reported to reconnect by Phan et al. (2020), with a low shear of 55°, a guide field of 1.9 nT, and a distance to the X-line of 0.012 $R_\odot$. The ion jet is visible in all velocity components (3.4c, 3.4d). Figure 3.5 displays reconnection jet in the *lmn* frame. The *lmn* frame is obtained through a hybrid minimum-variance method (Gosling & Phan (2013), also detailed in section 2.4.2) which often works best for low-magnetic-shear current sheets. When determining the direction of maximum variation $\mathbf{l}'$, we checked that the ratio of the maximum to intermediate eigenvalue obtained through regular variance analysis was high enough. In this case, the ratio was 39, which largely ensures that $\mathbf{l}'$ was accurately determined. The resulting transformation matrix is displayed in Table 3.1 and is consistent with the discontinuity

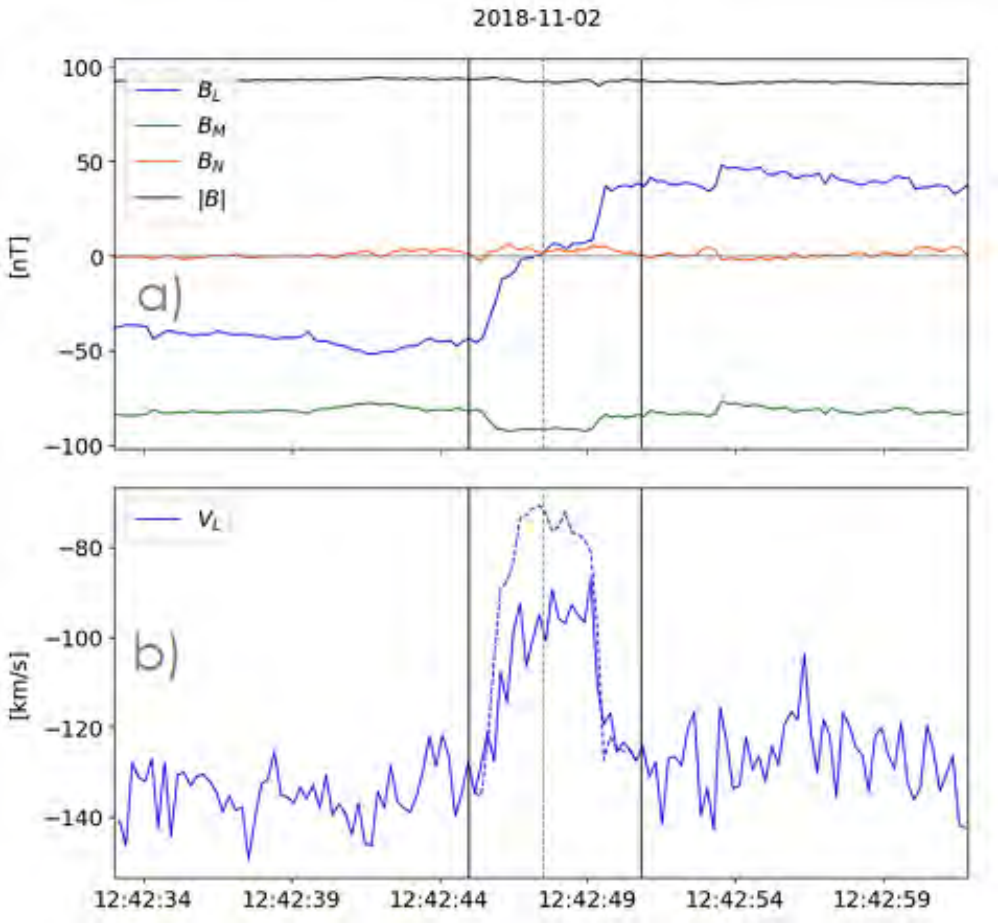

Figure 3.5: Reconnection jet for the November 2, 2018 MICCS, framed by two vertical black lines (which are used as a reference for the Walén test). The top panel (a) displays the magnetic field in the lmn frame; the bottom panel (b) shows the **l** component of the ion velocity, as well as the **l** component predicted from the Walén test and plotted as a dashed blue line.

	R	T	N
l	-0.35	0.90	-0.27
m	0.37	-0.14	-0.92
n	-0.86	-0.42	- 0.28

Table 3.1: Current sheet lmn orientation in the RTN frame (defined in section 1.4.2) for the November 2, 2018 reconnection jet event.

being mainly in the T direction. In this frame, the variation of velocity observed in the **l** direction is 40 km/s. In comparison, the theoretical velocity variation is found to be around 60 km/s. This overestimation of the jet speed by the Walén relation is usual in observations, as detailed in the introduction (section 1.2.3).

We note that this MICCS event occurs in the vicinity of some radial magnetic inversions commonly known as switchbacks (e.g., Kasper et al. (2019), Bale et al. (2019), Dudok de Wit et al. (2020), Horbury et al. (2020b)). From 12:18 to 13:18, the magnetic field deviates

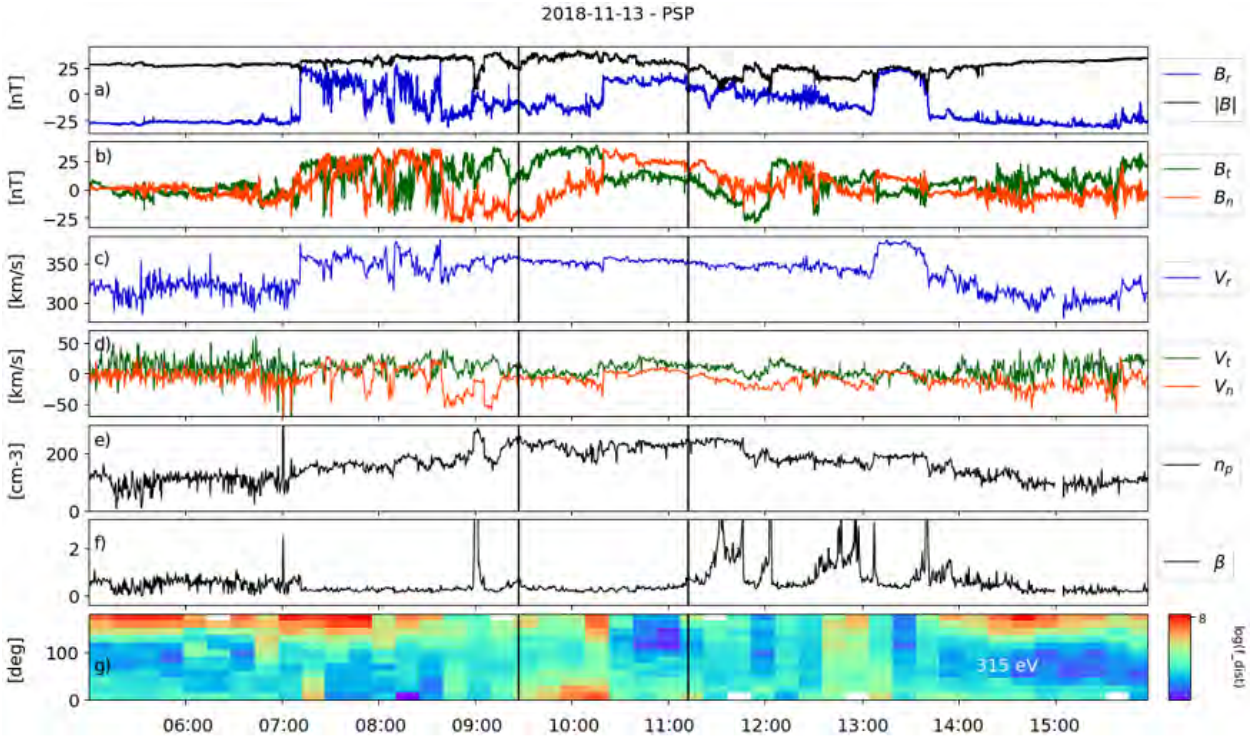

Figure 3.6: Event from November 13, 2018 (09:27 to 11:21, boundaries in black vertical lines). The data are presented in the same manner as in Figure 3.4.

from its ground state, corresponding to a Parker spiral of 166° (based on the average solar wind speed), and the radial magnetic field becomes positive once before the event (12:27) and once after (13:07) in what resemble two successive switchbacks. We discuss a possible link between MICCS and switchbacks in sections 3.4.6 and 3.5.

3.3.2 Event of November 13, 2018

Another impressive event was observed on November 13, 2018 and displayed in Figure 3.6. It is particularly interesting as PSP was crossing the HCS at this time (Szabo et al. (2020); Lavraud et al. (2020)). The structure was observed at 62 $R_\odot$ (0.3 AU) from the Sun and lasted 105 minutes from 09:27 to 11:12. The maximum magnetic field was measured at 41 nT at 10:04, and its average value at the boundaries is around 24 nT yielding a 71% increase. The wind speed was 350 km/s throughout the event; density was measured at 222 cm^{-3}, and the mean β was 0.28. The main differences with the event described in section 3.3.1 lie in both the location of the event (i.e., nearby or at the HCS in the sense described in section 3.1) and the PAD variations (3.6g). We first observe a strahl drop out (8:45 - 9:15) consistent with PSP beginning to cross the HCS (Lavraud et al., 2020). Then within the MICCS, the electrons are first isotropic, until bidirectional electrons are observed on four samples during the first part of the event that precedes the central current sheet. The PAD appears to have larger bidirectional fluxes for the sample closest to the current sheet, but this may be the result of time aliasing; it cannot be confirmed without higher time resolution. The second part of the event is dominated by a unidirectional parallel strahl population, before the PAD becomes isotropic again after the trailing boundary of the event at 11:12.

	R	T	N
l	0.59	-0.48	0.65
m	0.01	-0.8	-0.6
n	0.8	0.36	-0.47

Table 3.2: Current sheet *lmn* orientation in the *RTN* frame for the November 13, 2018 reconnection jet event.

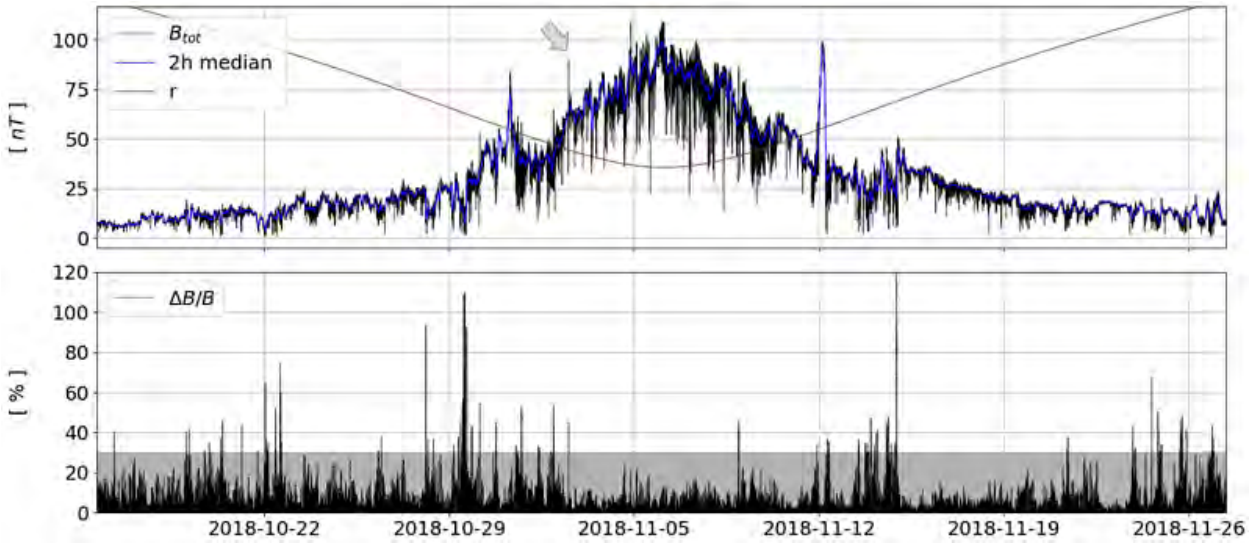

Figure 3.7: Search process illustration. The top panel displays the magnetic field's amplitude for the first encounter (B_{tot}), as well as a 2-hour running median (in blue) and r the radial distance to the Sun. The bottom panel shows the relative variation of B_{tot} regarding its 2h running median, with emphasis on over +30% relative variation (gray shading). The gray arrow in the top panel indicates the event occurring on November 2, 2018, which is detailed in section 3.3.1.

As reported by Phan et al. (2020), the central current sheet of the MICCS also reconnects, with signatures such as the ion jet visible in the R and N velocity components (3.6c, 3.6d), an indent in the magnetic field's amplitude (3.6a), and a flux enhancement in the PAD of the suprathermal electrons (3g); however, as previously mentioned, the apparent bidirectional PAD might be due to time aliasing. The *lmn* frame associated with the current sheet is given in Table 3.2, with a ratio of maximum to intermediate eigen value related to $\mathbf{l}'$ of 25. We note that this time the $\mathbf{l}$ vector is evenly distributed on the three *RTN* directions.

3.4 Statistical analysis

3.4.1 Selection process

To obtain a more complete view of the MICCS events measured by Parker Solar Probe in the inner heliosphere, we performed a survey covering the first four encounters. Our selection criteria were based on a magnetic field increase over 30% and a current sheet embedded in the structure. To automate the detection process, we searched for increases in the magnitude

of the magnetic field relative to a background determined by computing a running median. This was repeated over several running median time windows of 0.5, 2, 4, and 6 hours. Figure 3.7 illustrates this method for the 2-hour running median during E_1. Upon visual inspection of the data, we determined whether or not the event corresponded to a magnetic structure with an embedded current sheet. However, we noted that due to large and frequent variations of B, the running median method was biased when PSP was located in the HCS or in a magnetic hole. As such, we investigated these particular time intervals visually to detect possible MICCS. In particular, the second event analyzed in detail in section 3.3.2 was found this way. We also acknowledge that the running median method of detection tends to miss really small events in the solar wind. This does not preclude their existence as indeed some were detected in the HCS crossing of E_1 with a duration below 5 minutes, as observed in the list provided in Table 3.3. On the other hand, events lasting longer than 6 hours were not detected, but such cases typically would more likely correspond to large-scale structures, such as CMEs or CIRs.

Overall, we find 20 structures that correspond to our criteria (including the ones detailed in sections 3.3.1 and 3.3.2), their general properties are listed in Table 3.3, and their magnetic profile is shown in Figure 3.8. Among them, 13 were detected in the regular slow solar wind and 7 during or near HCS crossings (in bold in Table 3.3 and with a bold frame in Figure 3.8). Table 3.4 displays the result of some quantitative analysis we performed on the central current sheet and the surrounding switchbacks.

3.4.2 General properties

The MICCS events reported in this paper last between 26 seconds and 111 minutes. For the whole set of events, the mean duration is 29 minutes, while the median duration is 15 minutes, and most events last between 5 minutes (first quartile) and 42 minutes (third quartile). It is interesting to note that all MICCS that were detected nearby HCS crossings are at the tails of the duration distribution, with extreme values over 91 minutes or below 5 minutes. On the other hand, the other MICCS have more homogeneous durations mainly between 12 and 24 minutes (mean 20 minutes, median 15 minutes). As noted in section 3.4.1, it is possible that some events below 5 minutes were missed by our automatic detection method in the solar wind. The relative increase in the magnetic field amplitude goes from 30% at minimum (by selection) to 111% at maximum, with a mean increase of 53%. This does not significantly differ, regardless of the context (regular slow solar wind or HCS).

In Figure 3.9, we display the density distributions of MICCS properties in the solar wind (also available in Table 3.3 for each event). Overall, the MICCS have standard solar wind parameters, within the range of the distribution for the complete period of observation. Their magnetic field strength goes from 12 to 129 nT and their density from 17 to 222 cm^{-3}. They are mainly detected in the slow solar wind with speeds ranging from 260 to 475 km/s. Their β parameter goes from 0.05 to 0.67. Figure 3.10 displays the locations of the observed events for E_1 to E_4. The represented frame is the heliocentric inertial system with the XY plane being the ecliptic. The first three PSP orbits follow the same trajectory, while the fourth approaches closer to the Sun. Hollow circles mark the locations of MICCS detected near HCS crossings, which were only observed in E_1 and E_4. Overall the MICCS are quite evenly distributed along the orbit of PSP and they do not display obvious spatial clustering.

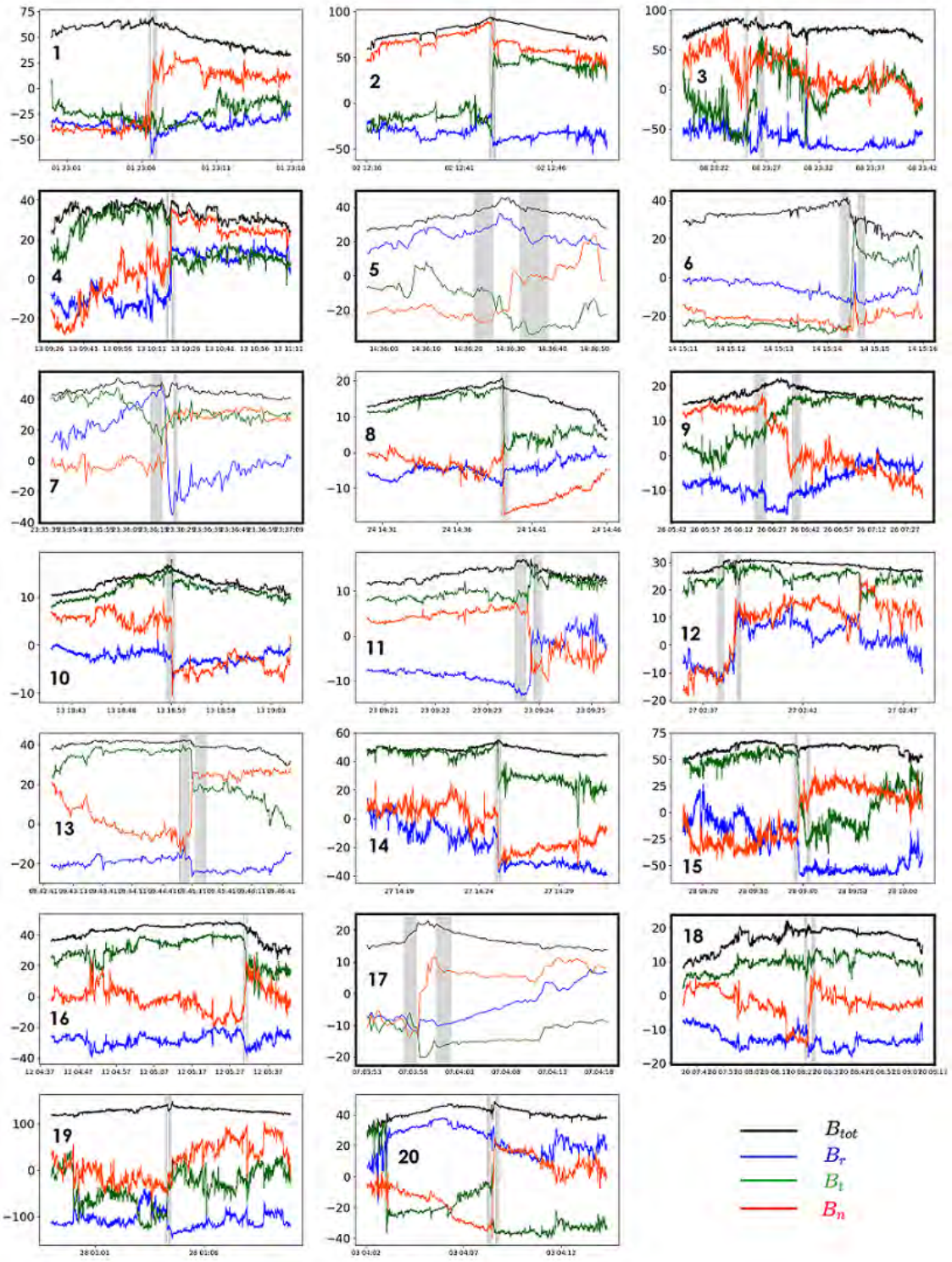

Figure 3.8: MICCS magnetic field profile, numbered as in Table 3.3, with the magnetic field amplitude in black, radial in blue, tangential in green, and normal in red. The shaded areas indicate the intervals used to determine the central current sheet orientation. Event detected during or near HCS crossings are framed in bold, those detected in the regular slow solar wind have a normal frame

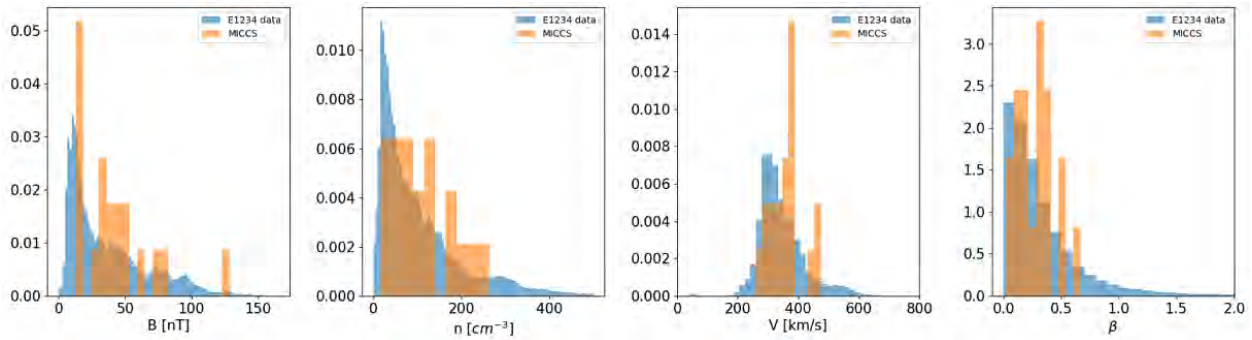

Figure 3.9: Density distributions of (*a*) B, (*b*) n, (*c*) V, and (*d*) β for MICCS (averaged values). Data from the whole period of observation (E_1, E_2, E_3, E_4) are displayed in blue and the distribution corresponding to the MICCS observation is in orange.

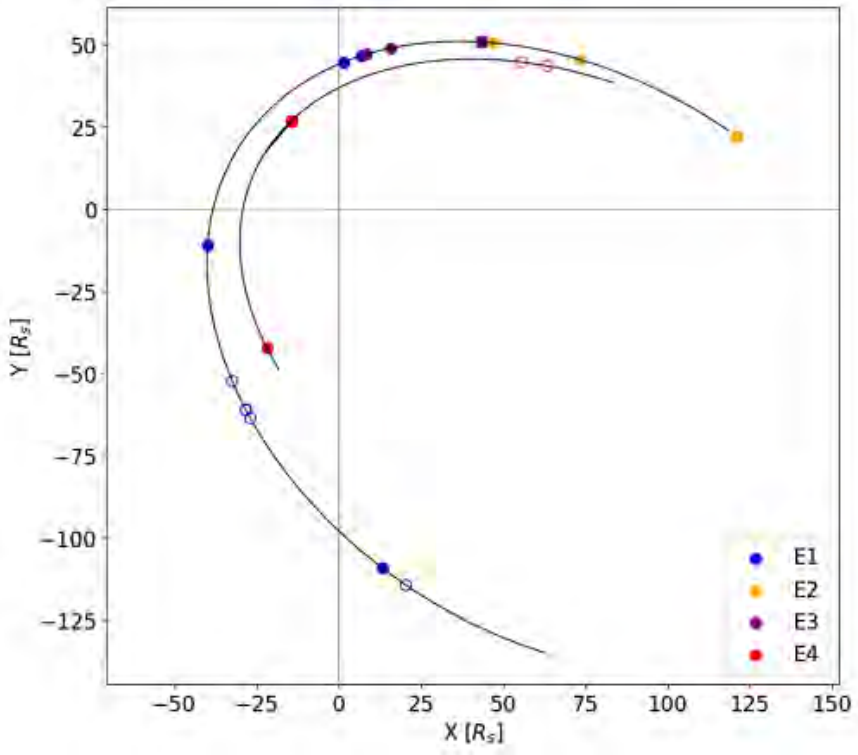

Figure 3.10: Detected MICCS positions represented in the heliocentric inertial system for encounters 1 to 4. Full dots represent MICCS that were detected in the regular slow solar wind, while empty dots are MICCS that were detected near an HCS crossing

3.4.3 Central current sheets orientation

To determine the main orientation of the events' current sheet, we used the hybrid minimum variance analysis described in section 2.4.2 and ensured that the direction of maximum variation was reliably determined by checking the ratio of maximum to intermediate eigenvalue. For all current sheets, the ratio ranges from 3.5 to 88.6, with only one value below 5. The mean ratio is 30 and the median ratio is 23. The boundary magnetic fields used in the method were averaged on each side of the current sheets on time spans indicated as gray

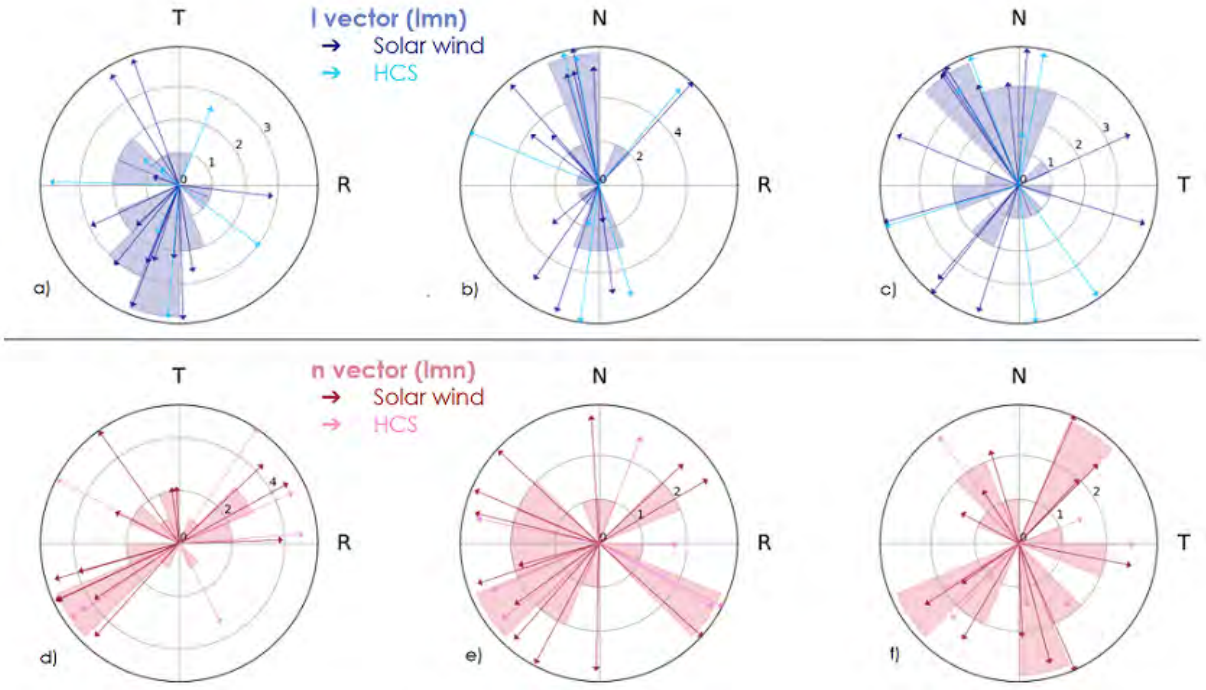

Figure 3.11: MICCS central current sheet lmn orientation. The top panels display the **l** vectors projected onto the RT (a), RN (b), and TN (c) planes, with solar wind events in dark blue and HCS events in light blue. A polar bar chart is over plotted counting the number of arrows in a 22.5° bin. Bottom panels display the **n** vectors in a similar manner, with solar wind events in dark red and HCS events in magenta. In these plots, each projected vector is depicted as an arrow, with the bold black outer circle representing a norm of 1. In other words, if an arrow reaches the unit circle in the RT plane, then it has no component in the N direction. On the contrary, if the norm of the projected arrow is significantly smaller than unity, then its component in the out-of-plane direction is non-negligible

shaded areas in Figure 3.8.

The results are displayed in Figure 3.11 and show that the central current sheets of MICCS display a preferential orientation. What stands out in these distributions, and what is also visible when carefully studying Figure 3.8, is that the direction of **l** corresponding to the maximum variance is mainly located within the TN plane of the RTN frame. In panels (3.11a) and (3.11b), we can see that even if some vectors have significant R components, none of them are mainly oriented along R, that is to say with a norm close to unity along the R axis except for one HCS event that has an important R component (event 7 in Table 3.3). This preferential orientation is also visible in the polar bar plot, where we can see that most of the **l** vectors are observed within ± 45 degrees of the T axis (12 out of 20) when projected in the RT plane; and this is even higher for the N axis (16 out of 20) when projected in the RN plane. This is also confirmed when we look at the projections of **l** in the TN plane (3.11c) where almost all vectors have a norm close to unity. The bottom panels displays the **n** vectors, and they are mostly oriented along R. In the RT plane (3.11d), 13 events are within ± 45 degrees of the R axis while this is the case for 15 events in the RN plane (3.11e). In the TN plane (3.11f), we can see no preferential orientation, but we notice

that almost all vectors have a norm smaller than unity and, as such, present an important R component. This tendency for the current sheets to be oriented in a particular direction (i.e., with a normal preferred in the R direction and a maximum variance in the TN plane) does not change when considering only regular slow solar wind events. We discuss this result in section 3.5.

3.4.4 Reconnecting current sheets

To determine if a current sheet was reconnecting, we searched for a reconnection jet in the SPC moments coincidental with the magnetic field rotation. We also checked the consistency with variations in the magnetic field magnitude, ion density, plasma β, and electron pitch angles. It is unfortunate that for the majority of the studied events, data other than the magnetic field were not sufficiently resolved due to either a duration of the event that was too short or a location that was too far out from perihelion. To make the best of the situation, we checked if the observed current sheets were bifurcated, that is, if the magnetic field presented a step in its rotation. This information is a hint as to the magnetic reconnection, as it is a necessary but not sufficient condition (e.g., (Phan et al., 2020)). Results are presented in column 4 (jet) and 5 (bifurcated current sheet (CS)) of Table 3.4.

Among the 20 current sheets studied, we identified 5 that were associated with a reconnection jet plainly visible in the ion velocity, including the cases described in sections 3.3.1 and 3.3.2. For two events, the diagnosis is less clear and we have marked them as probable jets. For three of them, no jet was visible and the structure was alfvénic throughout. The fact that five out of ten resolved events present a clear reconnection jet hints that MICCS might be a preferential location for magnetic reconnection. Indeed, reconnecting current sheets are not common in PSP measurements, as noted by Phan et al. (2020), because most of the current sheets are located at the boundary of switchbacks. Switchback boundaries are alfvénic structures that propagate in the same direction, contrary to reconnection exhausts, which are bound by two rotational-type discontinuities propagating in opposite directions away from the X-line. In addition, at least four of the remaining unresolved current sheets are clearly bifurcated. They thus potentially reconnect, although we cannot be sure as alfvénic structures can also have bifurcated current sheets, as shown by Phan et al. (2020).

3.4.5 Pitch angle distribution

We investigated the PAD of suprathermal electrons throughout the structures, as they are good tracers of the large-scale magnetic topology. We visually determined if the PAD showed significant variations, upstream and downstream of the current sheet (and within the structure's boundaries), focusing on changes in the maximum flux location, a broadening of the PAD distribution, and the presence of counter-streaming electrons. The results are presented in the PAD variation column of Table 3.4. Five events present clear variations in their strahl properties across the current sheet (indicated by a yes in Table 3.4), while others are either unresolved or unclear, and four of them rather clearly show no variation. Of the four events with a PAD variation, only the one described in section 3.3.2 (#4) is located near the HCS, while the four other events (#1, 3, 14, 16) are located in the regular slow solar wind. The four events with no variation of PAD (#2, 15, 19, 20) are also located in the regular slow solar wind and present no particular feature in strahl properties.

In the four events with a PAD variation, a counter-streaming electron population is present in only one part of the structure and vanishes across the current sheet, as in Figure 3.6g. Given their often much lower fluxes, it is not clear whether these counter-streaming electrons are indicative of closed field lines, or if they may come from reflections farther down the field lines by some distant CIR or shock (Steinberg et al., 2005; Skoug et al., 2006; Lavraud et al., 2010)). Yet, close to the HCS, closed field lines may form more easily, as flux ropes of various sizes with clearly closed field lines have been observed frequently in that region up to 1 AU (e.g., Kilpua et al. (2009), Rouillard et al. (2011), Sanchez-Diaz et al. (2019)). As such, closed field lines during the first part of event #4 (section 3.3.2) remain a plausible configuration. But in either case, it is clear that for these five events (# 1, 3, 4, 14, 16), the large-scale connectivity of the field lines before and after the current sheet is drastically different.

3.4.6 Relation to switchbacks

As the first event analyzed in section 3.3.1 was observed near switchbacks, we checked whether this connection was true for all MICCS. In column 7 of Table 3.4, we indicated if the regular slow solar wind events were located in the vicinity of switchbacks (abbreviated SB) or rather with no switchback around. Events located near HCS events were not considered here. Most of the regular slow solar wind events were observed in close relation to a switchback except for one (#19). But we can see no clear tendency for them to be before or after, or a direct part of the switchbacks. As switchbacks are omnipresent in PSP data, the proximity of the MICCS structure and switchbacks is as likely to be random as it is to be significant. Additional work is required to conclude on the possible link between these two types of structures.

3.4.7 PSP dust measurements

One model that has been proposed to explain the formation of magnetic peaks with central current sheets in the solar wind is the dust-plasma interaction, that was studied with regards to IFE formation Russell (1990); Jones et al. (2003a,b). Here, we analyze PSP dust measurements made by the FIELDS instrument at the time of observation of the MICCS structures. Dust, when impacting the spacecraft, creates voltage spikes on the electric antenna with amplitudes well above the instrument noise level (Szalay et al. (2020), Page et al. (2020)). We looked at the voltage provided by the second antenna of PSP (V2) and analyzed the number of spikes superior to 50 mV (as done in Szalay et al. (2020)) with a binning of 5 minutes, considering this quantity to be a good approximation for the number of dust impacts on the spacecraft. As an illustration, this number of spikes is plotted on the top panel of Figure 3.12 for the event described in section 3.3.2. We computed the average and standard deviation of the number of spikes on a $\pm$ 3h interval outside of the event (red curve and shaded area in 3.12a) and compared it to the average inside the event (blue curve in 3.12a). The latter was computed with a $\pm$ 5 minute interval around the MICCS to be sure that we obtained at least two points for the shorter events.
We then computed these quantities for all the MICCS under study; the results for all events are displayed in the bottom panel of Figure 3.12. We find that for all events, except for one (#6), the average number of spikes inside the MICCS falls within 1σ of the outside average.

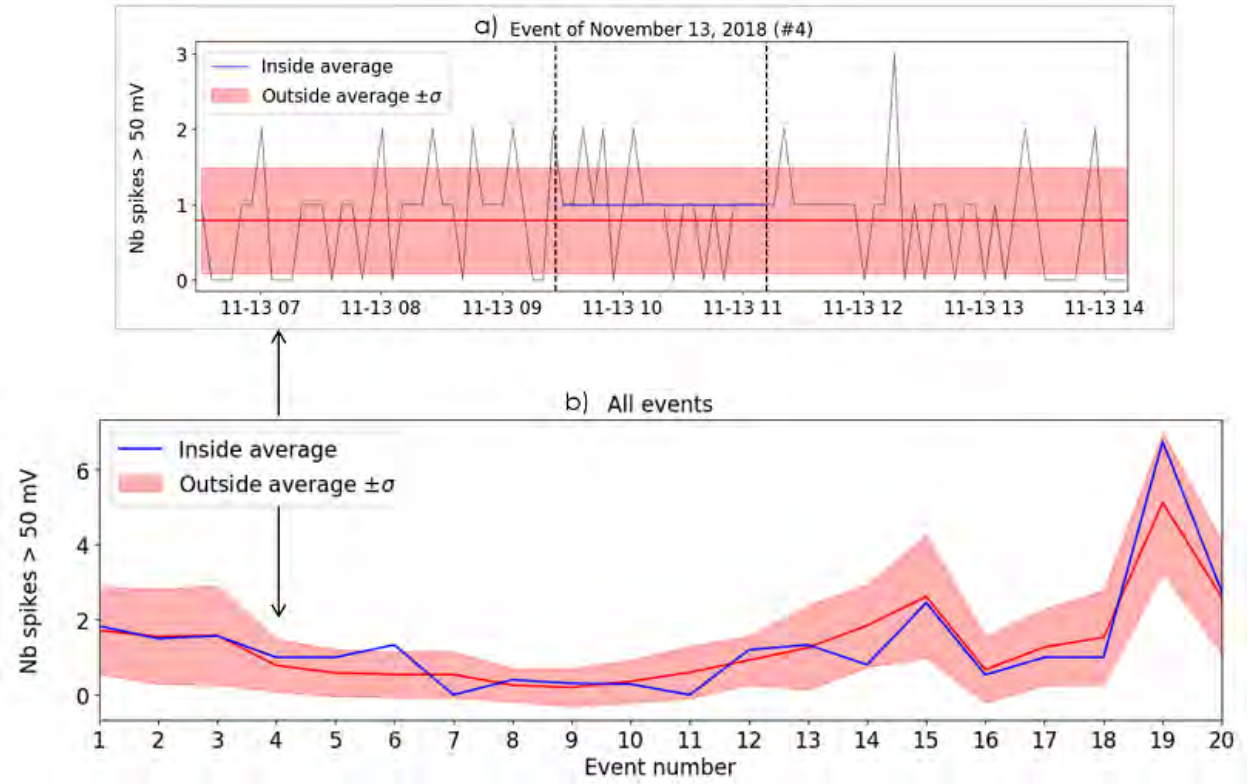

Figure 3.12: Analysis of PSP dust measurements in the vicinity of MICCS. The top panel (a) displays the number of voltage spikes superior to 50mV from the V2 antenna as a function of time, around the event described in section 3.3.2 (delimited with dashed lines). The red line is the average of the number of spikes on a ± 3h interval around the MICCS, and the red shaded area delimits a 1 σ standard deviation. The blue line is the average inside the structure. The bottom panel (b) displays the same statistical quantities for all events. The red curve is the averaged number of spikes for each event surrounded by the $\pm 1\sigma$ shaded area, and the blue curve is the average number of spikes inside each MICCS.

We conclude that there is no significant change in the dust impact rate (through the number of spikes) in the vicinity of the MICCS events studied here.

3.5 Impacts on the structures formation process

In section 3.2, we have presented two models that may explain the formation of these magnetic peaks with central current sheet in the solar wind. Regarding the dust-plasma interaction process studied with regards to IFE formation (Russell, 1990; Jones et al., 2003b,a), we investigated PSP dust measurements in section 3.4.7 and found no significant change in the dust impact rate measured by PSP at the time of observation of the MICCS. The most probable conclusion is that dust plays no role in the formation and evolution of the MICCS structures. However, it is possible that dust plays a role in their formation while its signature has faded over time, or that the population of dust grains responsible for the MICCS formation has sizes and velocities that are not detected by PSP. Measurements by Solar Orbiter will prove interesting to further confirm or contradict our result.

On the other hand, at the Earth's magnetopause, FTE-like structures with a magnetic reconnection in their core were identified as interlaced flux tubes. Following this view, the MICCS structures may also be interlaced flux tubes embedded in and advected by the solar wind. The fact that PADs vary across the current sheets for several events is consistent with this view of two flux tubes connected to different strahl source regions, as discussed in section 3.4.5.

At the Earth's magnetopause, it was argued that an IMF strongly tilted duskward or dawnward would create complex configurations at the subsolar point with several X-lines, and thus facilitate the creation of interlaced flux tubes (Fargette et al., 2020). In the solar wind, the flux tubes on each side of the current sheet may well originate from very distinct sources on the photosphere (explaining the often very different properties of the flux tubes) and be transported into the heliosphere where the 3D expansion of the solar wind may allow for their interaction. This would be consistent with the tendency for the current sheets to have a normal - that is a minimum variation direction - along R. Indeed, in the flux tube texture view of Borovsky (2008), the flux tubes that constitute the solar wind remain rooted to the photosphere despite often forming strong current sheets at their boundaries and potentially entangling themselves significantly. A strong interaction between two flux tubes may lead to an increased magnetic field and interlacing such that the plane of interaction may preferentially be perpendicular to the main direction of the flow, thus explaining the preferred orientation of the current sheet normal vectors with the radial direction. The MICCS observed near the HCS easily fit in this scenario. They may even be more frequent since the HCS is a location where it is even easier to form adjacent flux tubes with drastically different magnetic connectivity.

Regarding the relation to switchbacks, one may easily imagine that SBs can entangle with other SBs or with the background solar wind to form complex structures such as MICCS. Yet, at this point, the apparent frequent vicinity of SBs appears marginal given the large recurrence of SBs in PSP data overall.

3.6 Conclusion

In this work, we performed a systematic study of structures made of a magnetic field increase with a clear central current sheet, resembling solar wind interplanetary field enhancements (IFEs) or magnetospheric interlaced flux tubes (IFTs), observed by the Parker Solar Probe mission and below 0.3 AU. We first reported on two of these events in detail. One occurred in the regular slow solar wind and the other was near an HCS crossing, and both displayed reconnection signatures at their central current sheet.

We identified 20 MICCS detected by PSP throughout its first four encounters with the Sun. They were selected based on an increase in the magnetic field strength over 30% and the presence of a central current sheet. The following points summarize our results.

- We find that these structures can be detected in the regular slow solar wind (13 events) as well as during HCS crossings (7 events) at all longitudes and distances from the Sun.
- Their general characteristics are standard, with B, n, V, and β values consistent with the slow solar wind, and with a maximum speed of 475 km/s. The PSP orbit,

potential bias in our selection method, and the current low statistics do not allow us to be conclusive yet, but as of now these structures have not been observed in the fast solar wind by PSP.

- They last on average 29 minutes, with extreme durations from less than a minute to close to 2 hours. The extreme durations are often associated with HCS events. MICCS in the regular slow solar wind are more likely to last between 12 and 24 minutes.
- Several of the central current sheets showed reconnection jets (five identified, two probable) and/or bifurcated magnetic field signatures (ten identified) in their core. But many cases had insufficient data resolution to determine if reconnection was in fact occurring.
- For five events, the suprathermal electron PAD varies across the central current sheet, hinting that there is a significant change in connectivity between the first and second part of the events, as delimited by the central current sheet. For four events, the PAD shows no variation suggesting no significant change in connectivity to the Sun.
- The central current sheets display a preferential orientation, with a maximum variance direction in the TN plane of the RTN frame and a normal oriented in the R direction.
- When detected in the regular slow solar wind, the structures are often close to switchbacks. However, considering the omnipresence of switchbacks in PSP data, it is difficult to draw a significant conclusion as to a possible relation.
- We find no significant change in the dust impact rate in the vicinity of the MICCS under study, leading us to conclude that dust probably plays no role in the MICCS formation and evolution.

Overall our observations are consistent with MICCS being constituted of two entangled flux tubes embedded in the solar wind plasma that interact at their current sheet boundary. The flux tubes would remain rooted at the Sun as indicated by the preferential orientation of their current sheet in the TN plane and PAD properties within the structure. Some show significant strahl variation across their current sheet and we conclude that they are either connected to different sources back at the Sun on one end, or that they extend to different regions in the heliosphere on the other end (CIRs, shocks). Magnetic reconnection is frequently observed at their current sheet, which makes them a favored place in which to search and study this process as we approach closer to the Sun.

Future observations by PSP of such structures with a higher time resolution and those that are lower in the corona will unveil more about their properties and formation process. Combined observations with the Solar Orbiter mission (Müller et al., 2013, 2020) would also enable detailed studies regarding their early evolution.

# #	Enc	Start time	End time	Duration (min)	ΔB (%)	Context	R ($R_\odot$)	B (nT)	n (cm^{-3})	V (km/s)	β
1	1	01/11/2018 23:00	01/11/2018 23:16	16	63	Solar wind	46.91	52	263	329	0.50
2	1	02/11/2018 12:36	02/11/2018 12:50	14	45	Solar wind	44.48	79	186	321	0.11
3	1	08/11/2018 23:19	08/11/2018 23:42	23	37	Solar wind	41.42	76	183	438	0.30
4	**1**	**13/11/2018 09:27**	**13/11/2018 11:12**	**105**	**71**	**nearby HCS**	**61.67**	**33**	**222**	**353**	**0.28**
5	**1**	**14/11/2018 14:35**	**14/11/2018 14:36**	**1**	**67**	**nearby HCS**	**67.36**	**35**	**124**	**375**	**0.67**
6	**1**	**14/11/2018 15:11**	**14/11/2018 15:16**	**5**	**57**	**nearby HCS**	**67.49**	**31**	**99**	**380**	**0.37**
7	**1**	**14/11/2018 23:35**	**14/11/2018 23:37**	**1**	**31**	**nearby HCS**	**69.17**	**45**	**73**	**475**	**0.37**
8	1	24/11/2018 14:30	24/11/2018 14:46	16	111	Solar wind	110.28	15	17	464	0.15
9	**1**	**26/11/2018 05:47**	**26/11/2018 07:35**	**108**	**40**	**nearby HCS**	**116.34**	**18**	**18**	**379**	**0.02**
10	2	13/03/2019 18:41	13/03/2019 19:05	24	70	Solar wind	123.31	12	33	288	0.33
11	2	23/03/2019 09:20	23/03/2019 09:25	5	42	Solar wind	86.28	14	45	306	0.51
12	2	27/03/2019 02:36	27/03/2019 02:48	12	35	Solar wind	69.13	29	60	388	0.20
13	3	24/08/2019 09:42	24/08/2019 09:46	4	30	Solar wind	66.75	39	87	353	0.21
14	3	27/08/2019 14:17	27/08/2019 14:32	15	30	Solar wind	51.32	48	116	353	0.20
15	3	28/08/2019 09:16	28/08/2019 10:04	48	52	Solar wind	47.62	61	85	388	0.13
16	3	12/09/2019 04:40	12/09/2019 05:43	63	74	Solar wind	...	42	...	...	...
17	**4**	**19/01/2020 07:03**	**19/01/2020 07:04**	**0,4**	**64**	**nearby HCS**	**76.82**	**17**	**44**	**345**	**0.23**
18	**4**	**20/01/2020 07:42**	**20/01/2020 09:13**	**91**	**82**	**nearby HCS**	**71.42**	**17**	**91**	**260**	**0.31**
19	4	28/01/2020 00:59	28/01/2020 01:10	11	30	Solar wind	30.28	129	139	374	0.05
20	4	03/02/2020 04:02	03/02/2020 04:14	12	36	Solar wind	47.69	41	213	301	0.37

Table 3.3: General characteristics of MICCS events. Event detected during or near HCS crossings are in bold font, those detected in the regular slow solar wind are in normal font.

#	Start time	Duration (*min*)	Jet	Bifurcated CS	PAD variation	Switchbacks
1	01/11/2018 23:00	16	no	no	yes	yes
2	02/11/2018 12:36	14	yes	yes	no	yes
3	08/11/2018 23:19	23	no	no	yes	yes
4	**13/11/2018 09:27**	**105**	**yes**	**yes**	**yes**	**...**
5	**14/11/2018 14:35**	**1**	**not resolved**	**maybe**	**not resolved**	**...**
6	**14/11/2018 15:11**	**5**	**not resolved**	**no**	**not resolved**	**...**
7	**14/11/2018 23:35**	**1**	**not resolved**	**maybe**	**not resolved**	**...**
8	24/11/2018 14:30	16	not resolved	yes	not resolved	yes
9	**26/11/2018 05:47**	**108**	**not resolved**	**yes**	**unclear**	**...**
10	13/03/2019 18:41	24	not resolved	yes	not resolved	yes
11	23/03/2019 09:20	5	not resolved	yes	not resolved	yes
12	27/03/2019 02:36	12	not resolved	maybe	not resolved	yes
13	24/08/2019 09:42	4	yes	yes	no	yes
14	27/08/2019 14:17	15	probable jet	yes	yes	yes
15	28/08/2019 09:16	48	yes	yes	yes	yes
16	12/09/2019 04:40	63	no data	maybe	not resolved	yes
17	**19/01/2020 07:03**	**0.4**	**not resolved**	**maybe**	**not resolved**	**...**
18	**20/01/2020 07:42**	**91**	**no**	**no**	**unclear**	**...**
19	28/01/2020 00:59	11	probable jet	maybe	no	no
20	03/02/2020 04:02	12	yes	yes	no	yes

Table 3.4: Quantitative analysis on MICCS events. Event detected during or near HCS crossings are in bold font, those detected in the regular slow solar wind are in normal font.

Summary

We conclude this part of the manuscript that focused on flux ropes and interlaced flux tubes, drawing a parallel between observations made at the Earth's magnetopause and in the solar wind.

We first focused on magnetic structures called Flux Transfer Events (FTEs) observed at the Earth's magnetopause, formed through magnetic reconnection in the subsolar region. Their structure is that of magnetic flux ropes with a helical internal magnetic field, and for that matter we implemented a model of magnetic flux ropes that can be fitted to data, adapted from Burlaga (1988) and akin to Lepping et al. (1990). We performed a statistical analysis on FTE-like structures observed by the MMS mission, with particular emphasis on the occurrence of magnetic reconnection inside these structures. We found that events looking like FTEs but inconsistent with their classical description occur frequently, as they present a marked reconnecting current sheet in their core. By analysing the parallel electron heat flux inside FTEs (as it is a good tracer of magnetic connectivity) and the solar wind conditions prior to the FTEs, we found results consistent with the recent work by Kacem et al. (2018) and Øieroset et al. (2019), where FTE-like structures are described as interlaced flux tubes. We proposed a formation mechanism based on a magnetic shear angle model of the magnetopause (Trattner et al., 2007), which can lead to the interlacing of flux tubes from two spatially distinct X-lines at the same longitude.

We then moved from the Near-Earth environment to the inner heliosphere, and focused on similar structures observed by the PSP mission in the solar wind. We chose to call these events "Magnetic Increases with Central Current Sheet" (MICCS), and they show a similar structure to reconnecting magnetospheric FTEs. These MICCS were thought to be formed through interaction between dust particles and the magnetic field, but through an analysis of 20 of these events, we did not find a correlation between dust enhancement and MICCS observation. We rather conclude that, similarly to the reconnecting FTEs, they are overall consistent with a double flux tube-configuration that would result from initially distinct flux tubes which interact during solar wind propagation.

When studying these events in the solar wind, we did not miss that while MICCS were interesting because of the characteristics they shared with magnetospheric FTEs, they were not a dominating feature of the young solar wind. Unexpected large magnetic deflections pervaded PSP measurements below 0.3 AU, puzzling the space-plasma community. In the next part of the manuscript, we move on from flux-rope like structures to focus on these deflections called magnetic switchbacks, and present several studies that investigate their origins and formation process.

Part II

Switchbacks and magnetic reconnection

Chapter 4

Introduction on magnetic switchbacks

Contents

From the very first encounter of Parker Solar Probe (PSP) with the Sun, in-situ data showed striking unexpected features: the solar wind was pervaded with frequent magnetic deflections, Alfvénic in nature, associated with velocity spikes and large radial magnetic field changes (Kasper et al. (2019), Bale et al. (2019)). Because they often present reversals of the radial magnetic field component, they are usually called magnetic switchbacks. In this chapter, we propose an overview of the literature on magnetic switchbacks to the date of writing (sections 4.1 to 4.2), and present the inherent difficulty to analyse them in in-situ data (section 4.3). Parts of this chapter are taken or adapted from the introduction and methodology sections of Fargette et al. (2020) and Fargette et al. (2021a).

4.1 Observations and properties

4.1.1 Observations

Before being identified as a dominant feature of the young solar wind in PSP in-situ data, similar structures reversing their radial magnetic field component had been observed by previous missions. Balogh et al. (1999) report on magnetic field polarity inversions at high heliographic latitudes with the Ulysses spacecraft, and interpret them as large-scale folds in the magnetic field. By performing a statistical analysis of inversions compared to the Parker spiral direction, they find a significant preference for the deflections to orient in the "less tightly wounded" (anti-clockwise) direction of the Parker spiral. By analysing differential streaming between alpha particles and protons, Yamauchi et al. (2004) also confirms that these reversals are folds in the magnetic field. In ACE data, Gosling et al. (2009) report on large accelerated Alfvénic fluctuations occurring in the equatorial plane and propagating outward from the Sun. Gosling et al. (2011) also identified similar accelerated Alfvénic

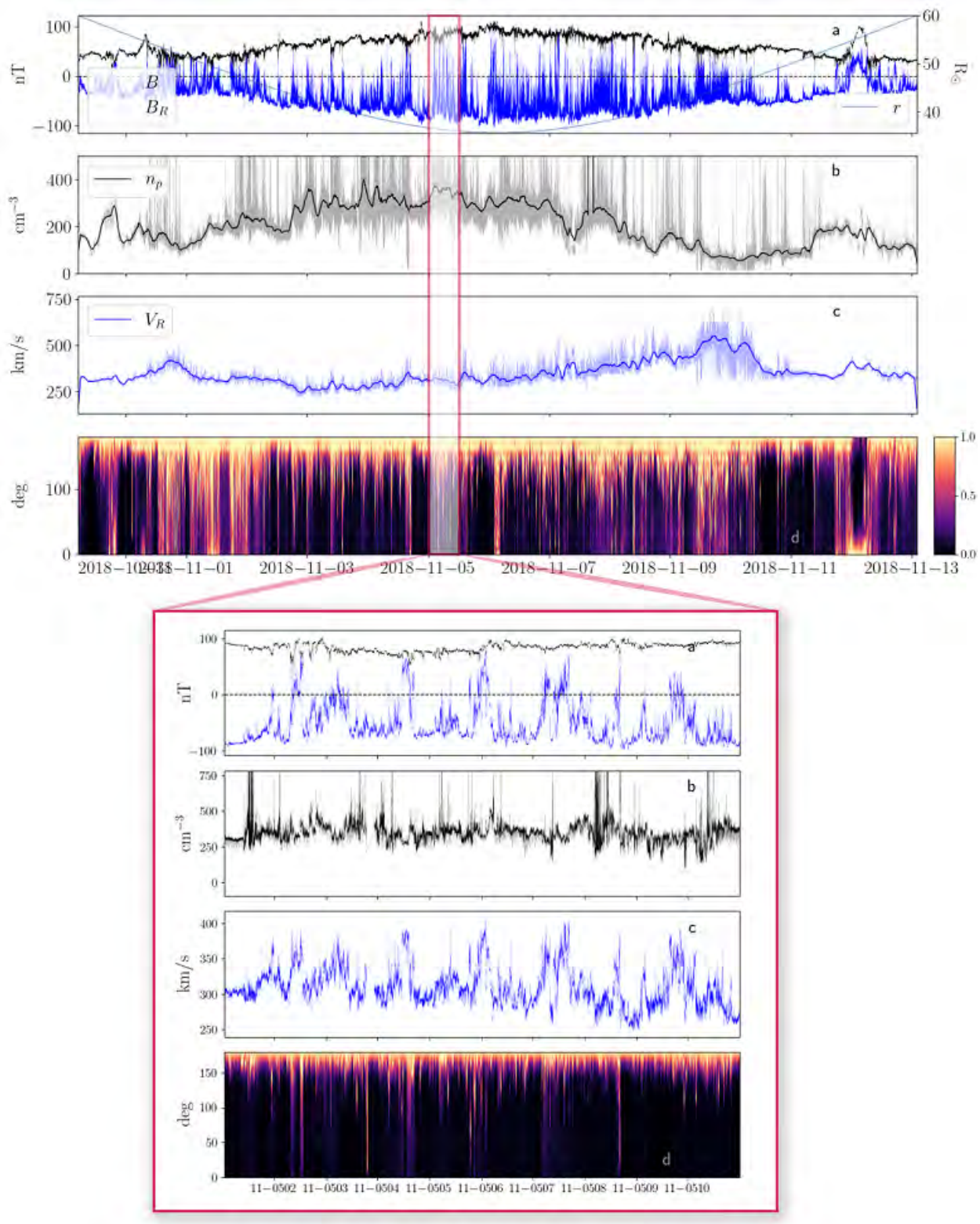

Figure 4.1: Data from PSP's first orbit, with (a) the magnetic field amplitude and radial component as well as radial distance of the spacecraft to the Sun; (b) the proton density together with a 2h average; (c) the radial solar wind speed with a 2h average; (d) the PAD of suprathermal electrons (300-2000 eV) normalised to the maximum flux at a given time. In the inset, we zoom on 11 hours of data presented in a similar way.

structures in WIND data, during solar wind intervals of 320 to 550 km/s at 1 AU. More recently, Horbury et al. (2018) analyzed velocity spikes at 0.3 AU in Helios data in fast solar wind streams (700 km/s) associated with large magnetic field deflections. They report that these events occur about 5% of the time and are at the same temperature as the surrounding plasma. Macneil et al. (2020) make a systematic analysis of magnetic field inversions in Helios data from 0.3 to 1 AU and find an increasing occurrence with radial distance, and Macneil et al. (2021) highlight in addition that magnetic field reversals become less Alfvénic and more compressible with radial distance.

While magnetic field reversals associated with velocity enhancements are observed from 0.3 to 1 AU in missions such as Ulysses, Helios, WIND or ACE, they are most striking closer to the Sun in PSP data. In Figure 4.1, we display the magnetic field and particle data for the PSP's first encounter with the Sun. We show data from October 30, 2018 to November 13, 2018 when PSP was scanning the solar wind between 35 and 60 $R_\odot$ in the negative polarity sector. The solar wind speed averaged over two hours varies from 250 to 550 km/s, and the density from 100 to 400 cm^{-3}. Two CMEs are observed during the inbound and outbound legs of the encounter, visible as increases of the magnetic field amplitude. In this figure, it is easy to see that magnetic switchbacks pervade the solar wind and are particularly visible in the radial component of the magnetic field. In the inset, we zoom on some switchback structures, to show that the magnetic field deflections are clearly associated with velocity spikes while other plasma parameters (field amplitude, density and strahl) remain essentially constant while the vector field deflects.

As detailed in section 2.4.5, the suprathermal electrons are a tracer of magnetic topology. The fact that the PAD remains constant throughout the magnetic field reversals indicates that, at least in the structure's core, the suprathermal electrons are flowing towards the Sun. This rules out the possibility of a disconnected flux tube of inverted polarity, and as such switchbacks are today interpreted as large-scale folds of the magnetic field propagating away from the Sun (Balogh et al., 1999; Kasper et al., 2019; Bale et al., 2019). They are often represented as a zig-zag structure as illustrated in Figure 4.2, even though their structure is probably more complex.

4.1.2 Statistical properties

The main in-situ signatures of magnetic switchbacks are the visible large deflections of the magnetic field that occur while the magnetic field amplitude and the strahl orientation remain constant, and that are coincidental with enhancements in the radial velocity. The latter stems from the highly Alfvénic nature of the deflections (Matteini et al., 2014; Larosa et al., 2021). Several additional characteristics have been underlined through statistical studies on early PSP data. Switchbacks do not present a characteristic duration, they last from seconds to hours, and they have a different magnetic field power spectral density compared to the pristine solar wind (Dudok de Wit et al., 2020). They tend to aggregate in "patches", meaning that their occurrence is modulated at large scales (Bale et al., 2019; Dudok de Wit et al., 2020; Bale et al., 2021; Fargette et al., 2021a), and their duration distribution is also found to be consistent with high aspect ratio structures, i.e. elongated in the radial direction (Horbury et al., 2020b; Laker et al., 2021). Within switchback patches, the plasma properties seem to differ from the background solar wind with an enhanced proton parallel temperature

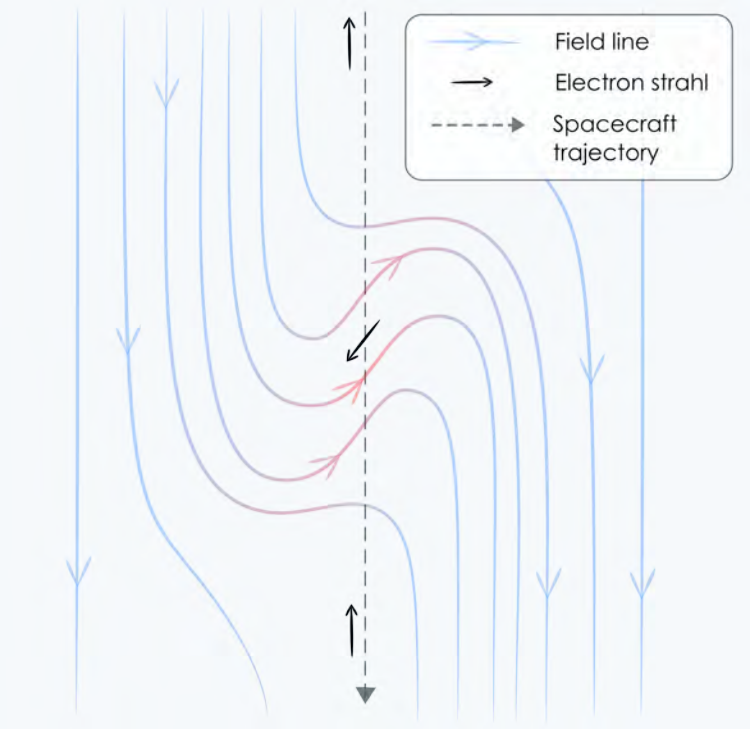

Figure 4.2: Simplified sketch of a magnetic switchback, adapted from Kasper et al. (2019). The color of the magnetic field lines is an indication of the radial component being negative (blue) or positive (red).

leading to an isotropisation of the ion distribution function (Woodham et al., 2021). This result needs however to be confirmed, as other work focusing on the largest switchbacks do not find an increase in parallel temperature (Woolley et al., 2020). Switchback patches show as well a different plasma composition with an increased proportion of alpha particles (Bale et al., 2021). When focusing on their boundaries, they are found to be mostly rotational discontinuities (Larosa et al., 2021; Akhavan-Tafti et al., 2021), and the sharpest boundaries coincide with variations in the magnetic field amplitude, proton density and solar wind speed (Farrell et al., 2020). Surprisingly, despite being thin localised current sheets, most of the magnetic switchback do not display magnetic reconnection signatures at their boundaries (Phan et al., 2020). A few exceptions were observed (Froment et al., 2021; Lavraud et al., 2021) potentially pointing to a dissipation of the structures through magnetic reconnection. Finally, the dependency of the occurrence rate of switchbacks with solar distance r is unclear. It is found to either increase with solar distance (Macneil et al., 2020; Mozer et al., 2020; Tenerani et al., 2021) or to be independent of r (Mozer et al., 2021; Fargette et al., 2021a).

Overall, the origin of these magnetic structures remains poorly understood, and their formation process is to date highly debated.

4.2 Existing formation models

It is now clear that at least part of the switchbacks are formed below PSP's orbit, either in the low atmosphere, or in between the Sun and the spacecraft. In the first case they would

be remnants of the solar wind formation process, and in the second case a byproduct of solar wind evolution. In this section, we propose an overview of the potential formation scenarii proposed in the literature.

4.2.1 In-situ formation processes

One possibility is that magnetic switchbacks are formed in situ in the solar wind. The fact that switchbacks are strikingly highly Alfvénic makes turbulence a natural candidate as a source for the phenomenon. Low-amplitude Alfvén waves generated near the low corona can, through radial expansion and non-linear evolution, naturally reproduce some switchback signatures including radial magnetic field reversals (Squire et al., 2020; Mallet et al., 2021; Shoda et al., 2021). Shear-driven turbulence is also found to reverse the magnetic field Ruffolo et al. (2020). All of these works are able to reproduce through MHD simulations the reversal of the radial magnetic field, the Alfvénicity and the constant field magnitude, born purely out of turbulence in the solar wind. They predict that the occurrence rate of switchbacks should increase with radial distance, and as such are consistent with part of the litterature (Macneil et al., 2020; Mozer et al., 2020; Tenerani et al., 2021). However, simulations conducted to form switchbacks through Alfvén wave expansion fail to account for the occurrence rate of switchbacks and their ubiquity observed in PSP data (Shoda et al., 2021).

4.2.2 Formation processes in the low atmosphere

The main competing theory postulates a formation in the low solar atmosphere through the process of interchange reconnection, where open magnetic field lines reconnect with closed ones in the low corona (Nash et al., 1988; Wang et al., 1989). The resulting footpoint exchange of magnetic field lines also provides a theoretical basis to explain how the magnetic field lines can sustain a quasi-rigid rotation in the corona while being anchored in a differentially rotating photosphere (Wang et al., 1996; Fisk, 1996; Fisk et al., 1999). To keep up with the shear induced by the different rotation rates of the two domains, field lines reconnect at their base and allow coronal hole boundaries to remain unaffected by the photosphere differential rotation (Wang & Sheeley, 2004; Lionello et al., 2005, 2006). The newly reconnected magnetic configuration features a folded magnetic field line topology, and Fisk & Kasper (2020) propose that this fold could propagate and become a magnetic switchback at PSP's orbit. In Figure 4.3, we illustrate the process of interchange reconnection as viewed by Fisk & Kasper (2020). In this figure, an open magnetic field line is first dragged against a closed coronal loop by global circulation in the corona (1), magnetic reconnection is then triggered (1,2) and the magnetic footpoint of the open field line changes location (2). In this view, an S-shaped switchback in the magnetic field is proposed to be launched and to propagate through the corona (3).

However, how such folds could subsist in a low-β plasma is unclear, since the tension force should rapidly remove kinks in the magnetic field lines, and variations around this mechanism have been proposed. One possibility is for interchange reconnection to generate complex structures that propagate upward in the solar atmosphere and can reverse their radial field (Zank et al., 2020; Liang et al., 2021), or to excite and launch Alfvénic wave pulses along the newly reconnected and post-reconnected open flux tube (He et al., 2021). Coronal jets

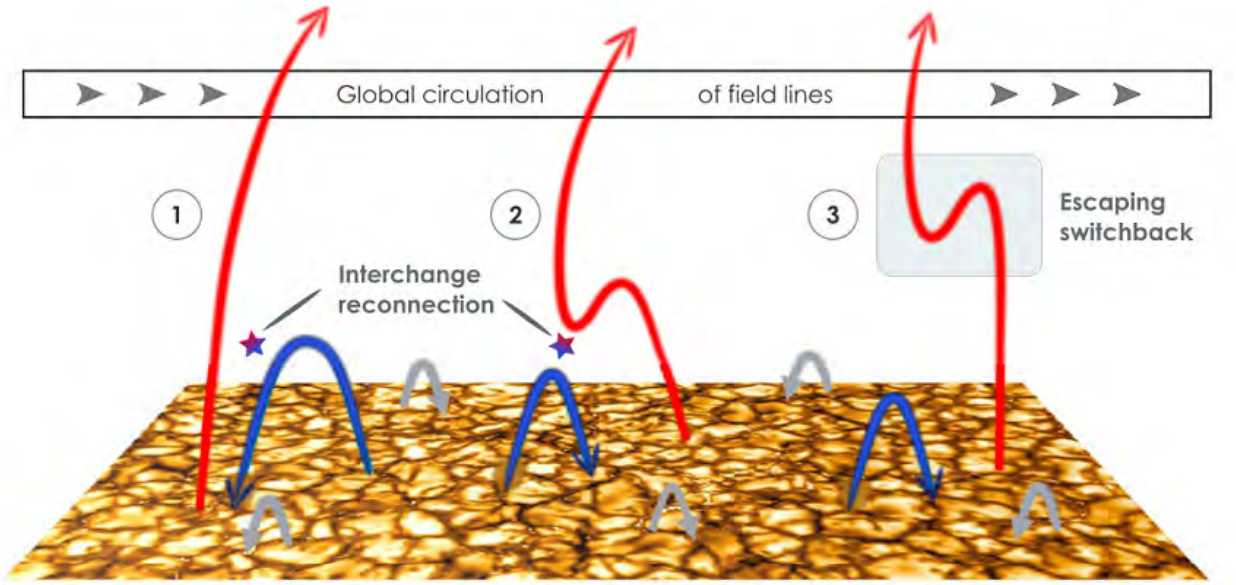

Figure 4.3: The process of interchange reconnection, adapted from Fisk & Kasper (2020).

are also considered as a source of switchbacks, with erupting mini-filaments generating an Alfvénic fluctuation that would steepen during propagation and become a switchback (Sterling & Moore, 2020). Another proposed process is that interchange reconnection may lead to a solar wind velocity gradient along open field lines. Subsequently, fast wind overcoming slower wind is able to reverse the magnetic field and create a fold beyond the Alfvén point (Owens et al., 2018, 2020; Schwadron & McComas, 2021). In a shift of perspective, switchbacks are also viewed not as simple folds of the magnetic field as in Figure 4.2, but as propagating flux ropes presenting some of the observed signatures and also resulting from interchange reconnection (Drake et al., 2021; Agapitov et al., 2022). This last process has the advantage of producing a stable structure that may subsist more easily through propagation in the solar corona and solar wind, but has not been statistically compared to the in-situ data.

All of these works assume that switchbacks are created in the low corona through magnetic reconnection. One major uncertainty with this formation process is the propagation of the structure from the high β chromosphere up to the higher corona. While Tenerani et al. (2020) find that switchbacks could survive up to PSP distances, several simulations with different assumptions find that switchbacks should unfold before reaching the orbit of PSP (Landi et al., 2006; Magyar et al., 2021a,b)

4.3 Methodology of switchback analysis

4.3.1 Different approaches

In order to discriminate between the existing formation theories, it is natural to assess their properties statistically, since observations of switchbacks in PSP data are plentiful. However, a definition problem arises from the start. Indeed, switchbacks are mainly identified as a deflection from a background magnetic field, and it is obvious that the choice of this

background field will directly affect the results one may obtain on their orientation. In the literature, various background magnetic field definitions have been used to identify switchbacks in statistical analysis and case studies, for instance:

- The radial direction (e.g. Horbury et al. (2018); Larosa et al. (2021); Akhavan-Tafti et al. (2021); Woolley et al. (2020))
- A 6h median field (Dudok de Wit et al., 2020)
- A 1h mode field (Bale et al., 2019)
- A modeled Parker spiral field (e.g.Horbury et al. (2020a); Laker et al. (2021); Fargette et al. (2021a))

Various threshold were used from 30 to 90^o, as well as additional selection criteria such as duration, field magnitude, Alfvénicity, density, etc., that are not discussed here. Two kinds of approaches are typically used. One seeks to determine the background magnetic field through post treatment of the data in an attempt to differentiate switchbacks from the background solar wind, using different statistical parameters of the magnetic field distribution like mean, median or mode values. The other consists in modeling independently the expected background field using either a radial magnetic field assumption or the Parker spiral model. All methods have caveats. If the solar wind dynamics is dominated by switchbacks over long periods, as is often the case, then it will be reflected in the mean, median and mode values of the distributions considered, with associated biases. The appropriateness of the modeling approach, on the other hand, will depend on the reliability of the model used and its potential limitations.

4.3.2 The modeled Parker spiral

Let us first introduce how we compute the Parker spiral angle as well as its associated magnetic field. The Parker spiral angle $\alpha_p(t)$ is the trigonometric angle between the radial direction and the spiral direction in the RTN plane. It is given by (Parker, 1958):

$$\alpha_p(t) = \arctan\left(\frac{-\omega\,(r(t) - r_0)}{< V_R(t) >}\right) + k\pi \tag{4.1}$$

where $\omega = 2.9 \times 10^{-6}$ s^{-1} is the Sun's angular moment taken at the equator, $r(t)$ is the distance of the spacecraft to the center of the Sun, $r_0 = 10\ R_\odot$ is the source of the Parker spiral, k is a dimensionless integer equal to 0 (anti-sunward field) or 1 (sunward field), and $< V_R(t) >$ is the processed radial speed of the solar wind measured by the spacecraft. For the analyses performed in this thesis, we used the velocity processed with a low pass filter characterized by a cutting wavelength at 2h. This allows for the removal of spurious data, as well as short timescale variations and transient structures that are not relevant to the Parker spiral angle. We then reconstruct a semi-empirical vector for the Parker spiral magnetic field $\mathbf{B_p}(t)$, contained in the RT plane while keeping the field amplitude $B(t)$ measured by PSP :

$$\mathbf{B_p}(t) = B(t) \begin{bmatrix} \cos\alpha_p(t) \\ \sin\alpha_p(t) \\ 0 \end{bmatrix}_{RTN} \tag{4.2}$$

This magnetic field is hereafter considered as the background field associated with the Parker spiral model

4.3.3 Method comparison

The backgrounds obtained through the use of the various methods presented in section 4.3.1 can vary drastically and lead to different, and sometimes contradictory, results. It is essential to have in mind that this first assumption regarding background modeling may impact results significantly. In Figure 4.4, we illustrate this fact by comparing the different structures one might consider to be a switchback based on these selection processes. We display the magnetic field components (normalised by the Sun-to-spacecraft distance r) measured by PSP in panels a, b and c during E_2, from 2019-03-29 00h to 2019-04-11 17h (centered on perihelion). PSP is here connected to the negative polarity solar hemisphere throughout the 13 days of data, and goes from 60 to 35 $R_\odot$ at perihelion. Over the data, we plot three different background fields: a purely radial magnetic field, the magnetic field expected from the Parker spiral (eq.(4.2)) and a 6h-mode magnetic field. The B_N component of the Parker field and the B_T and B_N components of the radial field are equal to zero throughout the interval. While all models seem to find a similar radial component B_R for the background field, differences arise in the B_T and B_N components, and are particularly striking in the B_T component, where the three curves are almost never equal.

In the bottom panels, we show the 2D distributions of the magnetic field components for the complete encounter (white contours) and for deviations from the background field (2D histograms). The core of the total distribution (white contours) has a non-zero B_T component, visible in panels d, f and h. This positive B_T component is consistent with the Parker spiral value also highlighted in panel b. In all the bottom panels (d to i) it is clear that the distributions of the deviations obtained through the three methods differ significantly. With the radial method, the B_T component of a modeled Parker spiral is neglected and as a direct consequence, the deviations one detects are strongly biased toward a positive B_T. By contrast the distribution 60° away from the Parker spiral includes more points with a negative B_T while keeping a preference toward a positive B_T. Finally, when we set the switchback definition 60^o away from a sliding mode, the tangential distribution of the magnetic field is even more isotropic. The B_N distributions obtained differ as well, with fairly different distributions shown in panels e, g and i.

From these plots, it is clear that we cannot define switchbacks based solely on the radial direction because the tangential component of the Parker spiral is significant. Defining switchbacks as a perturbation relative to the Parker spiral, as done by Horbury et al. (2020a), appears as the most physically motivated approach and is increasingly done in the literature. To study deviations compared to a median or mode field may also be useful in some contexts but calls for a different interpretation of the results, as one then studies rapid fluctuations compared to slower fluctuations of the field, rather than fluctuations compared to an expected model of the background solar wind. In the remainder of this work, we choose the Parker spiral as the modeled background field.

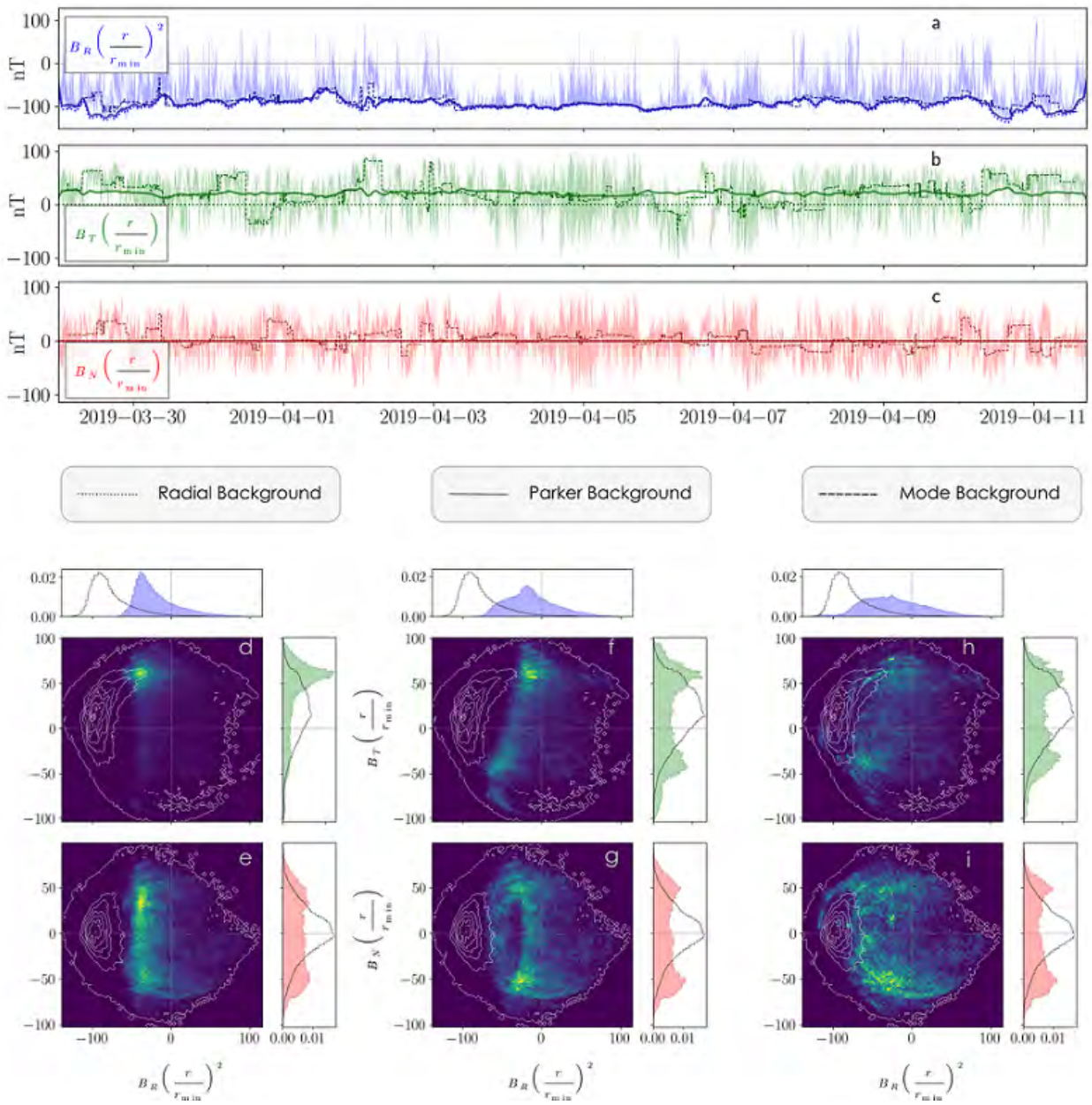

Figure 4.4: On the impact of switchback definition. Panels a, b and c show the magnetic field components in the RTN frame, normalised by the radial distance of the spacecraft to the Sun. Several background fields are over-plotted: the radial field (dotted lines), the Parker spiral field (full lines) and the 6h-mode field (dashed lines). In panels d to i, we plot in white the 2D distribution contours of the normalised magnetic field components (B_R, B_T) (panels d, f, i) and (B_R, B_N) (panels (e, g, h). Superimposed, are the 2D histograms of the points that are located more than 60^o away from the computed background fields, i.e. the radial direction (d, e), the Parker spiral (f, g) and the 6h-mode vector (h, i). The colorscale represents the number of samples in each bin and we also add the normalized projected distributions on the side, as a black line for the full 2D distribution and color-shaded for the "more than 60^o away" points.

In this chapter, we described the characteristics of magnetic switchbacks, as well as their numerous associated mysteries. To paraphrase the youtube channel Surprising Science[1], *"the creativity of theoreticians knows no limit"*. As such, the formation processes devised to explain the observation of magnetic switchbacks are legions. In the following chapters, we present two statistical studies focusing on discriminating between the potential formation processes of magnetic switchbacks.

[1] Surprising Science, a crisis in cosmology ?

Chapter 5

Characteristic scales of magnetic switchback patches near the Sun

Contents

In this chapter, we investigate the temporal and spatial characteristic scales of magnetic switchback patches. We define switchbacks as a deviation from the nominal Parker spiral direction and detect them automatically for PSP encounters 1, 2, 4 and 5. We perform a wavelet transform of the solid angle between the magnetic field and the Parker spiral and find periodic spatial modulations with two distinct wavelengths, respectively consistent with solar granulation and supergranulation scales. In addition we find that switchback occurrence and spectral properties seem to depend on the source region of the solar wind rather than on the radial distance of PSP. These results suggest that switchbacks are formed in the low corona and modulated by the solar surface convection pattern. This chapter is mainly a transposition from Fargette et al. (2021b), with some additional explanation regarding the methodology used.

5.1 Motivation

One main hypothesis discussed in this chapter is that if switchbacks are formed close to the solar surface as proposed by for instance Fisk & Kasper (2020), Drake et al. (2021) or Schwadron & McComas (2021), then they are probably affected - if not caused - by physical phenomena that impact the structure of the low corona. This includes structures related to active regions (coronal loops, prominences, that may erupt into flares or coronal mass ejections), coronal bright points and plumes, spicules (Meyer-Vernet, 2007), as well as the convective motions at the Sun's surface observed as granulation (Nordlund et al., 2009) and supergranulation (Rieutord & Rincon, 2010). The latter are indeed believed to play

a role in heating and accelerating the solar wind, as surface convection generates Alfvén waves that propagate along magnetic field lines, and some dissipate in the higher corona for instance through turbulent cascade and wave-particle interactions (e.g. Velli et al. (1989), Cranmer et al. (2007), van Ballegooijen & Asgari-Targhi (2016)). Interchange reconnection as proposed by Fisk & Kasper (2020) would also occur at or near the supergranular network, as indeed the closed and open field lines involved should have magnetic footpoints rooted in the network, which in turn outlines the boundaries of supergranules (Roudier et al. (2009); Rieutord & Rincon (2010), see also section 1.3.1 and Figure 5.7). Finally, in earlier work on Helios Data, Thieme et al. (1989) found structures in the solar wind density and velocity that were consistent in angular size with supergranulation, suggesting that its signature can be detected in the solar wind up to 0.7 AU.

In this work we investigate typical temporal and spatial scales associated with the switchback phenomenon through wavelet transforms, that could hint to a specific formation process. Our results mainly concern the in-situ modulation (patches) of switchback occurrence, hence corresponding to a larger scale phenomenon than individual magnetic switchbacks. In section 5.2, we present the different data products and detail the process of switchback identification, as well as the spatial projection and the spectral analysis we perform. In section 5.3, we first focus on E_5 and perform both temporal (5.3.3) and spatial (5.3.4) wavelet analyses on switchbacks for a 5.1-day interval. We then present the spatial analysis of E_2 in a similar manner (5.3.5). Finally in section 5.4 we discuss scales associated with potential formation processes, in particular those related to solar wind turbulence and solar convection patterns.

5.2 Method

5.2.1 Data analysis

We analyze magnetic field data provided by the FIELDS instrument suite and particle data provided by SPC from the SWEAP instrument suite (section 1.4). We focus on data taken by PSP below 60 $R_\odot$ during encounters 1, 2, 4 and 5 (thereafter noted E_x) with an emphasis on E_5 and E_2 (see table 1.1). We do not consider E_3 as SPC data were not available for most of the encounter. In order to discard high frequency kinetic effects, as well as to reduce instrumental noise, we re-sample all data products from SPC and FIELDS to a constant time step taken at 2 seconds (Dudok de Wit et al., 2020). The sampling is done by using a 1 dimensional B-spline interpolation, a method available through the scipy.interpolate package in Python (Dierckx, 1993).

5.2.2 Switchback definition and identification

To identify switchbacks in a systematic manner, we define them as a deviation from the Parker spiral, as explained in section 4.3. We use eq. (4.1) and (4.2) to compute the Parker spiral angle $\alpha_p(t)$ and the associated background field $\mathbf{B_p}(t)$. We then define the normalized solid angle $\widetilde{\Omega}$ between $\mathbf{B_p}$ and $\mathbf{B}$ (Dudok de Wit et al., 2020), given by:

$$\widetilde{\Omega}(t) = \frac{1}{2}\left(1 - \cos\gamma(t)\right) \tag{5.1}$$

with

$$\cos\gamma(t) = \frac{\mathbf{B_p}(t)\cdot\mathbf{B}(t)}{B(t)^2} \tag{5.2}$$

$\widetilde{\Omega}$ reflects whether both vectors are aligned ($\widetilde{\Omega} = 0$) or diametrically opposed ($\widetilde{\Omega} = 1$). Switchbacks can then be detected automatically by setting a threshold on $\widetilde{\Omega}$. This threshold will necessarily impact our results, and it has been taken in the literature at $\widetilde{\Omega} = 0.15$ ($\gamma = 45^o$) (Macneil et al., 2020), or $\widetilde{\Omega} = 0.07$ ($\gamma = 30^o$) (Horbury et al., 2020a). One may also take $\widetilde{\Omega} = 0.5$ ($\gamma = 90^o$) to be consistent with the very idea implied by the name "switchback" (a reversal of the radial magnetic field component). We add an additional detection condition that five consecutive points are needed to detect a switchback, this means that our study can only address timescales longer than 10 seconds. This is motivated by the fact that wave activity is present within switchbacks, and may lead to several crossings of the threshold line within one switchback.

The accuracy of this method depends on the adequacy of the Parker spiral model to represent the undisturbed magnetic field. Thus, in our study we discard intervals identified as heliospheric current sheet crossings and plasma sheets (see Szabo et al. (2020) and Lavraud et al. (2020) for E_1), MICCS structures (Fargette et al., 2021a), CMEs (Nieves-Chinchilla et al. (2020), Korreck et al. (2020)), as well as periods of strahl drop out where magnetic field lines are most likely disconnected from the Sun (Gosling et al., 2006). All of these intervals are identified visually while scanning through the data, and are given in the appendix of Fargette et al. (2021b).

5.2.3 Space-time bijection

To study potential spatial scales associated with switchbacks, we need to transform the PSP time series into functions of a given spatial parameter. This might be achieved by different methods with varying degrees of complexity, for instance by

- directly taking the Carrington longitude of the spacecraft
- computing the Parker spiral footpoint coordinates (Rouillard et al., 2020a; Bale et al., 2021)
- calculating its connectivity coordinates with Potential Field Source Surface (PFSS) (Badman et al., 2020)
- performing MHD simulations (Réville et al., 2020).

In this study, we chose not to use a ballistic projection of the Parker spiral on the Sun's surface, as it is poorly suited for spectral analysis. Indeed, when the radial velocity of the solar wind changes, the spiral footpoint can turn around, hence losing the one-to-one correspondence between time and space and folding the signal over itself. Instead, we decided to use a direct projection of the spacecraft path on the Sun's surface, using the angular displacement s defined by:

$$s(t) = \int_0^t ds \tag{5.3}$$

and

$$ds = \sqrt{d\theta^2 + \cos^2\theta\ d\phi^2} \tag{5.4}$$

where θ and ϕ are the Carrington latitude and longitude of the projected orbit over time. We also resample the data over a constant spatial step taken as $ds = \max(s)/N_{point}$. This way, we keep a similar number of measurement points N_{point} between the spatial and temporal analysis. To convert s to regular distances, one only needs to multiply it by the considered radius.

This choice of metric ensures a bijection between time and space, and takes into account the variation in both latitude and longitude. We note, however, that with this projection s we make the assumption that when PSP remains within a given source area on the solar surface, the displacement of its footpoint is equivalent to the assumed displacement of the spacecraft projection. We discuss limitations in section 5.4.4.

5.2.4 Wavelet analysis

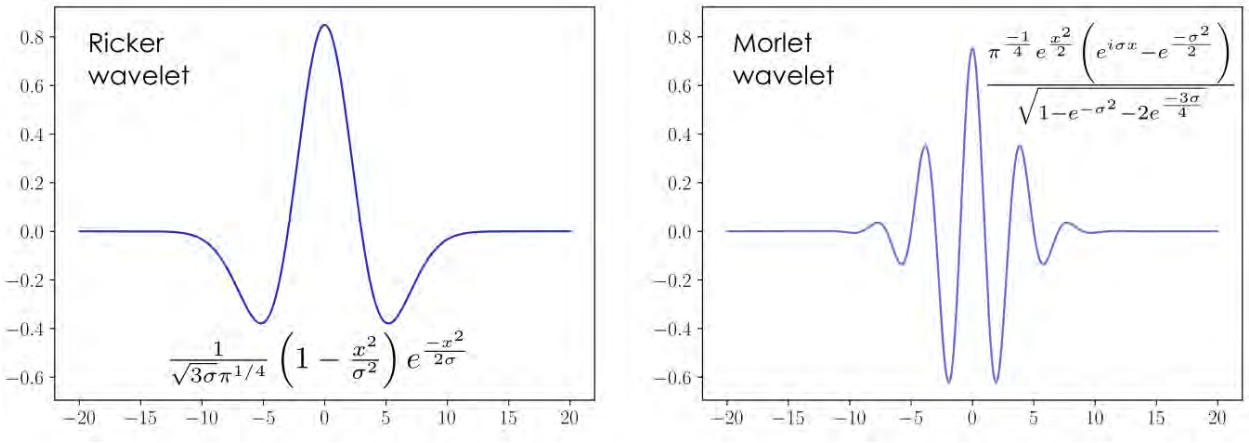

Figure 5.1: Illustration of the Ricker and the Morlet wavelets.

In our analysis, we use a wavelet transform to determine the significant frequencies of our considered signal. Contrary to the Fourier transform which is a purely spectral analysis, a wavelet transform includes a temporal dimension. The signal is convoluted by a localised semi-periodical function - called a wavelet - which is characterised by two parameters : its scale and its localisation. By changing the wavelet scale, one investigates the significant frequencies of the signal at a given localisation; and by shifting the localisation, one may then characterise the complete signal. This process adds a dimension compared to the Fourier transform, which only allows to change the signal scale. We display in Figure 5.1 two examples of wavelet functions, the Ricker wavelet (also called the 'Mexican hat' wavelet) and the Morlet wavelet. In this work, we use the Morlet wavelet similarly to Torrence & Compo (1998).

5.3 Identification of characteristic scales

5.3.1 Illustration of encounter 5

In Figure 5.2, we display PSP data taken throughout E_5. B scales as r^{-2} and reaches 137 nT at perihelion on 2020-06-07 08:20. The polarity is negative until the HCS crossing

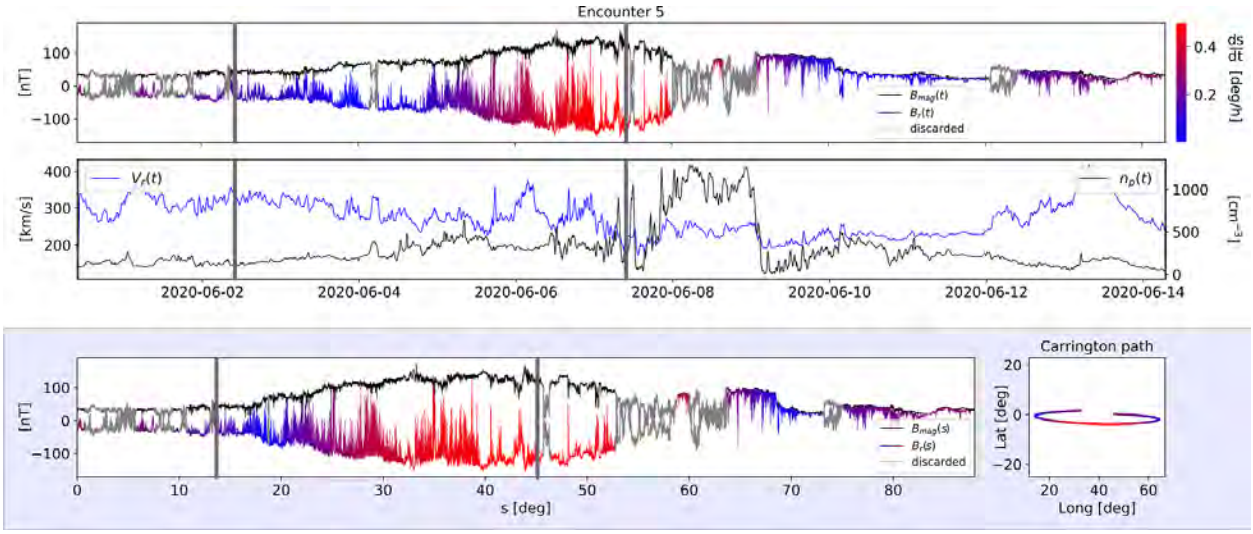

Figure 5.2: E_5 context. *a*) Magnetic field amplitude B and radial component B_R, which is color coded by the spacecraft absolute velocity with respect to the solar surface, ds/dt in degree/hour (see text for details). Grey data denote intervals that are discarded because they are irrelevant to the switchback study. Vertical grey lines indicates the region analysed. *b*) Solar wind radial velocity V_R and ion density n_p averaged over 30 minutes; *c*) B and B_R are displayed in the same manner as in panel *a* but now as a function of the angular distance s, *d*) PSP trajectory projected in Carrington coordinates and color coded with ds/dt.

(from 2020-06-08 00:00 to 2020-06-09 01:40) and remains positive thereafter. The spacecraft is sampling slow solar wind below 420 km/s with an average value of 274 ($\pm$ 46) km/s. The density increases as expected during plasma sheet and HCS crossings, reaching up to 1200 cm^{-3}. Outside these intervals, n_p scales as r^{-2} and reaches around 400 cm^{-3} at perihelion. To illustrate the spatial projection we perform, B_R in panel 5.2*a* is color coded with the absolute speed of the spacecraft relative to the Sun's surface, defined in equation 5.4. In Figure 5.2*c*, B and B_R are plotted relative to s with the same color scale, and Figure 5.2*d* displays the path of PSP on the Sun's surface in Carrington coordinates. Logically, periods of co-rotation (in blue) are shortened in the spatial representation (5.2*c*) compared to the temporal one (5.2*a*).

We now restrict our analysis to the period comprised between 2020-06-02 09:10 and 2020-06-07 11:00 (vertical lines in Figure 5.2). This interval is indeed characterized by persistent and stable patches of switchbacks, and the frequency analysis performed next requires a signal as continuous as possible. The succession of strahl drop outs and flux ropes before 2020-06-02 09:10 or the HCS crossing after perihelion would bias our analysis. We also consider in this case that the plasma sheet observed around 2020-06-04 04:30 is sufficiently small to be included in our signal. Overall we are studying 5.1 days of data, covering 32.1° of angular distance with a constant spatial step of $ds = 1.5 \times 10^{-4}$ degrees. In Figure 5.3, we display the temporal analysis of switchbacks over the selected time period.

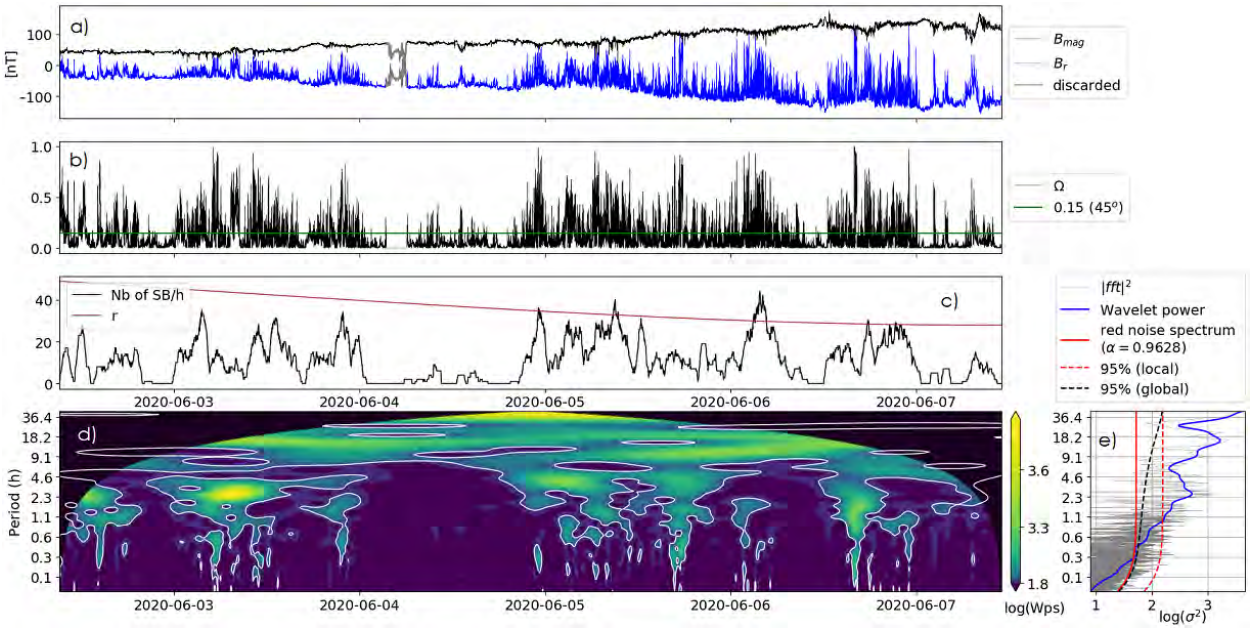

Figure 5.3: Temporal analysis for E_5. *a*) B and B_R plotted as a function time; *b*) the solid angle $\widetilde{\Omega}$ with a horizontal green line indicating the switchback detection threshold set at 0.15 (45°) (during the 2-hour partial heliospheric plasma sheet crossing (in grey in panel 5.3*a*) $\widetilde{\Omega}$ is set to zero); *c*) the number of switchback detected per hour together with r the radial distance of PSP to the Sun; *d*) Wavelet Power Spectrum (WPS) of $\widetilde{\Omega}$ performed over periods of 0.08 to 42.6 h and represented in a logarithmic color scale, where white contours represent the local 95% confidence level. The blackened area denotes the cone of influence where the WPS is affected by edge effects and is not relevant; *e*) FFT of $\widetilde{\Omega}$ in light gray, integrated WPS in blue, theoretical red noise spectrum in red, 95% local confidence level in dashed red and global 95% confidence level in dashed black (units similar to panel *d*).

5.3.2 Radial dependence of switchback occurrence

The number of switchbacks (5.3*c*) is on average 11 h^{-1} over this whole 5.1-day period. Even though r decreases from 50 to 28 $R_\odot$, the number of switchbacks does not seem to follow a conjugate decrease. During the patches occurring on June 3, r decreases from 45.2 to 39.6 $R_\odot$ and the average switchback frequency is 14.8± 7.6 h^{-1}. On the other hand from June 5 to June 7, r decreases from 34.4 to 28.0 $R_\odot$ and the average switchback frequency is of 15.2 ± 9.0 h^{-1}. We also observe that following the plasma sheet observed on June 4, and preceding the one observed on June 7 (not shown, cf Figure 5.2), the number of switchbacks drops significantly below 5 h^{-1}on average. This suggests that the number of switchback detected with our method is uncorrelated to the radial distance during this period, and is by contrast sensitive to the plasma environment and spacecraft connectivity.

5.3.3 Temporal spectral analysis

To further investigate the possible timescales associated with switchbacks we perform a wavelet analysis on the solid angle $\widetilde{\Omega}(t)$ based on Torrence & Compo (1998). One difference with Torrence & Compo (1998) is that we do not detrend our data (i.e. we do not substract

the low-frequency component to our signal) as advised by Auchère et al. (2016) for instance. We use a Morlet wavelet as a mother wavelet (see Figure 5.1), and all spectra are hereafter normalized by $N_{point}/(2\sigma^2)$, σ^2 being the data variance. We display the wavelet power spectrum (WPS) of the signal in panel 5.3*d* with a logarithmic colormap, for periods from 5 minutes (150**dt*) to 42.6 hours (one third of the considered period). We investigated below the 5 minute scale but found no distinct wavelength that stood out in the WPS. This is consistent with previous results showing that individual switchbacks seen by PSP do not display any preferential duration. As done by Torrence & Compo (1998) we use a red noise model as a background spectrum based on the lag-1 autoregressive process, and find a correlation coefficient of α=0.9628.

Figure 5.3*e* shows that several timescales are detected through this interval. At large scales, the WPS first peaks at a period between 13h and 18h, these periods correspond to the duration of the three large patches of switchbacks visible by eye in panel 5.3*b* on June 3. Then from June 5, the large scale period is less well defined but increases from 8h to 18h by the end of June 6. At shorter periods, the most visible feature occurs on June 3 where a large switchback dominates the spectrum and a periodicity of 2 to 5 hour is present, producing a broad peak in the global wavelet power (5.3*e*). This wavelength persists on the beginning of June 5 and there corresponds to the duration of small patches of switchbacks. Overall, some significant wavelengths arise locally throughout the 5.1 day interval, but they are not particularly coherent or well organized. We nevertheless observe that patches of switchbacks last from 5 to 18 hours. The next section supports that when analyzed spatially the signatures are more consistent.

5.3.4 Spatial spectral analysis

To identify potential spatial scales associated with magnetic switchbacks, we repeat the analysis of section 5.3.3 but as a function of s (see section 5.2.3). We display the results in Figure 5.4 in the same manner as Figure 5.3. In panel 5.4*c* we plot the number of SB for a spatial window of 0.26°, this value is consistent with the 1h scale shown in Figure 5.3. The spectral analysis is performed on scales from 0.02 deg (150**ds*) to 10.7 deg (one third of the considered interval). Regarding the red noise model we find a correlation coefficient of α=0.9804.

A striking feature in the number of switchbacks in panel 5.4*c* is that marked periodicities arise in the signal, most visible between $11^o < s < 13.5^o$ and $22^o < s < 25.5^o$ (wavelength of 0.5°), and $3^o < s < 5^o$, $6^o < s < 10^o$ and $20^o < s < 22^o$ (wavelength of 1°). Of course this observation depends strongly on the scale of 0.26° chosen here. Since we did not include a hysteresis in our detection, this regularity can be attributed to fluctuations of $\mathbf{B}$ around the chosen threshold of $\widetilde{\Omega} = 0.15$. Nonetheless it is the signature of a possible periodicity that we investigate further through the wavelet transform of $\widetilde{\Omega}(s)$ (5.4*d*).

Overall the WPS over s highlights spatial scales that were not clearly present in the temporal analysis. First we can see that the three main patches of switchbacks visible to the eye in panel 5.4*b* from $s = 5^o$ to $s = 27^o$ have the same scale in order of magnitude. This is quantified by the WPS reaching its maximum consistently through the spatial series (5.4*d*) and coincident with a peak in the integrated WPS (5.4*e*) between periods of 2.6° and 10.7°. Moreover, significant power is found at scales comprised between 0.3° and 1.6°, particularly

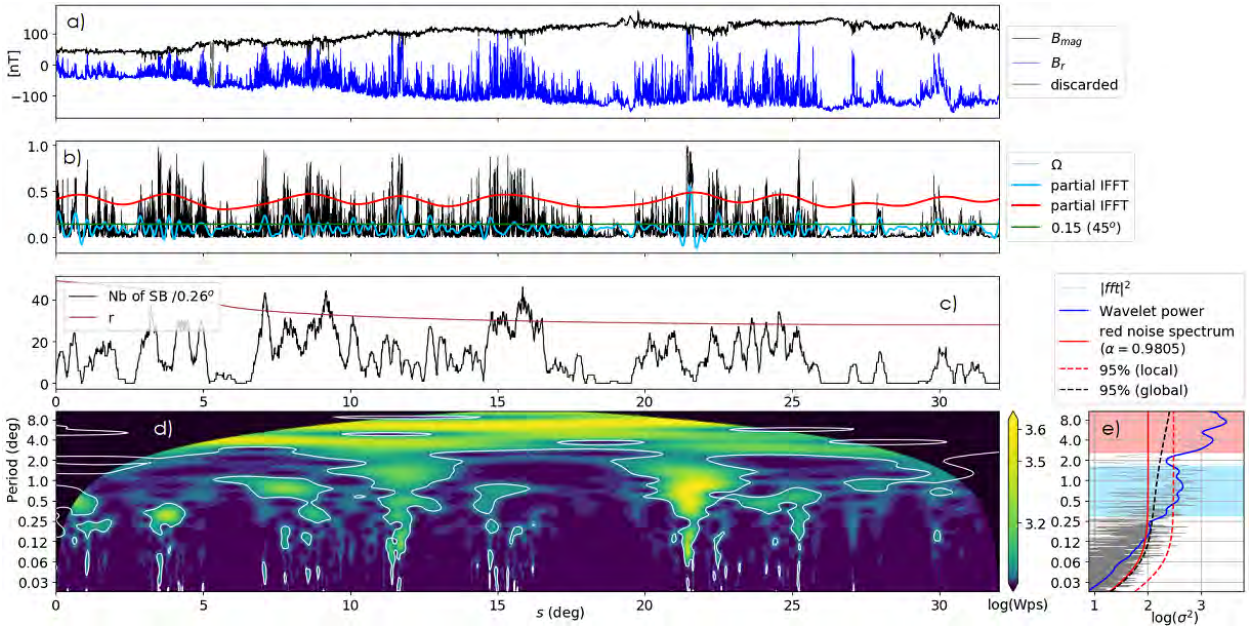

Figure 5.4: Spatial analysis for E_5 *a*) B and B_R plotted as a function of the angular displacement s, *b*) the solid angle Ω with the horizontal green line indicating the switchback detection threshold set at 0.15 (45°), and partial inverse FFT of the peaks highlighted in panel *e* are over plotted, *c*) the number of switchbacks detected per 0.26° together with r the radial distance of PSP to the Sun, *d*) Wavelet Power Spectrum (WPS) of Ω performed over periods of 0.02 to 10.7° and represented in a logarithmic scale. White contours represent the local 95% confidence level, *e*) FFT of Ω in light gray, integrated WPS in blue, theoretical red noise spectrum in red, 95% confidence level to the local spectrum in dashed red and 95% confidence level to the global spectrum in dashed black, while peaks in the FFT are highlighted in light red and light blue.

for $6^o < s < 10^o$ (wavelength of 0.8°) and for $22^o < s < 25.5^o$ (wavelength of 0.5°). This is consistent with the periodicity previously observed in panel 5.4*c*. The two peaks detected are broad, separated by one order of magnitude, and not always coincidental, meaning that the higher frequency one is unlikely to be a harmonic.

To further stress these wavelengths in the signal, we overplot in panel 5.4*b* the inverse of the signal's truncated Fourier transform, selecting only the peaks located between wavelength 0.3° and 1.6° (shaded in blue in panel 5.4*e*) and 2.6° and 10.7° (shaded in red in panel 5.4*e*). These partial inverse Fourier transform (IFFT) are translated upward in the panel by a constant value for clarity. They follow nicely the solid angle fluctuations for large (red) and meso-scale (light blue) patches.

What is remarkable in these spectral features is that the detected periodicity lasts for several wavelengths and they are moreover consistently observed throughout E_5 (see appendix of Fargette et al. (2021b)). These results indicate that significant periodicity may arise locally in the magnetic field fluctuations. Comparison of these scales to physical phenomena are discussed in section 5.4.

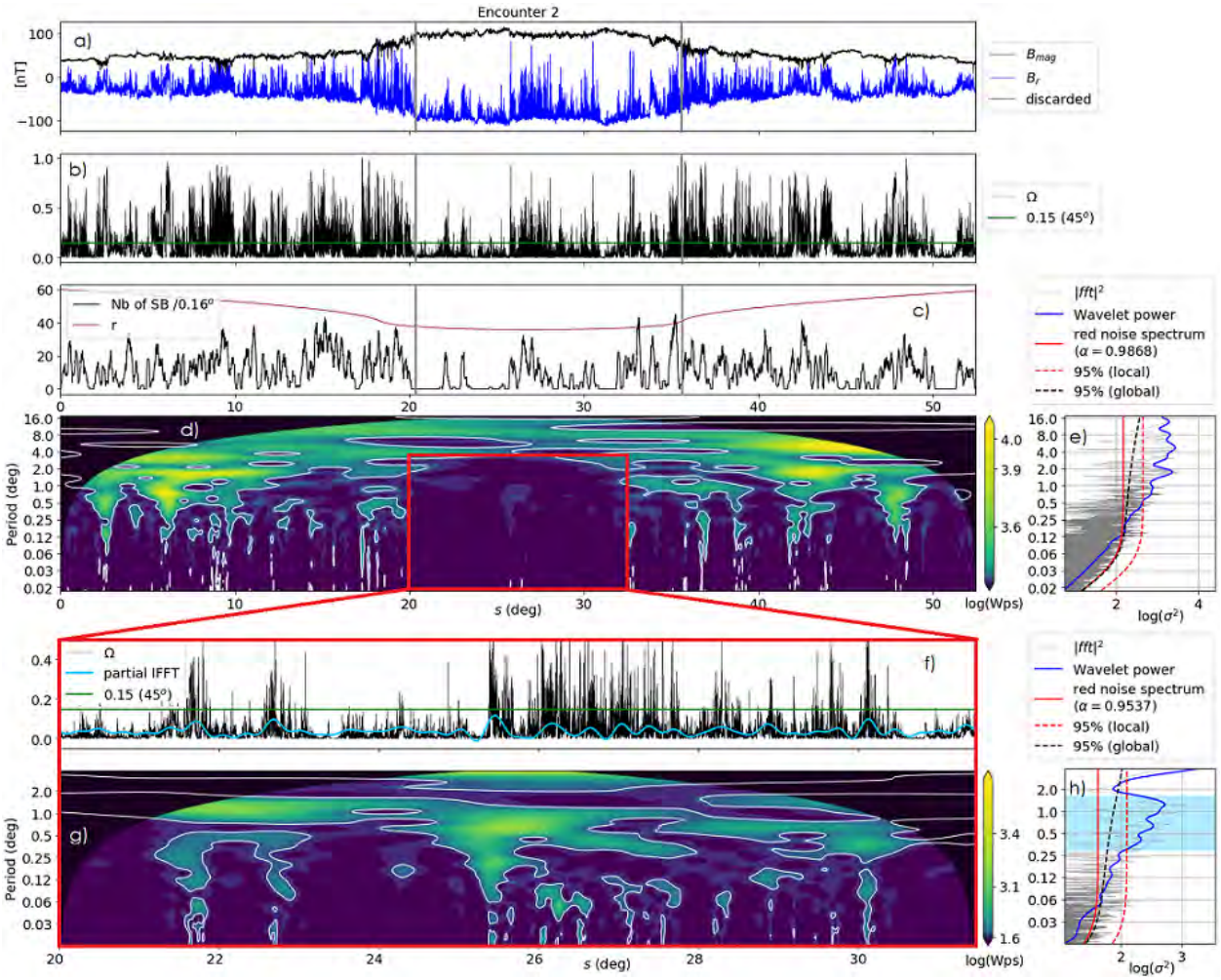

Figure 5.5: Spatial analysis for E_2. We plot the parameters in the same manner as in Figure 5.4 for panels a to e. The vertical grey lines at $s = 20.3°$ and $s = 35.6°$ denotes the change in plasma properties between streamer and coronal hole plasmas (see text for further details). In panels f to h we present a zoom-in on the red rectangle indicated in panel d. We display in panel f the solid angle $\widetilde{\Omega}$ with a green horizontal line for switchback threshold detection. The light blue curve represents the inverse Fourier transform of the peak visible in panel h between 0.3° and 1.6° shaded in light blue. In panel g and h we display the WPS and Fourier transform in the same manner as in panels d and e.

5.3.5 Extension of the results to encounter 2

In this section we highlight some interesting features of the spatial analysis performed for E_2. This flyby of the Sun is particularly relevant because for one the observation of switchbacks is not interrupted by HCS crossings, CMEs or too frequent strahl dropouts, and in addition the spacecraft samples two different types of solar wind (Rouillard et al. (2020a), Griton et al. (2021)). Until April 3, 2019 09:00 UT and from April 7, 2019 18:00 UT, PSP is sampling a high density slow solar wind that Rouillard et al. (2020a) associate with streamer belt plasma through a white light imaging analysis. In between these dates it scans a lower density solar wind more probably associated with a coronal hole.

In Figure 5.5 we display the spatial analysis for E_2 as done in Figure 5.4 (panels a to e). This represents 15 days of data and 52° covered. Vertical gray lines separate the regions identified by Rouillard et al. (2020a) in panels a, b and c. In panel 5.5c we observe that the number of switchbacks decreases in the coronal hole around perihelion. In streamer belt plasma, no obvious trend is visible while r vary significantly. This is consistent with section 5.3.2, where we find that switchback occurrence is sensitive to the plasma environment. Furthermore, it is obvious in panel 5.5d that spectral properties are different between the different types of plasma. In both intervals of streamer belt plasma, two peaks are detected with scales of respectively 2° and 5°. By contrast in the coronal hole, no significant structures is visible below 4°. This suggests that the fluctuation properties differ with the solar wind source. We renew the analysis on the area highlighted with a red rectangle in panel 5.5d, during which PSP covers 12° (lower panels f to h). We find that a periodicity between 0.3° and 1.6° is strongly present, further confirming our result for E_5. As before we overplot in panel 5.5f the IFFT of this peak (shaded in light blue in panel 5.5f), that follows closely the solid angle mid-scale fluctuations as in Figure 5.4b.

5.4 Consequences on current formation theories

The full time window wavelet analyses of the encounters 1, 2, 4 and 5 are available in the appendix of Fargette et al. (2021b), both over time and space. They are consistent with the above findings, the most striking periods being the ones detailed in sections 5.3. We now compare the observed scales to those expected from potential formation process.

5.4.1 Turbulent generation of switchbacks

It has been proposed that switchbacks may form as the solar wind evolves, being produced by turbulence or velocity shears (Squire et al. (2020), Ruffolo et al. (2020)). This is supported by the studies of Mozer et al. (2020) and Macneil et al. (2020) who found that the occurrence of switchbacks increases with radial distance from the Sun r. While we cannot conclude on switchback occurrence at radial distances greater than 60 $R_\odot$, our analysis suggests that it is unrelated to heliocentric radial distance near Sun (see sections 5.3.3 and 5.3.5). This is also visible in all encounters (see plots in the appendix). This is at odds with Mozer et al. (2020)'s results which were based on the comparison of two days of data. Based on our analysis and its extension to four encounters, we rather propose that the occurrence of switchbacks depends on the solar wind properties and origin.

In a wider perspective, the solar wind turbulent cascade in magnetic fluctuations is expected to behave as a rather smooth power law of exponent between $-3/2$ and $-5/3$ in the inertial range, and as a -1 power law at lower frequencies (Matteini et al. (2019), Chen et al. (2020), Dudok de Wit et al. (2020)). In our temporal analysis (Figure 5.3), the significant periods we detect start from 2 h, and are well below the break frequency of 0.001 Hz ($\sim$ 17 minutes) found by Dudok de Wit et al. (2020). They more likely correspond to large spatial structures in the injection scales above the inertial range. We thus suggest that the modulation of the signal in large patches of switchbacks (3° - 9°) and the remarkable intermediate scale modulation (0.3° - 1.6°) are not part of the turbulent cascade, although they may contain significant energy available for the turbulence cascade.

5.4.2 Comparison to granulation and supergranulation

The Sun's supergranulation structure and dynamics are not well understood as of today. Using either dopplergrams, tessellation techniques or helioseismology, its typical spatial scale is consistently found around 30 Mm, with a distribution in size ranging from 20 to 75 Mm (Rieutord & Rincon (2010) and references therein). This range corresponds (by dividing by the Sun's radius) to a typical angular size 1.6° to 6.2°. Solar granulation is well explained by convective heat transport at the Sun's surface, and presents a typical scale of 1 Mm which yields a 0.08° angular size (Nordlund et al., 2009). The lifetimes of supergranules and granules are respectively around 24h and 10 minutes. Finally, what has sometimes been coined as mesogranulation with an intermediate scale, is now believed to be an artefact of detection techniques (Matloch et al., 2009; Rieutord et al., 2010).

In our work, we find significant power in the fluctuation WPS for spatial scales comprised between [0.3° - 1.6 °] and [2.6° - 10.7°] both in E_5 (5.4) and E_2 (5.5). At a first glance, our values are larger than those of granulation [0.08°] and supergranulation [1.6° - 6.2°]. Under the assumption that there is a link between the scales we find and those of granulation and supergranulation, this discrepancy may be explained by the spacecraft connectivity. In our analysis we use the raw projection of the spacecraft position on the Carrington map, hence landing around the equator. However, latitude plays a role when converting distance covered on a flat map to distance covered on a sphere, as highlighted in equation 5.4. To estimate the actual latitude where PSP is connected, we use the connectivity tool developed by the *Solar Orbiter Data Analysis Working Group* (MADAWG) (Rouillard et al., 2020b) and accessible at this website[1], tracing field lines to the Sun with PFSS (potential field source surface) modeling. We thus determine that throughout the interval we study for E_5, the spacecraft is most probably connected to a latitude between -33° to -57° as indicated in Figure 5.6. When we run our analysis with s computed at a 40° latitude, our characteristic scales for E_5 become [0.2 - 1.3]° and [2.0-8.3]°

In addition, it may be argued that the super expansion of the solar wind can lead to an underestimation of expected convection scale sizes at the spacecraft. To assess this we use the connectivity tool cited above with ADAPT magnetograms to determine $B_\odot$ the solar surface magnetic field, which is plotted over time in Figure 5.6*a*. We compare it to the value measured by PSP $|B| \left(\frac{r}{r_\odot}\right)^2$ (in black in panel 5.6*a*) and derive the expansion factor

[1] http://connect-tool.irap.omp.eu/

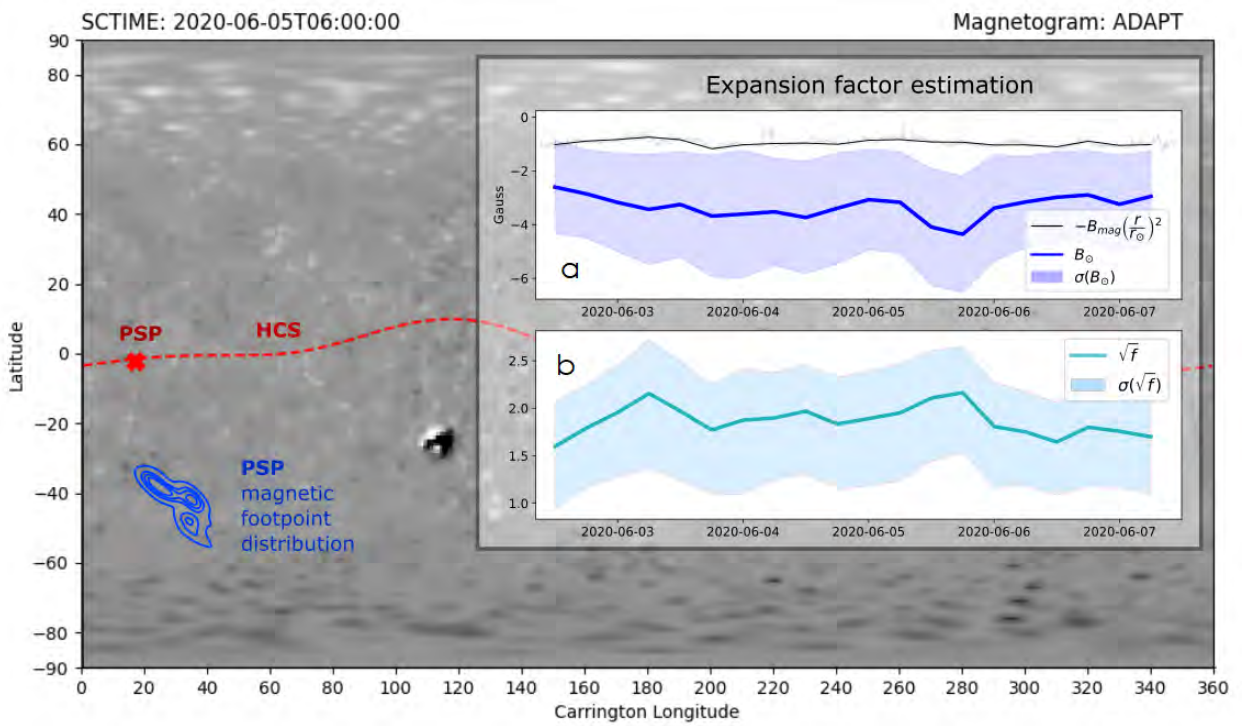

Figure 5.6: Connectivity analysis performed with the MADAWG connectivity tool[1], displaying in blue the distribution of PSP magnetic footpoints over the 5.1-day period analyzed for E_5, with an ADAPT magnetogram as a background for context. In panel *a*, the footpoint magnetic field measured over time (solid blue) with its uncertainty (blue shade), and compared to the one measured by PSP (in black). The square root of the derived expansion factor is then plotted over time in panel *b* with its uncertainty (light blue shade).

Expected scales	**granulation** (°)	**supergranulation** (°)
	0.08	[1.6 - 6.2]
Detected scales	**medium** (°)	**large** (°)
0° lat	[0.3- 1.6]	[2.6 - 10.7]
40° lat	[0.2- 1.3]	[2.0- 8.3]
40° lat + expansion	[0.12- 0.7]	[1.1 - 4.4]

Table 5.1: Summary of detected scales and expected scales for granulation and supergranulation under various assumptions. All values can be converted to Mm by converting to radians and multiplying by $r_\odot$

$f = \frac{B_\odot}{|B|}\left(\frac{r_\odot}{r}\right)^2$ (e.g. Stansby et al. (2021)), which is on average 3.5±2 over this period. Since f is a ratio between surfaces and considering that we compare characteristic lengths, our detected scales should be divided by a factor $\sqrt{f} = 1.9 \pm 0.6$ (panel 5.6*b*) to be compared to surface processes, yielding [0.12 - 0.7]° and [1.1 - 4.4]°. All of these values are summarized within table 5.1 and can be converted to Mm by converting to radians and multiplying by $r_\odot$. We conclude that the large scales we detect for switchback patches are compatible with

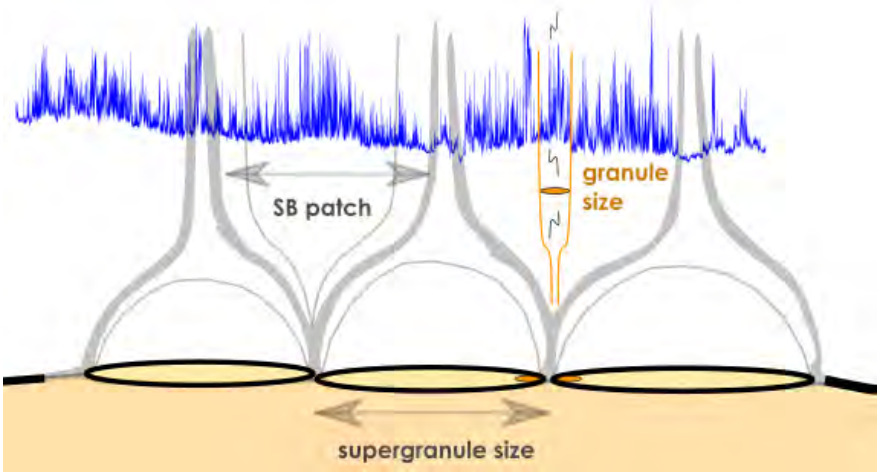

Figure 5.7: Illustration of switchback modulation by granules and supergranules, with the quantity $B_R(s)$ (E_5) overplotted in blue for clarity. Grey lines denote magnetic field lines, with thicker ones indicating the separation between closed and open field lines

supergranulation scales, and that the smaller scales remain slightly larger than granulation size.

5.4.3 Proposed origin of switchback patches

The modulation of switchback occurrence in patches matching the supergranulation scales and to a lesser extent the granulation scale, leads us to believe that at least significant part of the observed switchbacks are produced in the low atmosphere of the Sun. Their occurrence frequency may then indeed be spatially structured by granules and supergranules, as open field lines are rooted at their boundaries. It is interesting to note that Thieme et al. (1989) found signatures of spatial variations between 2 and 8° in Helios data between 0.3 and 1 AU, though they analyzed variations in density and velocity rather than magnetic field fluctuations. They also underline that the spatial signatures they found were clearer below 0.7 AU, suggesting a solar origin and making a parallel to solar supergranulation. In future work it would be of interest to see if a similar variation in plasma parameters is seen by PSP in association with switchback patches.

We propose an illustration that associates spatial scales of patches and surface structures in Figure 5.7. We observe in addition that the background B_R is modulated by the supergranular size, which may be consistent in the overall change in expansion factor within supergranules. The fact that granulation and supergranulation are omnipresent at the Sun's surface while calm solar wind periods devoid of switchbacks are sometimes observed by PSP (Bale et al., 2019; Dudok de Wit et al., 2020; Malaspina et al., 2020) is not in contradiction with our result. Indeed, if convection modulates the switchback phenomenon, switchback generation itself might still depend on local surface conditions that remain to be determined, and it is also possible that temporal dependencies arise in their formation and contribute to the observed trends (although a fortuitous correlation with granular and supergranular scales appears unlikely). The solar wind evolution to PSP might also damp the switchbacks in some places, for yet unknown reasons. The lifetime of granules and supergranules are not relevant in this view, as they would not affect the spatial scales of patches detected by

PSP. To conclude, we believe that the fluctuations we observe in switchback occurrence are a superposition of several phenomena: high-frequency fluctuations generated at the Sun's surface either through interchange reconnection or by turbulent processes, and larger scales spatial modulations by both supergranulation and granulation, both seen if looking at Figure 5.7.

5.4.4 Limitations

In this work, we use the direct projection of the spacecraft orbit on the Carrington surface of the Sun to determine the spatial projection of our data. This relies strongly on the hypothesis that the magnetic footpoints of PSP all follow a similar and linear path, and this is of course not fully adequate as the connection jumps from one source region to another. It is also possible that while the spacecraft skims the edge of a coronal hole, jumps in longitude or latitude occur. To avoid these pitfalls we focused on intervals where, based on in-situ measurements, PFSS modelling, white light analysis and past work, the spacecraft was thought to remain connected to the same source region. Instead of a direct spatial projection we also could have used a ballistic projection of the Parker spiral on the Sun's surface. This technique, however, is poorly suited for spectral analysis, as while the radial velocity of the wind changes, the spiral footpoint can turn around, hence losing the bijection between time and space and folding the signal over itself. In addition, Figure 5.2 shows that at least for E_5 the velocity is not changing much during the interval, making the use of Parker spiral connectivity most likely of little impact.

Another point that is not taken into account with our method is that if the source to which PSP is connected has a limited size, like the small equatorial hole in E1 (Bale et al., 2019; Badman et al., 2020), the resulting footpoint path could be significantly smaller than the projected orbit. This is actually consistent with the spatial analysis performed over E1 (appendix of Fargette et al. (2021b)) where both the large-scale and mid-scale modulations appear to have lower wavelengths than for E_5. To this extent, in future work, it will be interesting to model more precisely the path of the satellite's magnetic footpoint for this type of analysis.

5.4.5 Conclusion

We investigated the phenomena known as magnetic switchbacks observed by PSP, which are interpreted as localised folds in the magnetic field lines. We defined switchbacks as a deviation to the Parker spiral and implement an automatic detection on the solid angle between the Parker spiral and the measured magnetic field. We investigated both their temporal and spatial characteristics, using the spacecraft path in curvilinear abscissa s, to work in the frame of a spatial projection (expressed in degrees in Carrington coordinates, see Figure 5.2). We performed a wavelet analysis on the solid angle fluctuation, focusing on a 5-day period during E_5 and on the complete second encounter of PSP with the Sun. We found that:

- The detected temporal scales vary over time but do not obviously repeat in a coherent manner throughout the 5-day interval of E_5 or the other encounters (see Figure 5.3 and appendix). Large patches of switchback last from 5 to 18 hours.

- By contrast, significant and persistent local spatial scales are detected throughout the 5-day interval studied on E5. They are also found during E2. Large patches of switchbacks present typical spatial extent of 2.6 to 10.7°. The analysis also underlines switchback patches of intermediate scales between 0.3 and 1.6° that appear consistently throughout the encounter (see Figures 5.4 and 5.5).
- Switchback occurrence and spectral properties seem to depend on the source region of the solar wind rather than on the radial distance of PSP. In E_2, the power spectrum of the signal was found to be lower in the coronal hole plasma compared to the streamer plasma, even though the dominant scales remained the same (Figure 5.5).

The wavelengths we detect are outside of the turbulence inertial range and cover lower frequencies, they more likely correspond to large spatial structures in the injection range. When we compare them to the scales of solar granulation and supergranulation, and obtain values that are consistent with the scales of both features. We conclude that supergranulation and granulation are associated with switchback formation, and that their typical scales are the source of the large-scale modulation of switchbacks called switchback patches, and the reported mid-scale modulation. While we cannot conclude on the physical process at stake regarding individual switchback formation (magnetic reconnection, turbulence or yet another process), our result nevertheless suggests that switchbacks most probably originate in the low solar atmosphere since their occurrence appears to be modulated by the effects of solar surface motion at the granular and supergranular scales.

Chapter 6

The preferential orientation of magnetic switchbacks

Contents

Following the study of characteristic scales of switchbacks presented in the previous chapter, we now investigate statistically the orientation of the magnetic deflections measured by PSP. Horbury et al. (2020a) performed this type of analysis on a four-day period around the first perihelion of PSP, and our work aims to extend this analysis to several encounters, as the identification of a preferential orientation of magnetic switchbacks might help discriminate between formation mechanisms. We first investigate in more detail the validity of the Parker spiral assumption, then adopt a modeling approach to detect significant deflections of the magnetic field relative to the background solar wind. This chapter is adapted from Fargette et al. (2022).

6.1 Introduction

Based on the systematic analysis of data acquired by PSP during its first 9 encounters, the aim of the present chapter is to determine whether magnetic field deflections during switchbacks display a preferential orientation. Horbury et al. (2020a) report a tendency of long-duration switchbacks to deflect in the +T direction of the radial-tangential-normal (RTN) frame. They also highlight that nearby switchbacks tend to orient themselves in the same direction. In addition, a clockwise preference was observed in switchbacks identified in

Helios data by Macneil et al. (2020), and the same tendency was identified very recently by Meng et al. (2022) in encounters 1 and 2 in PSP data.

To compare the magnetic field orientation to the expected local Parker spiral (eq. (4.1)), we transformed each data point into its local Parker frame, $\mathbf{x}, \mathbf{y}, \mathbf{z}$, where $\mathbf{x}$ points in the direction of the local spiral, $\mathbf{z} = \mathbf{N}$ remains unchanged from the RTN frame, and $\mathbf{y}$ completes the direct orthogonal frame. An important point is that this frame rotates as a function of the polarity of the solar magnetic field, and a magnetic field matching the local spiral perfectly is then written as $\mathbf{B} = B_x\mathbf{x}$, with B_x positive. Finally, when studying orientation, it is convenient to use a spherical coordinate system $(||\mathbf{B}||, \phi, \theta)$, where ϕ and θ are the azimuthal and elevation angle in this xyz Parker frame spanning, respectively, $[-180, 180]°$ and $[-90, 90]°$. We hereafter write the vector containing the orientation angles of the magnetic field as $\boldsymbol{\psi} = [\phi, \theta]^\intercal$. The different frames and angles used are illustrated in Figure 6.1.

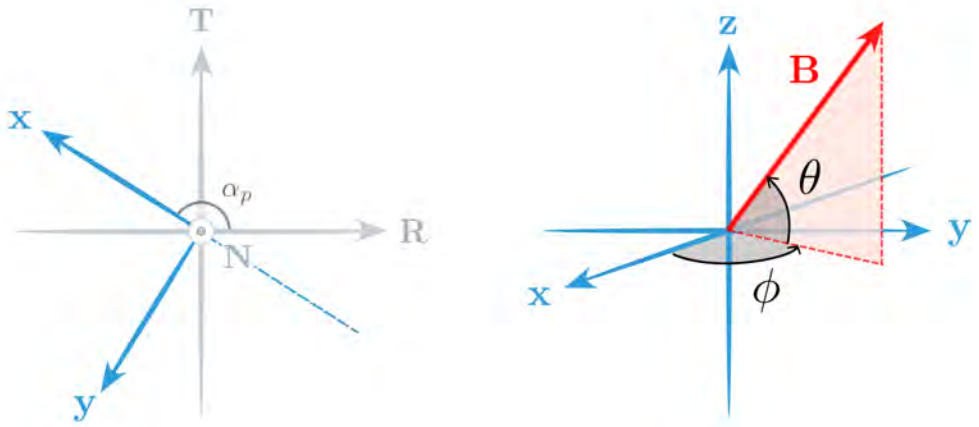

Figure 6.1: On the left, the Parker frame defined by the α_p angle (xyz, in blue) is illustrated in the RTN frame viewed from the top, in a magnetic sector of negative polarity ($\mathbf{x}$ toward the Sun). On the right panel, we show the orientation angles ϕ and θ of an arbitrary magnetic field vector (in red) in the Parker frame.

6.2 Quiet wind orientation

The first step of our study was to quantify the accuracy of the Parker model that we wanted to use for the background field. To do so, we manually selected periods of quiet solar wind in the time series as periods that were not dominated by large-scale fluctuations. We chose periods that lasted at least one hour with no or very few deviations greater than 60° from the expected spiral direction. This selection was performed visually, which may have led to a selection bias despite our best efforts. We hence give the timetable of the selected intervals in the appendix of Fargette et al. (2022). In Figure 6.2 we display the distribution of the orientation angles ϕ and θ inside these quiet solar wind intervals, with the colors differentiating the different encounters. The magnetic field orientation in these quiet solar

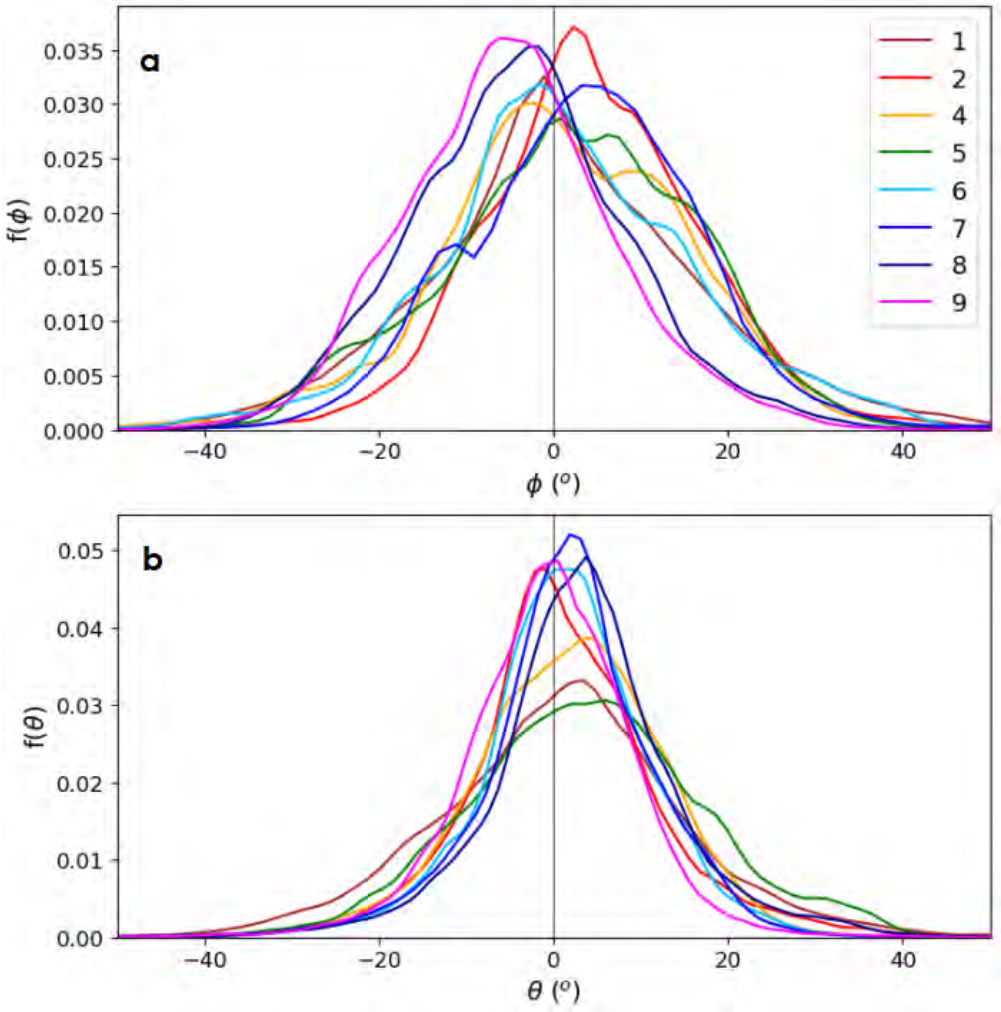

Figure 6.2: Distributions of orientation angles ϕ (panel a) and θ (panel b) for quiet solar wind intervals over encounters 1 to 9.

wind intervals matches the Parker spiral direction given by $\boldsymbol{\psi} = [0°, 0°]^{\mathsf{T}}$ reasonably well.[1] The statistical parameters of the distributions are given in Table 6.1, with on average a median vector of $[0.4°, 1.8°]^{\mathsf{T}}$ and associated standard deviations of $[13.9°, 11.3°]^{\mathsf{T}}$.

Interestingly, we note a tendency for E_8 and E_9 to have a median value and peak biased toward negative ϕ values. We investigated if this could be due to PSP approaching closer to the Sun for the latest encounters. In Figure 6.3 we plot for each quiet solar wind interval the median orientation of the angles ϕ (panel 6.3a) and θ (panel 6.3b) as a function of the spacecraft distance r (gray dots), and we add the associated standard deviation (gray bars). We find a Spearman correlation coefficient (which measures the degree of monotonicity between two variables) of 0.28 for (ϕ, r) with an associated p-value of 3.10^{-4}, and of 0.05 for (θ, r) with an associated p-value of 0.5. Even though the correlation coefficient of ϕ with r is low, the small p-value indicates that the probability of observing such a data set with randomly distributed variables is 3.10^{-4} (and as such, unlikely). This shows that, although

[1]To give the reader a range of comparison, this $\boldsymbol{\psi} = [0°, 0°]^{\mathsf{T}}$ direction corresponds to angles relative to the radial direction between 5.6° and 29.6° depending on r and V_R.

Table 6.1: Median vectors and associated dispersion of the quiet solar wind distributions displayed in Figure 6.2.

Enc	$\boldsymbol{\psi}$ Median (°)	$\boldsymbol{\psi}$ Dispersion (°)
1	[0.4 , 1.2]	[16.6 , 14.6]
2	[4.0 , 0.5]	[12.7 , 11.2]
4	[0.8 , 2.1]	[14.3 , 10.8]
5	[2.4 , 3.7]	[14.5 , 13.9]
6	[1.1 , 1.7]	[14.8 , 9.7]
7	[3.7 , 1.8]	[13.4 , 10.2]
8	[-3.9 , 3.3]	[12.5 , 10.7]
9	[-5.3 , -0.4]	[12.0 , 9.7]

weak, the correlation between ϕ and r seems significant, while that between θ and r does not. We also fit a linear model to the data and find that $\phi = 0.235^{+0.081}_{-0.128} r - 6.0^{+3.3}_{-4.4}$ and $\theta = 0.049^{+0.072}_{-0.122} r + 0.4^{+3.8}_{-3.3}$, once again hinting that ϕ slightly increases with distance, r. The fits are shown in Figure 6.3, with the uncertainty of the fit indicated. This does not necessarily mean that the relation between the two variables is linear, as indeed the increase is mainly visible below 30 $R_\odot$ and in data from E_8 and E_9. This result should be confirmed by measurements from further encounters; nonetheless, we discuss its implications in section 6.5.1.

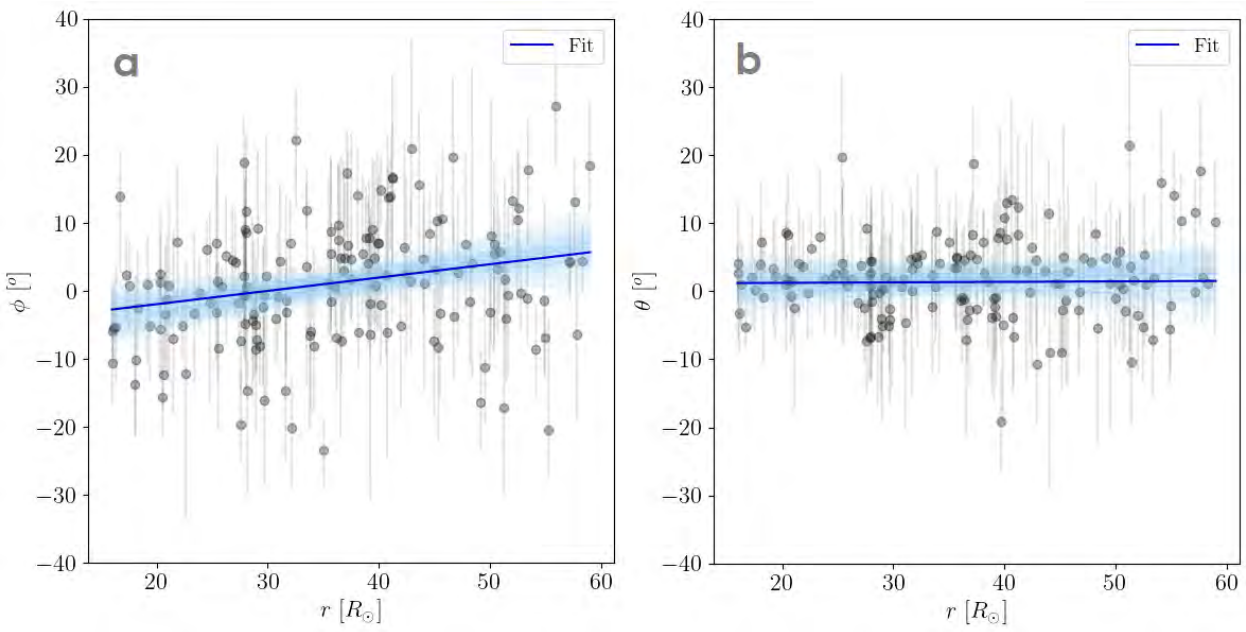

Figure 6.3: Orientation angles of the quiet solar wind intervals given in the appendix of Fargette et al. (2022), as a function of radial distance to the Sun. The median value of each interval is plotted (gray dots) with the dispersion inside the interval (error bar) for both ϕ (panel a) and θ (panel b)

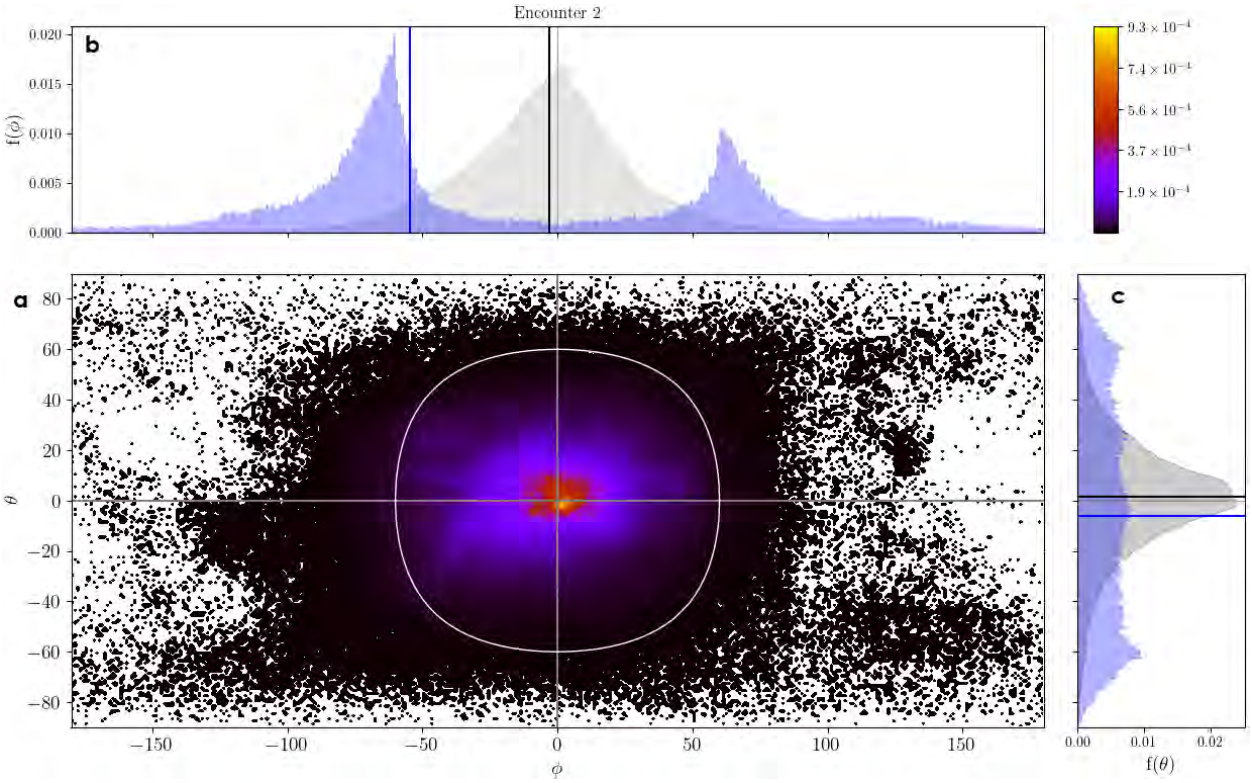

Figure 6.4: 2D normalized distribution of magnetic field orientation angles for E_2 (panel a) together with the marginal distributions of ϕ and θ in light gray in panels b and c. Black lines indicate the median values of the marginal distributions. The white line in panel a corresponds to a 60° threshold angle (see the text for more details), and in panels b and c we overlay in light blue the distribution of the points outside this 60° threshold. The blue lines indicate the median values of these truncated blue distributions.

6.3 Switchback orientation

We next considered the complete 2D distribution of magnetic field orientation angles for E_2, $f(\boldsymbol{\psi})$, which spans 13 days of data with a 2-second timestep. It is displayed in Figure 6.4a together with the marginal (i.e., projected) distributions of ϕ (6.4b) and θ (6.4c). The distribution is characterized by a median vector of $\boldsymbol{\psi} = [-2.9°, 1.4°]^\mathsf{T}$ (black lines in 6.4b and c) with an associated standard deviation of $[34.7°, 22.6°]^\mathsf{T}$, hence wider than the quiet solar wind distribution and consistent with the presence of a population of larger fluctuations. We can see that the peak of the distribution remains around $[0°, 0°]^\mathsf{T}$, as it was for the quiet solar wind.

6.3.1 The threshold method

A usual method chosen to study switchbacks is to segregate the two populations – background wind and switchbacks – based on a chosen threshold angle. Given the quiet solar wind distribution displayed in Figure 6.2, we find that this threshold should be taken at a minimum of around 40° (three standard deviations away) in the ϕ direction. This threshold is usually taken on the angle between $\mathbf{B}$ and $\mathbf{x}$ (with $\mathbf{x}$ the unit vector of the Parker spiral; see

section 6.1), which is linked to ϕ and θ through $\mathbf{b}.\mathbf{x} = \cos\theta\cos\phi$, with $\mathbf{b}$ the unit vector of $\mathbf{B}$. In panel 6.4*a* we draw the limit corresponding to a 60° threshold angle, characterized by $\cos\theta = (2\cos\phi)^{-1}$, and we overlay the distribution of the points outside this limit in panels *b* and *c*. These points are characterized by a median vector of $[-54.7°, -6.2°]^\mathsf{T}$ (blue lines in 6.4b and c) and with associated standard deviations $[79.6°, 43.4°]^\mathsf{T}$. We notice that large-scale fluctuations occur in all directions around the Parker spiral angle and that their distribution is biased toward negative values of ϕ and θ, which correspond to the +T and -N directions in a magnetic field of negative polarity. By construction, in this threshold approach the switchback distribution (in blue) is a truncated distribution. Its two apparent peaks in the ϕ component are not physical, the bimodal shape clearly being a result of the cut we performed. In addition, the standard mathematical tools like the median, the mean or the standard deviation are not sufficient to characterise this kind of distribution. This leads us to adopt a more continuous probabilistic approach, and model the solar wind as the superposition of two populations with distinct normal distributions in deflection angles. Importantly, we underline here that both methods – segregation or mixing and fitting of the two populations – find consistent results in terms of switchback preferential direction.

6.3.2 Switchback modeling : a probabilistic approach

To overcome the artefacts introduced with the threshold approach, we now model the solar wind as two populations with distinct distribution properties, respectively representing the background, quiet solar wind and the population of switchbacks characterized by larger fluctuations. In accordance with the results of section 6.2, we assume that the quiet solar wind magnetic field deflections follow a 2D normal distribution, $\mathcal{N}(\boldsymbol{\mu_0}, \Sigma_0)$, that should remain close to the Parker spiral, together with a superposed second population of larger deflections, $\mathcal{N}(\boldsymbol{\mu}, \Sigma)$, that represents the switchbacks, where $\boldsymbol{\mu}$ and Σ are respectively the mean vector and the covariance matrix of the considered distributions. The total distribution we observe in Figure 6.4 can then be modeled by the sum of the two normal distributions, weighted with a given proportion γ. This model is written as

$$f_m(\boldsymbol{\psi}, \mathbf{P}) = (1-\gamma)\ \mathcal{G}(\boldsymbol{\psi}, \boldsymbol{\mu_0}, \Sigma_0) + \gamma\ \mathcal{G}(\boldsymbol{\psi}, \boldsymbol{\mu}, \Sigma), \tag{6.1}$$

where f_m is the modeled distribution, $\mathcal{G}(\boldsymbol{\psi}, \boldsymbol{\mu_0}, \Sigma_0)$ and $\mathcal{G}(\boldsymbol{\psi}, \boldsymbol{\mu}, \Sigma)$ are 2D Gaussian functions of respective mean vectors $\boldsymbol{\mu_0} = [\mu_{0\phi}, \mu_{0\theta}]^\mathsf{T}$, $\boldsymbol{\mu} = [\mu_\phi, \mu_\theta]^\mathsf{T}$ and covariance matrices $\Sigma_0 = \text{diag}\ (\sigma_{0\phi}, \sigma_{0\theta})$, $\Sigma = \text{diag}\ (\sigma_\phi, \sigma_\theta)$, and $\mathbf{P}$ is the parameter vector to the fit and contains nine parameters:

$$\mathbf{P} = \begin{bmatrix} \mu_{0\phi} & \mu_{0\theta} & \sigma_{0\phi} & \sigma_{0\theta} & \mu_\phi & \mu_\theta & \sigma_\phi & \sigma_\theta & \gamma \end{bmatrix}^\mathsf{T}. \tag{6.2}$$

We assume that our data (i.e., the distribution f) follow our model f_m with a white noise model, and we take the associated dispersion, σ_ϵ, to be 10% of the maximum of f. For a given set of parameter $\mathbf{P}$, the likelihood of the data follows a 2D normal distribution and can be written as:

$$\mathrm{p}(f \mid \boldsymbol{\psi}, \mathbf{P}) = \mathcal{G}\left(f,\ f_m(\boldsymbol{\psi}, \mathbf{P}),\ \sigma_\epsilon \mathbb{1}\right), \tag{6.3}$$

where $\mathrm{p}(X)$ is the probability of X and $\mathbb{1}$ is the identity matrix. We use uniform priors $\mathrm{p}(\mathbf{P})$ on all the parameters, with the constraints $\mu_{0\phi}, \mu_{0\theta} \in [-10°, 10°]$, $\sigma_{0\phi}, \sigma_{0\theta} \in [0.1°, 30°]$.

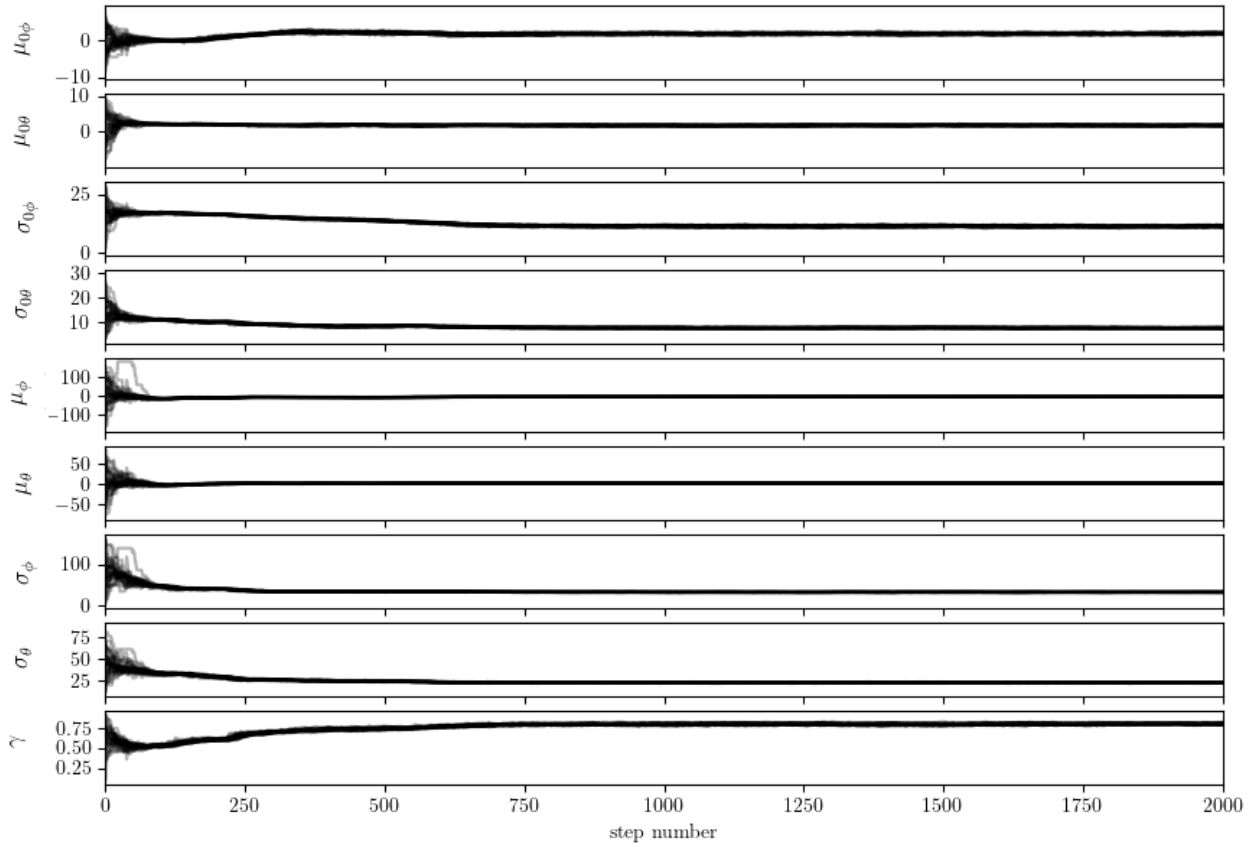

Figure 6.5: Walker path in the parameter space over 2000 iterations.

These constraints are based on the results from section 2, where we find a mean close to zero and a dispersion around 15°. We can now seek to maximize the log-posterior probability of the model through the Bayes equation:

$$\ln \mathrm{p}(\mathbf{P} \mid \boldsymbol{\psi}, f) = \ln \mathrm{p}(\mathbf{P}) + \ln \mathrm{p}(f \mid \boldsymbol{\psi}, \mathbf{P}) + \mathrm{C}, \tag{6.4}$$

where C is a constant. We sample the parameter space using the *emcee*[2] python library (Foreman-Mackey et al., 2019), which is based on a Monte Carlo Markov Chain algorithm, using 32 walkers and 2000 iterations (see appendix A). We use the *Chain Consumer*[3] library to visualize the fitting results. In Figure 6.5 we display the convergence of the fitting algorithm over 2000 iterations. After 1000 steps the results are stable, and so we display the probability distribution function of walker positions in the 9D parameter space in Figure 6.6, discarding the first 1000 iterations[4]. This yields the most probable parameter vector **P,** which is summarized in Table 6.2.

6.3.3 Fitting results for Encounter 2

In Figure 6.7 we present the 2D distribution of the magnetic deflection angles in the same manner as in Figure 6.4, together with the fitting result. What is striking is first that the

[2] https://emcee.readthedocs.io/en/stable/
[3] https://samreay.github.io/ChainConsumer/chain_api.html
[4] The associated python code is available here: fit_double_gaussian.py

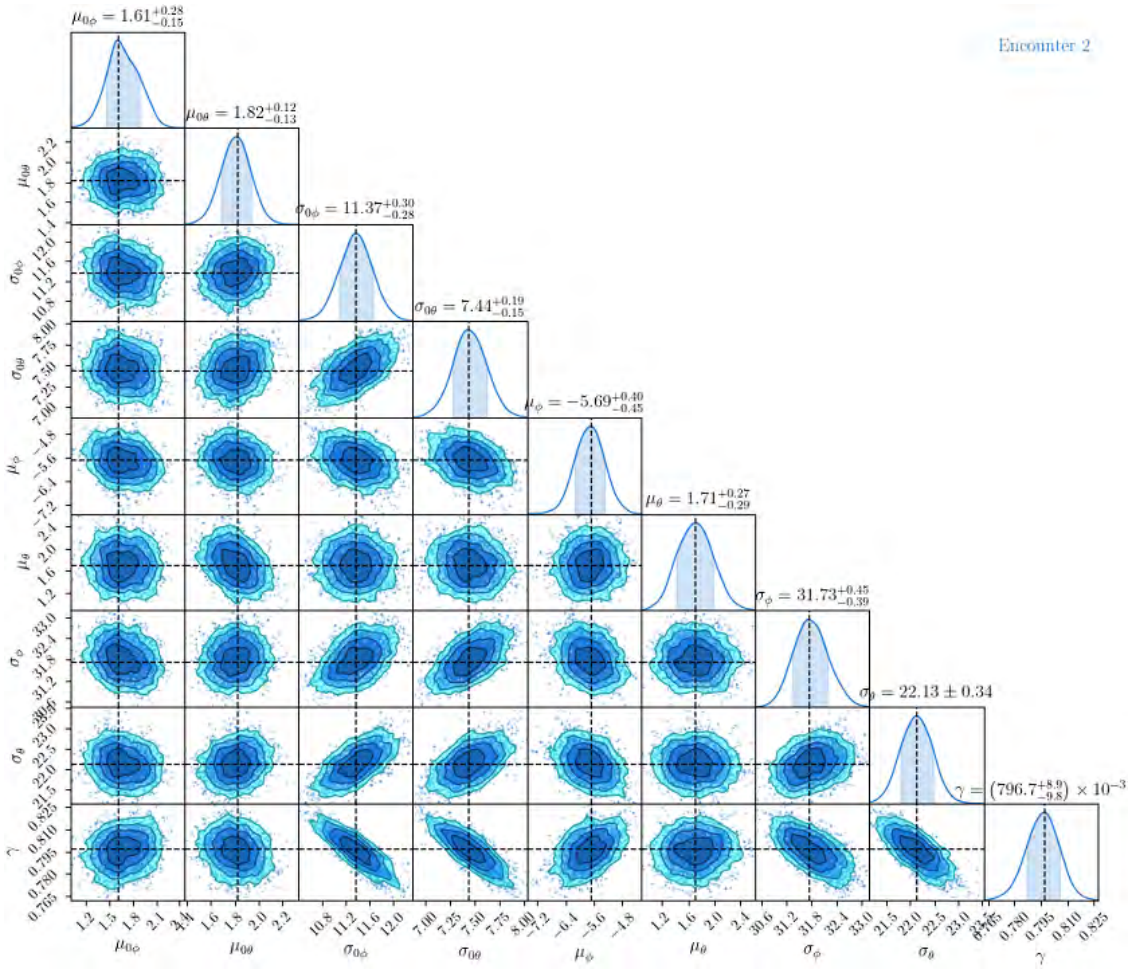

Figure 6.6: 9D probability distribution function of walker positions, discarding the first 1000 iterations.

Table 6.2: Most probable (maximum a posteriori) parameter vector **P**, obtained after fitting the double Gaussian model described in the text to the deflection angle distribution of E_2. The first line presents the parameters associated with the background quiet solar wind model, the second line those associated with the switchback population, and the third line the proportion of the switchback population.

$\mu_{0\phi}$	$\mu_{0\theta}$	$\sigma_{0\phi}$	$\sigma_{0\theta}$
$1.61^{+0.23}_{-0.18}$	$1.81^{+0.14}_{-0.12}$	$11.32^{+0.32}_{-0.28}$	$7.44^{+0.15}_{-0.19}$
μ_{ϕ}	μ_{θ}	σ_{ϕ}	σ_{θ}
$-5.68^{+0.42}_{-0.48}$	$1.71^{+0.29}_{-0.25}$	$31.75^{+0.43}_{-0.44}$	$22.13^{+0.29}_{-0.42}$
γ			
$0.7975^{+0.0095}_{-0.0094}$			

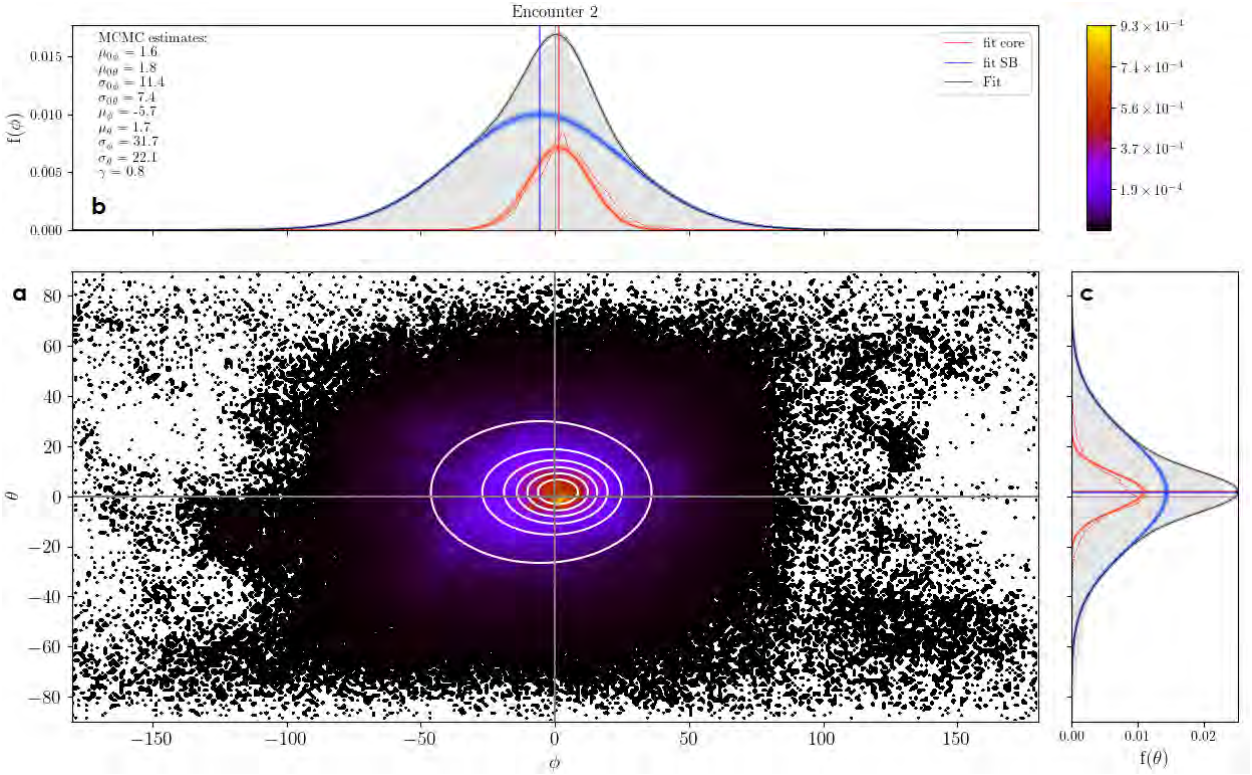

Figure 6.7: 2D distribution of magnetic field orientation angles for E_2 (panel a) together with the marginal distributions of ϕ and θ in light gray in panels b and c. The white contours in panel a represent the fitted function corresponding to the parameters in Table 6.2, and its marginal distributions are in black in panels b and c. We also plot in panels b and c the marginal distributions corresponding to quiet solar wind distribution $(1-\gamma) * \mathcal{G}(\boldsymbol{\psi}, \boldsymbol{\mu_0}, \Sigma_0)$ (red) and switchback distribution $\gamma * \mathcal{G}(\boldsymbol{\psi}, \boldsymbol{\mu}, \Sigma)$ (blue), with lines indicating their mean. We also plot in lighter red, blue and black a hundred similar functions with parameters drawn randomly from the parameter probability distribution displayed in Figure 6.6, to give a sense of the fit precision. Finally, in dashed red we display the quiet solar wind distribution found for E_2 2 as displayed in Figure 6.2 but multiplied by $(1-\gamma)$ so that the scales are comparable.

fitted function (in white in panel a and black in panels b and c) follows the 2D data distribution quite closely, and second that the fitting algorithm finds a Parker spiral distribution (in red in panels b and c) with characteristics very similar to the one found in section 2 in an independent manner (see Table 6.1 line 2 and Table 6.2 line 1). We can see that, as expected, the switchback population presents a larger dispersion in both dimensions. Its mean vector, however, is different from that of the quiet solar wind population. It presents a negative value in the ϕ dimension, $\mu_\phi = -5.68^{+0.42}_{-0.48}$. This negative μ_ϕ is consistent with the result found with the previous method (Figure 6.4) when we considered the median of points with a large deviation from the Parker spiral. In the θ dimension, however, we find no difference between the means of the core and the switchback population, while in the previous method we had found a slight tendency toward negative θ. This discrepancy can be explained by the fact that the tail of the marginal distribution in negative θ is not well reproduced by the fit (panel 6.7c). Finally, we find that the proportion of the switchback population in the

solar wind is close to 80%. This high proportion is due to the method we are using and can be interpreted as the proportion of the observed solar wind that is dominated by magnetic switchbacks.

To summarize, in our method we assumed that the solar wind magnetic field fluctuations were composed of two populations, each with orientation angles that followed a 2D normal distribution. The first is assumed to follow the Parker spiral with a rather small dispersion, and the second is the switchback population with a wider dispersion. After fitting this model to our data, we find that the background population we retrieve is consistent with the quiet solar wind distribution described in section 6.2. We also find that the switchback population is biased, with an offset in the $-\phi$ direction. These results are confirmed with the simpler analysis we performed in Figure 6.4, where we analyze the median values of points more than 60° away from the spiral and also find a preferential $-\phi$ orientation.

6.3.4 A systematic bias in the deflections

We next applied the same methodology to the remaining encounters. For each, we considered the available data below 60 $R_\odot$ and discarded intervals where the Parker spiral model was not relevant, that is, where we identified HCS crossings, CMEs or flux ropes. This selection was done manually by analyzing the magnetic field, plasma moments, and the PAD of suprathermal electrons; it can be reviewed in Appendix C of Fargette et al. (2022). In order to identify a potential influence of the magnetic field polarity, we also restrained our study to the main polarity of each encounter. This means that we considered only the data points when the spacecraft was sampling a negative polarity solar wind (south of the HCS) for encounters 1, 2, 4, 5, 6, and 9, and a positive polarity solar wind (north of the HCS) for encounters 7 and 8. We computed the orientation angles of the magnetic field in the local Parker frame and fitted the obtained distribution for the most probable parameters in the same manner as in section 6.3.2. The fitting results for all encounters are available in Table 6.3, and are visualised in Figures 6.8 and 6.9.

In Figure 6.8, we visualize all the fits we performed for the different encounters by looking at the marginal distributions. We note that the plots shown for E_2 in Figure 6.8 are the same as the ones detailed in Figs. 6.7b and 6.7c. This visualization shows that, to first order, the data are accurately reproduced by the model we use (i.e., the weighed superposition of two Gaussian functions). We also see that the switchback distribution (in blue) clearly shows a biased mean shifted toward smaller values of ϕ (and θ to a lesser degree) compared to the quiet solar wind, for all encounters independently apart from E_6.

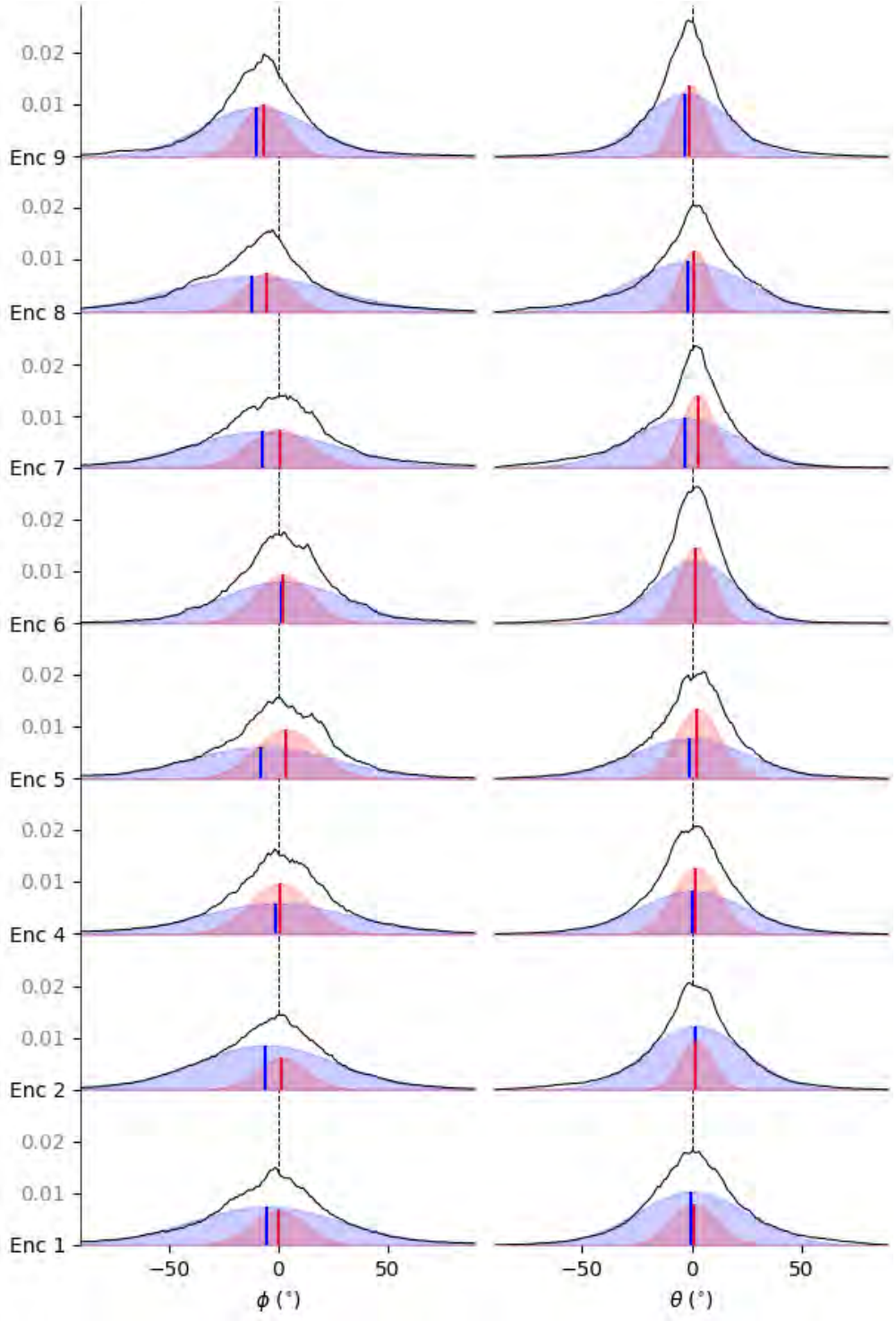

Figure 6.8: Marginal distributions of observed magnetic field orientation angles $f(\phi)$ (a) and $f(\theta)$ (b) displayed in black for all encounters, with a shared y axis. The fitting results are also plotted: in light red the marginal distributions corresponding to quiet solar wind, and in light blue the marginal distribution corresponding to switchbacks. Vertical lines indicate their mean, and the dashed line in the background is the zero value.

Table 6.3: Most probable (maximum a-posteriori) parameter vectors $\mathbf{P}$, obtained after fitting the double Gaussian model described in the text to the data for all the encounters

Enc	$\mu_{0\phi}$	$\mu_{0\theta}$	$\sigma_{0\phi}$	$\sigma_{0\theta}$	μ_ϕ	μ_θ	σ_ϕ	σ_θ	γ
1	$0.04^{+0.16}_{-0.20}$	$1.17^{+0.14}_{-0.16}$	$12.39^{+0.30}_{-0.38}$	10.53 ± 0.24	$-5.37^{+0.54}_{-0.38}$	$-0.06^{+0.28}_{-0.34}$	$34.77^{+0.66}_{-0.59}$	$25.01^{+0.41}_{-0.38}$	$0.755^{+0.01}_{-0.002}$
2	$1.61^{+0.28}_{-0.15}$	$1.82^{+0.12}_{-0.13}$	$11.37^{+0.30}_{-0.28}$	$7.44^{+0.19}_{-0.15}$	$-5.69^{+0.40}_{-0.45}$	$1.71^{+0.27}_{-0.29}$	$31.73^{+0.45}_{-0.39}$	22.13 ± 0.34	$0.797^{+0.009}_{-0.01}$
4	$0.69^{+0.16}_{-0.14}$	$1.711^{+0.109}_{-0.099}$	$14.04^{+0.26}_{-0.17}$	$10.75^{+0.14}_{-0.15}$	-0.89 ± 0.50	$0.24^{+0.39}_{-0.44}$	$34.51^{+0.70}_{-0.69}$	$24.62^{+0.50}_{-0.46}$	$0.598^{+0.012}_{-0.017}$
5	$3.85^{+0.18}_{-0.17}$	$2.60^{+0.11}_{-0.12}$	$14.23^{+0.20}_{-0.18}$	$10.19^{+0.16}_{-0.15}$	$-7.59^{+0.86}_{-0.63}$	$-1.33^{+0.44}_{-0.63}$	$33.37^{+0.64}_{-0.66}$	$26.42^{+0.50}_{-0.45}$	0.603 ± 0.012
6	$2.11^{+0.15}_{-0.14}$	$1.642^{+0.096}_{-0.090}$	$12.46^{+0.22}_{-0.23}$	$7.99^{+0.15}_{-0.13}$	$1.79^{+0.37}_{-0.38}$	$1.46^{+0.25}_{-0.22}$	$27.80^{+0.47}_{-0.51}$	$18.50^{+0.41}_{-0.30}$	0.660 ± 0.016
7	$0.51^{+0.14}_{-0.19}$	$2.778^{+0.098}_{-0.068}$	$14.22^{+0.16}_{-0.21}$	$7.56^{+0.14}_{-0.12}$	-7.46 ± 0.49	$-2.81^{+0.38}_{-0.40}$	$33.83^{+0.56}_{-0.48}$	$24.71^{+0.40}_{-0.32}$	$0.688^{+0.0074}_{-0.0094}$
8	$-5.15^{+0.15}_{-0.13}$	$1.161^{+0.093}_{-0.078}$	$10.91^{+0.16}_{-0.17}$	$6.886^{+0.097}_{-0.124}$	$-11.98^{+0.49}_{-0.56}$	$-1.76^{+0.30}_{-0.43}$	$37.35^{+0.57}_{-0.50}$	$26.71^{+0.46}_{-0.34}$	$0.760^{+0.0055}_{-0.0057}$
9	$-6.57^{+0.16}_{-0.18}$	$-0.73^{+0.11}_{-0.10}$	$9.93^{+0.26}_{-0.24}$	$7.31^{+0.16}_{-0.18}$	$-9.67^{+0.40}_{-0.45}$	$-2.75^{+0.32}_{-0.37}$	$25.29^{+0.58}_{-0.47}$	$19.66^{+0.41}_{-0.45}$	0.707 ± 0.015

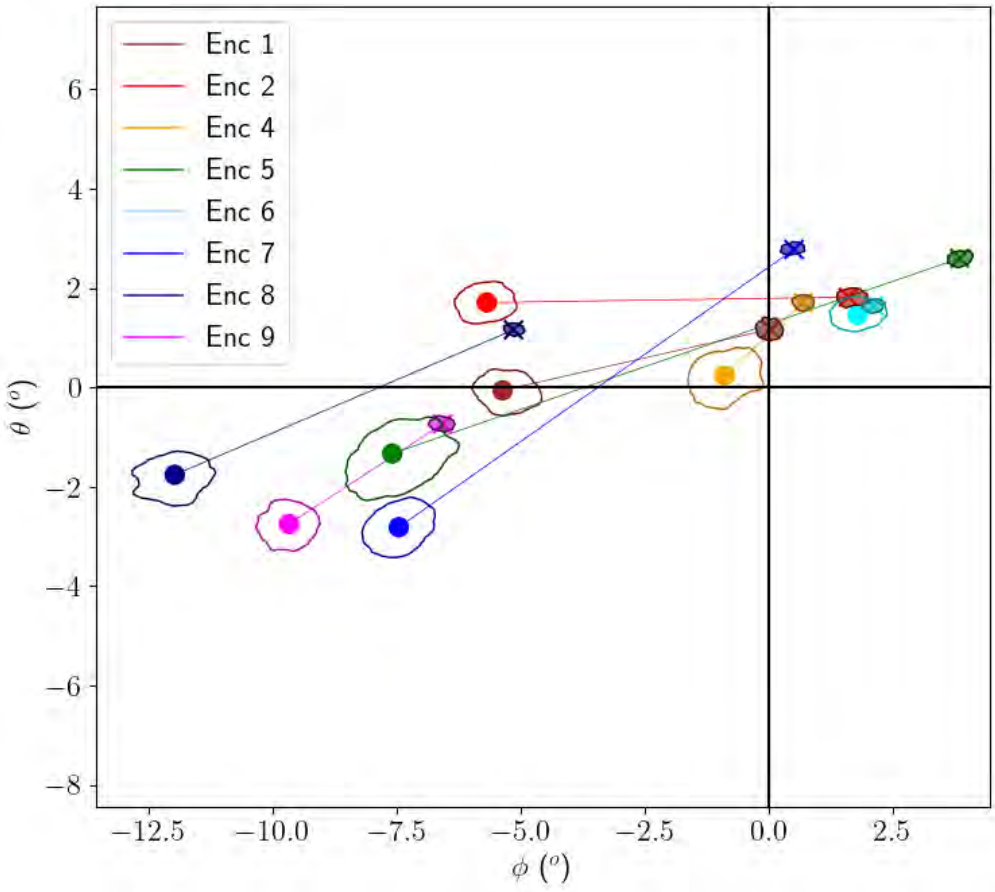

Figure 6.9: Mean vectors of the quiet solar wind (cross) and switchback (dot) populations for each encounter. Both are linked by a line for visualization purposes. Contours around the markers (filled for quiet solar wind, transparent for switchbacks) indicate the uncertainty of the fit we performed.

Enc	1	2	4	5	6	7	8	9	$\langle\cdot\rangle$
$\Delta\mu_\phi$ (°)	-5.41	-7.25	-1.60	-11.47	-0.37	-8.06	-6.86	-3.12	-5.52
$\Delta\mu_\theta$ (°)	-1.22	-0.11	-1.38	-3.81	-0.18	-5.58	-2.87	-2.02	-2.15

Table 6.4: Shift between the quiet solar wind and switchback distribution means. The last column is the average over all encounters.

In Figure 6.9 we display a scatter plot of the mean vector of each population for all encounters. We show the mean vectors found for the quiet solar wind population $\boldsymbol{\mu_0} = [\mu_{0\phi}, \mu_{0\theta}]^\mathsf{T}$ (corresponding to the red vertical lines in Figure 6.8) and the mean vectors found for the switchback population $\boldsymbol{\mu} = [\mu_\phi, \mu_\theta]^\mathsf{T}$ (vertical blue lines in Figure 6.8). For E_8 and E_9, the quiet solar wind means have negative ϕ values, which is consistent with the observations presented in section 6.2. The shifts between the means of the quiet solar wind and switchback distributions are given for each encounter in Table 6.4, with $\Delta\mu_\phi = -5.52$ ° and $\Delta\mu_\theta = -2.15°$ on average. For all encounters except E_6, the switchback population is shifted significantly to lower values of ϕ, while for all encounters except E_2 and E_6 it is also somewhat shifted toward lower values of θ, although the trend is less significant. These results are further discussed in section 6.5.2.

6.4 Case study of a unidirectional planar patch of switchbacks

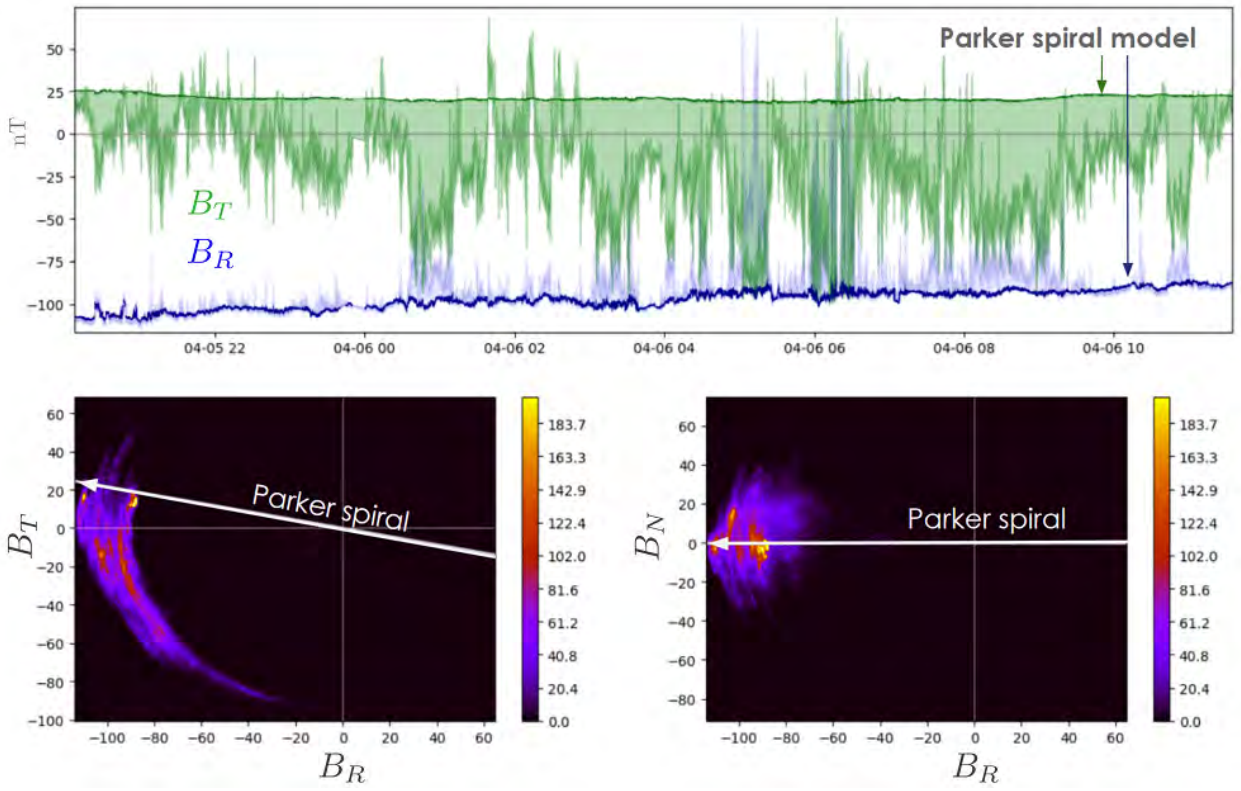

Figure 6.10: Illustration of a one-sided patch of switchbacks. The top panel shows the radial and tangential component of the magnetic field, B_R and B_T, as well as the expected components of the Parker spiral magnetic field. The difference between model and data is lightly shaded. In the bottom panels, we plot the 2D distributions $f(B_R, B_T)$ and $f(B_R, B_N)$; with the color scale indicating the number of points inside each bin. An arrow indicates the average expected direction of the Parker spiral.

In addition to the large-scale systematic bias found over the different encounters (section 6.3), we want to highlight in this section that on smaller temporal scales, switchbacks can be deflected very consistently in the same direction. As such, we report on a patch of switchbacks that occur during E_2 from 2020 April 5 at 20:00 to 2020 April 6 at 12:00, for a total duration of 16 h, which is displayed in Figure 6.10. In these plots, it is clear that the magnetic field deviates in one direction during the entire patch, which is B_T negative in the ecliptic plane. This corresponds to the $+\phi$ direction with the notation adopted in this chapter. The path taken to deflect and return to the Parker spiral remains unchanged within a given plane (here the ecliptic) rather than moving randomly in three dimensions.

This further confirms the results from Horbury et al. (2020a), who find that the larger switchbacks within a patch tend to deflect in the same direction. Here we do not have a notion of switchback duration but show that deviations are contained within the ecliptic plane ($\theta < 30°$, not shown) and are one-sided with regard to the Parker spiral ($+\phi$ direction). This event interestingly goes in the opposite direction compared to the systematic bias we

find in section 6.3. This is not unexpected, as the data displayed in Figs. 6.4 to 6.8 show that switchbacks may deflect in any direction despite the average having a tendency toward negative ϕ.

6.5 Comparison to the prediction of existing theories

6.5.1 The Parker spiral accuracy

We show in section 6.2 that, as the distance of PSP to the Sun decreases, the magnetic field data of quiet solar wind intervals seem to deviate from the Parker spiral model predictions. This is mainly visible in the data from E_8 and E_9, when PSP was diving down to 16 $R_\odot$ at perihelion (while data above 30 $R_\odot$ show no obvious trend, which is consistent with the results in Badman et al. 2021). Geometrically, this means that we are overestimating the algebraic value of the Parker spiral angle, α_p, and that the spiral is wound less tightly than expected. The Parker spiral model computed in the present study is given by Eq. (4.1), with $\omega = 2.9 \times 10^{-6}$ s^{-1}, $r_0 = 10$ $R_\odot$, and where $V_R(t)$ is the measured radial speed of the solar wind processed with a 2h low pass filter. However, this model implicitly assumes a constant solar wind speed between the source surface of radius r_0 and the spacecraft, and this hypothesis is likely no longer valid so close to the Sun, especially in the slow solar wind that accelerates until 10-20 solar $R_\odot$ (see, e.g., Bruno & Bavassano 1997). With these values in mind, and seeing that the average value of solar wind speed during E_8 and E_9 is around 200 to 300 km/s, it is highly probable that at such heights, PSP is located within the acceleration region of the solar wind; recently, Kasper et al. (2021) reported that PSP even went down to the magnetically dominated corona during its latest orbits. This is consistent with our results, since the spiral we observe is straighter than the expected Parker spiral associated with the wind speed measured by PSP. Indeed, overestimating the algebraic value of α_p amounts to overestimating the value of the solar wind speed, V_R, from the source. Hence, this gives more weight to the weak but significant tendency we find (ϕ decreasing with r), as it is consistent with the physics at stake in the acceleration region.

6.5.2 Switchback orientation

In section 6.3, we show that for all considered encounters, the switchback population presents a preferential deflection orientation toward lower values of the ϕ and θ angles. This result holds for all encounters (albeit being less clear in E_6) and is not impacted by the polarity of the magnetic field. We highlight the implication of this result in a more visual manner in Figure 6.11. In this sketch we represent in panel a a top view of the Sun (N is in the out-of-plane direction), two field lines with positive (red) and negative (blue) polarity, and the associated Parker frame at a given radius as previously defined in section 6.1. It is easier to see in this visualization that for a positive polarity field, negative ϕ values correspond to the $-\mathbf{T}$ direction, while for a negative polarity field it corresponds to the $+\mathbf{T}$ direction (except for very large deflections close to $-\pi$, where the T component would reverse in both cases); both of these situations correspond to a clockwise rotation. This is consistent with the results of Horbury et al. (2020a), who find that switchbacks present a preferential orientation in the +T direction during E_1, where PSP mainly samples the negative polarity hemisphere of the Sun. This clockwise preference was observed in Helios data by Macneil

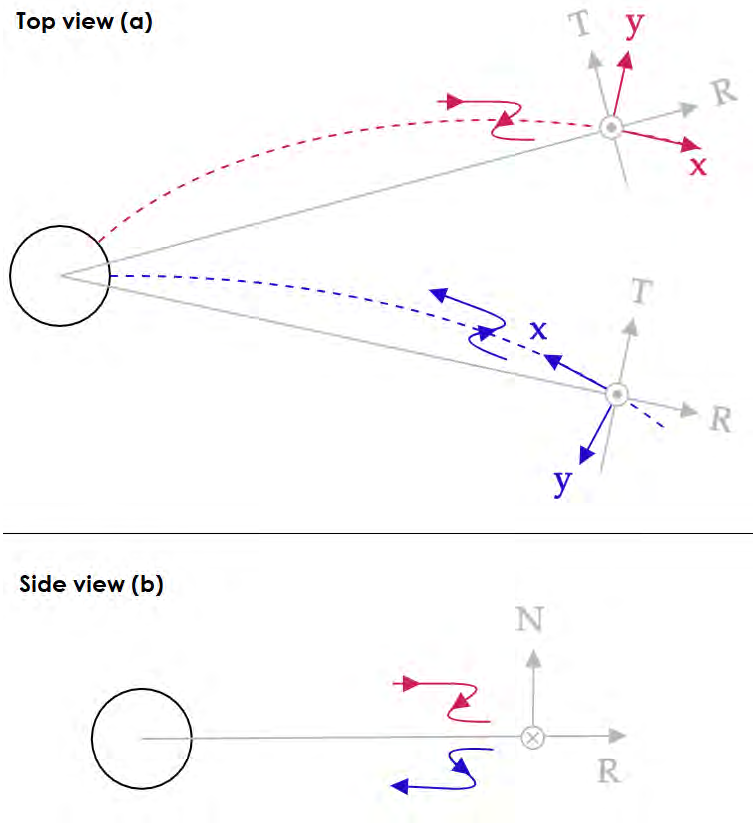

Figure 6.11: Illustration of the favored geometry of switchbacks in negative (blue) and positive (red) polarity

et al. (2020) and more recently identified by Meng et al. (2022) in E_1 and E_2 in PSP data, which further confirms our result. In Figure 6.11 we draw a switchback illustration consistent with the negative ϕ preference for each polarity, and one can see that the geometry remains unchanged. In addition, switchbacks are accelerated structures (sometimes called "velocity spikes" due to their associated increase in V_R; Kasper et al. 2019) with Alfvénic properties. Hence, in the negative (respectively positive) magnetic sector, the magnetic field is correlated (anticorrelated) with the velocity vector. This leads to the field line configurations displayed in Figure 6.11, which are associated with positive tangential flows. On the other hand, the less marked bias toward $-\theta$ values corresponds to the -N direction regardless of the polarity. One can realize that, in this case, this indicates a symmetry of the switchback geometry in the two hemispheres. We illustrate this configuration in panel *b*, with a side view of the Sun (T is in the in-plane direction) and a switchback with negative B_N for each polarity.

To summarize, we find that switchbacks – viewed as a population of large magnetic deflections with respect to the Parker spiral – occur in all directions, while their deflection distribution presents a systematic bias in the $-\phi$ direction and to a lesser extent in the $-\theta$ direction. We now discuss this result in light of the existing potential formation process for magnetic switchbacks presented in the introduction.

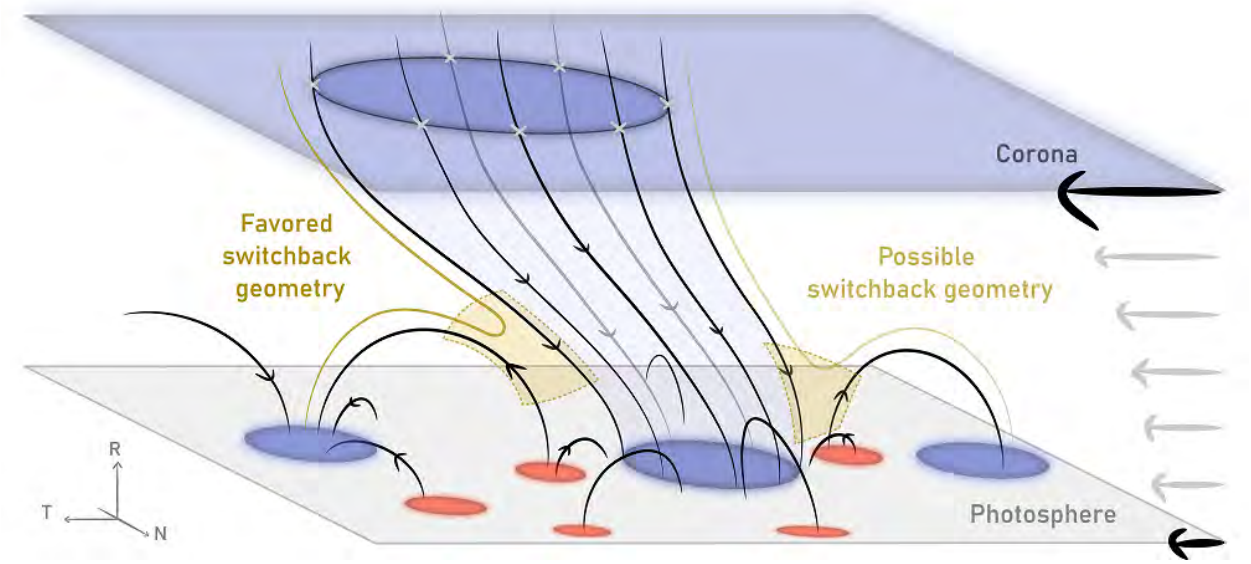

Figure 6.12: Illustration of a possible explanation for the preferential orientation of a switchback, assuming interchange reconnection in the low corona as the initial mechanism. The sketch displays an element of open flux tubes from the photosphere expanding out into a faster corona, along closed loops that form the magnetic carpet. The blue (red) color is associated with the negative (positive) polarity of the field lines. Some potential reconnection sites are highlighted in light yellow (non-exhaustive) and reconnected field lines are displayed in yellow. The arrows on the right highlight the relative speed gradient that exists between the differentially rotating photosphere and the quasi-rigidly rotating corona.

6.5.3 Possible interpretation

Interchange reconnection is a mechanism that allows the open magnetic field lines of the Sun to reconnect at their base with closed loops that emerge from the magnetic carpet. This phenomenon mitigates the shear induced by the differential rotation of the photosphere – where field line footpoints rotate at different speeds depending on latitude – and the quasi-rigid rotation of the corona at equatorial rates due to force balance with the large-scale coronal structure, including transients (Wang et al., 1996; Fisk, 1996; Fisk et al., 1999; Wang & Sheeley, 2004; Lionello et al., 2005, 2006). In the reference frame of a coronal hole that is corotating quasi-rigidly at the equatorial rotation rate, magnetic loops appear to drift in the direction opposite to that of solar rotation, from west to east. This relative drift can induce strong magnetic shears that force magnetic reconnection between magnetic loops and open field lines. Subsequently, this leads to a footpoint displacement due to magnetic reconnection favored in the direction of solar rotation. Of course, if the photosphere is somehow going faster than the corona (locally, near the equator, for instance), then the favored motion is reversed. In general, however, the process may be random and in all directions for the majority of the events because of localized photospheric motions associated with the magnetic carpet and solar granulation. The phenomenology at stake is illustrated in Figure 6.12. There, the sketch displays an element of open flux tubes from the photosphere expanding out into a faster corona, inducing a shear in the magnetic field lines as just described. The sketch is valid for all such flux bundles that escape from the otherwise mixed polarity patchwork of closed field lines of the magnetic carpet. At the bottom of the flux

tube, magnetic reconnection can occur randomly and in all directions between the open field lines and closed loops that emerge from the magnetic carpet. As the photosphere lags behind the solar corona, a particular geometry could be favored as footpoint motion tends to mitigate the speed shear and jump in the direction of solar rotation. We suggest that this process could induce the bias in switchback orientation we present in this paper. This is consistent with Bale et al. (2021), who also interpret E_6 data in terms of a shear between the photosphere and corona.

Our results seem to be consistent with such reconnection occurring in regions where the photosphere is going, on average, slower than the solar corona, which would lead to the geometry highlighted in Figures 6.11*a* and 6.12. This situation of a slower photosphere is particularly valid at mid to higher latitudes, typically over 30° in latitude, as studies of the coronal hole rotation rate indicate (e.g., Giordano & Mancuso 2008; Mancuso & Giordano 2011; Bagashvili et al. 2017; Mancuso et al. 2020). However, analysis of the spacecraft connectivity throughout E_1 indicates that the measured solar wind observed by PSP was emerging from an equatorial coronal hole (Bale et al., 2019; Badman et al., 2020; Réville et al., 2020), which would supposedly rotate close to the photospheric speed. We thus expect a lower $-\phi$ bias in this case. Nonetheless, we must consider the small but existing latitudinal extent of the coronal hole, as well as potential additional solar wind sources, in the interpretation of E_1 data. Future work on the connectivity of PSP during switchback observation is needed for the different encounters, to confirm or rule out a potential link between the $-\phi$ bias and the interchange reconnection induced by differential rotation.

Regarding the bias in elevation, Fisk et al. (1999) interestingly highlight a potential circulation of field line footpoints at the photosphere from the poles toward the equator, which would be consistent with the slight bias we find toward negative θ values (i.e., negative B_N; see Figure 6.11b). Indeed, a field line rooted in the northern (southern) hemisphere would then be dragged downward (upward) and favor reconnection in the configurations displayed in Figure 6.11b. However, considering that the bias we find in $-\theta$ is small, we advise caution in the interpretation of this result and consider it less robust than the bias found in the ecliptic plane.

The preferential orientation we find – for switchbacks to deflect in the clockwise direction – does not seem to fit with a formation process involving either solely solar wind turbulence, as developed by Squire et al. (2020), Mallet et al. (2021), and Shoda et al. (2021), or in situ velocity shears, as developed by Ruffolo et al. (2020). It seems that both of these processes would produce fluctuations that should appear as rather isotropic in the data. However, most of the studies cited above focus on the radial component of the magnetic field only. An analysis of the distribution of the magnetic field orientation angles in simulations from Squire et al. (2020), Mallet et al. (2021), and Shoda et al. (2021) (for turbulent generation) and Ruffolo et al. (2020) (for in situ velocity shears) would be of interest here, to investigate whether these other mechanisms can also introduce anisotropy in switchback properties.

We conclude that our results seem overall consistent with interchange reconnection in the low atmosphere being a plausible source of the preferential orientation of switchbacks. The bias we find helps reconcile the differential rotation of the photosphere and a more rigid rotation of the corona. We point out that we studied the switchback phenomenon in a probabilistic approach, without identifying exact structures in the data. Hence, we cannot conclude if the

bias we find is due to switchbacks appearing more frequently in this direction, or if longer switchbacks tend to orient themselves in this direction. Finally, we realize that our study is not sufficient to determine how reconnection would create, propagate, and preserve the switchbacks all the way to PSP's location (see for instance Tenerani et al. (2020); Magyar et al. (2021a,b)). Several explanations stemming from interchange reconnection are currently being investigated. We here provide an additional observational constraint, consistent with the results from Horbury et al. (2020a), that models and simulations should reproduce.

6.6 Conclusion

As cautioned in section 4.3.1, the choice of definition used to identify a magnetic switchback impacts the results. Here we chose to consider fluctuations away from the Parker spiral by using a locally defined Parker frame and two orientation angles in azimuth (ϕ) and elevation (θ) (section 6.1).

We characterize the quiet solar wind orientation (section 6.2) and find that the Parker spiral model indeed remains accurate at such short distances from the Sun. We notice that an offset appears for the latest encounters (E_8 and E_9) and is linked to the lower radial distance. This is expected and shows that PSP is located near the acceleration region of the solar wind.

We then investigated the large fluctuation orientation (section 6.3). To do so, we assumed that the wind was composed of two populations with distinct distribution properties, respectively representing the background and perturbed solar winds. We assumed a normal distribution of orientation angles for both distributions and fit our data with this model. This method allows us to define the switchback population without having to choose an arbitrary threshold in the magnetic field deviation. We find that the actual distribution of orientation angles is well reproduced using this method. We derived from this fit that the mean value of the switchback population is biased by a few degrees toward lower ϕ for all encounters except E_6 (a -5.5° shift on average), and toward lower θ for all encounters except E_2 and E_6 (a -2.1° shift on average; see Figure 6.9 and Table 6.4). This occurs regardless of the main polarity of the field. We conclude that switchbacks occur in all directions but present a preferential orientation in the $-\phi$ direction (clockwise), and to a lesser extent in the $-\theta$ direction (toward the equator) .

As a strong representative example that switchbacks tend to have a preferential orientation, we also report the observation of a patch of magnetic switchbacks that consistently deflected in the same direction for over 16h. The deflections are all contained within the ecliptic plane and are one-sided with respect to the Parker spiral.

We discuss the implications of the preferred orientation we find (section 6.5), showing that it favors an invariant geometry in the equatorial plane associated with a clockwise rotation and positive V_T flows, while it may favor a symmetrical geometry north and south of the HCS (Figure 6.11). These results are globally consistent with the observations of Horbury et al. (2020a), Macneil et al. (2020), and Meng et al. (2022). The bias in $-\phi$ might find its cause in the interchange reconnection process occurring in the low corona, which would reconcile the shear induced by the different rotation rates of the photosphere and the corona. By contrast, the preferential orientation we find is inconsistent with a turbulence generation as developed by Squire et al. (2020), Mallet et al. (2021), and Shoda et al. (2021), or in situ

velocity shears, as developed by Ruffolo et al. (2020), that ought to produce more isotropic fluctuations.

Summary

We conclude this part of the manuscript that focused on magnetic switchbacks, mainly reporting that they are more likely to form near the Sun's surface than in situ in the solar wind.

We first described the characteristics of magnetic switchbacks, as well as their numerous associated mysteries, and highlight that the formation processes devised to explain their observation are legions. We chose from the start to define switchbacks as a deviation from the Parker spiral.

We investigated the temporal and spatial characteristic scales of magnetic switchback patches by performing a wavelet transform of the magnetic deflection angle to the Parker spiral. We found periodic spatial modulations at two distinct wavelengths, respectively consistent with solar granulation and supergranulation scales. In addition we found that switchback occurrence and spectral properties seemed to depend on the source region of the solar wind rather than on the radial distance of PSP. Our result suggests that switchbacks most probably originate in the low solar atmosphere since their occurrence appears to be modulated by the effects of solar surface motion at the granular and supergranular scales.

We then investigated statistically the orientation of the magnetic deflections measured by PSP. We first characterized the quiet solar wind orientation and found that the Parker spiral model indeed remains accurate at such short distances from the Sun, even though the influence of the acceleration region is felt in the latest encounters. We then adopted a modeling approach and assumed that the wind was composed of two populations with distinct distribution properties, respectively representing the background and perturbed solar winds. We find that the actual distribution of orientation angles is well reproduced by this method and we were able to characterise the deflection angles of the switchback population. We concluded that switchbacks occur in all directions but present a preferential orientation in the clockwise direction. We additionally report on the observation of a patch of magnetic switchbacks that consistently deflect in the same direction for over 16h. The deflections are all contained within the ecliptic plane and are one-sided with respect to the Parker spiral.

The systematic clockwise bias we find in the deflection angles is inconsistent with turbulence that should produce isotropic deviations, and consistent with the interchange reconnection process that occurs in the low corona, which would reconcile the shear induced by the different rotation rates of the photosphere and the corona.

Part III

Ubiquity of magnetic reconnection

Chapter 7

Automatic detection of magnetic reconnection in the solar wind

Contents

7.1 Introduction

Throughout this manuscript, we highlighted the key role of magnetic reconnection in the formation and dynamics of coherent structures in the heliosphere. At the Earth's magnetopause, magnetic reconnection is at the origin of flux transfer events (FTE) formation; in the solar corona, flux ropes are formed through reconnection at the tip of the helmet streamers and expelled in the solar wind; in the low corona, interchange reconnection redistributes the magnetic topology at the solar surface and may be responsible for the creation of the switchback structures observed throughout the heliosphere. Particularly, the work presented in the previous chapters underlined how observing or not observing reconnection exhausts can greatly improve our understanding of the global processes at stakes. Examples are legions: studying reconnecting jet occurrence inside FTEs allowed us to challenge the flux rope structure usually put forward (Øieroset et al., 2016; Kacem et al., 2018; Fargette et al., 2020), exhausts at the boundaries of magnetic switchbacks hint at their erosion through this process (Froment et al., 2021), jets systematically observed at HCS crossings near the Sun tell us of the continuously reconnecting tip of the helmet streamers (Lavraud et al., 2020; Phan et al., 2021).

More generally, magnetic reconnection is key to understanding energy dissipation in space plasmas. However, these jets usually scale from seconds to minutes, and as such they can be quite tedious to find in months or years of data. To this day, the main method for detecting reconnection exhausts remains direct data inspection (Gosling et al., 2005; Phan et al., 2009, 2010, 2020, 2021). Considering the amount of data now available, it is unrealistic to aim

for the exhaustive detection of reconnection jets in the decades of in-situ data provided by Wind, ACE, Helios, PSP and Solar Orbiter, to name a few. Even for smaller periods, the eye tires and might miss some events, while the selection criteria may vary subjectively over time (not to mention the will required for such a lengthy task). Recently, Tilquin et al. (2020) developed a new algorithm to automatise this process and applied it to Helios data. They managed to identify 88 reconnection events over 10 years of Helios data, observed from 0.3 to 1 AU. Their method allowed a significant time reduction in the process of identifying reconnection exhausts. However, they still had to check manually hundreds of potential detections to confirm these 88 events.

In this section, we describe a new approach to the automatic detection of magnetic reconnection exhausts in the solar wind that is inspired from the visual identification process. The method, based on Bayesian probabilities, is still under development but show promising results on Solar Orbiter data. We first present the jet detection algorithm (section 7.2) and evaluate its performance over one month of Solar Orbiter data (section 7.3) where we manage to detect around a hundred of reconnection jets.

7.2 Jet detection algorithm

When searching for magnetic reconnection signatures in situ, we primarily look for ion jets that are centered on coincidental thin, bifurcated current sheets and perform the Walén test to check if the exhaust boundaries are consistent with rotational discontinuities of opposite correlations (see for instance sections 1.2.3, 2.4.1, 3.3). It is this process, which seems quite simple at first glance, that we aim to automatise:

- the algorithm first detects interval where a change of correlation occurs between $\mathbf{B}$ and $\mathbf{V}$ using the Walén relation and probabilistic considerations (section 7.2.1)
- All detected intervals are then rotated to their corresponding lmn frames and several conditions are imposed to check for a reconnection exhaust (section 7.2.2)

7.2.1 Detecting a change of correlation

The first feature we focus on detecting is a quantifiable change of correlation in the in-situ data. To do this, we test the Walén relation and compare different models on various scales using a sliding window method.

Model definitions

Let $\widehat{t}$ be a time vector centered on a time t_0 and containing n_p data points spaced by a constant dt. (We note that as $\widehat{t}$ is completely characterised by t_0, n_p and dt. Since we use regularly sampled data sets, meaning that dt remains constant throughout the analysis, a dependence in $\widehat{t}$ can be re-writen as a dependence in (t_0, n_p)). We call $\mathbf{V}(\widehat{t})$ the velocity vector measured by the spacecraft on this given temporal window. Since the Walén relation that we want to test applies to the variation of this vector, we take a point of reference at the window's center t_0 and consider the relative variation vector $\Delta\mathbf{V}(\widehat{t}) = \mathbf{V}(\widehat{t}) - \mathbf{V}(t_0)$, which means that $\Delta\mathbf{V}(t_0) = 0$.

We aim to compare this relative velocity vector $\Delta\mathbf{V}(\widehat{t})$ to a modeled velocity $\Delta\mathbf{V}_{\mathcal{M}}(\widehat{t},\boldsymbol{\Theta})$ that is defined as follows :

$$\Delta\mathbf{V}_{\mathcal{M}}(\widehat{t},\boldsymbol{\Theta}) = \begin{cases} \Theta_a\ \Delta\mathbf{V}_{\mathbf{A}}(\widehat{t}), & \text{if } t \leq t_0 \\ \Theta_b\ \Delta\mathbf{V}_{\mathbf{A}}(\widehat{t}), & \text{otherwise} \end{cases} \tag{7.1}$$

where $\boldsymbol{\Theta} = [\Theta_a, \Theta_b]^{\mathrm{T}}$ is a two component parameter vector with $\Theta_{a,b} = \pm 1$, and $\mathbf{V}_{\mathbf{A}}(\widehat{t})$ is the Alfvén speed computed over the considered time window. As before, we take the point of reference at the window's center t_0 and $\Delta\mathbf{V}_{\mathcal{M}}(t_0,\boldsymbol{\Theta}) = 0$. Four cases arise, each corresponding to a model $\mathcal{M}_x$:

1. the correlated model $\mathcal{M}_1$ with $\boldsymbol{\Theta}_1 = [+1,+1]^{\mathrm{T}}$
2. the anti-correlated model $\mathcal{M}_2$ with $\boldsymbol{\Theta}_2 = [-1,-1]^{\mathrm{T}}$
3. the model of a correlated / anti-correlated jet $\mathcal{M}_3$ with $\boldsymbol{\Theta}_3 = [+1,-1]^{\mathrm{T}}$
4. the model of an anti-correlated / correlated jet $\mathcal{M}_4$ with $\boldsymbol{\Theta}_4 = [-1,+1]^{\mathrm{T}}$

Likelihood computation

For each model, the log-likelihood of the data may be computed, using a process similar to the one described in section 2.3.3 and using equation (2.15). If we rewrite the latter using the notations of this section, it yields:

$$\ln\Big(\mathrm{p}(\Delta\mathbf{V} \mid \widehat{t},\boldsymbol{\Theta})\Big) = -\frac{1}{2\sigma^2}\sum_{i=1}^{n_p}|\Delta\mathbf{V}(t_i) - \Delta\mathbf{V}_{\mathcal{M}}(t_i,\boldsymbol{\Theta})|^2 - \frac{3n_p}{2}\ln\left(2\pi\sigma^2\right) \tag{7.2}$$

where σ is the noise dispersion we assume for our data $\Delta\mathbf{V}(t_i)$ around its expected value $\Delta\mathbf{V}_{\mathcal{M}}(t_i,\boldsymbol{\Theta})$. For our purpose, we take $\sigma = 3$ km/s, which corresponds to the typical error on the velocity vector for the PAS instrument on Solar Orbiter (Louarn et al., 2021). Equation (7.2) quantifies the probability of observing our dataset $\Delta\mathbf{V}(\widehat{t})$ assuming a parameter vector $\boldsymbol{\Theta}$, or equivalently assuming a model $\mathcal{M}$ (see appendix A).

Let us take as an illustration of a reconnection jet observed by the Solar Orbiter mission on July 16 2020, from 18h30 to 18h40 (Lavraud et al., 2021). We consider a window centered on t_0 = 18h34:52 and with a 900 s width ($dt = 4$ s, $n_p = 225$). In Figure 7.1, we display the components of $\Delta\mathbf{V}$ (colored scatter plot) on this time window, with the jet mainly observed in the R and N components. t_0 is indicated as a vertical dashed line. Let us assume a correlated model, and visualise the associated likelihood of the data. We plot as thin white lines the components of $\Delta\mathbf{V}_{\mathcal{M}_1} = +\Delta\mathbf{V}_{\mathbf{A}}$ (which then roughly corresponds to the magnetic field variation), and the background is colored by the local marginalised likelihood $\mathrm{p}(\Delta V_x \mid t_i,\boldsymbol{\Theta})$. As expected for each component, it takes the shape of a Gaussian with a 3 km/s width and centered on the modeled velocity. As such, we can read from this figure the probability of observing the component value of each data point[1]. The log-likelihood of the correlated model on this interval is then given by equation (7.2).

[1]This is mainly illustrative as the total probability distribution function of the likelihood is a 3D Gaussian function, and each data point is associated with a unique likelihood value.

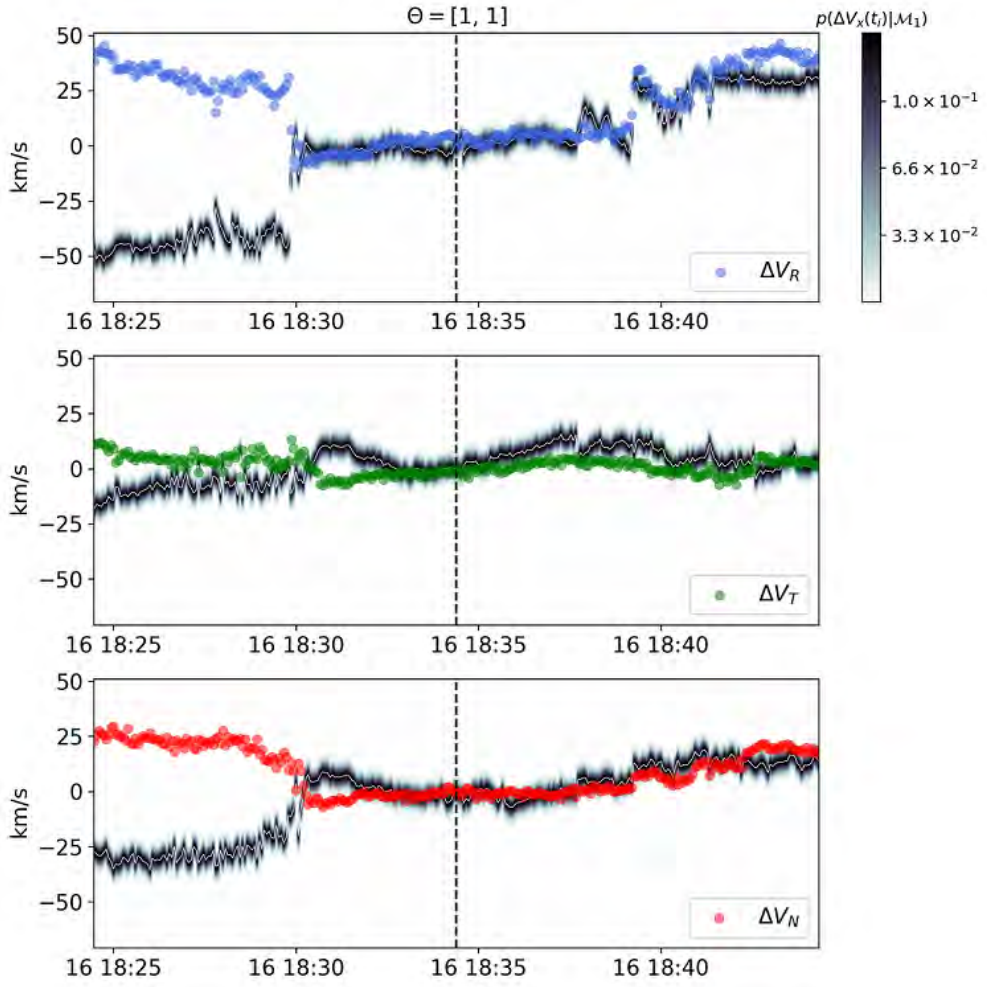

Figure 7.1: Likelihood map of a correlated model : on each panel, a scatter plot of the velocity variation $\mathbf{\Delta V}$ is displayed over a background colored by the local likelihood associated with the correlated model for each component $\mathrm{p}(\Delta V_x \mid t_i, \mathbf{\Theta})$. The dashed line indicates the window's center t_0 and the thin white line is the modeled correlated velocity $\mathbf{\Delta V}_{\mathcal{M}_1} = +\mathbf{\Delta V_A}$

Prior and posterior computation

We have computed the likelihood of the data for each model or, in other words, we now know which model is best at explaining the data. However, as underlined in appendix A, the likelihood of observing a data set given by a model (eq. (7.2)) is not equivalent to the accuracy of this model. We need to compute the posterior probability for each model through the Bayes equation ((A.8)) and compare these models through equation (A.17). We then need to define a prior probability for the different models, i.e. for the different values of $\mathbf{\Theta}$.

In this prior definition lays the core of the detection algorithm, as this decision amounts to setting a threshold on the detection. It is at this step that we inject our prior knowledge of the solar wind and magnetic reconnection, by defining the *a priori* probability of observing a change of correlation in the solar wind. The log-posterior probability writes according to

the Bayes formula :

$$\ln \mathrm{p}(\mathbf{\Theta} \mid \widehat{t}, \Delta\mathbf{V}) = \ln \mathrm{p}(\mathbf{\Theta}) + \ln \mathrm{p}(\Delta\mathbf{V} \mid \widehat{t}, \mathbf{\Theta}) + \mathrm{C} \tag{7.3}$$

with C a constant (the evidence, which is model independent). If we assume that each data point has a 10% chance of being part of a change of correlation, i.e. the prior $p(jet) = 0.1$, then the different priors take the values $p(\mathbf{\Theta_1}) = p(\mathbf{\Theta_2}) = \frac{0.1}{2} n_p$ and $p(\mathbf{\Theta_3}) = p(\mathbf{\Theta_4}) = \frac{0.9}{2} n_p$.

Model Comparison

We may now compare our four different models and pick the one with the highest log-posterior probability. To avoid comparing the models two by two and since we are only interested in the jet detection regardless of the correlation order, we may use the maximum log-posteriors of similar models and define q the log-probability of observing a change of correlation on our defined window as:

$$\begin{aligned} q(\widehat{t}) = \ln \mathrm{p}(\text{correlation change} \mid \widehat{t}, \Delta\mathbf{V}) = &\max\left(\ln \mathrm{p}(\Delta\mathbf{V} \mid \widehat{t}, \mathbf{\Theta}_3), \ln \mathrm{p}(\Delta\mathbf{V} \mid \widehat{t}, \mathbf{\Theta}_4)\right) \\ &- \max\left(\ln \mathrm{p}(\Delta\mathbf{V} \mid \widehat{t}, \mathbf{\Theta}_1), \ln \mathrm{p}(\Delta\mathbf{V} \mid \widehat{t}, \mathbf{\Theta}_2)\right) \end{aligned} \tag{7.4}$$

A change of correlation is detected on our considered window if the scalar value given by equation (7.4) is positive.

Expanding to the complete data set

Until now, we only considered a given time window $\widehat{t}$, characterised by its center t_0 and width n_p. For this time window, we computed a scalar value which is the log-probability of observing a correlation change knowing the data on this given window. This quantity can be written $q(t_0, n_p)$ or, equivalently $q_s(t_0)$, with the subscript s designating the scale of the temporal window used, i.e $n_p dt$. Let us now expand to a complete data set characterised by a time vector t. To sweep through this data set, we only need to repeat the process we just described while shifting t_0. This yields a continuous log-probability over time $q_s(t)$. To detect correlation changes on different scales, one then needs to iterate over s. A potential jet is flagged whenever the quantity $q_s(t)$ becomes positive.

In Figure 7.2, we illustrate the flagged intervals detected by our algorithm at this point. We show around 3 h of data observed on 2020-07-16, from 21h15 to 23h59. Panels a to c display the magnetic field and velocity components, while panel d shows the quantity $q_{80}(t)$ that indicates the probability of observing a reconnection exhaust on a 80 s scale. The intervals where $q_{80}(t)$ becomes positive are shaded in light blue. At this point, we only detect probable changes of correlation between $\mathbf{B}$ and $\mathbf{V}$. Some are indeed reconnection jets while others are not. The following section aims to determine which are actual reconnection exhausts.

7.2.2 Jet detection

A change of correlation is a necessary condition for detecting reconnection jets. However, it is not a sufficient condition. After running our first part of the detection algorithm, we

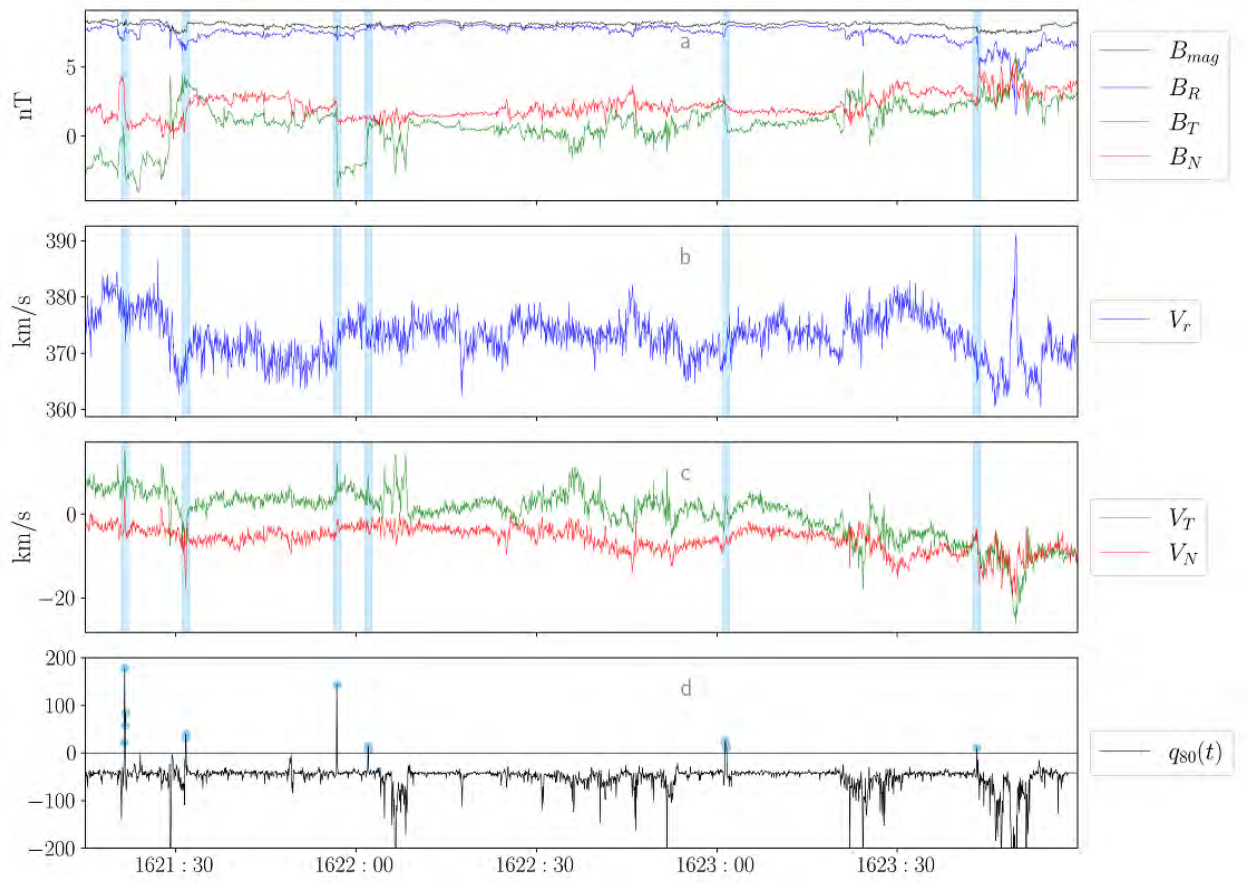

Figure 7.2: Log-posterior probability of a correlation change on 07-16, from 21h15 to 23h59: panels a to c display the RTN components of the magnetic field and velocity vector, and panel d shows the log-posterior probability $q_{80}(t)$. Intervals where this quantity is positive are shaded in light blue.

end up with a list of intervals that potentially harbor a reconnection jet, as illustrated on Figure 7.2, but we still need to remove false detections. Before imposing further constraints our detected intervals, we require a detection of the correlation change on a minimum of two consecutive points.

Current sheet frame

The first step we take is to transform each interval to its associated lmn frame. Here we need the l direction to be the maximum variance direction of the magnetic field, and to this extent we use the minimum variance analysis technique (Sonnerup & Cahill, 1967). This way, the **B** variation as well as the velocity jet should only be carried by the l direction. Similarly to Tilquin et al. (2020), we impose that the B_l component should reverse over the interval. In Figure 7.2, this condition accurately removes the second detection made around 21h31:40.

A condition on the electric current

Since we are searching for a change of correlation coincidental to a current sheet, there always exists a magnetic shear and an associated current. In the limit of null magnetic shear and current, of course reconnection may not occur, but this constitutes a singularity. In practice, we should define a minimum current for our algorithm to detect an exhaust. Current measurements are not available as a data product on Solar Orbiter and PSP, hence we devise an approximation for the electric current based on the Maxwell Ampere equation ((1.8d)). In the lmn frame, the rotational of $\mathbf{B}$ writes:

$$\boldsymbol{\nabla} \wedge \mathbf{B} = \begin{bmatrix} \partial_m B_n - \partial_n B_m \\ \partial_n B_l - \partial_l B_n \\ \partial_l B_m - \partial_m B_l \end{bmatrix} \tag{7.5}$$

We assume no variation of $\mathbf{B}$ along m ($\partial_m = 0$), and we neglect the terms $\partial_n B_m$, $\partial_l B_m$ and $\partial_l B_n$ compared to the B_l variation. Indeed, $\mathbf{l}$ is the direction of maximum variance of the magnetic field, and the Hall field (B_m) should be negligible far from the IDR while B_n should remain essentially constant throughout the exhaust. The equation is then simplified into

$$\boldsymbol{\nabla} \wedge \mathbf{B} = \partial_n B_l \mathbf{u_m} \tag{7.6}$$

where $\mathbf{u_m}$ is the unit vector in the m direction. From there we may derive an approximation for the electric current :

$$j_e = \frac{\Delta B_l}{\mu_0 \Delta n} \tag{7.7}$$

The term ΔB_l is computed at the edges of our considered window, and $\Delta n = V_n \Delta t$. After some trial and errors, we set the minimum current required for detection at $j = 0.04$ nA/m^2. This part of the detection algorithm relies on several assumptions and may be improved in the future.

The existence of a jet

Finally, we need to ensure that a jet is indeed observed on the l component of the velocity. To this extent, we require two additional conditions:

- The signs of the V_l variation between the window's center and both edges of the interval should be the same,
- The velocity variation between the window's center and both edges of the interval should be at least 30% of the maximum V_l variation of the interval.

The first point is there to discard changes of correlations that associate with a rotation of $\mathbf{V}$. The second requirement discards intervals where V_l does not display a sufficiently clear jet signature, but this is at the expense of removing the most asymmetric reconnection cases. In Figure 7.2, these conditions accurately remove the last detection made around 23h45, leaving four true exhaust detections for this interval at the 80 s scale.

7.2.3 Assumption summary

In the algorithm just presented, we make several assumptions that impact the detection and some may be improved in the future. We list them here for the sake of clarity :

- the instrumental noise on the measured velocity is taken at 3 km/s for all components (Louarn et al., 2021). Considering the geometry and design of the instrument, the accuracy could be different between the R and T, N components of the velocity, but these are not studied in detail in the context of the present study,
- we assume a 10% chance of observing a change of correlation. This prior is subjective, and increasing or decreasing this value significantly impacts the number of detections of the algorithm,
- we impose the detection of a correlation change on a minimum of two consecutive points
- we require a B_l reversal over the interval,
- we require a minimum electric current of $j = 0.04$ nA/m^2. This value was found by trial and errors and should be better justified in future work.
- We require a V_l variation of at least 30% of the maximum V_l variation at each exhaust boundary. This value was found by trial and errors and should also be justified in future work.

#	Duration (s)	Start time	End time	Status
1	20	06:56:51.716	06:57:11.716	Lavraud et al. (2021)
2	172	07:40:23.721	07:43:15.721	False detection
3	124	12:35:15.749	12:37:19.749	Lavraud et al. (2021)
4	184	12:57:15.751	13:00:19.752	False detection
5	28	13:50:43.757	13:51:11.757	Potential detection
6	24	14:28:03.760	14:28:27.760	New detection
7	20	14:56:19.763	14:56:39.763	Lavraud et al. (2021)
8	20	16:26:59.772	16:27:19.772	Potential detection
9	684	18:28:19.783	18:39:43.785	Lavraud et al. (2021)
10	20	21:21:23.800	21:21:43.800	New detection
11	28	21:31:27.801	21:31:55.801	Potential detection
12	20	21:56:39.804	21:56:59.804	Lavraud et al. (2021)
13	44	22:01:39.804	22:02:23.804	New detection
14	52	23:01:03.810	23:01:55.810	Lavraud et al. (2021)

Table 7.1: Intervals flagged as potential reconnection jets by the algorithm on 2020-07-16

7.3 Detection in Solar Orbiter data

7.3.1 Jet detection on 24h of data

Let us now test our algorithm on a 24h interval corresponding to 2020-07-16. We plot the magnetic field and velocity vector components in Figure 7.3. This day was studied by Lavraud et al. (2021), who visually identified 6 reconnection jets. In our automatic search, we investigate 20 scales from 30 s to 900 s that are logarithmically spaced. Our algorithm runs in 4 seconds and retrieves 14 potential reconnection jets that are listed in table 7.1 and

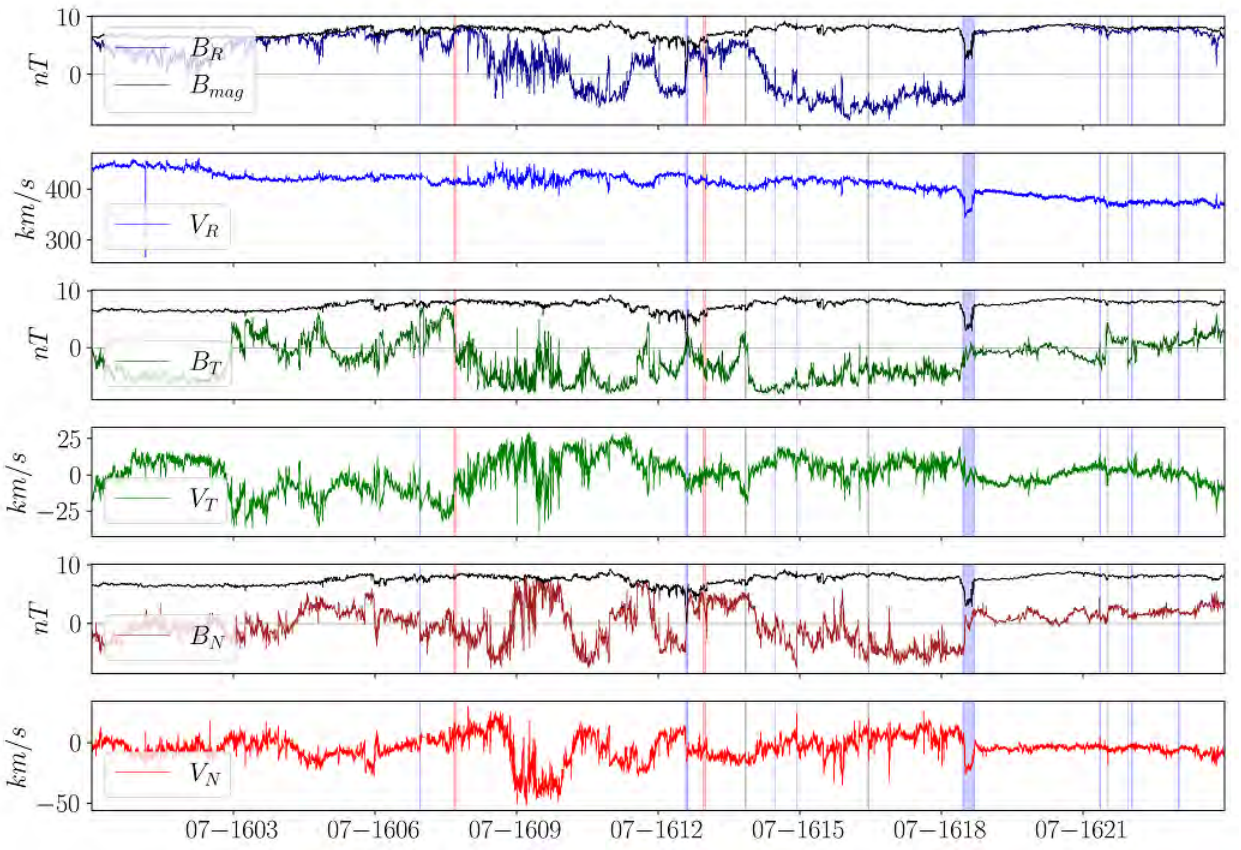

Figure 7.3: Detection of reconnection exhausts on a 1-day interval. The different panels show the RTN components of the magnetic field and the velocity, and intervals detected by the algorithm are shaded blue for true detections, in red for false detection and in grey for potential detections.

shaded in Figure 7.3. After a visual inspection of the potential detections, we identified false detections (red), true detections (blue), and a less clear potential detections. The algorithm accurately finds the 6 reconnection jets identified in Lavraud et al. (2021) and adds 3 new true detections. Two intervals are flagged but are not reconnection exhausts.

7.3.2 Jet detection on one month of data

We repeat our analysis on one month of data, from 2020-07-14 05:15:35 to 2020-08-12 23:59:55. Our algorithm runs in around 1 hour, and the resulting 412 preliminary detections are shown in Figure 7.4. The algorithm takes longer to run for this long period as the data sample is larger. In addition, periods of less Alfvénic winds take longer to investigate, as the algorithm yields more false positive detections. After a first visual inspection of the jets, we were able to confirm 107 actual reconnection jets in this one month of data, which we provide in table 7.2. As the algorithm is still under development, this list is preliminary and additional jets might be detected in the near future. We also have a lot of room to reduce the number of false detections.

To conclude, the algorithm in its current state seems promising for greatly decreasing the de-

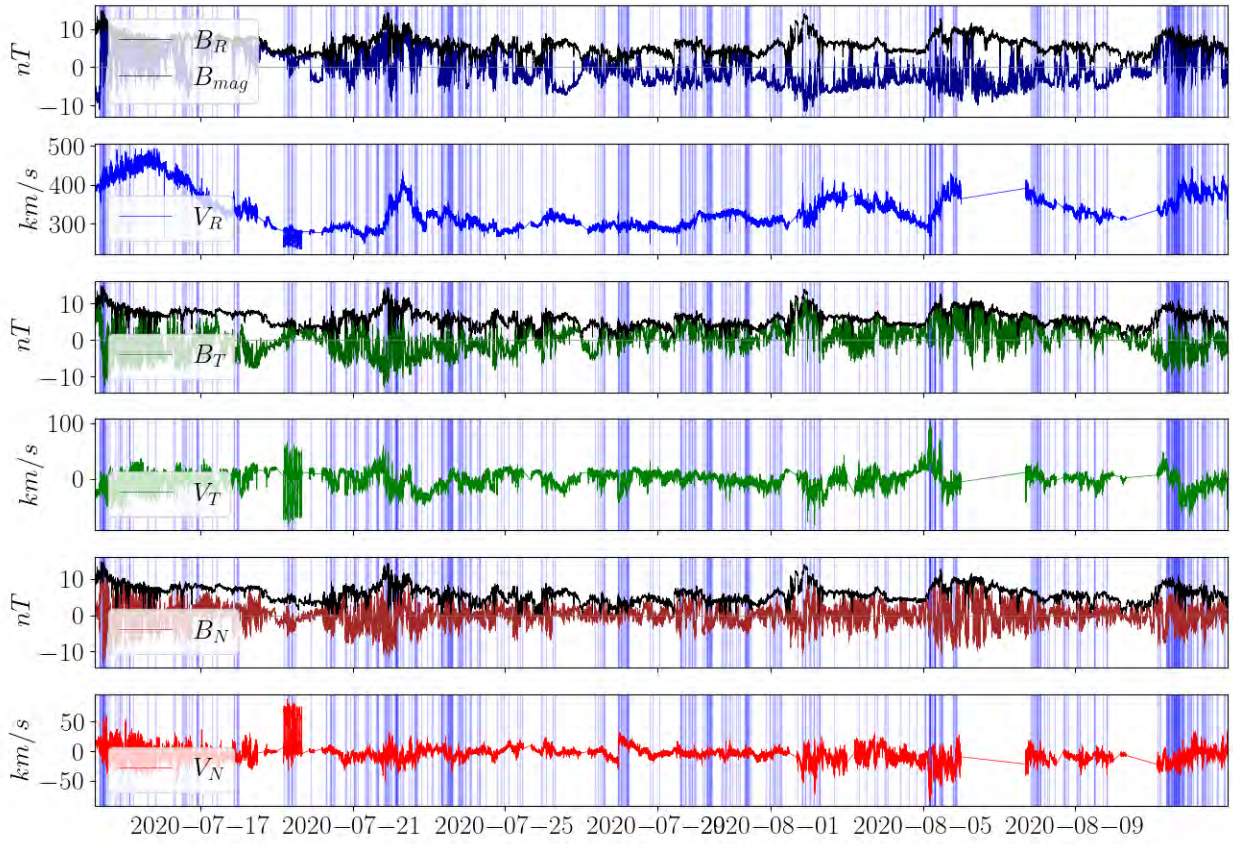

Figure 7.4: Detection of reconnection exhausts on a 1-month interval, from 2020-07-14 05:15:35 to 2020-08-12 23:59:55, presented in the same manner of Figure 7.3. All potential detections are highlighted in blue.

tection time of reconnection exhausts in an Alfvénic plasma, compared to manual detection. Several paths may be investigated to reduce the number of false positives while keeping the true detections. Refining the thresholds defined in section 7.2 is a first option, and several additional constraints also may be introduced based on the physics of magnetic reconnection. Future work is required to achieve a satisfactory balance between false and true detections.

#	Date	Start time	End time
1	07-14	09:35:47.452	09:36:07.452
2	07-14	09:53:39.454	09:54:31.454
3	07-14	10:42:43.459	10:43:07.459
4	07-14	10:45:15.459	10:46:51.459
5	07-14	11:05:35.461	11:05:59.461
6	07-14	12:01:35.466	12:01:59.4664
7	07-14	20:54:47.518	20:56:59.518
8	07-15	03:09:27.555	03:09:51.555
9	07-16	06:56:43.716	06:57:19.716
10	07-16	12:34:39.749	12:37:59.749
11	07-16	14:56:19.763	14:56:39.763
12	07-16	18:27:43.783	18:41:03.785
13	07-16	21:21:11.800	21:21:51.800
14	07-16	21:56:27.804	21:57:07.804
15	07-17	20:58:15.938	20:58:39.938
16	07-19	07:08:04.137	07:08:44.137
17	07-20	10:29:36.296	10:35:20.297
18	07-22	00:05:56.515	00:06:52.515
19	07-22	03:29:16.535	03:29:40.535
20	07-22	03:46:13.000	03:46:36.536
21	07-22	04:20:40.540	04:21:36.540
22	07-22	11:12:04.580	11:13:00.580
23	07-22	13:12:16.591	13:12:40.591
24	07-22	16:01:24.608	16:02:00.608
25	07-22	19:03:08.625	19:03:32.625
26	07-23	08:45:28.705	08:47:40.705
27	07-23	09:19:52.709	09:20:28.709
28	07-23	10:02:32.713	10:02:56.7134
29	07-23	11:05:36.719	11:06:16.719
30	07-23	12:12:20.725	12:13:16.725
31	07-23	12:51:16.729	12:51:56.729
32	07-23	13:55:16.735	13:56:12.735
33	07-23	16:08:20.748	16:08:44.748
34	07-23	18:31:08.762	18:31:48.762
35	07-23	21:02:12.777	21:02:36.777
36	07-24	01:29:28.803	01:39:24.804
37	07-24	06:26:48.831	06:32:28.832
38	07-24	07:41:48.839	07:42:44.839
39	07-26	01:55:53.085	01:56:17.085
40	07-26	05:57:17.108	05:57:57.108
41	07-27	14:27:33.297	14:27:57.297
42	07-27	23:28:29.350	23:30:45.350
43	07-28	01:13:09.360	01:23:05.361
44	07-28	01:24:09.361	01:29:49.362
45	07-28	19:10:45.465	19:11:25.465
46	07-29	14:35:17.578	14:36:13.578
47	07-29	18:02:49.598	18:03:09.598
48	07-30	04:22:57.658	04:32:53.659
49	07-31	03:17:29.791	03:18:09.791
50	07-31	04:13:41.797	04:15:57.797
51	07-31	07:53:49.818	07:56:05.818
52	07-31	09:53:57.830	09:59:37.830
53	07-31	10:00:21.830	10:01:13.831
54	08-01	16:51:38.010	16:52:54.010
55	08-01	22:30:58.043	22:31:22.043
56	08-02	00:32:54.055	00:33:50.055
57	08-03	17:23:58.293	17:24:34.293
58	08-03	18:17:30.298	18:17:54.298
59	08-03	19:08:50.303	19:09:30.303
60	08-03	23:46:34.330	23:47:54.330
61	08-05	04:28:18.497	04:29:14.497
62	08-05	05:19:26.502	05:20:02.502
63	08-05	07:11:54.513	07:12:18.513
64	08-05	07:14:22.513	07:14:58.513
65	08-05	07:29:42.515	07:30:22.515
66	08-05	08:40:58.522	08:41:54.522
67	08-05	08:49:06.522	08:49:30.522
68	08-05	09:32:58.527	09:33:38.527
69	08-05	10:08:18.530	10:09:50.530
70	08-05	10:20:46.531	10:21:10.531
71	08-05	10:49:22.534	10:49:46.534
72	08-05	11:34:58.538	11:37:18.539
73	08-05	11:41:10.539	11:42:34.539
74	08-05	20:23:18.590	20:23:42.590
75	08-05	20:35:02.591	20:37:14.591
76	08-07	20:01:50.867	20:03:06.867
77	08-07	22:10:38.880	22:10:58.880
78	08-08	00:10:06.891	00:10:46.891
79	08-08	00:12:02.891	00:13:22.892
80	08-09	02:33:11.045	02:33:51.045
81	08-09	11:56:51.100	12:00:07.100
82	08-09	22:28:23.161	22:29:19.161
83	08-11	09:32:19.365	09:32:43.365
84	08-11	11:19:19.375	11:19:43.375
85	08-11	12:19:39.381	12:20:19.381
86	08-11	13:48:27.390	13:48:51.390
87	08-11	13:53:07.390	13:53:31.390
88	08-11	15:49:55.402	15:50:31.402
89	08-11	16:53:03.408	16:55:15.408

90	08-11	17:08:47.409	17:09:27.409
91	08-11	17:17:47.410	17:18:43.410
92	08-11	18:22:03.416	18:22:39.417
93	08-11	19:35:11.424	19:35:35.424
94	08-11	19:43:03.424	19:43:27.424
95	08-11	20:10:59.427	20:11:19.427
96	08-11	20:48:59.431	20:49:23.431
97	08-11	20:56:55.431	20:57:35.432
98	08-11	23:11:51.445	23:12:27.445
99	08-12	04:32:15.476	04:32:47.476
100	08-12	04:59:27.478	04:59:47.478
101	08-12	07:24:23.492	07:26:35.493
102	08-12	07:34:35.493	07:35:39.493
103	08-12	09:01:15.502	09:01:55.502
104	08-12	09:02:35.502	09:02:55.502
105	08-12	09:10:23.503	09:10:47.503
106	08-12	09:47:11.506	09:48:07.506
107	08-12	10:10:51.509	10:11:15.509

Table 7.2: Timetable of jets detected between 2020-07-14 05:15:35 and 2020-08-12 23:59:55 by Solar Orbiter

Chapter 8

Moving forward

To conclude this manuscript, this chapter outlines the perspectives and paths that might be explored in future research projects.

8.1 Conclusions and perspectives (EN)

8.1.1 Part one

In the first part of the manuscript (part I), we focused on flux ropes and interlaced flux tubes, drawing a parallel between observations made at the Earth's magnetopause and in the solar wind. We found that interlaced flux tubes are often observed at the magnetopause and that they form under peculiar IMF orientation (chapter 2). We proposed a formation mechanism based on the interlacing of flux tubes originating from two spatially distinct X-lines located on the same longitude at the magnetopause. We then report on similar structures observed in the solar wind, and show that their signatures are consistent with interlaced flux tubes (chapter 3).

The catalogue of magnetospheric FTEs we computed (chapter 2) provides a basis for further statistical study of these events. Kieokaew et al. (2021) used this catalogue for instance to further confirm their link to the IMF orientation by finding a clear correlation with the helicity sign of flux rope FTEs. Further work is ongoing regarding the statistical orientation of these FTEs and its compatibility with the X-line orientation at the subsolar region. In the same perspective, another interesting path would be to investigate the global orientation of IFTs (i.e FTEs with reconnecting current sheets) as well as the geometry of their core reconnection site, and to compare this to the IMF orientation and global topology of the magnetosphere. These studies would give further insights into the formation process of these structures through dayside magnetic reconnection. Several studies also investigate the conditions required for magnetic reconnection to occur, proposing that the pile up of magnetic energy observed in IFTs allows reconnection to develop (Øieroset et al., 2021). Similar investigations regarding orientation and pile-up could be carried out in the solar wind interlaced flux tubes (or MICCS) that we report on in chapter 3. In addition, magnetic reconnection is not as frequent in the regular solar wind near the Sun compared to 1 AU, and MICCS structures could be a favored place to look for magnetic reconnection and understand

its characteristics in the turbulent solar wind.

8.1.2 Part two

In the second part of the manuscript (part II), we focused on magnetic switchbacks, a key feature of the near-Sun solar wind. We found that switchbacks most probably originate in the low solar atmosphere since their occurrence appears to be modulated by the effects of solar surface motion at the granular and supergranular scales (chapter 5). We also found that their preferred orientation of their deflection is consistent with the interchange reconnection process that occurs in the low corona, in response to the shear induced by the different rotation rates of the photosphere and the corona (chapter 6).

The closest encounters of PSP with the Sun should help improve our understanding of switchbacks, as linking the in-situ data to the Sun's surface should become more straightforward as the probe gets closer to the star. Their properties compared to the spacecraft's accurate connectivity would bring much constraints on their source regions. Additional statistical study could also highlight other properties, and checking their in-situ signatures to the flux-rope structure proposed by (Drake et al., 2021) would be important since it is the only scenario producing structures stable enough to propagate in the corona. Aside observations, numerical simulations of interchange reconnection should investigate whether there exists circumstances under which it is able to produce switchback structures that would propagate stably throughout the solar corona. Observations from Solar Orbiter could additionally prove decisive and provide the first remote observation of magnetic switchbacks. Finally, the impact of switchbacks on their surrounding in the solar wind is yet not known, and quantifying how much and how they transfer energy to the regular solar wind can lead to several breakthroughs in our understanding of the solar wind properties at 1 AU.

8.1.3 Part three

The last part of the manuscript (part III) presents a new approach to automatically detect magnetic reconnection exhausts in solar wind from in-situ data. This algorithm has yet to be improved and fully implemented to analyse in-situ data efficiently. Obtaining an accurate algorithm without too many false detections would greatly decrease the time necessary to detect magnetic reconnection, making it possible to perform large statistical analysis of reconnection jets in the solar wind. This would be a significant step forward in understanding the process of magnetic reconnection in the solar wind.

8.2 Conclusions et perspectives (FR)

8.2.1 Première partie

Dans la première partie de ce manuscrit (partie I), nous avons étudié les cordes de flux et les tubes de flux entrelacés, en établissant un parallèle entre les observations faites à la magnétopause terrestre et dans le vent solaire. Nos observations montrent que les tubes de flux entrelacés (IFT) sont observés fréquemment à la magnétopause, et qu'ils se forment lorsque l'IMF présente une orientation particulière (chapitre 2). En partant de ces observations, nous avons proposé un mécanisme de formation basé sur deux lignes de reconnection magnétique

à la magnétopause, spatialement distinctes situées sur la même longitude. Nous présentons ensuite l'observation de structures similaires dans le vent solaire (MICCS), et montrons que leurs signatures sont cohérentes avec une structure en tubes de flux entrelacés (chapitre 3).

Le catalogue de FTEs magnétosphériques produit (chapitre 2) fournit une base pour de futures études statistiques approfondies de ces événements. Kieokaew et al. (2021) a par exemple utilisé ce catalogue pour confirmer leur lien avec l'orientation de l'IMF, en soulignant une corrélation claire avec le signe de l'hélicité des FTEs en corde de flux. D'autres travaux sont en cours concernant l'orientation statistique de ces FTE, et la compatibilité de cette orientation avec l'orientation de la ligne X dans la région subsolaire de la magnétopause. De la même manière, il sera intéressant d'étudier l'orientation globale des IFTs (c'est-à-dire des FTEs avec des signatures de reconnection en leur centre) ainsi que la géométrie de leur site de reconnexion central, et de comparer les résultats avec l'orientation de l'IMF et la topologie globale de la magnétosphère. Ces études permettront de mieux comprendre le processus de formation de ces structures par la reconnexion magnétique côté jour. Une autre piste de recherche porte sur les conditions requises pour que la reconnexion magnétique se déclenche, plusieurs études s'intéressant notamment à l'accumulation de flux magnétique comme une condition nécessaire à son apparition (Øieroset et al., 2021). Des études similaires pourraient être menées sur l'orientation des MICCS observés dans le vent solaire, ainsi que sur le rôle de l'accumulation du flux magnétique dans ces structures. Enfin, la reconnection magnétique est moins fréquemment observée dans le vent solaire proche du soleil qu'à une unité astronomique, et les structures MICCS pourraient être des endroits privilégiés pour rechercher la reconnexion magnétique et comprendre ses caractéristiques dans le vent solaire turbulent.

8.2.2 Deuxième partie

Dans la deuxième partie de ce manuscrit, (partie II), nous avons étudié les switchbacks magnétiques, des structures omniprésentes dans le vent solaire proche du Soleil. Nos résultats montrent que les switchbacks sont probablement formés dans la basse atmosphère solaire, puisque leur fréquence d'observation est modulée par des effets de surface aux échelles de granulation et supergranulation (chapitre 5). Nous montrons également que l'orientation préférentielle de ces défections est cohérente avec le mécanisme de reconnexion d'interchange qui a lieu dans la basse couronne, et qui atténuerait le cisaillement induit par les différentes vitesses de rotation entre la photosphère et la couronne (chapitre 6).

Les orbites les plus récentes de PSP (plus proches du Soleil) devraient améliorer notre compréhension de la formation des switchbacks. En effet, lier les observations in-situ avec la surface du Soleil devient plus aisé à proximité de l'étoile. Une comparaison des propriétés des switchbacks par rapport à la connectivité du satellite apporterait de fortes contraintes sur leurs régions de formation à la surface. Des études statistiques pourraient par ailleurs être menées pour mettre en avant d'autres propriétés des switchbacks, et particulièrement comparer leurs signatures au modèle de corde de flux proposé par Drake et al. (2021). Ce modèle est en effet le seul à proposer un scénario produisant des structures suffisamment stables pour se propager dans la couronne solaire. En dehors des observations, les simulations numériques de la reconnexion d'interchange permettraient de déterminer si elle est capable dans certaines circonstances de produire des structures stables se propagenat dans la

couronne solaire. Les observations de Solar Orbiter pourraient en outre s'avérer décisives et fournir la première observation à distance des switchbacks. Enfin, l'impact des switchbacks sur leur environnement dans le vent solaire n'est pas encore connu, et comprendre comment leur énergie est transférée dans le vent solaire et en quelle quantité pourrait mener à des avancées majeures dans notre compréhension des propriétés du vent solaire à 1 AU.

8.2.3 Troisième partie

La dernière partie de ce manuscrit (partie III) présente une nouvelle approche pour détecter automatiquement les jets de reconnexion magnétique dans le vent solaire à partir de données in-situ. Cet algorithme est encore en cours de développement et a pour but d'analyser efficacement les données in-situ. Un tel algorithme de détection automatique permet d'envisager des études statistiques de jets de reconnexion observés dans le vent solaire, ce qui serait une avancée importante dans la compréhension du phénomène de la reconnexion magnétique.

In the end, only scientific consensus can aim for the status of established knowledge. With the work carried out during the past three years, we hope we have succeeded in taking one small step towards that direction.

Part IV

Appendix

Appendix A

Notions of Bayesian statistics

Bayes' theorem is one of the most important formula in the world of probabilities. It is a powerful tool, used for instance in machine learning and artificial intelligence, and central to scientific discovery. In this appendix, we aim to give an overview of the Bayesian approach and give a sense of its importance. We also present the derivations of several calculations used in this manuscript.

A.1 Definitions

First, let us begin with some basic useful definitions. A *probability density function* (PDF) $p(x)$ describes the probability for random variable X to take the value x, with the normalisation condition :

$$\int_x p(x)\,dx = 1 \tag{A.1}$$

The *joint PDF* $p(x, y)$ of two random variables X and Y is then the probability distribution of all possible pairs $(X = x) \cap (Y = y)$. By taking a slice of the joint PDF at a given value of x or y, we get a *conditional PDF* which correspond to the density function of one variable knowing the value of the other. These conditional probabilities are written $p(y|x)$[1] or $p(x|y)$, and verify:

$$\int_x p(x|y)\,dx = \int_y p(y|x)\,dy = 1 \tag{A.2}$$

The *marginal PDF* is the probability distribution of one variable regardless of the other variable. It is defined by:

$$p(x) = \int_y p(x, y)\,dy \tag{A.3}$$

and $p(y)$ is defined similarly. These different distributions are illustrated in Figure A.1.

[1] reads "the probability of y given x"

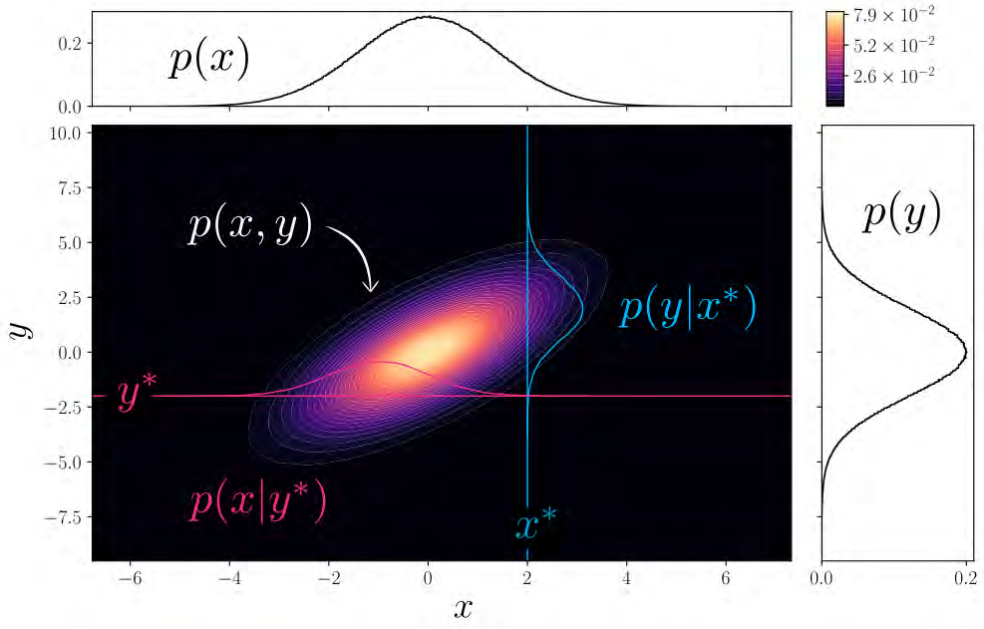

Figure A.1: Illustration of a 2D joint PDF $p(x, y)$, the conditional PDFs $p(y|x^*)$ (in blue) and $p(x|y^*)$ (in red), and the marginal PDFs $p(x)$ (top) and $p(y)$ (right). The conditional PDFs are not to scale for illustrative purposes.

A.2 Bayes identity

A.2.1 Derivation

One can note through the above definitions that $p(x, y) \neq p(x|y)$. Let us suppose that a certain function $c(y)$ verifies:

$$p(x, y) = c(y)p(x|y) \tag{A.4}$$

Then through the normalisation conditions:

$$\begin{aligned} p(y) &= \int_x p(x, y)\, dx \\ &= \int_x c(y)p(x|y)\, dx \\ &= 1 \cdot c(y) \end{aligned} \tag{A.5}$$

Considering the $c(y)$ introduction, we thus have the fundamental relation:

$$p(x, y) = p(y)p(x|y) \tag{A.6}$$

Symmetrically we have

$$p(x, y) = p(x)p(y|x) \tag{A.7}$$

Let x be the parameter vector $\boldsymbol{\theta}$ and y the data vector $\mathbf{d}$, then the Bayes identity follows :

$$\boxed{p(\boldsymbol{\theta}|\mathbf{d})p(\mathbf{d}) = p(\mathbf{d}|\boldsymbol{\theta})p(\boldsymbol{\theta})} \tag{A.8}$$

In this formula, each term has a specific interpretation[2]:

[2]see Bayes theorem, the geometry of changing beliefs

- the prior $p(\boldsymbol{\theta})$ is the probability of a hypothesis (or parameter vector) *before* seeing any evidence (or data)
- the likelihood $p(\mathbf{d}|\boldsymbol{\theta})$ is the probability of seeing the evidence if the hypothesis is true
- the evidence $p(\mathbf{d})$ is the probability of seeing the evidence
- the posterior $p(\boldsymbol{\theta}|\mathbf{d})$ is the probability that the hypothesis is true given some evidence

The posterior is eventually the probability we would like to compute.

A.2.2 An illustration

Let us give an example here to illustrate how the Bayes' rule may apply in our everyday life, and why it is fundamentally different from only computing the likelihood. This example is taken from the youtube channel 3blue1brown, in the video The medical test paradox, and redesigning Bayes' rule.

In this story, a woman, Alice, gets a positive test result for breast cancer in a routine mammography screening. So the doctors wonder : what is the probability of Alice actually having breast cancer given that she just tested positive ? To answer this question, we additionally know that:

- the prevalence of breast cancer in the population is around 1%,
- the sensitivity of the test, i.e the rate of true positive detections, is around 90%,
- the specificity of the test, i.e the rate of true negative detections, is around 91%.

Viewing those numbers, Alice gets alarmed : she has a 90% chance of having breast cancer, knowing that the rate of true detections is 90%! Let us walk through the calculation to check whether or not Alice is correct.

We consider a population of a thousand women. Given the prevalence, 10 of these women do have breast cancer and 990 do not. All women undergo a routine screening, and given the accuracy of the test, 9 out of the 10 women with breast cancer test positive, while 901 out of 990 (91%) of the the women without breast cancer test negative. This situation is illustrated in Figure A.2. The probability of Alice having breast cancer when all you know is that she tested positive, is actually easily readable from the figure:

$$p(ill|test^+) = \frac{9}{9+89} = 9\% \tag{A.9}$$

Or equivalently using Bayes' equation and decomposing the evidence with the law of total probability:

$$p(ill|test^+) = \frac{p(test^+|ill) \cdot p(ill)}{p(test^+)} \tag{A.10}$$

$$= \frac{p(test^+|ill) \cdot p(ill)}{p(test^+|ill) \cdot p(ill) + p(test^+|not\ ill)p(not\ ill)} \tag{A.11}$$

$$= \frac{0.9 \cdot 0.01}{0.9 \cdot 0.01 + 0.99 \cdot 0.09} \tag{A.12}$$

$$= 0.09 \tag{A.13}$$

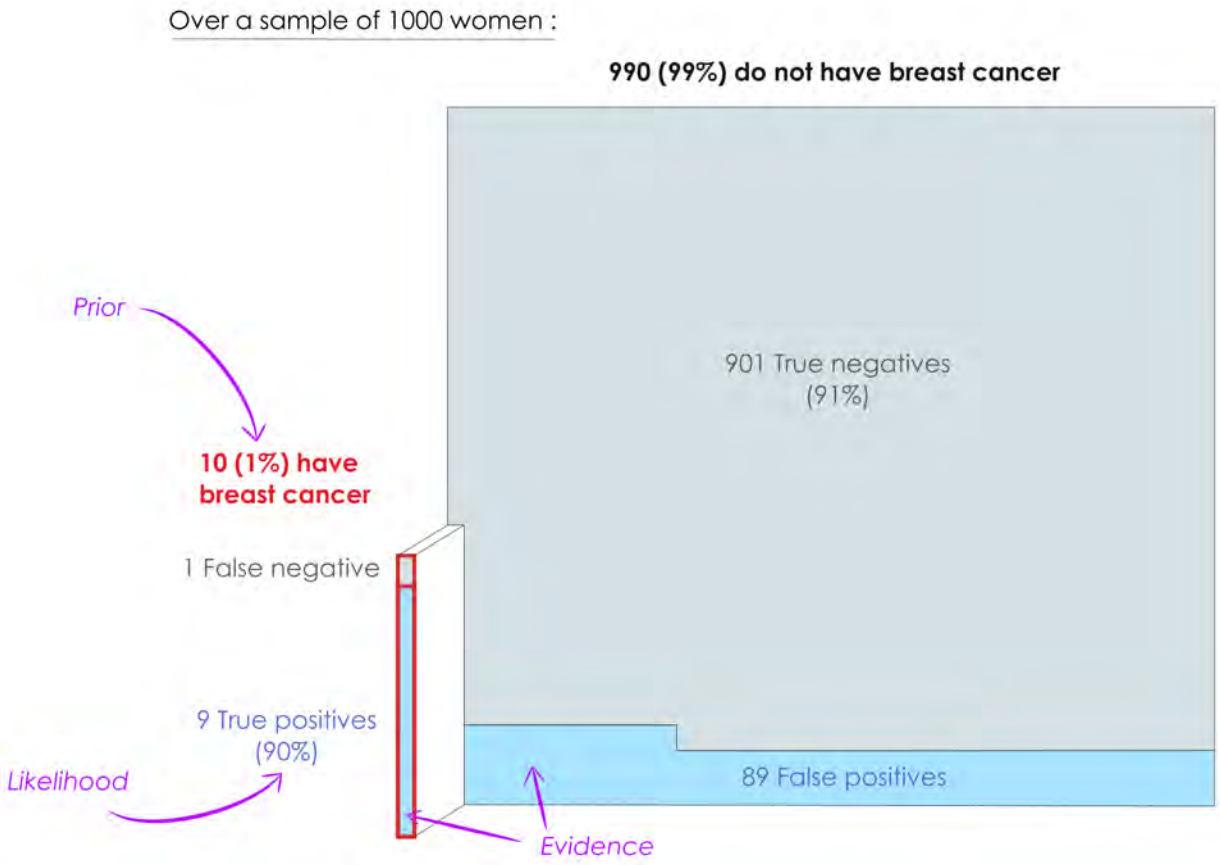

Figure A.2: What is the probability of having breast cancer when tested positive ? The proportion of the population actually having breast cancer is framed in red, and positive test results are colored in blue.

The key point here is that the inclusion of the prior in the computation completely shifts the weight one should give to a positive test result. Alice went from a 1% chance of having breast cancer to a 9% chance, and changing the prevalence of the illness in the population (i.e. the prior) would change the significance of the test result. The Bayes' theorem basically states that new evidence we observe should not completely determine our beliefs from scratch, but rather lead us to update our prior beliefs with regards to new evidence.

A.3 Bayesian inference

A.3.1 Prior choice

In the example presented above, we reasoned with numbers for the sake of illustration. It is usual however to work with probability distribution functions when using the Baye's equation. There are various ways to choose a prior distribution on a parameter, depending on the information collected. It can for instance be deduced from the posterior of a previous experiment, or it can include constraints on the parameter domain (i.e. setting $p(\boldsymbol{\theta}) = 0$ in unallowed regions), or it can be deduced from expert information, e.g. from a location and a scale of width. In this case the minimum information PDF at a given location μ and

with a scale σ is the Gaussian PDF $\mathcal{G}(x, \mu, \sigma^2)$. If no information is at one's disposal, it is legitimate to wonder which prior is relevant. The latter can be given by Jeffrey's prior, which can be defined by satisfying the problem symmetries and can be considered as the complete ignorance prior.

A.3.2 Model comparison

For now, we have only considered Bayes identity for a given model $\mathcal{M}$:

$$p(\boldsymbol{\theta}|\mathbf{d}, \mathcal{M})p(\mathbf{d}|\mathcal{M}) = p(\mathbf{d}|\boldsymbol{\theta}, \mathcal{M})p(\boldsymbol{\theta}|\mathcal{M}) \tag{A.14}$$

Could we find $p(\mathcal{M}|d)$? Or, in other terms how to quantify the credency of a given model $\mathcal{M}$ considering the collected data ? By considering the joint PDF $p(\mathcal{M}, \mathbf{d})$, we get:

$$\begin{aligned} p(\mathcal{M}, \mathbf{d}) &= p(\mathcal{M}|\mathbf{d})p(\mathbf{d}) \\ &= p(\mathbf{d}|\mathcal{M})p(\mathcal{M}) \end{aligned} \tag{A.15}$$

Or equivalently:

$$p(\mathcal{M}|\mathbf{d}) = \frac{p(\mathbf{d}|\mathcal{M})p(\mathcal{M})}{p(\mathbf{d})} \tag{A.16}$$

If we wanted to compare $\mathcal{M}_1$ and $\mathcal{M}_2$, supposing that they are the 2 only possible models (implying $p(\mathcal{M}_1|\mathbf{d}) + p(\mathcal{M}_2|\mathbf{d}) = 1$), we could compare their posterior ratio:

$$\boxed{\frac{p(\mathcal{M}_1|\mathbf{d})}{p(\mathcal{M}_2|\mathbf{d})} = \frac{p(\mathbf{d}|\mathcal{M}_1)p(\mathcal{M}_1)}{p(\mathbf{d}|\mathcal{M}_2)p(\mathcal{M}_2)}} \tag{A.17}$$

The ratio $p(\mathbf{d}|\mathcal{M}_1)/p(\mathbf{d}|\mathcal{M}_2)$ is sometimes called the *Bayes factor*, it shows how well the model $\mathcal{M}_1$ predicts the data compared to $\mathcal{M}_2$.

Each term $p(\mathbf{d}|\mathcal{M})$ can be computed as follows:

$$\begin{aligned} \int_{\boldsymbol{\theta}} p(\boldsymbol{\theta}|\mathbf{d}, \mathcal{M})p(\mathbf{d}|\mathcal{M})\,\mathbf{d}\boldsymbol{\theta} &= \int_{\boldsymbol{\theta}} p(\mathbf{d}|\boldsymbol{\theta}, \mathcal{M})p(\boldsymbol{\theta}|\mathcal{M})\,\mathbf{d}\boldsymbol{\theta} \\ \Rightarrow \qquad p(\mathbf{d}|\mathcal{M}) \cdot 1 &= \int_{\boldsymbol{\theta}} p(\mathbf{d}|\boldsymbol{\theta}, \mathcal{M})p(\boldsymbol{\theta}|\mathcal{M})\,\mathbf{d}\boldsymbol{\theta} \end{aligned} \tag{A.18}$$

A.4 Sampling methods

Evaluating a posterior distribution can quickly become complex as the number of dimensions increases (since high dimensional integrals are hidden in our probabilities). To solve the "curse of dimensionality" when $dim(\boldsymbol{\theta}) > 3$, the idea is that instead of computing directly the posterior $p(\boldsymbol{\theta}|\mathbf{d})$, we shall sample from it. This is powerful because doing integrals of sampled functions is trivial, and that way we may compute satisfying approximations for the posterior distribution.

Markov Chain Monte Carlo

A standard algorithm is the Metropolis Hastings MCMC, used to sample from an arbitrary distribution $p(\boldsymbol{\theta})$. A chain starts from an initial value $\boldsymbol{\theta} = \boldsymbol{\theta}_0$, then at the i^{th} iteration, the algorithm:

1. Proposes a new $\widetilde{\boldsymbol{\theta}}$ drawn from a defined proposal PDF $q(\widetilde{\boldsymbol{\theta}}|\boldsymbol{\theta}_i)$ (a usual choice for this proposal PDF is a Gaussian distribution centered on $\boldsymbol{\theta}_i$)
2. Computes the so-called acceptance ratio $a = \dfrac{p(\widetilde{\boldsymbol{\theta}})}{p(\boldsymbol{\theta}_i)} \dfrac{q(\boldsymbol{\theta}_i|\widetilde{\boldsymbol{\theta}})}{q(\widetilde{\boldsymbol{\theta}}|\boldsymbol{\theta}_i)}$
3. Depending on the acceptance ratio value:
   - if $a \geq 1$, then accepts $\widetilde{\boldsymbol{\theta}}$ so that $\boldsymbol{\theta}_{i+1} = \widetilde{\boldsymbol{\theta}}$ $\quad [i \to i+1]$
   - if $0 \leq a < 1$ then accepts $\widetilde{\boldsymbol{\theta}}$ with a probability a, i.e. draws r from the uniform distribution $U(0,1)$ and:
     $\longrightarrow$ if $r > a$, $\boldsymbol{\theta}_{i+1} = \widetilde{\boldsymbol{\theta}}$ $\quad [i \to i+1]$
     $\longrightarrow$ if $r > a$, then rejects $\widetilde{\boldsymbol{\theta}}$ and $\boldsymbol{\theta}_{i+1} = \boldsymbol{\theta}_i$ $\quad [i \to i+1]$
4. Returns to 1) with the new value $\boldsymbol{\theta}_{i+1}$ or stop if $i = N$

One can prove that as $i \to \infty$, the set of $\boldsymbol{\theta}_i$ will converge to the target $p(\boldsymbol{\theta})$, with the condition that q can access the full parameter space. As such one should choose q as broad as possible. However, in the general problem there is no evident choice of the proposal distribution as of the number of iteration N, both can be considered as free parameters of the method. The sampling result of a 5D multivariate Gaussian is displayed in Figure A.3.

Apart from the Metropolis Hasting algorithm, a large number of more or less complex sample methods exist in the literature, and most of them rely on a random walk (proposal of a new state and random acceptance). The website MCMC interactive gallery offers a good visualisation of several samplers, including the Metropolis Hasting one just described.

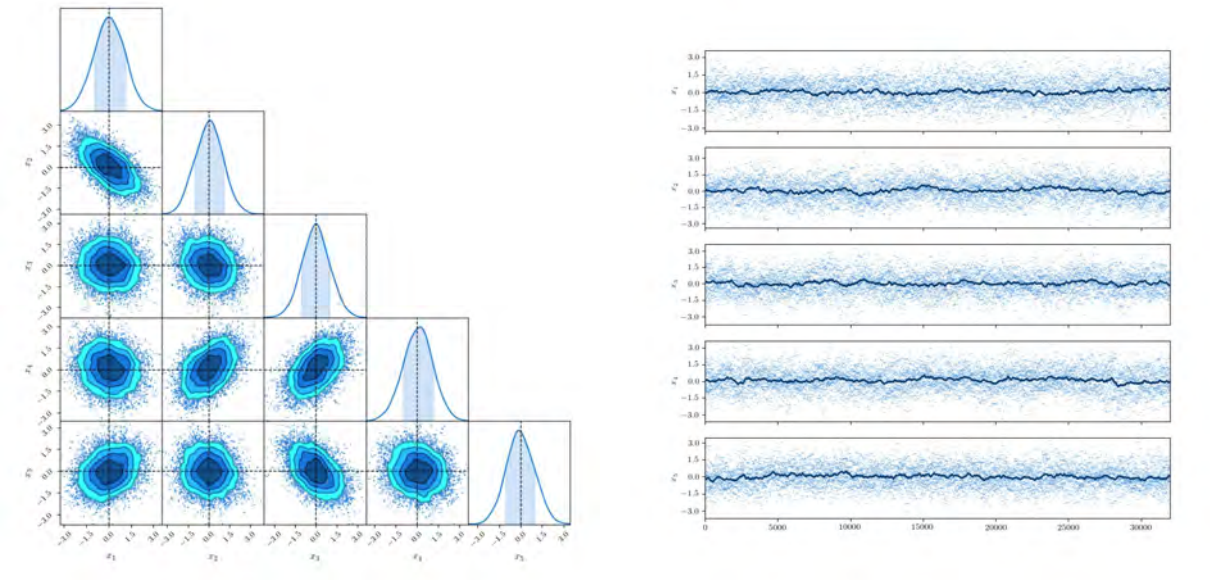

(a) 5D Corner plot of a multivariate Gaussian sampling.

(b) The associated walks on each dimension.

Figure A.3: MCMC sampling of a 5D multivariate Gaussian

List of Figures

List of Tables

List of abbreviations

AU	Astronomical Unit
CH	Coronal Hole
CIR	Corotating Interaction Region
CME	Coronal Mass Ejection
CS	Current Sheet
DES	Dual Electron Sensor
DIS	Dual Ion Sensonr
EDR	Electron Diffusion Region
E_x	Encounter x
FPI	Fast Plasma Instrument
FTE	Flux Transfer Events
GSE	Geocentric Solar Ecliptic
HCS	Heliospheric Current Sheet
IDR	Ion Diffusion Region
IFE	Interplanetary Field Enhancement
IFT	Interlaced Flux tubes
IMF	Interpanetary Magnetic Field
KDE	Kernel Density Estimation
lmn	Current sheet frame
MCMC	Markov Chain Monte Carlo
MHD	Magnetohydrodynamic
MICCS	Magnetic Increases with Central Current Sheet
MMS	Magnetospheric MultiScale mission
MVA	Minimum Variance Analysis
PA	Pitch Angle
PAD	Pitch Angle Distribution
PAS	Proton Alpha Sensor
PDF	Probability Density Function
PFSS	Potential Field Source Surface
PSP	Parker Solar Probe
RHS	Right Hand Side
RTN	Radial Tangential Normal
SPAN	Solar Probe ANalyzer

SPC	Solar Probe Cup
SITL	Scientists In The Loop
SWEAP	Solar Wind Electrons Alphas and Protons
WPS	Wavelet Power Spectrum

List of publications

As a first author:

- Fargette et al. (2020), On the ubiquity of magnetic reconnection inside flux transfer event s at the earth's magnetopause, GRL, 10.1029/2019GL086726
- Fargette et al. (2021a), Magnetic increases with central current sheets: observations with Parker Solar Probe, A&A, 10.1051/0004-6361/202039191
- Fargette et al. (2021b), Characteristic scales of magnetic switchback patches near the sun and their possible association with solar supergranulation and granulation, ApJ, 10.3847/1538-4357/ac1112
- Fargette et al. (2022), The preferential orientation of magnetic switchbacks, implications for solar magnetic flux transport, A&A, 10.1051/0004-6361/202243537

Significantly contributed to:

- Froment et al. (2021), Direct evidence for magnetic reconnection at the boundaries of magnetic switchbacks with Parker Solar Probe, A&A, 10.1051/0004-6361/202039806
- Kieokaew et al. (2021), Statistical Relationship Between Interplanetary Magnetic Field Conditions and the Helicity Sign of Flux Transfer Event Flux Ropes, GRL, 10.1029/2020GL091257
- Réville et al. (2022), Flux rope and dynamics of the heliospheric current sheet. Study of the Parker Solar Probe and Solar Orbiter conjunction of June 2020, A&A, 10.1051/0004-6361/202142381

Provided insights in:

- Lavraud et al. (2020), The Heliospheric Current Sheet and Plasma Sheet during Parker Solar Probe's First Orbit, ApJL, 10.3847/2041-8213/ab8d2d
- Kieokaew et al. (2020), Magnetic Reconnection Inside a Flux Transfer Event-Like Structure in Magnetopause Kelvin-Helmholtz Waves, JGR, 10.1029/2019JA027527
- Lavraud et al. (2021), Magnetic reconnection as a mechanism to produce multiple thermal proton populations and beams locally in the solar wind, A&A, 10.1051/0004-6361/202141149

- Kieokaew et al. (2021) Solar Orbiter observations of the Kelvin-Helmholtz waves in the solar wind, A&A, 10.1051/0004-6361/202140915
- Poirier et al. (2021), Exploiting white-light observations to improve estimates of magnetic connectivity, FASS, 10.3389/fspas.2021.684734
- Pinto et al. (2021), Solar wind rotation rate and shear at coronal hole boundaries. Possible consequences for magnetic field inversions, A&A, 10.1051/0004-6361/202040180

Bibliography

[1] Agapitov, O. V., Drake, J. F., Swisdak, M., et al. 2022, Flux Rope Merging and the Structure of Switchbacks in the Solar Wind, The Astrophysical Journal, 925, 213, doi: 10.3847/1538-4357/ac4016

[2] Akhavan-Tafti, M., Kasper, J., Huang, J., & Bale, S. 2021, Discontinuity analysis of the leading switchback transition regions, Astronomy and Astrophysics, 650, A4, doi: 10.1051/0004-6361/202039508

[3] Antiochos, S. K., Mikić, Z., Titov, V. S., Lionello, R., & Linker, J. A. 2011, A Model for the Sources of the Slow Solar Wind, The Astrophysical Journal, 731, 112, doi: 10.1088/0004-637X/731/2/112

[4] Aschwanden, M. J. 2005, Physics of the Solar Corona. An Introduction with Problems and Solutions (2nd edition) (Springer)

[5] Auchère, F., Froment, C., Bocchialini, K., Buchlin, E., & Solomon, J. 2016, On the Fourier and Wavelet Analysis of Coronal Time Series, The Astrophysical Journal, 825, 110, doi: 10.3847/0004-637X/825/2/110

[6] Badman, S. T., Bale, S. D., Martínez Oliveros, J. C., et al. 2020, Magnetic Connectivity of the Ecliptic Plane within 0.5 au: Potential Field Source Surface Modeling of the First Parker Solar Probe Encounter, ApJ Supplements, 246, 23, doi: 10.3847/1538-4365/ab4da7

[7] Badman, S. T., Bale, S. D., Rouillard, A. P., et al. 2021, Measurement of the open magnetic flux in the inner heliosphere down to 0.13 AU, Astronomy and Astrophysics, 650, A18, doi: 10.1051/0004-6361/202039407

[8] Bagashvili, S. R., Shergelashvili, B. M., Japaridze, D. R., et al. 2017, Statistical properties of coronal hole rotation rates: Are they linked to the solar interior?, Astronomy and Astrophysics, 603, A134, doi: 10.1051/0004-6361/201630377

[9] Bale, S. D., Goetz, K., Harvey, P. R., et al. 2016, The FIELDS Instrument Suite for Solar Probe Plus. Measuring the Coronal Plasma and Magnetic Field, Plasma Waves and Turbulence, and Radio Signatures of Solar Transients, Space Science Review, 204, 49, doi: 10.1007/s11214-016-0244-5

[10] Bale, S. D., Badman, S. T., Bonnell, J. W., et al. 2019, Highly structured slow solar wind emerging from an equatorial coronal hole, Nature, 576, 237, doi: 10.1038/s41586-019-1818-7

[11] Bale, S. D., Horbury, T. S., Velli, M., et al. 2021, A Solar Source of Alfvénic Magnetic Field Switchbacks: In Situ Remnants of Magnetic Funnels on Supergranulation Scales, The Astrophysical Journal, 923, 174, doi: 10.3847/1538-4357/ac2d8c

[12] Balogh, A., Forsyth, R. J., Lucek, E. A., Horbury, T. S., & Smith, E. J. 1999, Heliospheric magnetic field polarity inversions at high heliographic latitudes, Geophysical Research Letters, 26, 631, doi: 10.1029/1999GL900061

[13] Berchem, J., & Russell, C. T. 1984, Flux transfer events on the magnetopause: Spatial distribution and controlling factors, Journal of Geophysical Research, 89, 6689, doi: 10.1029/JA089iA08p06689

[14] Borovsky, J. E. 2008, Flux tube texture of the solar wind: Strands of the magnetic carpet at 1 AU?, Journal of Geophysical Research (Space Physics), 113, A08110, doi: 10.1029/2007JA012684

[15] Borovsky, J. E., & Valdivia, J. A. 2018, The Earth's Magnetosphere: A Systems Science Overview and Assessment, Surveys in Geophysics, 39, 817, doi: 10.1007/s10712-018-9487-x

[16] Brun, A. S., & Toomre, J. 2002, Turbulent Convection under the Influence of Rotation: Sustaining a Strong Differential Rotation, The Astrophysical Journal, 570, 865, doi: 10.1086/339228

[17] Bruno, R., & Bavassano, B. 1997, On the winding of the IMF spiral for slow and fast wind within the inner heliosphere, Geophysical Research Letters, 24, 2267, doi: 10.1029/97GL02183

[18] Bruno, R., & Carbone, V. 2013, The Solar Wind as a Turbulence Laboratory, Living Reviews in Solar Physics, 10, 2, doi: 10.12942/lrsp-2013-2

[19] Burch, J. L., Moore, T. E., Torbert, R. B., & Giles, B. L. 2016, Magnetospheric Multiscale Overview and Science Objectives, Space Science Review, 199, 5, doi: 10.1007/s11214-015-0164-9

[20] Burlaga, L. F. 1988, Magnetic clouds and force-free fields with constant alpha, Journal of Geophysical Research, 93, 7217, doi: 10.1029/JA093iA07p07217

[21] Cardoso, F. R., Gonzalez, W. D., Sibeck, D. G., Kuznetsova, M., & Koga, D. 2013, Magnetopause reconnection and interlinked flux tubes, Annales Geophysicae, 31, 1853, doi: 10.5194/angeo-31-1853-2013

[22] Case, A. W., Kasper, J. C., Stevens, M. L., et al. 2020, The Solar Probe Cup on the Parker Solar Probe, ApJ Supplements, 246, 43, doi: 10.3847/1538-4365/ab5a7b

[23] Chapman, S., Ferraro, V. C. A., Chapman, S., & Ferraro, V. C. A. 1930, A New Theory of Magnetic Storms., Natur, 126, 129, doi: 10.1038/126129A0

[24] Chen, C. H. K., Bale, S. D., Bonnell, J. W., et al. 2020, The Evolution and Role of Solar Wind Turbulence in the Inner Heliosphere, ApJ Supplements, 246, 53, doi: 10.3847/1538-4365/ab60a3

[25] Cranmer, S. R. 2009, Coronal Holes, Living Reviews in Solar Physics, 6, 3, doi: 10.12942/lrsp-2009-3

[26] Cranmer, S. R., van Ballegooijen, A. A., & Edgar, R. J. 2007, Self-consistent Coronal Heating and Solar Wind Acceleration from Anisotropic Magnetohydrodynamic Turbulence, ApJ Supplements, 171, 520, doi: 10.1086/518001

[27] de Hoffmann, F., & Teller, E. 1950, Magneto-Hydrodynamic Shocks, Physical Review, 80, 692, doi: 10.1103/PhysRev.80.692

[28] Dierckx, P. 1993, Curve and surface fitting with splines (Oxford science publications)

[29] Drake, J. F., Agapitov, O., Swisdak, M., et al. 2021, Switchbacks as signatures of magnetic flux ropes generated by interchange reconnection in the corona, Astronomy and Astrophysics, 650, A2, doi: 10.1051/0004-6361/202039432

[30] Dudok de Wit, T., Krasnoselskikh, V. V., Bale, S. D., et al. 2020, Switchbacks in the Near-Sun Magnetic Field: Long Memory and Impact on the Turbulence Cascade, ApJ Supplements, 246, 39, doi: 10.3847/1538-4365/ab5853

[31] Dungey, J. W. 1962, The Interplanetary Field and Auroral Theory, Journal of the Physical Society of Japan Supplement, 17, 15

[32] Fargette, N., Lavraud, B., Rouillard, A. P., et al. 2022, The preferential orientation of magnetic switchbacks, implications for solar magnetic flux transport, Astronomy and Astrophysics, doi: 10.1051/0004-6361/202243537

[33] Fargette, N., Lavraud, B., Øieroset, M., et al. 2020, On the Ubiquity of Magnetic Reconnection Inside Flux Transfer Event-Like Structures at the Earth's Magnetopause, Geophysical Research Letters, 47, e86726, doi: 10.1029/2019GL086726

[34] Fargette, N., Lavraud, B., Rouillard, A., et al. 2021a, Magnetic increases with central current sheets: observations with Parker Solar Probe, Astronomy and Astrophysics, 650, A11, doi: 10.1051/0004-6361/202039191

[35] Fargette, N., Lavraud, B., Rouillard, A. P., et al. 2021b, Characteristic Scales of Magnetic Switchback Patches Near the Sun and Their Possible Association With Solar Supergranulation and Granulation, The Astrophysical Journal, 919, 96, doi: 10.3847/1538-4357/ac1112

[36] Farinas Perez, G., Cardoso, F. R., Sibeck, D., et al. 2018, Generation Mechanism for Interlinked Flux Tubes on the Magnetopause, Journal of Geophysical Research (Space Physics), 123, 1337, doi: 10.1002/2017JA024664

[37] Farrell, W. M., MacDowall, R. J., Gruesbeck, J. R., Bale, S. D., & Kasper, J. C. 2020, Magnetic Field Dropouts at Near-Sun Switchback Boundaries: A Superposed Epoch Analysis, ApJ Supplements, 249, 28, doi: 10.3847/1538-4365/ab9eba

[38] Fear, R. C., Palmroth, M., & Milan, S. E. 2012, Seasonal and clock angle control of the location of flux transfer event signatures at the magnetopause, Journal of Geophysical Research (Space Physics), 117, A04202, doi: 10.1029/2011JA017235

[39] Fisk, L. A. 1996, Motion of the footpoints of heliospheric magnetic field lines at the Sun: Implications for recurrent energetic particle events at high heliographic latitudes, Journal of Geophysical Research, 101, 15547, doi: 10.1029/96JA01005

[40] Fisk, L. A., & Kasper, J. C. 2020, Global Circulation of the Open Magnetic Flux of the Sun, ApJ Letters, 894, L4, doi: 10.3847/2041-8213/ab8acd

[41] Fisk, L. A., Zurbuchen, T. H., & Schwadron, N. A. 1999, On the Coronal Magnetic Field: Consequences of Large-Scale Motions, The Astrophysical Journal, 521, 868, doi: 10.1086/307556

[42] Foreman-Mackey, D., Farr, W., Sinha, M., et al. 2019, emcee v3: A Python ensemble sampling toolkit for affine-invariant MCMC, The Journal of Open Source Software, 4, 1864, doi: 10.21105/joss.01864

[43] Fox, N. J., Velli, M. C., Bale, S. D., et al. 2016, The Solar Probe Plus Mission: Humanity's First Visit to Our Star, Space Science Review, 204, 7, doi: 10.1007/s11214-015-0211-6

[44] Froment, C., Krasnoselskikh, V., Dudok de Wit, T., et al. 2021, Direct evidence for magnetic reconnection at the boundaries of magnetic switchbacks with Parker Solar Probe, Astronomy and Astrophysics, 650, A5, doi: 10.1051/0004-6361/202039806

[45] Galtier, S. 2016, Introduction to Modern Magnetohydrodynamics

[46] Gary, G. A. 2001, Plasma Beta above a Solar Active Region: Rethinking the Paradigm, Solar Physics, 203, 71, doi: 10.1023/A:1012722021820

[47] Giordano, S., & Mancuso, S. 2008, Coronal Rotation at Solar Minimum from UV Observations, The Astrophysical Journal, 688, 656, doi: 10.1086/591923

[48] Gosling, J. T., Borrini, G., Asbridge, J. R., et al. 1981, Coronal streamers in the solar wind at 1 AU, Journal of Geophysical Research, 86, 5438, doi: 10.1029/JA086iA07p05438

[49] Gosling, J. T., McComas, D. J., Roberts, D. A., & Skoug, R. M. 2009, A One-Sided Aspect of Alfvenic Fluctuations in the Solar Wind, ApJ Letters, 695, L213, doi: 10.1088/0004-637X/695/2/L213

[50] Gosling, J. T., McComas, D. J., Skoug, R. M., & Smith, C. W. 2006, Magnetic reconnection at the heliospheric current sheet and the formation of closed magnetic field lines in the solar wind, Geophysical Research Letters, 33, L17102, doi: 10.1029/2006GL027188

[51] Gosling, J. T., & Phan, T. D. 2013, Magnetic Reconnection in the Solar Wind at Current Sheets Associated with Extremely Small Field Shear Angles, ApJ Letters, 763, L39, doi: 10.1088/2041-8205/763/2/L39

[52] Gosling, J. T., Skoug, R. M., McComas, D. J., & Smith, C. W. 2005, Direct evidence for magnetic reconnection in the solar wind near 1 AU, Journal of Geophysical Research (Space Physics), 110, A01107, doi: 10.1029/2004JA010809

[53] Gosling, J. T., Tian, H., & Phan, T. D. 2011, Pulsed Alfvén Waves in the Solar Wind, ApJ Letters, 737, L35, doi: 10.1088/2041-8205/737/2/L35

[54] Griton, L., Rouillard, A. P., Poirier, N., et al. 2021, Source-dependent Properties of Two Slow Solar Wind States, The Astrophysical Journal, 910, 63, doi: 10.3847/1538-4357/abe309

[55] Haggerty, C. C., Shay, M. A., Chasapis, A., et al. 2018, The reduction of magnetic reconnection outflow jets to sub-Alfvénic speeds, Physics of Plasmas, 25, 102120, doi: 10.1063/1.5050530

[56] Hasegawa, H., Wang, J., Dunlop, M. W., et al. 2010, Evidence for a flux transfer event generated by multiple X-line reconnection at the magnetopause, Geophysical Research Letters, 37, doi: 10.1029/2010GL044219

[57] He, J., Zhu, X., Yang, L., et al. 2021, Solar Origin of Compressive Alfvénic Spikes/Kinks as Observed by Parker Solar Probe, ApJ Letters, 913, L14, doi: 10.3847/2041-8213/abf83d

[58] Hesse, M., Birn, J., & Schindler, K. 1990, On the topology of flux transfer events, Journal of Geophysical Research, 95, 6549, doi: 10.1029/JA095iA05p06549

[59] Horbury, T. S., Matteini, L., & Stansby, D. 2018, Short, large-amplitude speed enhancements in the near-Sunfast solar wind, Monthly Notices of the Royal Astronomical Society, 478, 1980, doi: 10.1093/mnras/sty953

[60] Horbury, T. S., O'Brien, H., Carrasco Blazquez, I., et al. 2020a, The Solar Orbiter magnetometer, Astronomy and Astrophysics, 642, A9, doi: 10.1051/0004-6361/201937257

[61] Horbury, T. S., Woolley, T., Laker, R., et al. 2020b, Sharp Alfvénic Impulses in the Near-Sun Solar Wind, ApJ Supplements, 246, 45, doi: 10.3847/1538-4365/ab5b15

[62] Hudson, P. D. 1970, Discontinuities in an anisotropic plasma and their identification in the solar wind, Planetary and Space Science, 18, 1611, doi: 10.1016/0032-0633(70)90036-X

[63] Jones, G. H., Balogh, A., McComas, D. J., & MacDowall, R. J. 2003a, Strong interplanetary field enhancements at Ulysses—evidence of dust trails' interaction with the solar wind?, Icarus, 166, 297, doi: 10.1016/j.icarus.2003.09.007

[64] Jones, G. H., Balogh, A., Russell, C. T., & Dougherty, M. K. 2003b, Possible Distortion of the Interplanetary Magnetic Field by the Dust Trail of Comet 122P/de Vico, ApJ Letters, 597, L61, doi: 10.1086/379750

[65] Kacem, I., Jacquey, C., Génot, V., et al. 2018, Magnetic Reconnection at a Thin Current Sheet Separating Two Interlaced Flux Tubes at the Earth's Magnetopause, Journal of Geophysical Research (Space Physics), 123, 1779, doi: 10.1002/2017JA024537

[66] Kasper, J. C., Abiad, R., Austin, G., et al. 2016, Solar Wind Electrons Alphas and Protons (SWEAP) Investigation: Design of the Solar Wind and Coronal Plasma Instrument Suite for Solar Probe Plus, Space Science Review, 204, 131, doi: 10.1007/s11214-015-0206-3

[67] Kasper, J. C., Bale, S. D., Belcher, J. W., et al. 2019, Alfvénic velocity spikes and rotational flows in the near-Sun solar wind, Nature, 576, 228, doi: 10.1038/s41586-019-1813-z

[68] Kasper, J. C., Klein, K. G., Lichko, E., et al. 2021, Parker Solar Probe Enters the Magnetically Dominated Solar Corona, Physical Review Letters, 127, 255101, doi: 10.1103/PhysRevLett.127.255101

[69] Kieokaew, R., Lavraud, B., Foullon, C., et al. 2020, Magnetic Reconnection Inside a Flux Transfer Event-Like Structure in Magnetopause Kelvin-Helmholtz Waves, Journal of Geophysical Research (Space Physics), 125, e27527, doi: 10.1029/2019JA027527

[70] Kieokaew, R., Lavraud, B., Fargette, N., et al. 2021, Statistical Relationship Between Interplanetary Magnetic Field Conditions and the Helicity Sign of Flux Transfer Event Flux Ropes, Geophysical Research Letters, 48, e91257, doi: 10.1029/2020GL091257

[71] Kilpua, E. K. J., Luhmann, J. G., Gosling, J., et al. 2009, Small Solar Wind Transients and Their Connection to the Large-Scale Coronal Structure, Solar Physics, 256, 327, doi: 10.1007/s11207-009-9366-1

[72] King, J. H., & Papitashvili, N. E. 2005, Solar wind spatial scales in and comparisons of hourly Wind and ACE plasma and magnetic field data, Journal of Geophysical Research (Space Physics), 110, A02104, doi: 10.1029/2004JA010649

[73] Kivelson, M. G., & Russell, C. T. 1995, Introduction to Space Physics, Cambridge atmospheric and space science series (Cambridge University Press). https://books.google.fr/books?id=qWHSqXGfsfQC

[74] Korreck, K. E., Szabo, A., Nieves Chinchilla, T., et al. 2020, Source and Propagation of a Streamer Blowout Coronal Mass Ejection Observed by the Parker Solar Probe, ApJ Supplements, 246, 69, doi: 10.3847/1538-4365/ab6ff9

[75] Kuo, H., Russell, C. T., & Le, G. 1995, Statistical studies of flux transfer events, Journal of Geophysical Research, 100, 3513, doi: 10.1029/94JA02498

[76] Lai, H. R., Russell, C. T., Jia, Y. D., Wei, H. Y., & Angelopoulos, V. 2015, Momentum transfer from solar wind to interplanetary field enhancements inferred from magnetic field draping signatures, Geophysical Research Letters, 42, 1640, doi: 10.1002/2015GL063302

[77] Laker, R., Horbury, T. S., Bale, S. D., et al. 2021, Statistical analysis of orientation, shape, and size of solar wind switchbacks, Astronomy and Astrophysics, 650, A1, doi: 10.1051/0004-6361/202039354

[78] Landi, S., Hellinger, P., & Velli, M. 2006, Heliospheric magnetic field polarity inversions driven by radial velocity field structures, Geophysical Research Letters, 33, L14101, doi: 10.1029/2006GL026308

[79] Lang, K. 2013, Essential Astrophysics, Undergraduate Lecture Notes in Physics (Springer Berlin Heidelberg). https://books.google.fr/books?id=PVJEAAAAQBAJ

[80] Lapenta, G., & Knoll, D. A. 2005, Effect of a Converging Flow at the Streamer Cusp on

the Genesis of the Slow Solar Wind, The Astrophysical Journal, 624, 1049, doi: 10.1086/429262

[81] Larosa, A., Krasnoselskikh, V., Dudok de Wit, T., et al. 2021, Switchbacks: statistical properties and deviations from Alfvénicity, Astronomy and Astrophysics, 650, A3, doi: 10.1051/0004-6361/202039442

[82] Lavraud, B., Opitz, A., Gosling, J. T., et al. 2010, Statistics of counter-streaming solar wind suprathermal electrons at solar minimum: STEREO observations, Annales Geophysicae, 28, 233, doi: 10.5194/angeo-28-233-2010

[83] Lavraud, B., Fargette, N., Réville, V., et al. 2020, The Heliospheric Current Sheet and Plasma Sheet during Parker Solar Probe's First Orbit, ApJ Letters, 894, L19, doi: 10.3847/2041-8213/ab8d2d

[84] Lavraud, B., Kieokaew, R., Fargette, N., et al. 2021, Magnetic reconnection as a mechanism to produce multiple thermal proton populations and beams locally in the solar wind, Astronomy and Astrophysics, 656, A37, doi: 10.1051/0004-6361/202141149

[85] Lee, L. C., & Fu, Z. F. 1985, A theory of magnetic flux transfer at the Earth's magnetopause, Geophysical Research Letters, 12, 105, doi: 10.1029/GL012i002p00105

[86] Lee, L. C., Ma, Z. W., Fu, Z. F., & Otto, A. 1993, Topology of magnetic flux ropes and formation of fossil flux transfer events and boundary layer plasmas, Journal of Geophysical Research, 98, 3943, doi: 10.1029/92JA02203

[87] Lepping, R. P., Jones, J. A., & Burlaga, L. F. 1990, Magnetic field structure of interplanetary magnetic clouds at 1 AU, Journal of Geophysical Research, 95, 11957, doi: 10.1029/JA095iA08p11957

[88] Liang, H., Zank, G. P., Nakanotani, M., & Zhao, L. L. 2021, Assessing the Role of Interchange Reconnection in Forming Switchbacks, The Astrophysical Journal, 917, 110, doi: 10.3847/1538-4357/ac0a73

[89] Lin, R. L., Zhang, X. X., Liu, S. Q., Wang, Y. L., & Gong, J. C. 2010, A three-dimensional asymmetric magnetopause model, Journal of Geophysical Research (Space Physics), 115, A04207, doi: 10.1029/2009JA014235

[90] Lionello, R., Linker, J. A., Mikić, Z., & Riley, P. 2006, The Latitudinal Excursion of Coronal Magnetic Field Lines in Response to Differential Rotation: MHD Simulations, ApJ Letters, 642, L69, doi: 10.1086/504289

[91] Lionello, R., Riley, P., Linker, J. A., & Mikić, Z. 2005, The Effects of Differential Rotation on the Magnetic Structure of the Solar Corona: Magnetohydrodynamic Simulations, The Astrophysical Journal, 625, 463, doi: 10.1086/429268

[92] Liu, R. 2020, Magnetic flux ropes in the solar corona: structure and evolution toward eruption, Research in Astronomy and Astrophysics, 20, 165, doi: 10.1088/1674-4527/20/10/165

[93] Liu, Y.-H., Drake, J. F., & Swisdak, M. 2011, The effects of strong temperature anisotropy on the kinetic structure of collisionless slow shocks and reconnection exhausts. II. Theory, Physics of Plasmas, 18, 092102, doi: 10.1063/1.3627147

[94] Liu, Z. Q., Lu, J. Y., Wang, C., et al. 2015, A three-dimensional high Mach number asymmetric magnetopause model from global MHD simulation, Journal of Geophysical Research (Space Physics), 120, 5645, doi: 10.1002/2014JA020961

[95] Lockwood, M., Cowley, S. W. H., & Sandholt, P. E. 1990, Transient reconnection: Search for ionospheric signatures, EOS Transactions, 71, 709, doi: 10.1029/EO071i020p00709-02

[96] Louarn, P., Fedorov, A., Budnik, E., et al. 2004, Cluster observations of complex 3D magnetic structures at the magnetopause, Geophysical Research Letters, 31, L19805, doi: 10.1029/2004GL020625

[97] Louarn, P., Fedorov, A., Prech, L., et al. 2021, Multiscale views of an Alfvénic slow solar wind: 3D velocity distribution functions observed by the Proton-Alpha Sensor of Solar Orbiter, Astronomy and Astrophysics, 656, A36, doi: 10.1051/0004-6361/202141095

[98] Lundquist, S. 1951, On the Stability of Magneto-Hydrostatic Fields, Physical Review, 83, 307, doi: 10.1103/PhysRev.83.307

[99] Macneil, A. R., Owens, M. J., Wicks, R. T., & Lockwood, M. 2021, Evolving solar wind flow properties of magnetic inversions observed by Helios, Monthly Notices of the Royal Astronomical Society, 501, 5379, doi: 10.1093/mnras/staa3983

[100] Macneil, A. R., Owens, M. J., Wicks, R. T., et al. 2020, The evolution of inverted magnetic fields through the inner heliosphere, Monthly Notices of the Royal Astronomical Society, 494, 3642, doi: 10.1093/mnras/staa951

[101] Magyar, N., Utz, D., Erdélyi, R., & Nakariakov, V. M. 2021a, Could Switchbacks Originate in the Lower Solar Atmosphere? I. Formation Mechanisms of Switchbacks, The Astrophysical Journal, 911, 75, doi: 10.3847/1538-4357/abec49

[102] —. 2021b, Could Switchbacks Originate in the Lower Solar Atmosphere? II. Propagation of Switchbacks in the Solar Corona, The Astrophysical Journal, 914, 8, doi: 10.3847/1538-4357/abfa98

[103] Malaspina, D. M., Halekas, J., Berčič, L., et al. 2020, Plasma Waves near the Electron Cyclotron Frequency in the Near-Sun Solar Wind, ApJ Supplements, 246, 21, doi: 10.3847/1538-4365/ab4c3b

[104] Mallet, A., Squire, J., Chandran, B. D. G., Bowen, T., & Bale, S. D. 2021, Evolution of Large-amplitude Alfvén Waves and Generation of Switchbacks in the Expanding Solar Wind, The Astrophysical Journal, 918, 62, doi: 10.3847/1538-4357/ac0c12

[105] Mancuso, S., & Giordano, S. 2011, Differential Rotation of the Ultraviolet Corona at Solar Maximum, The Astrophysical Journal, 729, 79, doi: 10.1088/0004-637X/729/2/79

[106] Mancuso, S., Giordano, S., Barghini, D., & Telloni, D. 2020, Differential rotation of the solar corona: A new data-adaptive multiwavelength approach, Astronomy and Astrophysics, 644, A18, doi: 10.1051/0004-6361/202039094

[107] Mann, I., Czechowski, A., & Meyer-Vernet, N. 2010, in American Institute of Physics Conference Series, Vol. 1216, Twelfth International Solar Wind Conference, ed. M. Maksimovic, K. Issautier, N. Meyer-Vernet, M. Moncuquet, & F. Pantellini, 491–496, doi: 10.1063/1.3395911

[108] Matloch, L., Cameron, R., Schmitt, D., & Schüssler, M. 2009, Modelling of solar mesogranulation, Astronomy and Astrophysics, 504, 1041, doi: 10.1051/0004-6361/200811200

[109] Matteini, L., Horbury, T. S., Neugebauer, M., & Goldstein, B. E. 2014, Dependence of solar wind speed on the local magnetic field orientation: Role of Alfvénic fluctuations, Geophysical Research Letters, 41, 259, doi: 10.1002/2013GL058482

[110] Matteini, L., Stansby, D., Horbury, T. S., & Chen, C. H. K. 2019, The rotation angle distribution underlying magnetic field fluctuations in the 1/ f range of solar wind turbulent spectra, Nuovo Cimento C Geophysics Space Physics C, 42, 16, doi: 10.1393/ncc/i2019-19016-y

[111] Mauk, B. H., Blake, J. B., Baker, D. N., et al. 2016, The Energetic Particle Detector (EPD) Investigation and the Energetic Ion Spectrometer (EIS) for the Magnetospheric Multiscale (MMS) Mission, Space Science Review, 199, 471, doi: 10.1007/s11214-014-0055-5

[112] McComas, D. J., Elliott, H. A., Schwadron, N. A., et al. 2003, The three-dimensional solar wind around solar maximum, Geophysical Research Letters, 30, 1517, doi: 10.1029/2003GL017136

[113] McComas, D. J., Alexander, N., Angold, N., et al. 2016, Integrated Science Investigation of the Sun (ISIS): Design of the Energetic Particle Investigation, Space Science Review, 204, 187, doi: 10.1007/s11214-014-0059-1

[114] Meng, M.-M., Liu, Y. D., Chen, C., & Wang, R. 2022, Analysis of the Distribution, Rotation and Scale Characteristics of Solar Wind Switchbacks: Comparison between the First and Second Encounters of Parker Solar Probe, Research in Astronomy and Astrophysics, 22, 035018, doi: 10.1088/1674-4527/ac49e4

[115] Meyer-Vernet, N. 2007, Basics of the Solar Wind (Cambridge Atmospheric and Space Science Series)

[116] Moffatt, H. K. 1978, Magnetic field generation in electrically conducting fluids (Cambridge University Press)

[117] Mozer, F. S., Bale, S. D., Bonnell, J. W., et al. 2021, On the Origin of Switchbacks Observed in the Solar Wind, The Astrophysical Journal, 919, 60, doi: 10.3847/1538-4357/ac110d

[118] Mozer, F. S., Agapitov, O. V., Bale, S. D., et al. 2020, Switchbacks in the Solar Magnetic Field: Their Evolution, Their Content, and Their Effects on the Plasma, ApJ Supplements, 246, 68, doi: 10.3847/1538-4365/ab7196

[119] Müller, D., Marsden, R. G., St. Cyr, O. C., & Gilbert, H. R. 2013, Solar Orbiter

. Exploring the Sun-Heliosphere Connection, Solar Physics, 285, 25, doi: 10.1007/s11207-012-0085-7

[120] Müller, D., St. Cyr, O. C., Zouganelis, I., et al. 2020, The Solar Orbiter mission. Science overview, Astronomy and Astrophysics, 642, A1, doi: 10.1051/0004-6361/202038467

[121] Nash, A. G., Sheeley, N. R., J., & Wang, Y. M. 1988, Mechanisms for the Rigid Rotation of Coronal Holes, Solar Physics, 117, 359, doi: 10.1007/BF00147253

[122] Neugebauer, M., & Snyder, C. W. 1966, Mariner 2 Observations of the Solar Wind, 1, Average Properties, Journal of Geophysical Research, 71, 4469, doi: 10.1029/JZ071i019p04469

[123] Nguyen, G., Aunai, N., Michotte de Welle, B., et al. 2022a, Massive Multi-Mission Statistical Study and Analytical Modeling of the Earth's Magnetopause: 2. Shape and Location, Journal of Geophysical Research (Space Physics), 127, e29774, doi: 10.1029/2021JA029774

[124] —. 2022b, Massive Multi-Mission Statistical Study and Analytical Modeling of the Earth's Magnetopause: 3. An Asymmetric Non Indented Magnetopause Analytical Model, Journal of Geophysical Research (Space Physics), 127, e30112, doi: 10.1029/2021JA030112

[125] Nieves-Chinchilla, T., Szabo, A., Korreck, K. E., et al. 2020, Analysis of the Internal Structure of the Streamer Blowout Observed by the Parker Solar Probe During the First Solar Encounter, ApJ Supplements, 246, 63, doi: 10.3847/1538-4365/ab61f5

[126] Nishida, A. 1989, Can random reconnection on the magnetopause produce the low latitude boundary layer?, Geophysical Research Letters, 16, 227, doi: 10.1029/GL016i003p00227

[127] Nordlund, Å., Stein, R. F., & Asplund, M. 2009, Solar Surface Convection, Living Reviews in Solar Physics, 6, 2, doi: 10.12942/lrsp-2009-2

[128] Odstrcil, D., Pizzo, V. J., Linker, J. A., et al. 2004, Initial coupling of coronal and heliospheric numerical magnetohydrodynamic codes, Journal of Atmospheric and Solar-Terrestrial Physics, 66, 1311, doi: 10.1016/j.jastp.2004.04.007

[129] Øieroset, M., Phan, T. D., Eastwood, J. P., et al. 2011, Direct Evidence for a Three-Dimensional Magnetic Flux Rope Flanked by Two Active Magnetic Reconnection X Lines at Earth's Magnetopause, Physical Review Letters, 107, 165007, doi: 10.1103/PhysRevLett.107.165007

[130] Øieroset, M., Phan, T. D., Haggerty, C., et al. 2016, MMS observations of large guide field symmetric reconnection between colliding reconnection jets at the center of a magnetic flux rope at the magnetopause, Geophysical Research Letters, 43, 5536, doi: 10.1002/2016GL069166

[131] Øieroset, M., Phan, T. D., Drake, J. F., et al. 2019, Reconnection With Magnetic Flux Pileup at the Interface of Converging Jets at the Magnetopause, Geophysical Research Letters, 46, 1937, doi: 10.1029/2018GL080994

[132] Øieroset, M., Phan, T. D., Ergun, R., et al. 2021, Spatial evolution of magnetic reconnection diffusion region structures with distance from the X-line, Physics of Plasmas, 28, 122901, doi: 10.1063/5.0072182

[133] Otto, A. 1995, Forced three-dimensional magnetic reconnection due to linkage of magnetic flux tubes, Journal of Geophysical Research, 100, 11863, doi: 10.1029/94JA03341

[134] Owen, C. J., Bruno, R., Livi, S., et al. 2020, The Solar Orbiter Solar Wind Analyser (SWA) suite, Astronomy and Astrophysics, 642, A16, doi: 10.1051/0004-6361/201937259

[135] Owens, M., Lockwood, M., Macneil, A., & Stansby, D. 2020, Signatures of Coronal Loop Opening via Interchange Reconnection in the Slow Solar Wind at 1 AU, Solar Physics, 295, 37, doi: 10.1007/s11207-020-01601-7

[136] Owens, M. J., Lockwood, M., Barnard, L. A., & MacNeil, A. R. 2018, Generation of Inverted Heliospheric Magnetic Flux by Coronal Loop Opening and Slow Solar Wind Release, ApJ Letters, 868, L14, doi: 10.3847/2041-8213/aaee82

[137] Page, B., Bale, S. D., Bonnell, J. W., et al. 2020, Examining Dust Directionality with the Parker Solar Probe FIELDS Instrument, ApJ Supplements, 246, 51, doi: 10.3847/1538-4365/ab5f6a

[138] Parker, E. N. 1957, Sweet's Mechanism for Merging Magnetic Fields in Conducting Fluids, Journal of Geophysical Research, 62, 509, doi: 10.1029/JZ062i004p00509

[139] —. 1958, Dynamics of the Interplanetary Gas and Magnetic Fields., The Astrophysical Journal, 128, 664, doi: 10.1086/146579

[140] —. 1979, Cosmical magnetic fields. Their origin and their activity (Oxford university press)

[141] Paschmann, G., Haerendel, G., Papamastorakis, I., et al. 1982, Plasma and magnetic field characteristics of magnetic flux transfer events, Journal of Geophysical Research, 87, 2159, doi: 10.1029/JA087iA04p02159

[142] Paschmann, G., Øieroset, M., & Phan, T. 2013, In-Situ Observations of Reconnection in Space, Space Science Review, 178, 385, doi: 10.1007/s11214-012-9957-2

[143] Petrinec, S. M., Trattner, K. J., Fuselier, S. A., & Stovall, J. 2014, The steepness of the magnetic shear angle "saddle": A parameter for constraining the location of dayside magnetic reconnection?, Journal of Geophysical Research (Space Physics), 119, 8404, doi: 10.1002/2014JA020209

[144] Phan, T. D., Gosling, J. T., & Davis, M. S. 2009, Prevalence of extended reconnection X-lines in the solar wind at 1 AU, Geophysical Research Letters, 36, L09108, doi: 10.1029/2009GL037713

[145] Phan, T. D., Paschmann, G., Gosling, J. T., et al. 2013, The dependence of magnetic reconnection on plasma β and magnetic shear: Evidence from magnetopause observations, Geophysical Research Letters, 40, 11, doi: 10.1029/2012GL054528

[146] Phan, T. D., Gosling, J. T., Paschmann, G., et al. 2010, The Dependence of Magnetic Reconnection on Plasma β and Magnetic Shear: Evidence from Solar Wind Observations, ApJ Letters, 719, L199, doi: 10.1088/2041-8205/719/2/L199

[147] Phan, T. D., Bale, S. D., Eastwood, J. P., et al. 2020, Parker Solar Probe In Situ Observations of Magnetic Reconnection Exhausts during Encounter 1, ApJ Supplements, 246, 34, doi: 10.3847/1538-4365/ab55ee

[148] Phan, T. D., Lavraud, B., Halekas, J. S., et al. 2021, Prevalence of magnetic reconnection in the near-Sun heliospheric current sheet, Astronomy and Astrophysics, 650, A13, doi: 10.1051/0004-6361/202039863

[149] Pinto, R. F., Poirier, N., Rouillard, A. P., et al. 2021, Solar wind rotation rate and shear at coronal hole boundaries. Possible consequences for magnetic field inversions, Astronomy and Astrophysics, 653, A92, doi: 10.1051/0004-6361/202040180

[150] Poirier, N., Rouillard, A. P., Kouloumvakos, A., et al. 2021, Exploiting white-light observations to improve estimates of magnetic connectivity, Frontiers in Astronomy and Space Sciences, 8, 84, doi: 10.3389/fspas.2021.684734

[151] Pollock, C., Moore, T., Jacques, A., et al. 2016, Fast Plasma Investigation for Magnetospheric Multiscale, Space Science Review, 199, 331, doi: 10.1007/s11214-016-0245-4

[152] Raeder, J. 2006, Flux Transfer Events: 1. generation mechanism for strong southward IMF, Annales Geophysicae, 24, 381, doi: 10.5194/angeo-24-381-2006

[153] Réville, V., Velli, M., Panasenco, O., et al. 2020, The Role of Alfvén Wave Dynamics on the Large-scale Properties of the Solar Wind: Comparing an MHD Simulation with Parker Solar Probe E1 Data, ApJ Supplements, 246, 24, doi: 10.3847/1538-4365/ab4fef

[154] Réville, V., Fargette, N., Rouillard, A. P., et al. 2022, Flux rope and dynamics of the heliospheric current sheet. Study of the Parker Solar Probe and Solar Orbiter conjunction of June 2020, Astronomy and Astrophysics, 659, A110, doi: 10.1051/0004-6361/202142381

[155] Rieutord, M., Meunier, N., Roudier, T., et al. 2008, Solar supergranulation revealed by granule tracking, Astronomy and Astrophysics, 479, L17, doi: 10.1051/0004-6361:20079077

[156] Rieutord, M., & Rincon, F. 2010, The Sun's Supergranulation, Living Reviews in Solar Physics, 7, 2, doi: 10.12942/lrsp-2010-2

[157] Rieutord, M., Roudier, T., Rincon, F., et al. 2010, On the power spectrum of solar surface flows, Astronomy and Astrophysics, 512, A4, doi: 10.1051/0004-6361/200913303

[158] Rijnbeek, R. P., Cowley, S. W. H., Southwood, D. J., & Russell, C. T. 1984, A survey of dayside transfer events observed by ISEE 1 and 2 magnetometers, Journal of Geophysical Research, 89, 786, doi: 10.1029/JA089iA02p00786

[159] Rimmele, T. R., Warner, M., Keil, S. L., et al. 2020, The Daniel K. Inouye Solar Telescope - Observatory Overview, Solar Physics, 295, 172, doi: 10.1007/s11207-020-01736-7

[160] Rincon, F., & Rieutord, M. 2018, The Sun's supergranulation, Living Reviews in Solar Physics, 15, 6, doi: 10.1007/s41116-018-0013-5

[161] Roudier, T., Rieutord, M., Brito, D., et al. 2009, Mesoscale dynamics on the Sun's surface from HINODE observations, Astronomy and Astrophysics, 495, 945, doi: 10.1051/0004-6361:200811101

[162] Rouillard, A. P., Sheeley, N. R., J., Cooper, T. J., et al. 2011, The Solar Origin of Small Interplanetary Transients, The Astrophysical Journal, 734, 7, doi: 10.1088/0004-637X/734/1/7

[163] Rouillard, A. P., Kouloumvakos, A., Vourlidas, A., et al. 2020a, Relating Streamer Flows to Density and Magnetic Structures at the Parker Solar Probe, ApJ Supplements, 246, 37, doi: 10.3847/1538-4365/ab579a

[164] Rouillard, A. P., Pinto, R. F., Vourlidas, A., et al. 2020b, Models and data analysis tools for the Solar Orbiter mission, Astronomy and Astrophysics, 642, A2, doi: 10.1051/0004-6361/201935305

[165] Ruffolo, D., Matthaeus, W. H., Chhiber, R., et al. 2020, Shear-driven Transition to Isotropically Turbulent Solar Wind Outside the Alfvén Critical Zone, The Astrophysical Journal, 902, 94, doi: 10.3847/1538-4357/abb594

[166] Russell, C. T. 1990, Interplanetary magnetic field enhancements: Evidence for solar wind dust trail interactions, Advances in Space Research, 10, 159, doi: 10.1016/0273-1177(90)90343-X

[167] —. 1993, Magnetic fields of the terrestrial planets, Journal of Geophysical Research, 98, 18681, doi: 10.1029/93JE00981

[168] —. 2000, The Polar Cusp, Advances in Space Research, 25, 1413, doi: 10.1016/S0273-1177(99)00653-5

[169] Russell, C. T., Arghavani, M. R., & Luhmann, J. G. 1984, Interplanetary field enhancements in the solar wind: Statistical properties at 0.72 AU, Icarus, 60, 332, doi: 10.1016/0019-1035(84)90194-5

[170] Russell, C. T., Berchem, J., & Luhmann, J. G. 1985, On the source region of flux transfer events, Advances in Space Research, 5, 363, doi: 10.1016/0273-1177(85)90162-0

[171] Russell, C. T., & Elphic, R. C. 1978, Initial ISEE Magnetometer Results: Magnetopause Observations (Article published in the special issues: Advances in Magnetospheric Physics with GEOS- 1 and ISEE - 1 and 2.), Space Science Review, 22, 681, doi: 10.1007/BF00212619

[172] Russell, C. T., Jian, L. K., Lai, H. R., et al. 2010a, in American Institute of Physics Conference Series, Vol. 1216, Twelfth International Solar Wind Conference, ed. M. Mak-

simovic, K. Issautier, N. Meyer-Vernet, M. Moncuquet, & F. Pantellini, 522–525, doi: 10.1063/1.3395917

[173] Russell, C. T., Le, G., & Kuo, H. 1996, The occurrence rate of flux transfer events, Advances in Space Research, 18, 197, doi: 10.1016/0273-1177(95)00965-5

[174] Russell, C. T., Priest, E. R., & Lee, L. C. 1990, Physics of magnetic flux ropes, Washington DC American Geophysical Union Geophysical Monograph Series, 58, doi: 10.1029/GM058

[175] Russell, C. T., Weimer, D. R., Omidi, N., et al. 2010b, Interplanetary field enhancements travel at the solar wind speed, Geophysical Research Letters, 37, L07204, doi: 10.1029/2010GL042618

[176] Russell, C. T., Anderson, B. J., Baumjohann, W., et al. 2016, The Magnetospheric Multiscale Magnetometers, Space Science Review, 199, 189, doi: 10.1007/s11214-014-0057-3

[177] Sanchez-Diaz, E., Rouillard, A. P., Davies, J. A., et al. 2017, The Temporal and Spatial Scales of Density Structures Released in the Slow Solar Wind During Solar Activity Maximum, The Astrophysical Journal, 851, 32, doi: 10.3847/1538-4357/aa98e2

[178] Sanchez-Diaz, E., Rouillard, A. P., Lavraud, B., Kilpua, E., & Davies, J. A. 2019, In Situ Measurements of the Variable Slow Solar Wind near Sector Boundaries, The Astrophysical Journal, 882, 51, doi: 10.3847/1538-4357/ab341c

[179] Saunders, M. A., Russell, C. T., & Sckopke, N. 1984, Flux transfer events: Scale size and interior structure, Geophysical Research Letters, 11, 131, doi: 10.1029/GL011i002p00131

[180] Scholer, M. 1988, Magnetic flux transfer at the magnetopause based on single X line bursty reconnection, Geophysical Research Letters, 15, 291, doi: 10.1029/GL015i004p00291

[181] Schwadron, N. A., & McComas, D. J. 2021, Switchbacks Explained: Super-Parker Fields—The Other Side of the Sub-Parker Spiral, The Astrophysical Journal, 909, 95, doi: 10.3847/1538-4357/abd4e6

[182] Shoda, M., Chandran, B. D. G., & Cranmer, S. R. 2021, Turbulent Generation of Magnetic Switchbacks in the Alfvénic Solar Wind, The Astrophysical Journal, 915, 52, doi: 10.3847/1538-4357/abfdbc

[183] Shue, J. H., Chao, J. K., Fu, H. C., et al. 1997, A new functional form to study the solar wind control of the magnetopause size and shape, Journal of Geophysical Research, 102, 9497, doi: 10.1029/97JA00196

[184] Shue, J. H., Song, P., Russell, C. T., et al. 1998, Magnetopause location under extreme solar wind conditions, Journal of Geophysical Research, 103, 17691, doi: 10.1029/98JA01103

[185] Sibeck, D. G., Lopez, R. E., & Roelof, E. C. 1991, Solar wind control of the magnetopause shape, location, and motion, Journal of Geophysical Research, 96, 5489, doi: 10.1029/90JA02464

[186] Sisti, M. 2021, PhD thesis, Universita di Pisa

[187] Skoug, R. M., Gosling, J. T., McComas, D. J., Smith, C. W., & Hu, Q. 2006, Suprathermal electron 90° pitch angle depletions at reverse shocks in the solar wind, Journal of Geophysical Research (Space Physics), 111, A01101, doi: 10.1029/2005JA011316

[188] Sonnerup, B. U. O., & Cahill, L. J., J. 1967, Magnetopause Structure and Attitude from Explorer 12 Observations, Journal of Geophysical Research, 72, 171, doi: 10.1029/JZ072i001p00171

[189] Southwood, D. J., Farrugia, C. J., & Saunders, M. A. 1988, What are flux transfer events?, Planetary and Space Science, 36, 503, doi: 10.1016/0032-0633(88)90109-2

[190] Spiegel, E. A., & Zahn, J. P. 1992, The solar tachocline., Astronomy and Astrophysics, 265, 106

[191] Squire, J., Chandran, B. D. G., & Meyrand, R. 2020, In-situ Switchback Formation in the Expanding Solar Wind, ApJ Letters, 891, L2, doi: 10.3847/2041-8213/ab74e1

[192] Stansby, D., Berčič, L., Matteini, L., et al. 2021, Sensitivity of solar wind mass flux to coronal temperature, Astronomy and Astrophysics, 650, L2, doi: 10.1051/0004-6361/202039789

[193] Steinberg, J. T., Gosling, J. T., Skoug, R. M., & Wiens, R. C. 2005, Suprathermal electrons in high-speed streams from coronal holes: Counterstreaming on open field lines at 1 AU, Journal of Geophysical Research (Space Physics), 110, A06103, doi: 10.1029/2005JA011027

[194] Sterling, A. C., & Moore, R. L. 2020, Coronal-jet-producing Minifilament Eruptions as a Possible Source of Parker Solar Probe Switchbacks, ApJ Letters, 896, L18, doi: 10.3847/2041-8213/ab96be

[195] Suess, S. T., Phillips, J. L., McComas, D. J., et al. 1998, The Solar Wind - Inner Heliosphere, Space Science Review, 83, 75

[196] Swisdak, M., Opher, M., Drake, J. F., & Alouani Bibi, F. 2010, The Vector Direction of the Interstellar Magnetic Field Outside the Heliosphere, The Astrophysical Journal, 710, 1769, doi: 10.1088/0004-637X/710/2/1769

[197] Swisdak, M., Rogers, B. N., Drake, J. F., & Shay, M. A. 2003, Diamagnetic suppression of component magnetic reconnection at the magnetopause, Journal of Geophysical Research (Space Physics), 108, 1218, doi: 10.1029/2002JA009726

[198] Szabo, A., Larson, D., Whittlesey, P., et al. 2020, The Heliospheric Current Sheet in the Inner Heliosphere Observed by the Parker Solar Probe, ApJ Supplements, 246, 47, doi: 10.3847/1538-4365/ab5dac

[199] Szalay, J. R., Pokorný, P., Bale, S. D., et al. 2020, The Near-Sun Dust Environment: Initial Observations from Parker Solar Probe, ApJ Supplements, 246, 27, doi: 10.3847/1538-4365/ab50c1

[200] Tenerani, A., Sioulas, N., Matteini, L., et al. 2021, Evolution of Switchbacks in the Inner Heliosphere, ApJ Letters, 919, L31, doi: 10.3847/2041-8213/ac2606

[201] Tenerani, A., Velli, M., Matteini, L., et al. 2020, Magnetic Field Kinks and Folds in the Solar Wind, ApJ Supplements, 246, 32, doi: 10.3847/1538-4365/ab53e1

[202] Thieme, K. M., Schwenn, R., & Marsch, E. 1989, Are structures in high-speed streams signatures of coronal fine structures?, Advances in Space Research, 9, 127, doi: 10.1016/0273-1177(89)90105-1

[203] Tilquin, H., Eastwood, J. P., & Phan, T. D. 2020, Solar Wind Reconnection Exhausts in the Inner Heliosphere Observed by Helios and Detected via Machine Learning, The Astrophysical Journal, 895, 68, doi: 10.3847/1538-4357/ab8812

[204] Torbert, R. B., Russell, C. T., Magnes, W., et al. 2016, The FIELDS Instrument Suite on MMS: Scientific Objectives, Measurements, and Data Products, Space Science Review, 199, 105, doi: 10.1007/s11214-014-0109-8

[205] Torrence, C., & Compo, G. P. 1998, A Practical Guide to Wavelet Analysis., Bulletin of the American Meteorological Society, 79, 61, doi: 10.1175/1520-0477(1998)079<0061:APGTWA>2.0.CO;2

[206] Trattner, K. J., Mulcock, J. S., Petrinec, S. M., & Fuselier, S. A. 2007, Probing the boundary between antiparallel and component reconnection during southward interplanetary magnetic field conditions, Journal of Geophysical Research (Space Physics), 112, A08210, doi: 10.1029/2007JA012270

[207] Trattner, K. J., Petrinec, S. M., Fuselier, S. A., Omidi, N., & Sibeck, D. G. 2012, Evidence of multiple reconnection lines at the magnetopause from cusp observations, Journal of Geophysical Research (Space Physics), 117, A01213, doi: 10.1029/2011JA017080

[208] van Ballegooijen, A. A., & Asgari-Targhi, M. 2016, Heating and Acceleration of the Fast Solar Wind by Alfvén Wave Turbulence, The Astrophysical Journal, 821, 106, doi: 10.3847/0004-637X/821/2/106

[209] Velli, M., Grappin, R., & Mangeney, A. 1989, Turbulent cascade of incompressible unidirectional Alfvén waves in the interplanetary medium, Physical Review Letters, 63, 1807, doi: 10.1103/PhysRevLett.63.1807

[210] Verscharen, D., Klein, K. G., & Maruca, B. A. 2019, The multi-scale nature of the solar wind, Living Reviews in Solar Physics, 16, 5, doi: 10.1007/s41116-019-0021-0

[211] Vourlidas, A., Howard, R. A., Plunkett, S. P., et al. 2016, The Wide-Field Imager for Solar Probe Plus (WISPR), Space Science Review, 204, 83, doi: 10.1007/s11214-014-0114-y

[212] Wang, Y., Shen, C., Liu, R., et al. 2018, Understanding the Twist Distribution Inside Magnetic Flux Ropes by Anatomizing an Interplanetary Magnetic Cloud, Journal of Geophysical Research (Space Physics), 123, 3238, doi: 10.1002/2017JA024971

[213] Wang, Y. L., Elphic, R. C., Lavraud, B., et al. 2006, Dependence of flux transfer events on solar wind conditions from 3 years of Cluster observations, Journal of Geophysical Research (Space Physics), 111, A04224, doi: 10.1029/2005JA011342

[214] Wang, Y. M. 1994, Two Types of Slow Solar Wind, ApJ Letters, 437, L67, doi: 10.1086/187684

[215] Wang, Y.-M., Hawley, S. H., & Sheeley, Neil R., J. 1996, The Magnetic Nature of Coronal Holes, Science, 271, 464, doi: 10.1126/science.271.5248.464

[216] Wang, Y. M., Nash, A. G., & Sheeley, N. R., J. 1989, Magnetic Flux Transport on the Sun, Science, 245, 712, doi: 10.1126/science.245.4919.712

[217] Wang, Y. M., & Sheeley, N. R., J. 2004, Footpoint Switching and the Evolution of Coronal Holes, The Astrophysical Journal, 612, 1196, doi: 10.1086/422711

[218] Wedemeyer-Böhm, S., Lagg, A., & Nordlund, Å. 2009, Coupling from the Photosphere to the Chromosphere and the Corona, Space Science Review, 144, 317, doi: 10.1007/s11214-008-9447-8

[219] Whittlesey, P. L., Larson, D. E., Kasper, J. C., et al. 2020, The Solar Probe ANalyzers—Electrons on the Parker Solar Probe, ApJ Supplements, 246, 74, doi: 10.3847/1538-4365/ab7370

[220] Woodham, L. D., Horbury, T. S., Matteini, L., et al. 2021, Enhanced proton parallel temperature inside patches of switchbacks in the inner heliosphere, Astronomy and Astrophysics, 650, L1, doi: 10.1051/0004-6361/202039415

[221] Woolley, T., Matteini, L., Horbury, T. S., et al. 2020, Proton core behaviour inside magnetic field switchbacks, Monthly Notices of the Royal Astronomical Society, 498, 5524, doi: 10.1093/mnras/staa2770

[222] Xu, F., & Borovsky, J. E. 2015, A new four-plasma categorization scheme for the solar wind, Journal of Geophysical Research (Space Physics), 120, 70, doi: 10.1002/2014JA020412

[223] Yamauchi, Y., Suess, S. T., Steinberg, J. T., & Sakurai, T. 2004, Differential velocity between solar wind protons and alpha particles in pressure balance structures, Journal of Geophysical Research (Space Physics), 109, A03104, doi: 10.1029/2003JA010274

[224] Young, D. T., Burch, J. L., Gomez, R. G., et al. 2016, Hot Plasma Composition Analyzer for the Magnetospheric Multiscale Mission, Space Science Review, 199, 407, doi: 10.1007/s11214-014-0119-6

[225] Zank, G. P., Nakanotani, M., Zhao, L. L., Adhikari, L., & Kasper, J. 2020, The Origin of Switchbacks in the Solar Corona: Linear Theory, The Astrophysical Journal, 903, 1, doi: 10.3847/1538-4357/abb828

[226] Zurbuchen, T. H., & Richardson, I. G. 2006, In-Situ Solar Wind and Magnetic Field Signatures of Interplanetary Coronal Mass Ejections, Space Science Review, 123, 31, doi: 10.1007/s11214-006-9010-4